



UNIVERSITÀ DEGLI STUDI DI MILANO

SCUOLA DI DOTTORATO  
FISICA, ASTROFISICA E FISICA APPLICATA

DIPARTIMENTO  
SCIENZE MOLECOLARI APPLICATE AI BIOSISTEMI

CORSO DI DOTTORATO DI RICERCA IN  
FISICA, ASTROFISICA E FISICA APPLICATA  
CICLO XXIII

**MAGNETIC PROPERTIES OF NOVEL  
NANOSTRUCTURED MATERIALS: FUNDAMENTAL  
ASPECTS AND BIOMEDICAL APPLICATIONS  
TOWARD THERANOSTICS**

Settore Scientifico disciplinare FIS/07

Tesi di Dottorato di:  
Houshang Amiri Doumari

Supervisore: Prof. Alessandro Lascialfari  
Coordinatore: Prof. Marco Bersanelli

A.A. 2009-2010

**Dedicated to:**

My beloved wife & Our upcoming little angle;

My family, All whom they love & All who love them;

My teachers.

## Acknowledgments

It is a pleasure to thank those who made this research possible. First and foremost, I am heartily thankful to my supervisor, Prof. Alessandro Lascialfari, whose guidance and support from the beginning to the end enabled me to get the present work done. Of course this thesis would not have been possible without having invaluable discussions with him.

It was an honor for me to have many discussions with Prof. Ferdinando Borsa regarding the fundamental aspects of the research and I owe my deepest gratitude to him.

I feel fortunate to have been at the NMR/MRI laboratory of physics department at Pavia University. The lab provided a fantastically friendly environment and I would like to thank the entire group and its director Prof. Maurizio Corti for making available his support in a number of ways.

I would also like to express my deep thanks to Dr. Manuel Mariani who supported me very kindly at the beginning of the project to get started the experiments.

I am grateful to the NMR group of Department of Molecular Sciences Applied to Biosystems, University of Milan and special thanks are due to Dr. Paolo Arosio and Dr. Francesco Orsini for their invaluable supports.

Dr. Morteza Mahmoudi from Institute for Nanoscience and Nanotechnology, Sharif University of Technology, Tehran-Iran, is appreciatively acknowledged for synthesizing the CNCs.

Prof. Fernando Palacio, Dr. Angel Millan, and Dr. Rodney Bustamante from Instituto de Ciencia de Materiales de Aragón, CSIC-Universidad de Zaragoza-Spain, are gratefully acknowledged for synthesizing the bio-ferrofluids and useful discussions.

The Italian Ministry of University and Research and the Consortium for Science and Technology of Materials (INSTM) are specially acknowledged for the financial support of the research.

Last but certainly not least, I offer my regards and blessings to all of those who supported me in any respect during the completion of the thesis, specially my beloved family.

---

## Contents

|                   |   |
|-------------------|---|
| Introduction..... | 1 |
|-------------------|---|

### **Chapter I: Introduction to NMR and MRI**

|                                                        |    |
|--------------------------------------------------------|----|
| 1.1 Nuclear Magnetic Resonance (NMR).....              | 4  |
| 1.2 Magnetic Materials in a Static Magnetic Field..... | 5  |
| 1.3 Magnetization and Radio Frequency Pulses.....      | 7  |
| 1.4 NMR Signal.....                                    | 11 |
| 1.5 Magnetic Resonance Imaging (MRI).....              | 12 |
| 1.5.1 Pulse Sequences.....                             | 14 |
| 1.6 References.....                                    | 20 |

### **Chapter II: MRI Contrast Agents**

|                                                      |    |
|------------------------------------------------------|----|
| 2.1 Image Contrast.....                              | 21 |
| 2.2 Magnetic Materials.....                          | 22 |
| 2.2.1 Nanoparticles and Single Domain Particles..... | 24 |
| 2.2.2 Magnetic Anisotropy of Nanoparticles.....      | 26 |
| 2.2.3 Superparamagnetism.....                        | 27 |
| 2.3 MRI Contrast Agents.....                         | 32 |
| 2.3.1 Introduction.....                              | 32 |
| 2.3.2 Positive and Negative CAs.....                 | 33 |
| 2.4 Relaxation Mechanisms of CAs.....                | 35 |
| 2.4.1 Paramagnetic Relaxation.....                   | 36 |
| 2.4.2 Superparamagnetic Relaxation.....              | 40 |
| 2.5 References.....                                  | 41 |

### **Chapter III: Materials and Methods**

|                                      |    |
|--------------------------------------|----|
| 3.1 Samples.....                     | 47 |
| 3.2 Magnetic Properties.....         | 54 |
| 3.2.1 SQUID-Based Magnetometers..... | 54 |
| 3.2.2 NMR Relaxometers.....          | 58 |
| 3.2.3 MRI Scanner.....               | 62 |
| 3.3 References.....                  | 64 |

### **Chapter IV: Experimental Results and Discussion**

|                                            |    |
|--------------------------------------------|----|
| 4.1 Bio-Ferrofluids.....                   | 67 |
| 4.1.1 TEM and X-Ray Characterizations..... | 67 |
| 4.1.2 SQUID Magnetometry.....              | 69 |
| 4.1.3 NMR Relaxometry.....                 | 71 |
| 4.1.4 In Vitro MRI Experiments.....        | 76 |

|                                              |    |
|----------------------------------------------|----|
| 4.2 CNCs.....                                | 76 |
| 4.2.1 Characterizations.....                 | 76 |
| 4.2.2 SQUID Magnetometry.....                | 78 |
| 4.2.3 NMR Relaxometry.....                   | 80 |
| 4.2.4 In Vitro MRI Experiments.....          | 84 |
| 4.2.5 Cell Endocytosis and Drug Release..... | 84 |
| 4.3 References.....                          | 86 |

## **Chapter V: Conclusions and Future Directions**

|                                                           |     |
|-----------------------------------------------------------|-----|
| 5.1 Conclusions.....                                      | 89  |
| 5.2 Future Directions .....                               | 92  |
| 5.3 References.....                                       | 92  |
| <i>Appendix A: Some Details About MRI</i> .....           | 93  |
| <i>Appendix B: Presentations &amp; Publications</i> ..... | 100 |

## Introduction

Due to its possibility of noninvasive, three-dimensional examination of biological events in living organisms and its capability to formulate diagnosis and follow treatments, magnetic resonance imaging (MRI) has been recognized as a powerful technique in medicine [1-4]. In order to increase the contrast of the MRI images, which is essential for a better and more precise detection, contrast agents (CAs) can be used [5,6].

The gadolinium chelates are the most common compounds used as CAs: they are characterized by a strong paramagnetism due to the seven unpaired electrons, thus giving a source of shortening of the longitudinal  $T_1$  and transverse  $T_2$  nuclear relaxation times. However, the recently acquired good control in the synthesis of superparamagnetic (SP) compounds [5-7] have given new perspectives to the use of low-toxicity novel and possibly multifunctional CAs. The ideal multifunctional SP-based compounds should be able to have applications not only in the diagnostics, e.g. MRI, but also in the treatment, e.g. drug delivery and hyperthermia. In this regard, superparamagnetic iron oxide nanoparticles (SPIONs), are the most promising candidate, not only for their efficacy in enhancing magnetic resonance image contrast but also for their high biocompatibility [8,9].

The SPIONs are currently commercially produced. Endorem<sup>®</sup> (by Guerbet Group, Feridex in the USA) is one of the most known commercial MRI contrast agents and it is constituted by a magnetic core (diameter  $\sim 6\div 7$ nm) of mixed  $\gamma$ - $\text{Fe}_2\text{O}_3$  and  $\text{Fe}_3\text{O}_4$  oxides coated with dextran, giving a nanoparticle which has an average  $\sim 150$  nm hydrodynamic diameter. Despite the undoubted efficacy of Endorem<sup>®</sup>, problems of reproducibility of the MR images are often encountered, possibly because the nanoparticles present high polydispersity and different batches of sample possess different mix of the two iron oxides. The limited reproducibility together with the necessity of obtaining systems with better controlled microscopic properties, have motivated many research groups to synthesize new monodispersed SPIONs families.

The central idea of the research activity reported in the thesis has been the study of novel magnetic nanoparticles (MNP) for application as contrast agent (CA) in MRI and future other diagnostics and therapeutics, such as optical imaging, targeted drug delivery, and magnetic hyperthermia. A second part of research was related to fundamental aspects of magnetism, in which the spin dynamics and magnetic properties of molecular nanomagnets were studied. Concerning the second part of research we have just reported the related publications [10,11] in the Appendix B while in the main body of the thesis we will focus on the application part of the research, i.e. biomedical applications of MNPs.

To test the efficiency of new samples in contrasting the MR images, we have investigated magnetic and relaxometric properties of two different types of novel superparamagnetic nanoparticles:

1. *Polymer-based nanostructured bio-ferrofluids.* These materials, in brief bio-ferrofluids, are candidates for the hyperthermia, optical imaging, and MRI. Bio-ferrofluids are a series of novel maghemite/polymer composite ferrofluids with variable magnetic core size. Our investigations have shown that they have a good

efficiency as MRI CAs. These biocompatible ferrofluids, which contain anchoring groups for bio-functionalization, can incorporate fluorescent dyes and have shown low cellular toxicity in previous studies. Therefore, they can be proposed as possible platforms for multifunctional biomedical applications. The NMRD profiles showed that the efficiency parameter, i.e. the nuclear transverse relaxivity  $r_2$ , for particles with sizes greater than 10nm assumes values comparable with or better than the ones of commercial samples. The best results have been obtained in particles with the biggest magnetic core. The MRI *in-vitro* experiments, at  $\nu=8.5$  MHz, using the gradient-echo and spin-echo sequences have confirmed the NMRD results, thus allowing us to suggest these superparamagnetic nanoparticles as novel multifunctional materials.

2. *Superparamagnetic colloidal nano-crystal clusters*. These compounds are candidates for the targeted drug delivery and MRI. They are a novel class of superparamagnetic colloidal nano-crystal clusters (CNCs) coated with different biocompatible coatings such as polyethylene glycol fumarate (PEGF). We have investigated cell endocytosis, drug release, NMR relaxometry and *in vitro* MRI of CNCs with various biocompatible coatings. It is shown that the transverse relaxivity  $r_2$  for the PVA-coated, PEGF-coated, and crosslinked PEGF-coated CNCs is efficient enough to contrast suitably the magnetic resonance images. The same samples have shown a good ability also in controlled drug releasing (particularly the crosslinked PEGF-coated compound), thus finally allowing us to propose this class of compounds for future applications in theranostics, i.e., therapy and diagnostics with the same compound.

By means of the work done in this thesis, we were able to conclude that both classes of compounds investigated can be proposed as novel theranostic, i.e. therapy and diagnostics with the same compound, agents.

## References

- [1] E. M. Haacke, R. W. Brown, M. R. Thompson and R. Venkatesan, in *"Magnetic Resonance Imaging. Physical Principles and Sequence Design"*, ed. Wiley-Liss, (1999).
- [2] M. V. Yigit, D. Mazumdar and Y. Lu, *Bioconjugate Chemistry*, **19**, 412-417, (2008).
- [3] J. Lee, M. J. Zylka, D. J. Anderson, J. E. Burdette, T. K. Woodruff and T. J. Meade, *Journal of the American Chemical Society*, 2005, **127**, 13164-13166.
- [4] L. Frullano, B. Tejerina and T. J. Meade, *Inorganic Chemistry*, 2006, **45**, 8489-8491.
- [5] *see various contributions in "The Chemistry of Contrast Agents in Medical Magnetic Resonance Imaging"*, ed. A.E. Merbach and E. Toth, J. Wiley and sons, (2001).

- [6] M. Mahmoudi, M. Hosseinkhani, S. Laurent, A. Simchi, H. Hosseinkhani, W. S. Journeay, K. Subramani and S. Broutry, *Chemical Reviews*, Accepted (2010).
- [7] A. G. Roca, R. Costo, A. F. Rebolledo, S. Veintemillas-Verdaguer, P. Tartaj, T. Gonzalez-Carreno, M. P. Morales and C. J. Serna, *J. Phys. D: Appl. Phys.*, **42**, 224002, (2009).
- [8] L. Josephson, J. Lewis, P. Jacobs, P. F. Hahn and D. D. Stark, *Magnetic Resonance Imaging*, 1988, **6**, 647-653, (2010).
- [9] M. Mahmoudi, S. Sant, B. Wang and T. Sen, *Advanced Drug Delivery Reviews*, **doi:10.1016/j.addr.2010.05.006**, (2010).
- [10] H. Amiri, M. Mariani, A. Lascialfari, F. Borsa, G. A. Timco, F. Tuna, and R. E. P. Winpenny, "Magnetic properties and spin dynamics in the Cr<sub>7</sub>Fe nanomagnet: A heterometallic antiferromagnetic molecular ring" *Journal of Phys. Rev. B*, **81**, 104408, (2010).
- [11] H. Amiri, A. Lascialfari, F. Borsa, "Comparison of the magnetic properties and the spin dynamics in heterometallic antiferromagnetic molecular nanomagnets", *Phys. Rev. B*, **82**, 144421, (2010)



---

A decorative graphic of a scroll with a black outline and a light gray shadow. The scroll is unrolled on the left side and has a small circular tab on the right side. The text is centered within the scroll.

# **Chapter I**

## **Introduction to NMR and MRI**

## Chapter I

# Introduction to NMR and MRI

### *Contents*

---

|                                                        |    |
|--------------------------------------------------------|----|
| 1.1 Nuclear Magnetic Resonance (NMR).....              | 4  |
| 1.2 Magnetic Materials in a Static Magnetic Field..... | 5  |
| 1.3 Magnetization and Radio Frequency Pulses.....      | 7  |
| 1.4 NMR Signal.....                                    | 11 |
| 1.5 Magnetic Resonance Imaging (MRI).....              | 12 |
| 1.5.1 Pulse Sequences.....                             | 14 |
| 1.6 References.....                                    | 20 |

---

## 1.1 Nuclear Magnetic Resonance (NMR)

Nuclear Magnetic Resonance (NMR) is a technique that uses a static magnetic field  $B_0$  and a Radio Frequency (rf) pulsed field  $B_1$ , which cause a specific kind of nuclei to absorb energy from the rf pulse and radiate this energy back out. The energy radiated back out is at a specific resonance frequency which depends on the strength of the magnetic field  $B_0$ . The received signal depends also on other experimental factors such as electronic noise, amplifier gain, receiver gain, etc. This allows the observation of specific quantum mechanical magnetic properties of an atomic nucleus. Many scientists exploit NMR phenomena to study molecules, liquids, crystals and non-crystalline materials. NMR with additional magnetic field gradients is also routinely used in advanced medical imaging, the so called Magnetic Resonance Imaging (MRI).

Spin is an intrinsic property of some atomic nuclei. Stern-Gerlach experiment, in which a beam of silver atoms were passed through a magnetic field and split into two beams, was the first approach to the existence of the spin in 1922. The two beams represent two spin states, up  $|\uparrow\rangle$  and down  $|\downarrow\rangle$  of the silver nuclei. The nuclear "spin"

represents the total intrinsic angular momentum and is represented by the vectorial symbol  $\mathbf{I}$ . According to the quantum mechanics laws, we can know simultaneously the length of  $\mathbf{I}$ , together with only one of its components, conventionally assumed as the z-component  $I_z$ , that is:

$$|\mathbf{I}|^2 = \hbar^2 [I(I+1)] \quad 1.1$$

$$I_z = \hbar m \quad 1.2$$

where  $I$  is the spin quantum number,  $m = (-I, -I+1, \dots, I-1, I)$  is the magnetic quantum number and  $\hbar$  is Planck's constant divided by  $2\pi$ . In the case of spin 1/2 nuclei ( $I = 1/2$ ), like the two most abundant silver isotopes or  $^1\text{H}$ ,  $m$  can only be equal to  $-1/2$  or  $1/2$ . A magnetic moment,  $\boldsymbol{\mu}$ , is associated to each nucleus with spin angular momentum, by the formula:

$$\boldsymbol{\mu} = \gamma \mathbf{I} \quad 1.3$$

Using the Eq. 1.2 we will have:

$$\mu_z = \gamma I_z = \gamma \hbar m \quad 1.4$$

where  $\gamma$  is the gyromagnetic ratio (magnetogyric ratio), an intrinsic property of each nucleus. At fixed abundance, nuclei with higher values of  $\gamma$  have higher sensitivity and, as a consequence, NMR spectra with better signal-to-noise (SNR) ratio. In fact,  $^1\text{H}$  is the most commonly used isotope in magnetic resonance because of his abundance and sensitivity.

## 1.2 Magnetic Materials in a Static Magnetic Field

For performing a NMR experiment, a sample is placed into a static magnetic field of magnitude  $B_0$ . The energy of a magnetic moment  $\boldsymbol{\mu}$  immersed in  $B_0$  is given by:

$$E = -\boldsymbol{\mu} \cdot \mathbf{B}_0 \quad 1.5$$

The  $z$  axis is conventionally chosen along  $\mathbf{B}_0$  so that:

$$\mathbf{B}_0 = B_0 \mathbf{k} \quad 1.6$$

The energy of one isolated nuclear spin with magnetic moment  $\boldsymbol{\mu}$ , with substitution of Eqs. 1.6 and 1.4 in Eq. 1.5, can be written as:

$$E = -\mu_z B_0 = -\gamma I_z B_0 \quad 1.7$$

Therefore, using Eq. 1.2, the energy of the spin state  $E_m$  with the specific quantum number  $m$  can be written as:

$$E_m = -m\gamma\hbar B_0 \quad 1.8$$

As typical case of materials let us now switch to a system composed of a collection of identical  $I=1/2$  nuclei; thus characterized by a total magnetic moment (i.e. nuclear magnetization)  $\mathbf{M} = \sum_i \boldsymbol{\mu}_i / V$ . We can re-apply the Eqs. 1.5-1.7 also to  $\mathbf{M}$  as we did for the  $\boldsymbol{\mu}$ .

As it is shown in Fig. 1.1, in zero field, the net magnetic moment of the system is zero, because the up  $|\uparrow\rangle$  and down  $|\downarrow\rangle$  states have the same energy and are equally populated. As sample feel an external magnetic field, a non-zero energy difference between the states (known as the *Zeeman splitting*) will appear, which by using Eq. 1.8 can be expressed as:

$$\Delta E = E_{|\downarrow\rangle} - E_{|\uparrow\rangle} = \gamma\hbar B_0 \quad 1.9$$

According to the Boltzmann distribution, just a *small* excess of nuclei fall into the lower energy  $|\uparrow\rangle$  state:

$$\frac{N_{|\uparrow\rangle}}{N_{|\downarrow\rangle}} = \exp\left(\frac{\Delta E}{k_B T}\right) \quad 1.10$$

where  $k_B$  is the Boltzmann's constant,  $T$  is the absolute temperature and  $N_{|\uparrow\rangle} / N_{|\downarrow\rangle}$  is the ratio between the populations of the states.

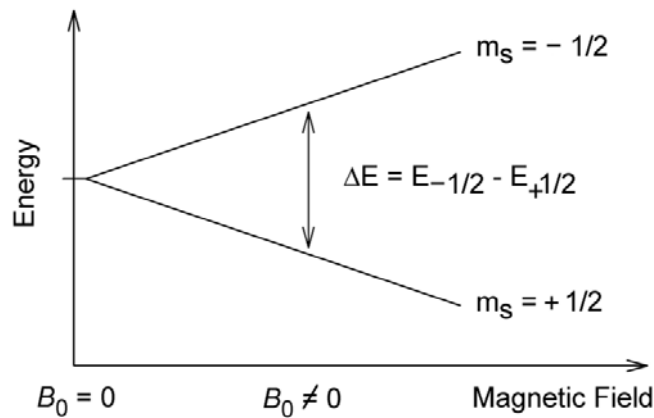


FIG. 1.1 Splitting of nuclei spin states in an external magnetic field.

As an example, the fractional population difference at equilibrium at  $B_0=1.5$  Tesla and 300 K is:

$$\frac{N_{|\uparrow\rangle} - N_{|\downarrow\rangle}}{N_{|\uparrow\rangle} + N_{|\downarrow\rangle}} = 5 \times 10^{-6} \quad 1.11$$

If now a rf field  $B_1$  at frequency  $\neq B_0$  is applied, the NMR signal, after switching off  $B_1$ , is produced by this very low number of excited nuclei.

### 1.3 Magnetization and Radio Frequency Pulses

From Planck's law,  $\Delta E = h\nu$ , and Eq. 1.9, the frequency  $\nu_0$  of an NMR transition in a magnetic field  $B_0$  is:

$$\nu_0 = \frac{\Delta E}{h} = \frac{\gamma B_0}{2\pi} \quad 1.12$$

or, given  $\nu_0 = \omega / 2\pi$ ,

$$\omega_0 = \gamma B_0 \quad 1.13$$

where  $\omega_0$  or  $\nu_0$  is called *Larmor frequency* (rad/sec or Hz),  $B_0$  is the static field strength (Tesla) [1].

When rf pulses, producing an electromagnetic field, are transmitted in a plane perpendicular to  $\mathbf{B}_0$ , NMR transitions are induced [2]. It is conventional to represent the oscillatory rf field as a sum of two circularly polarized components, each of amplitude  $B_1$ , counter-rotating in the  $xy$ -plane at angular velocity  $\omega$ . One of these components will rotate in the same sense of the nuclear spin precession:

$$\mathbf{B}_1(t) = B [\cos(\omega t)\mathbf{i} - \sin(\omega t)\mathbf{j}] \quad 1.14$$

This magnetic field is the responsible for the resonance phenomenon occurring when  $\omega = \omega_0$ . The counter-rotating component can be ignored provided that  $B_1 = B_0$ , which is invariably the case in NMR experiments.

The time dependence of  $\mathbf{M}(t)$  is deduced from a formula expressing the Larmor precession typical of classical (quantum) magnetic moments:

$$\frac{d\mathbf{M}(t)}{dt} = \gamma \mathbf{M}(t) \times \mathbf{B}(t) \quad 1.15$$

which is the equation of motion of  $\mathbf{M}$  in the laboratory reference frame and  $\mathbf{B}$  is the sum of the static field  $\mathbf{B}_0$  and the rotating rf field  $\mathbf{B}_1$ :

$$\mathbf{B}(t) = \mathbf{B}_0 + \mathbf{B}_1(t) \quad 1.16$$

Now it is worth to introduce a new reference frame,  $(x', y', z')$ , rotating with respect to the laboratory frame. In the rotating frame,  $z' \equiv z$  and the  $x'y'$ -plane rotates around  $z$  at frequency  $\omega$ . The magnetization components in the rotating frame versus the laboratory frame, in complex notation, can be written as:

$$M_{x'y'} = M_{xy} e^{i\omega t} \quad 1.17$$

$$M_{z'} = M_z \quad 1.18$$

where the magnetization vector is assumed to be:

$$\mathbf{M}_{xy} = M_x \mathbf{i} + M_y \mathbf{j} \quad 1.19$$

$$\mathbf{M}_{x'y'} = M_{x'} \mathbf{i} + M_{y'} \mathbf{j} \quad 1.20$$

Eq. 1.14 can be written in complex notation as:

$$B_{1,xy}(t) = B_1 e^{-i\omega t} \quad 1.21$$

Applying the transformation Eq. 1.17 and choosing the  $x'$ -direction along  $B_1$ , it is easily seen that in the rotating frame,  $B_1$  is a static field lying in the  $x'y'$ -plane.

In the rotating frame, Eq. 1.15 becomes (see [3]):

$$\frac{d\mathbf{M}'(t)}{dt} = \gamma \mathbf{M}'(t) \times \mathbf{B}_{eff}(t) \quad 1.22$$

where the effective field  $\mathbf{B}_{eff}$  is:

$$\mathbf{B}_{eff} = \mathbf{B} + \frac{\boldsymbol{\omega}}{\gamma} \quad 1.23$$

and:

$$\boldsymbol{\omega} = -\omega \mathbf{k} \quad 1.24$$

where  $\mathbf{k}$  coincides with  $\mathbf{k}'$ . Eq. 1.22 shows that, considering the fact that the magnetization will precess about  $\mathbf{B}_{eff}$ , the equations of motion in the laboratory frame and in the rotating frame are formally the same.

Using the Eq. 1.16,  $\mathbf{B}_{eff}$  can be written as:

$$\mathbf{B}_{eff} = \mathbf{B}_0 + \mathbf{B}_1 + \frac{\boldsymbol{\omega}}{\gamma} = (B_0 - \frac{\omega}{\gamma}) \mathbf{k} + \mathbf{B}_1 \quad 1.25$$

where Eqs 1.6 and 1.24 have been used. Under resonance conditions ( $\omega = \omega_0$ ), holds:

$$\mathbf{B}_{eff} = \left( \frac{\omega_0}{\gamma} - \frac{\omega_0}{\gamma} \right) \mathbf{k} + \mathbf{B}_1 = \mathbf{B}_1 \quad 1.26$$

where Eq. 1.13 has been used. Note that, the longitudinal component of the effective field gets cancelled.

According to Eq. 1.22 and last findings, when a rf pulse of length  $\tau$  is applied to the sample,  $\mathbf{M}$  precesses about  $\mathbf{B}_1$  (i.e.,  $x'$ ) with the frequency:

$$\omega_1 = \gamma B_1 \quad 1.27$$

Therefore, at the end of the pulse, the magnetization will form the angle  $\alpha$ , so called Flip Angle (FA), with the  $z$ -axis (see Fig. 1.2b):

$$\alpha = \omega_1 \tau \quad 1.28$$

FA is one of the most important parameters characterizing a rf pulse in NMR. For instance, a  $90^\circ (\pi/2)$ -pulse flips the magnetization down to the  $y'$ -axis and is some times called saturation pulse.

Actually, in the laboratory frame, the magnetization will follow a time evolution shown in Fig. 1.2a which includes also the precession of the magnetization vector around  $\mathbf{B}_0$ .

The behavior of the magnetization can be described by Bloch (Felix Bloch, 1946) equations [4], a set of coupled differential equations that describe the behavior of a nuclear spin in a static magnetic field, under the influence of rf pulses. Bloch modified Eq. 1.22 with the assumption that after switching off the rf pulses, the magnetization relaxes along  $z$ -axis and in the  $xy$ -plane at different rates, i.e.  $1/T_1$  and  $1/T_2$ , respectively.  $T_1$  and  $T_2$  are called longitudinal (or spin-lattice) and transverse (or spin-spin) relaxation times, respectively. Adding the relaxation times to the Eq. 1.22 we will have:

$$\frac{d\mathbf{M}}{dt} = \gamma \mathbf{M} \times \mathbf{B}_{eff} - \frac{M_{x'} \mathbf{i}' + M_{y'} \mathbf{j}'}{T_2} - \frac{(M_{z'} - M_0) \mathbf{k}'}{T_1} \quad 1.29$$

where  $M_0$  is the thermal equilibrium value of  $M_z$ , that is, at equilibrium:

$$\mathbf{M} = M_0 \mathbf{k}' \quad 1.30$$

When the rf pulse is switched off (in other words at the end of the rf pulse), according to Eq. 1.26,  $\mathbf{B}_{eff} = \mathbf{0}$  and the Bloch equations can be written as:

$$\frac{dM_{x'y'}}{dt} = -\frac{M_{x'y'}}{T_2} \quad 1.31$$

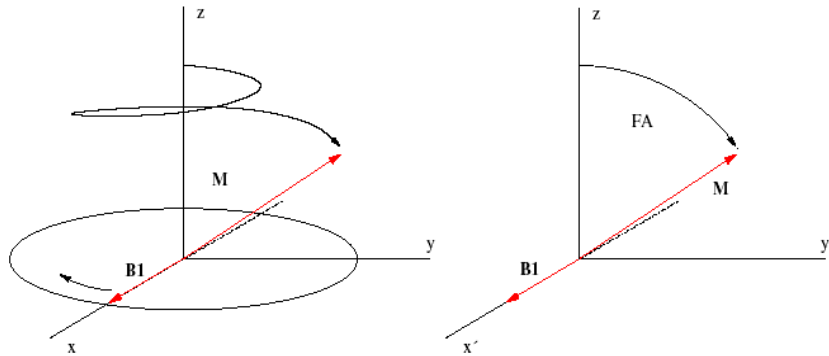


**FIG. 1.2** Evolution of the magnetization vector in the presence of an on-resonance rf pulse. In the laboratory frame (a), the magnetization simultaneously precesses about  $\mathbf{B}_0$  at  $\omega_0$  and about  $\mathbf{B}_1$  at  $\omega_1$ . In the rotating frame (b), the effective longitudinal field is zero and only the precession about  $\mathbf{B}_1$  is apparent. FA is the flip angle.

$$\frac{dM_{z'}}{dt} = -\frac{(M_{z'} - M_0)}{T_1} \quad 1.32$$

where  $M_{x'y'}$  and  $M_{z'}$  are the transverse and longitudinal magnetization components, respectively. Solutions for the Eqs 1.31 and 1.32 are:

$$M_{x'y'}(t) = M_{x'y'}(0) e^{-t/T_2} \quad 1.33$$

$$M_{z'}(t) = M_{z'}(0) e^{-t/T_1} + M_0 (1 - e^{-t/T_1}) \quad 1.34$$

where  $t = 0$  means immediately after the end of the pulse. If before applying the rf pulse the system is at thermal equilibrium, then we can write:

$$M_{x'y'}(0) = M_0 \sin \alpha \quad 1.35$$

$$M_{z'}(0) = M_0 \cos \alpha \quad 1.36$$

By putting the magnetization vector back to the laboratory frame, one can see the combined effect of free precession and relaxation. To do that, we apply the transformation rules of Eqs. 1.17 and 1.18 to Eqs. 1.33 and 1.34, respectively, which gives:



$$M_{xy}(t) = M_{xy}(0) e^{-t/T_2} e^{-i\omega_0 t} \quad 1.37$$

$$M_z(t) = M_z(0) e^{-t/T_1} + M_0 (1 - e^{-t/T_1}) \quad 1.38$$

where  $M_{xy}(0)$  is the transverse magnetization observed in the laboratory frame, immediately after the rf pulse. Eqs. 3.40 and 3.41 describe the magnetization precessing in the  $xy$ -plane of the laboratory frame at the Larmor frequency, while it is relaxing along the  $z$ -axis at a rate  $1/T_1$  and relaxing in the  $xy$ -plane at a rate  $1/T_2$ .

## 1.4 NMR Signal

The signal of the NMR experiments is detected by a receiver coil. This signal, according to Faraday induction law and the principle of reciprocity, represents the electromotive force (emf), in volts, induced by the precessing magnetization and can be expressed by: [5]

$$emf = -\frac{\partial \Phi_M(t)}{\partial t} = -\frac{\partial}{\partial t} \int_{sample} \mathbf{M}(\mathbf{r}, t) \cdot \mathbf{B}_{rec}(\mathbf{r}) d\mathbf{r} \quad 1.39$$

where  $\Phi_M$  is the magnetic flux in webers through the coil which is time dependent and  $\mathbf{B}_{rec}(\mathbf{r})$  is the reception magnetic field produced at location  $\mathbf{r}$  by a hypothetical unit current flowing in the coil. The symmetry axis of the coil is perpendicular to the applied field, so that only the transverse magnetization which places in the  $xy$ -plane can induce some signal and be detected by the coil. Usually, the rf coil that transmits the  $\mathbf{B}_1$  field, receives the induced signal as well.

Assume that the equilibrium magnetization of a system is placed in the  $xy$ -plane by applying a  $90^\circ$ -pulse. According to Eqs. 1.35 and 1.37, the transverse magnetization component in the laboratory frame at time  $t$ , following the pulse, is:

$$M_{xy}(t) = M_0 e^{-t/T_2} e^{-i\omega_0 t} \quad 1.40$$

where the pulse duration  $\tau$  is assumed to be negligible with respect to the Larmor precession time. This assumption allows to neglect the phase shift accumulated during  $\tau$  between  $M_{xy'}(0)$  and  $M_{xy}(0)$ . If the receiver coil has a homogeneous reception field  $\mathbf{B}_{rec}(\mathbf{r})$  over the sample, it can be shown that the signal takes the following expression:

$$S(t) = S_0 e^{-t/T_2} e^{-i\omega_0 t} \quad 1.41$$

where  $S_0$  is the signal amplitude immediately following the pulse, a number which depends on the hardware configuration and is proportional to  $M_0$ . The initial NMR signal is measured in the time domain as an oscillating, decaying *emf* induced by the

magnetization in free precession: it is therefore known as the Free Induction Decay (FID) signal. An example of FID is shown in Fig. 1.3.

The FID signal resulting from a generic  $\alpha$ -pulse of a sample with the spectral density function  $\rho(\omega)$  takes the following form:

$$S(t) = K \sin \alpha \int_{-\infty}^{+\infty} \rho(\omega) e^{-i\omega t} d\omega \quad 1.42$$

where  $K$  accounts for the hardware configuration and  $dM(\omega) = \rho(\omega) d\omega$ . The real part of the Fourier transform (FT) of the signal gives the absorption NMR spectrum.

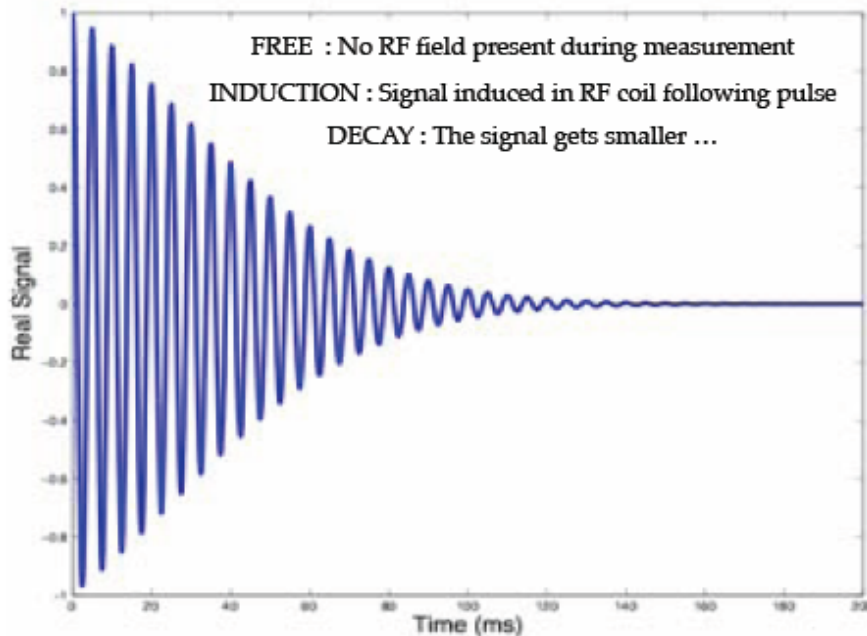


FIG. 1.3 Typical example of FID signal.

## 1.5 Magnetic Resonance Imaging (MRI)

The body is mainly composed of water molecules. Each water molecule has two hydrogen nuclei or protons. Actually, the MRI is mainly the  $^1\text{H}$  NMR applied to the body and its principles are the same as NMR. Although the research activity of the present thesis has not been concentrated on the MRI technique and the scanner has been used just

for performing the *in-vitro* images to find out the samples contrast efficiency, it would be worth to know the MRI hardware. So, in this section, first we will briefly introduce the MRI hardware and then some very important pulse sequences will be introduced. More details about a typical MRI system are given in the Appendix A.

In a MRI scanner, a permanent magnet, an electromagnet or more often a superconducting magnet, produces the required static field  $B_0$  for the imaging procedure (normally  $B_0=1.5$  Tesla, but could reach 11 Tesla). The first coil historically used in an NMR experiment was the multi-turn solenoid coil. After that, the birdcage coil (Fig. 1.4) was introduced by Hays [6] and became the most routinely used volume coil in MRI, especially for imaging the head and brain.

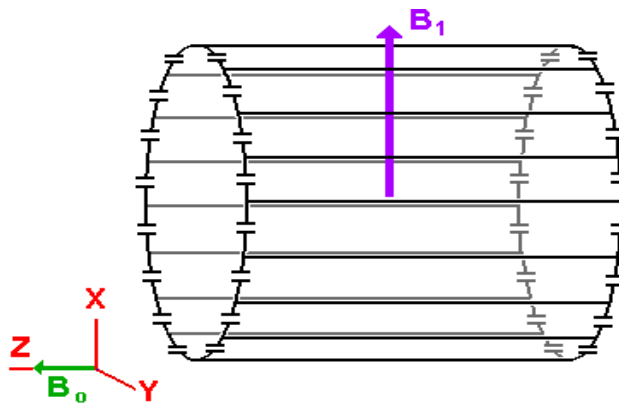


**FIG. 1.4** Scheme of a Birdcage Coil with the magnetic fields directions.

It is widely acceptable that the birdcage coil provides a better overall magnetic field homogeneity and improved SNR compared to older coil designs, such as the solenoid coils. Field homogeneity ensures that the atomic nuclei are excited by a uniform field, allowing a large field of view (FOV), while the high SNR allows obtaining high resolution images. Actually, the ability of birdcage coils to produce circularly polarized fields using quadrature excitation can increase the SNR by 41%, giving more resolution.[7]

Sometimes the birdcage coil is shielded from other coils (e.g., gradient coils) inside the MRI set-up to minimize any interference. The birdcage coil was the basis for further improvements in coil design and assembly. New designs were developed and used, such as end-capped birdcage resonator and the double tuned quadrature birdcage coil. A birdcage coil or other types of rf coils can alternatively be used as a transmitter coil, receiver coil, or both receiver and transmitter.

The transmitter coil creates the rf magnetic field  $B_1$  that excites the nuclei of the tissue. It is essential to have a uniform field  $B_1$  over the region of interest to provide a

spatially uniform excitation. If inhomogeneous magnetic field is created, some of the nuclei are either not excited or excited with different flip angles, leading to poor image contrast and SNR. The receiver coil detects the resonance signal resulting in an output voltage.

According to the NMR principles discussed before, as the nuclei relax back to their original state, they emit some rf energy that has the same frequency as the applied rf signal, i.e. the NMR signal. With different tissues, the nuclei are present at different densities and relax at different frequencies and/or rates leading to different time-varying signal levels and consequently different tissue contrast in the image. Using three further coils to generate magnetic field gradients in the three perpendicular directions ( $x,y,z$ ), the spatial location of different molecules is determined and the measured signal is transformed to an image via signal processing tools.

An important issue to be considered for using an appropriate coil is the size of the coil. The body organ to be imaged should be comparable with the coil size. In such case, one achieves a good SNR which is due to the fact that the system is less sensitive to the external thermal noise and the receiver coil is close to the region of interest. This factor becomes more important at high magnetic fields.

Surface rf coils are very popular because they serve as a receive-only coil, but their sensitivity drops off as the distance from the coil increases. They have a good SNR for tissues adjacent to the coil. The advantage of the surface coils is their ability to produce a strong and localized rf field that can provide a high SNR compared to other coils, especially in the imaging of relatively small volumes.

Scan room is surrounded by an rf shield. The shield prevents the various external rf signals (e.g. television and radio signals) from being detected by the imager. Some scan rooms are also surrounded by a magnetic shield, which prevents the magnetic field from extending too far into the hospital. In newer, powerful magnets, the magnet shield is an integral part of the assembly. The patient is positioned within the magnet by a computer controlled patient table. The table has a positioning accuracy of 1 mm.

The heart of the MRI system is the computer. It controls all the components of the scanner. The computer also controls the rf components: rf source and pulse programmer. The source produces a sinusoidal wave at predetermined frequency. The pulse programmer converts the rf pulses into desired pulse shapes as dictated by the operator. The rf amplifier increases the pulse power from milliwatts to kilowatts. The computer also controls the gradient pulse programmer, which sets the shape and amplitude of each of the magnetic field gradients which will be introduced later. The gradient amplifier increases the power of the gradient pulses to a level sufficient to operate the gradient coils.

### ***1.5.1 Pulse Sequences***

One of the confusing aspects of MRI is the variety of pulse sequences available from different equipment manufacturers. A pulse sequence is the measurement technique by which a MR image is obtained. It contains the hardware instructions (rf pulses, gradient pulses and timings) necessary to acquire the data in the desired manner.

As implemented by most manufacturers, the pulse sequence actually executed during the measurement is defined from parameters directly selected by the operator (e.g. TR and FOV) and variables defined in template files (e.g. relationships between rf pulses and slice selection gradients). This allows the operator to create a large number of pulse sequence combinations using a limited number of template files. It also enables the manufacturer to limit parameter combinations to those suitable for execution.

Sometimes, similar sequences may be known by a variety of names by the same manufacturer.[8] As a result, comparison of techniques and protocols between manufacturers is often difficult due to differences in sequence implementation. To have such a comparison, knowledge of confidential, proprietary information might be needed.

A pulse sequence sets the specific number, strength, and timing of the rf and gradient pulses. The signal intensity and consequently the image contrast of the MR image can be manipulated by changing the pulse sequence parameters. Generally, the signal intensity might be determined by four basic parameters: 1) proton or spin density, 2)  $T_1$  relaxation time, 3)  $T_2$  relaxation time, and 4) diffusion effects. Proton density is the concentration of protons (hydrogen atom nuclei) in the tissue belonging to water and macromolecules (proteins, fat, etc). The  $T_1$  and  $T_2$  relaxation times define the signal behavior after excitation as well as the way the protons revert back to their equilibrium after the initial rf pulse excitation.

In a pulse sequence, the most important parameters which affect the signal intensity are the repetition time (TR), the echo time (TE), and the tissue nuclear spin, e.g. proton, density  $\rho$ . The TR is the time between consecutive identical sequences. The TE is the time between the initial rf pulse and the time at which the signal is received. Therefore, the signal intensity  $SI$  (and consequently the image contrast in the MRI) can be written as:

$$SI(TR,TE) \propto \rho(1 - e^{-TR/T_1})e^{-TE/T_2} \quad 1.43$$

where  $\rho$  is the density of nuclear spins.

As one can see in Eq. 1.43, using the appropriate pulse sequences, it is possible to weight the image on  $T_1$ ,  $T_2$ , or the nuclear spin (e.g. proton) density, so called  $T_1$ -weighted,  $T_2$ -weighted and proton density (PD)-weighted sequences, respectively. In order to weight on a desired parameter and consequently eliminate the others, one has to rely on the relaxation times of the tissue. As given in Table 1.1, the  $T_1$ -weighted sequence uses a short TR and short TE (TR < 1000 ms, TE < 30 ms). The  $T_2$ -weighted sequence uses a long TR and relatively long TE (TR > 2000 ms, TE > 80 ms) while to have a PD-weighted image one has to use short TE and long TR values. More recently, the FLAIR (Fluid Attenuated Inversion Recovery) sequence has, in some cases, replaced the PD image. FLAIR images are  $T_2$ -weighted with the cerebrospinal fluid (CSF) signal suppressed [9]. Fig. 1.5 illustrates the possibilities of generating different contrast from two types of tissues with different relaxation characteristics. The examples of different generated contrasts are given in Fig. 1.6.

TABLE 1.1 TR and TE dependence of image weighting.

| TE    | TR    | Image weighting   |
|-------|-------|-------------------|
| short | long  | proton            |
| short | short | $T_1$             |
| long  | long  | $T_2$ ( $T_2^*$ ) |

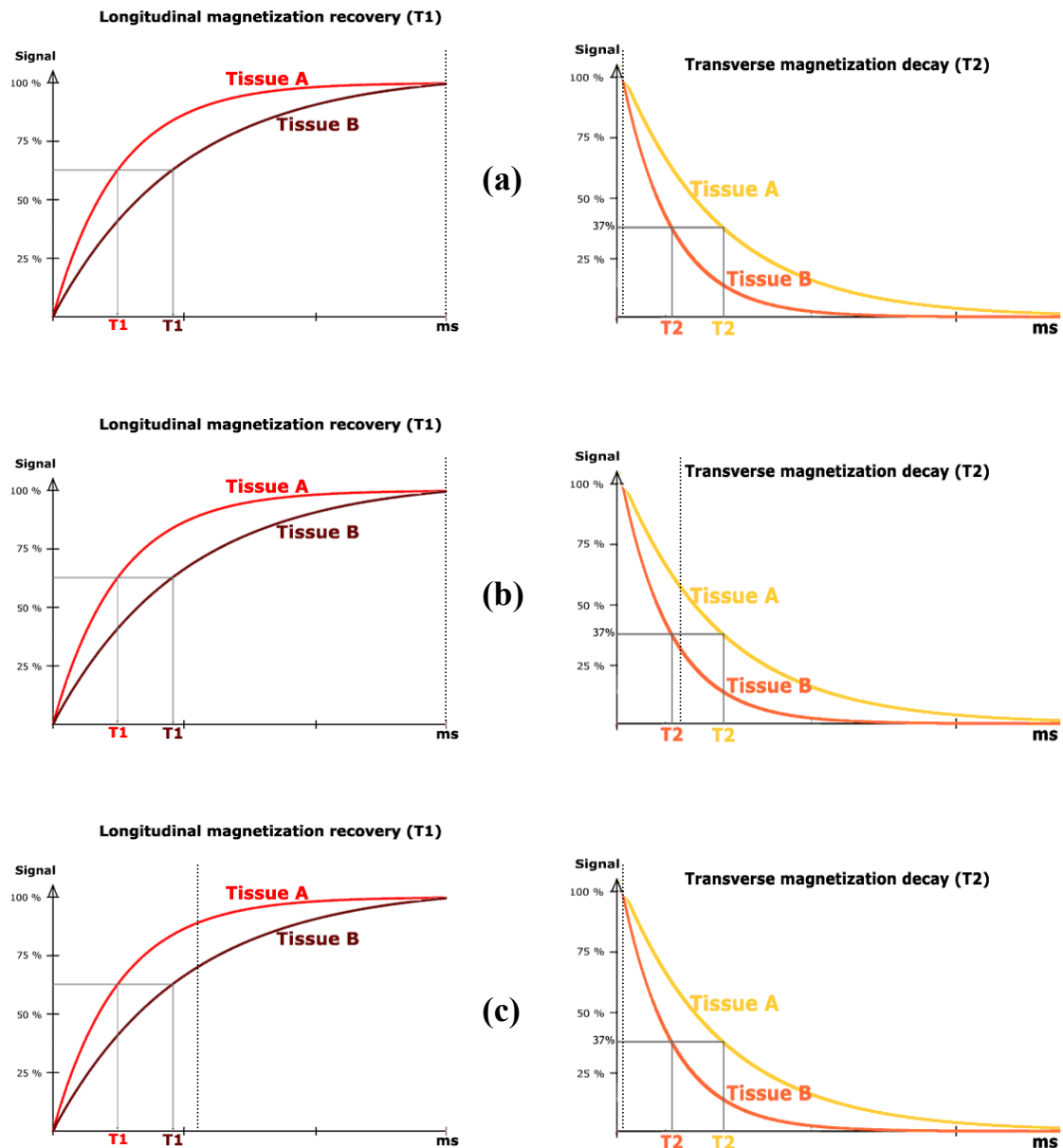
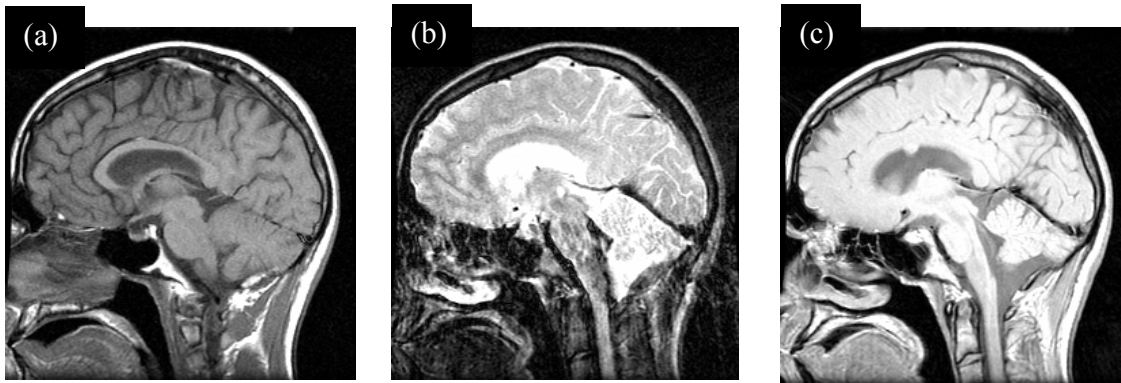


FIG. 1.5. Longitudinal magnetization recovery and transverse magnetization decay of two different tissues. Dashed lines show how appropriate values of TR (in the longitudinal magnetization recovery curves) and TE (in the transverse magnetization decay curves) gives the a) PD-weighted, b)  $T_2$ -weighted, and c)  $T_1$ -weighted images.



**FIG. 1.6** a) T<sub>1</sub>-weighted, b) T<sub>2</sub>-weighted, and c) PD-weighted images of the brain.

There are two most commonly used pulse sequences in MR imaging: 1) Spin Echo (SE) sequence, and 2) Gradient Echo (GRE) sequence.

The concept of the SE production was developed by Hahn in 1950 and that's why the Spin echoes are sometimes referred to as *Hahn spin echoes*. The Hahn Spin Echo sequence consists of a 90° flip pulse followed by a 180° flip pulse (after an interpulse delay time  $\tau$ ). A “spin echo” occurs at echo time TE ( $2\tau$ ) following the initial 90° flip. Fig. 1.7 shows how the magnetization flips, dephases in the  $x$ - $y$  plane, and gets in phase to produce the echo.

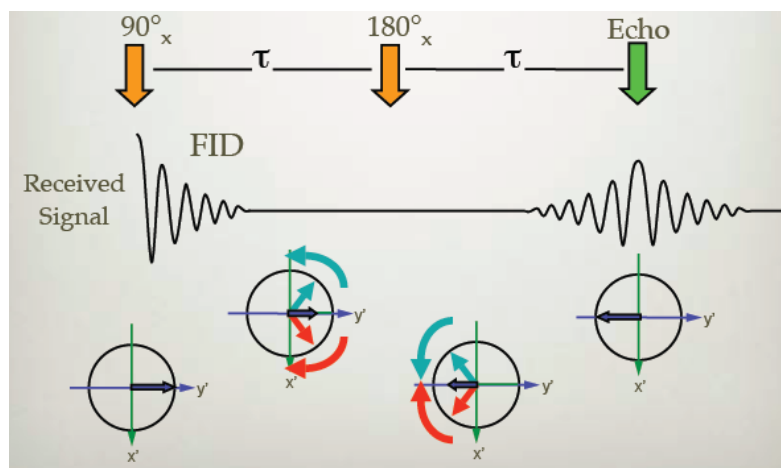


**FIG. 1.7** Scheme of the SE sequence.

The Hahn spin echo is used for the measurement of T<sub>2</sub> values. It is possible to measure T<sub>2</sub> since the spin echo technique compensates for the local inhomogeneities of

the static magnetic field. In order to measure  $T_2$ , the sequence has to be repeated with several different values of the interpulse delay  $\tau$  and it is necessary to wait approximately five times  $T_1$  for complete recovery between repeated sequences.

*Carr-Purcell-Meiboom-Gill* (CPMG) spin echo technique is a modified spin echo technique. The CPMG technique uses a  $90^\circ$  rf pulse followed by a train of equally spaced  $180^\circ$  rf pulses along the Y axis of the rotating frame. Each echo signal is positive in the CPMG technique [10]. It should be mentioned that the signal envelope following the  $90^\circ$  rf pulse follows the decay time so called  $T_2^*$  (see Fig. 1.8), while the signal envelope connecting the magnitude of succeeding echoes has a time constant  $T_2$ . The CPMG pulse sequence is illustrated in Fig. 1.8.

In a SE sequence a multi-slice loop structure is used to acquire signals from multiple slices within one TR time period.

On the other hand, the GRE sequences do not use a  $180^\circ$  pulse to refocus the protons. Rather, the echo signal is generated only through a refocusing external field gradient. The application of a first refocusing imaging gradient induces proton dephasing. Application of a second gradient pulse of double duration and same magnitude but of opposite polarity reverses this dephasing and produces an echo known as gradient echo. Fig. 1.9 is showing the timing diagram of the GRE pulse sequence.

In all of the GRE sequences the excitation angles (FA) are usually less than  $90^\circ$ .

The absence of the  $180^\circ$  rf pulse in gradient echo sequences has several important consequences. The sequence kernel time may be shorter than that for an analogous SE sequence enabling more slices to be acquired for the same TR if a multi-slice loop is used [11]. More information or details can be revealed once more slices are used. Moreover, it implies that less total rf power is applied to the patient, so that the total rf energy release is lower.

Additional contrast mechanisms are also possible. In fact the static sources for proton dephasing, which are magnetic field inhomogeneity and magnetic susceptibility differences, contribute to the signal decay. As such, the TE determines the amount of  $T_2^*$ -weighting in a gradient echo image rather than only  $T_2$ -weighting, as in a spin echo image.

The overall signal level in gradient echo images is expected to be less than that in spin echo images, with comparable acquisition parameters. The image quality of GRE sequences is also more sensitive to metal implants and to the region of anatomy under investigation. In addition, fat, protein and water protons within a voxel also contribute with different amounts of signal depending upon the chosen echo time, due to their different frequencies and hence different phases at echo time.



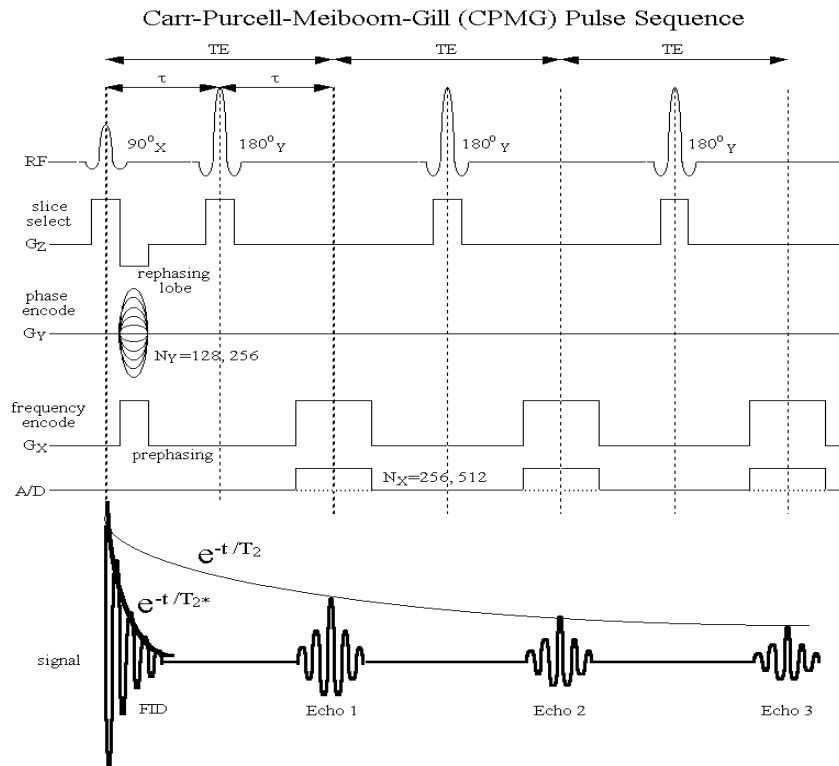


FIG. 1.8 CPMG pulse sequence timing diagram.

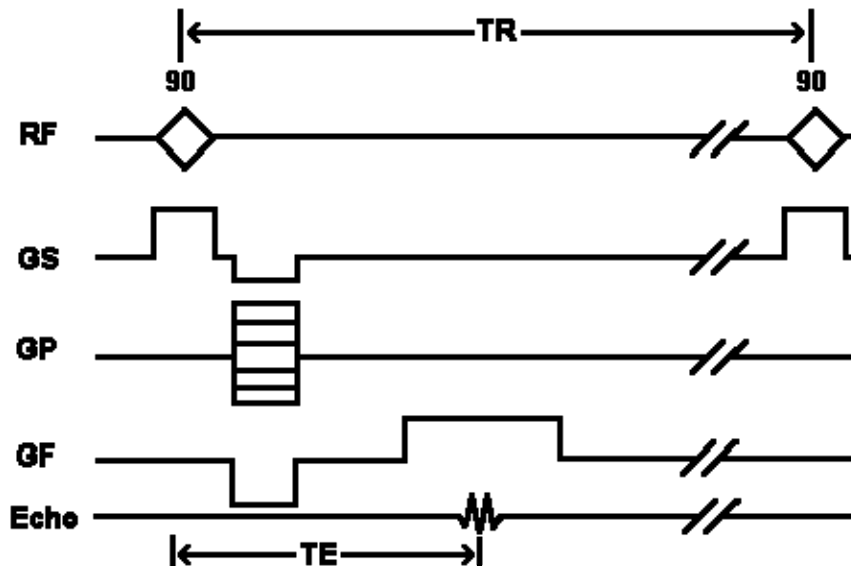
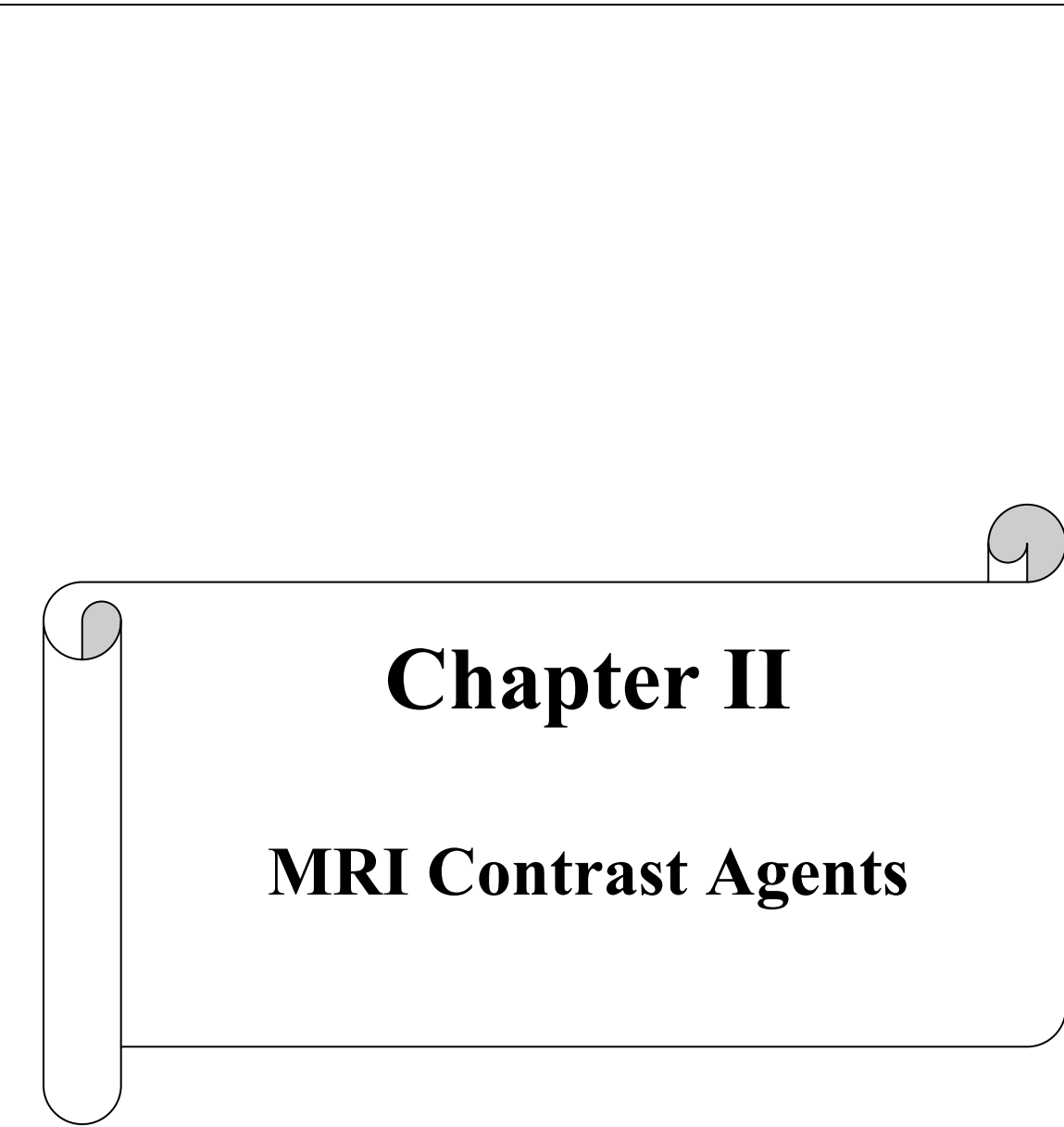


FIG. 1.9 gradient-echo pulse sequence timing diagram. The TE time is measured from the middle of the excitation pulse to the center of the echo.

## 1.6 References

- [1] Bernstein MA, King KF, Zhou XJ, Handbook of MRI Pulse Sequences, Academic Press, (2004).
- [2] McRobbie DW, Moore EA, Graves MJ and Prince MR, MRI from Picture to Proton, 2<sup>nd</sup> ED, Cambridge University Press, (2006).
- [3] Z.-P. Liang and P. C. Lauterbur. Principles of Magnetic Resonance Imaging, A Signal Processing Perspective, pages 72–76. IEEE Press Series in Biomedical Engineering. The Institute of Electrical and Electronics Engineers, (2000).
- [4] Bloch, F., Nuclear Induction. Physical Review, 70(7,8):460-474, (1947).
- [5] Z.-P. Liang and P. C. Lauterbur. Principles of Magnetic Resonance Imaging, A Signal Processing Perspective, page 94. IEEE Press Series in Biomedical Engineering. The Institute of Electrical and Electronics Engineers, (2000).
- [6] Hayes E C, Wdelstein W A, Schenck D F, Mueller O M and Eash M. An efficient highly homogeneous radiofrequency coil for whole-body NMR imaging at 1.5 T. J Magn Reson, 63:622–8, (1985).
- [7] Sank VJ, Chen C-N and Hoult A. A Quadrature Coil for the Adult Human Head. J Magn Reson, 69:236-242, (1986).
- [8] Kuperman. Magnetic Resonance Imaging - Physical Principles and Applications, (2000).
- [9] Filippi M, De Stefano N, Dousset V, McGowan JC. MRI in White Matter Diseases of the Brain and Spinal Cord. Med Radiol Diagnostic Imaging Series (Editors: A. L. Baert and K. Sartor, Springer-Verlag Berlin Heidelberg), (2005).
- [10] Weishaupt D, Köchli VD, Marincek B. How Does MRI Work, An Introduction to the Physics and Function of Magnetic Resonance Imaging, 2nd Ed, Springer-Verlag, (2006).
- [11] Brown, MA and Semelka, RC, MRI Basic Principles and Applications, 3rd Ed, John Wiley and Sons, Inc, (2003).



# **Chapter II**

## **MRI Contrast Agents**

## Chapter II

# MRI Contrast Agents

### *Contents*

---

|                                                       |    |
|-------------------------------------------------------|----|
| 2.1 Image Contrast .....                              | 21 |
| 2.2 Magnetic Materials .....                          | 22 |
| 2.2.1 Nanoparticles and Single Domain Particles ..... | 24 |
| 2.2.2 Magnetic Anisotropy of Nanoparticles .....      | 26 |
| 2.2.3 Superparamagnetism .....                        | 27 |
| 2.3 MRI Contrast Agents .....                         | 32 |
| 2.3.1 Introduction .....                              | 32 |
| 2.3.2 Positive and Negative CAs .....                 | 33 |
| 2.4 Relaxation Mechanisms of CAs .....                | 35 |
| 2.4.1 Paramagnetic Relaxation .....                   | 36 |
| 2.4.2 Superparamagnetic Relaxation .....              | 40 |
| 2.5 References .....                                  | 41 |

---

## 2.1 Image Contrast

The tissue contrast to noise ratio (CNR) appearing in MR image is the basis for a medical diagnosis. The CNR can be altered by the choice of specific pulse sequences (as discussed in chapter I, mentioned here after briefly) and the associated timing parameters. It is generally defined as:

$$CNR = \frac{SI_1 - SI_2}{noise} \quad 2.1$$

$SI_1$  and  $SI_2$  represent the signal intensities of two adjacent regions on an MR image. The magnitude of the detected signal depends upon the spin density (number of protons available),  $T_1$  and  $T_2$  characteristics of tissues, chemical shift, temperature, and flow phenomena. Among these parameters, the relaxation characteristics are mostly influencing the signal intensity. Therefore the conventional tissue contrast of an MR image, as explained in the first chapter, is usually proton-density-  $T_1$ - or  $T_2$ - weighted (see Eq. 1.43). A long TR ( $TR > 5 T_1$ ) allows enough time for a complete  $T_1$  relaxation and the longer the time interval TE the greater the extent of  $T_2$  relaxation. Spin echo images acquired with short TR ( $TR \sim T_1$ ) and a short TE ( $TE < T_2$ ) are  $T_1$ -weighted. With shorter TR values, tissues such as fat which have short  $T_1$  values appear brighter, whereas tissues such as tumors and edema, that have longer  $T_1$  values and therefore take more time to relax towards equilibrium, appear darker. The short TE value diminishes the importance of tissue  $T_2$  differences. On the other hand, images acquired with long TR and long TE ( $TE \sim T_2$ ) are  $T_2$ -weighted. Therefore, tissues with long  $T_2$ , such as tumors, edema, and cysts appear bright whereas tissues that have short  $T_2$ , such as muscle and liver, appear darker.

In summary, the MR image contrast is a function of several parameters and the image contrast between tissues with different physicochemical properties is determined by different image signal intensities that each tissue produces when the operator chooses specific values of TR and TE.

Despite the relatively high number of degrees of freedom for obtaining good MR images of the soft tissues of living beings, in some cases it is not possible to have enough image contrast to show the anatomy or pathology of interest. In such cases, one has to use a contrast agent (CA). The CAs should fulfill several requirements for clinical applications: adequate relaxivity and susceptibility effects, tolerance, safety, low toxicity, stability, optimal bio-distribution, easy elimination and good metabolism. In the following paragraphs we'll introduce briefly these systems, starting from their main physical properties.

## 2.2 Magnetic Materials

Magnetism is one of the basic properties of materials. When a material is placed in a magnetic field  $\mathbf{H}$ , it acquires a dipole moment. The magnitude of this dipole moment depends upon the nature of the material, the applied magnetic field strength, and is proportional to its volume. Therefore, we define the total dipole moment per unit volume induced in the material as *magnetization*  $\mathbf{M}$ , which is the sum of all the atomic/nuclear magnetic moments of the material. The response of the material to the applied magnetic field can be expressed, for  $H \rightarrow 0$ , as:

$$\mathbf{M} = \chi \mathbf{H} \quad 2.2$$

where  $\chi$  is defined as the *magnetic susceptibility*, the most important magnetic material property. In paramagnetic substances it depends on the temperature according to Curie-Weiss expression:

$$\chi = \frac{C}{T + \theta} \quad 2.3$$

where  $C$  and  $\theta$  are both characteristic constants of each material. As the applied field strength is increased for any particular material, the magnetization reaches a constant value, defined as saturation magnetization,  $M_s$ .

The magnetic properties of an ion or atom are determined by the orbital angular momentum  $\mathbf{L}$  and by the spin angular momentum  $\mathbf{S}$ , determined by the orientation and number of its electron spins. For magnetic metal oxides (transition metal oxides in particular), the spin of an ion is characterized by one total spin (atomic spin). The atomic spins of neighboring ions may be strongly correlated with each other to form a spin sub-lattice. Depending on the magnitude of the spin, the orientation and the number of spin sub-lattices, the material possesses a characteristic internal magnetic field, as well as characteristic responses to an applied magnetic field. Regarding the various kinds of responses of materials to a magnetic field, we introduce six basic categories: 1) ferromagnetic, 2) antiferromagnetic, 3) ferrimagnetic, 4) paramagnetic 5) diamagnetic and 6) superparamagnetic, materials.

The atomic spin arrangements of various types of magnetic materials are schematically represented in Fig. 2.1. In ferromagnetic materials, the atoms with permanent dipole moments interact one each other, to produce a parallel alignment of spins in the crystal lattice below a critical transition temperature  $T_c$ . This generates a large magnetic susceptibility, and therefore strong response to the applied magnetic field. On the contrary, in antiferromagnetic materials, the dipole moments interact one each other showing an anti-parallel alignment in the crystal lattice. This spontaneous anti-parallel coupling of atomic magnets is disrupted by heating and disappears entirely above a certain ordering transition temperature, called the Neel temperature, characteristic of each antiferromagnetic material. Above the Neel temperature the material is typically paramagnetic, i.e. the spins fluctuate almost independently with a correlation time  $\tau$  of the order of  $10^{-14}$ - $10^{-15}$ s. Similarly to the antiferromagnetic alignment, ferrimagnetic materials have an anti-parallel spins alignment in the crystal lattice. However, the magnitudes of the oppositely aligned dipole moments are not equal, resulting in a net magnetic moment when placed in a magnetic field. Ferrimagnetic materials therefore have generally a smaller magnetic susceptibility than ferromagnetic materials. In the case of paramagnetic materials, the dipoles in the crystal lattice are randomly oriented and do not interact with each other. When a paramagnetic material is placed in a magnetic field, the magnetic moment of the material increases slowly initially in a linear  $M$  vs.  $H$  way, following then the Langevin function until saturation magnetization is reached. The phenomenon of the diamagnetism is instead characterized by the opposition of the magnetic moments inside the material, to the external magnetic field.

In addition to the five categories of magnetic materials we have presented, there is a special magnetic phenomenon which shares properties of both paramagnetic and ferromagnetic materials, the so called *superparamagnetism*. Frenkel and Dorfman first predicted in 1930 that a particle of ferrimagnetic (or ferromagnetic) material could consist of a single magnetic domain below a certain critical size. It has been defined that a single domain particle will have a uniform magnetization at any field strength. In 1949, Néel pointed out that if a single domain particle was small enough, the thermal

fluctuations could cause changes of direction in opposite senses of its magnetization similar to that of Brownian rotation.

Bean and Livingston, in 1959, observed that the magnetization behavior of single domain particles (isotropic) in thermodynamic equilibrium at all fields is identical to that of atomic paramagnetism but that they have an extremely large moment. This large magnetic moment does not result from the individual atoms, but rather it comes from hundreds/thousands (depending upon the particle size) of atoms in the particle which are ferromagnetically coupled by exchange forces. When a magnetic field is applied to a suspension of small ferromagnetic particles, they are partially aligned by the field and partially disordered by the thermal motion, thereby exhibiting over-all paramagnetism.

In the following, we present some fundamental aspects of superparamagnetism.

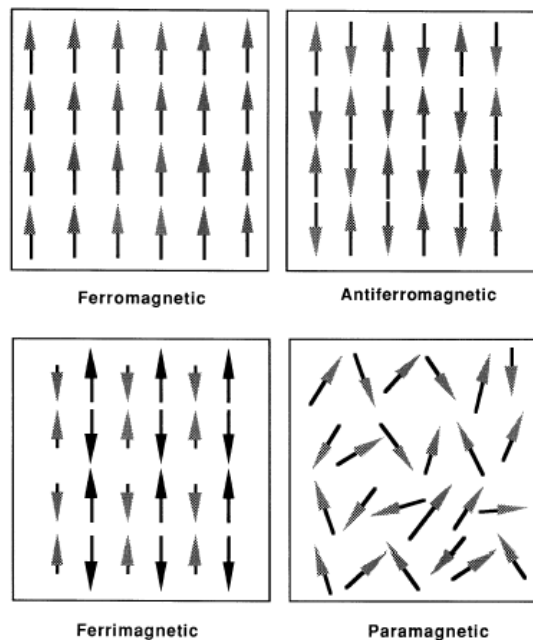


FIG. 2.1 Spins arrangements in various magnetic materials.

### 2.2.1 Nanoparticles and Single Domain Particles

When the volume of a particle is reduced below a certain value, called *critical domain size*  $D_c$ , the proximity of many domain walls in a small volume is not energetically favored, so that a *single-domain* [1] configuration is adopted. For spherical crystals, Kittel proposed the following expression for the critical diameter [2]:

$$D_c = 36 E_\sigma / \mu_0 M_s^2 \quad 2.4$$

where  $E_\sigma = 2 (A.K)^{1/2}$  is the surface energy of a Bloch wall in an infinite material with low anisotropy,  $K$  is the anisotropy constant,  $A$  is the exchange energy,  $\mu_0$  is the vacuum permeability, and  $M_s$  is the saturation magnetization.

In Table 2.1 we present the critical diameters of some common magnetic spherical nanoparticles together with the anisotropy, saturation magnetization, and exchange energy values used for their evaluation [3].

**TABLE 2.1** Examples of critical diameters for some common magnetic spherical nanoparticles together with the anisotropy, saturation magnetization, and anisotropy constants used for their evaluation [3].

| Magnetic Material                        | $A$ (J.m <sup>-1</sup> ) | $M_s$ (J.m <sup>-1</sup> )<br>(bulk) | $K$ (J.m <sup>-3</sup> ) | $D_c$<br>(nm) |
|------------------------------------------|--------------------------|--------------------------------------|--------------------------|---------------|
| Fe (bcc)                                 | 0.5                      | 0.5                                  | 59                       | 0.16          |
| Fe <sub>3</sub> O <sub>4</sub>           | 0.625                    | 0.5                                  | 62                       | 0.18          |
| $\gamma$ -Fe <sub>2</sub> O <sub>3</sub> | 1                        | 0.5                                  | 92                       | 0.15          |

The values of critical diameter in the table are indicative, and can change with the quality of the nanomaterials. Magnetite and maghemite present quite similarly magnetic properties (saturation magnetization and critical diameter of the same order). On the contrary, cobalt ferrite has a high anisotropy inducing a relatively low critical diameter. In case of pure iron the high saturation magnetization induces a critical diameter ten times lower than magnetite. Finally, as shown in Fig. 2.4, between single domain and multidomain size range there is a broad region called pseudo single-domain.

When a magnetic field is applied, for non-interacting nanoparticles, the magnetization reversal for single domain nanoparticles is realized by *coherent rotation*, meaning that all spins of the ions in nanoparticles are parallel to each other. One of the most recognized models describing the coherent rotation of magnetization for an assembly of non-interacting single domain magnetic nanoparticles with uniaxial anisotropy is the *Stoner-Wohlfarth theory* [4].

This model represents single particles through classical giant spin with a certain anisotropy. According to this model the hysteresis cycle of a single particle critically depends on the angle between the applied field and the anisotropy axis (or *easy axis*), which is defined as the energetically favorable direction of the spontaneous magnetization. Two extreme cases are possible at much lower than the anisotropy energy  $E_a$  (see below for the definition):



1. If the particle anisotropy axis is perpendicular to the direction of the applied field the hysteresis branches are superimposed, and there is no coercive field  $H_c$  and remanence magnetization  $M_r$ .
2. If the particle axis is instead parallel to the applied field, the hysteresis cycle is open and the coercive field can be obtained by:

$$H_c = 2K / \mu_0 M_s \quad 2.5$$

At intermediate angles one observes hysteresis cycles with coercive field and remanence that span between these two extreme positions.

For an assembly of randomly oriented non interacting particles, the curve is expected to behave like Fig. 2.2, the coercive field is  $\approx 0.5 H_c$ , while the remanent magnetization is  $0.5 M_s$ .

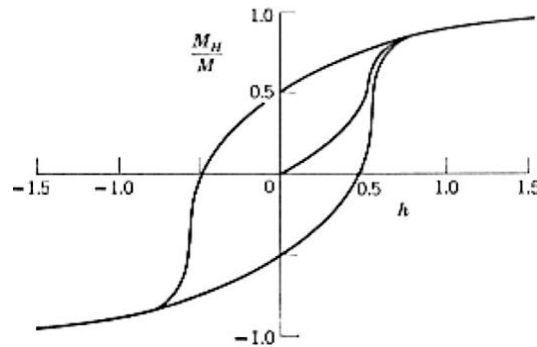


**FIG. 2.2** Theoretical hysteresis curve in Stoner-Wohlfarth model for a randomly oriented assembly of nanoparticles.

### 2.2.2 Magnetic Anisotropy of Nanoparticles

The magnetic properties of the nanoparticles are generally anisotropic. There are some low energy directions in the crystal, called easy directions, which are separated by an anisotropy energy barrier. Several different sources can give rise to the total anisotropy of the magnetization:

*i) Magnetocrystalline Anisotropy.* This property is intrinsic to the material and it is related to the crystal symmetry and to the arrangement of atoms in the crystal lattice. The origin of this contribution lies in the spin-orbit coupling. In fact, the orbital wave function will reflect the symmetry of the lattice and the spins are made aware of this anisotropy via the spin-orbit coupling.

*ii) Shape Anisotropy.* The source of this kind of anisotropy is the presence of free magnetic poles on the surface of a magnetized body. These poles create a magnetic field inside the system, called demagnetizing field. Variation from spherical form can induce competing shape anisotropy with respect to the magnetocrystalline contribution.

iii) *Surface Anisotropy*. When the surface atoms are present in a number comparable to that of atoms within the particle, another form of anisotropy is observable. This kind of anisotropy is very sensitive to the chemical environment of surface spins and may be different depending also on the chemical species bounded to the surface. The magnitude of this contribution increases on decreasing the size of the particle due to the increasing of surface to volume ratio. Néel has shown that the surface contribution becomes relevant only for particles smaller than 10nm [5].

iv) *Stress Anisotropy*. It is well known that when a specimen is magnetized in a given direction, there is a change of length in that direction. This phenomenon was first observed by Joule in 1842 and is called magnetostriction. Its existence indicates that there is an interaction between magnetization and strain, which is again due to spin-orbit coupling. Since the strain is related to any stress that may be acting on the considered system, this implies that the anisotropy energy depends on the stress state of the system.

v) *Exchange and Dipolar Anisotropies between Particles*. Two particles, close enough to each other, will have a magnetic interaction. This interaction, which can be either due to magnetic dipole interaction or to exchange interaction, leads to an additional anisotropy energy. In this case the easy direction is determined by the relative orientation of the two interacting magnetic moments.

The observed anisotropy energy depends on the relative magnitude of each contribution, which depends on the structure of the material, its shape and size [6].

### 2.2.3 Superparamagnetism

*Energy Barrier and Blocking Temperature*. In magnetic materials, the anisotropy can often be modeled as uniaxial in character and represented, in its simplest form, as:

$$E_a(\theta) = KV \sin^2 \theta \quad 2.6$$

where  $V$  is the volume of the particle and  $\theta$  is the angle between the magnetization direction and the easy axis, and  $K$  is the anisotropy constant.

From this equation comes out that there are two energy minima corresponding to  $\theta = 0$  and  $\theta = \pi$  (Fig. 2.3). The energy barrier  $E_a = KV$  is defined as the energy required to move from one stable state to another.

At a temperature  $T$  the magnetic state of the particle will be determined by the competition between  $E_a$  and the thermal energy  $k_B T$ , where  $k_B$  is the Boltzmann constant.

At a given temperature  $T$  for which the thermal energy is much lower than the energy barrier ( $k_B T < E_a$ ), the probability that the magnetization forms an angle  $\theta$  with the easy axis has a finite value only in correspondence of the two minima. Thus the magnetization will be blocked in one of the two easy directions.

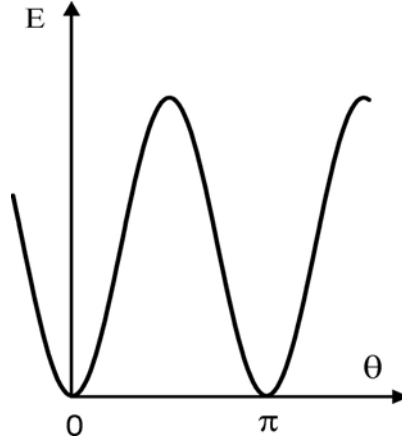


**FIG. 2.3** Anisotropy energy profile as a function of the angle between the magnetic moment and the easy axis for a single domain NP with pure uniaxial symmetry.

On increasing temperature the allowed  $\theta$  values will have a broader distribution around the two minima and the magnetization can begin to fluctuate around the easy directions (vibrations in the potential well). The vibration amplitude will increase up to a temperature at which thermal energy equals the energy barrier. This temperature is called *blocking temperature*,  $T_B$ . Above  $T_B$  thermal excitations will make the magnetic moment to freely rotate and therefore the net magnetization will average to zero in the absence of an external field. In this condition the assembly of particles behaves like a paramagnetic system, while individual atomic moments maintain their ordered state relative to each other. The blocking temperature ( $T_B$ ) is defined as the temperature at which the relaxation time is equal to the measuring time  $\tau_M$ , and is given by:

$$T_B = \frac{KV}{k_B \ln \tau_M / \tau_0} \quad 2.7$$

The Eq. 2.7 shows that the blocking temperature  $T_B$  depends on the measuring time window,  $\tau_M$ , of each experimental technique. For example, a typical *dc* magnetization measurement spans an experimental time  $\tau_M$  of  $\sim 10^2$  s while  $\tau_M = 10^{-8}$  s for  $^{57}\text{Fe}$  Moessbauer spectroscopy and is between 0.16 and  $10^{-4}$  s at frequencies between 1 and 1000 kHz for *ac* susceptibility.

Blocking temperature of nanomaterials depends on the energy barrier and then on the anisotropy constant and on the dimension of particles. At a given temperature, below a critical dimension  $d_s$ , the nanoparticles will be superparamagnetic (Fig. 2.4). This value depends strongly on the anisotropy of the system.

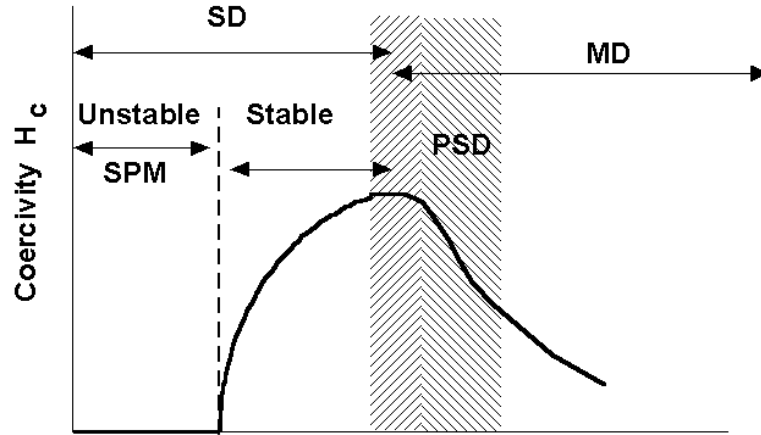


**FIG. 2.4** Coercivity at room temperature as a function of the size for nanoparticles; SPM: superparamagnetic, SD: single domain, MD: multidomain and PSD: pseudo-single domain.

A superparamagnetic material is blocked (no remanence or coercivity) at room temperature. For the non interacting SPM particles, temperature variation in coercivity  $H_C$  is expressed as [7]:

$$H_C = H_{C0}(1 - T/T_B)^{1/2} \quad 2.8$$

where  $H_{C0}$  is the value of  $H_C$  when  $T \rightarrow 0$ . Thus, the measured  $H_C$  as a function of  $T^{1/2}$  would be linear for noninteracting particle systems.

At low temperatures the  $H_C$  increases with the particle size  $d$  according to the law [7]:

$$H_C(d) = 0.5 H_k [1 - (d_s/d)^{3/2}] \quad 2.9$$

Where  $H_k = 2K / \mu_0 M_s$  is the anisotropy field defined for uniaxial magnet.

This model, however, makes the assumption that the nanoparticles are non-interacting, which is not always the case for the most of real systems. Indeed, magnetic interactions can have a strong influence on the reversal dynamics of the magnetic moment [8].

*Superparamagnetic Relaxation.* The reversal mechanism of the magnetization is characterized by the probability of switching the particle's magnetic moment  $\mu$  among different spatial orientations or, in terms of the Néel model [9], by the relaxation time  $\tau$ .

Being a thermally activated process, the relaxation time of  $\mu$  is described by the Arrhenius law:

$$\tau = \tau_0 e^{-E_a/k_B T} \quad 2.10$$

Where  $\tau_0$  is the pre-exponential factor referred to as "attempt time", and commonly is of the order of  $10^{-9}$ - $10^{-12}$  s.

Superparamagnetic particles align with the applied magnetic field by one of the two following mechanisms: (i) Néel rotation (ii) Brownian rotation. The Néel rotation occurs when particles are either in a fluid or in a solid matrix and results from the rotation of the magnetic moment of a stationary particle by overcoming the energy barrier.

Brownian rotation only occurs when particles are in a fluid and results from the physical rotation of a particle towards the direction of the applied magnetic field (Fig. 2.5) [10].

Each of these processes is characterized by a relaxation time:  $\tau_B$  for the Brownian process depends on the hydrodynamic properties of the fluid while  $\tau_N$  for the Néel process is determined by the magnetic anisotropy energy of the superparamagnetic particles relative to the thermal energy.

The relaxation times  $\tau_B$  and  $\tau_N$  depend differently on particle size. In the case of Néel relaxation the characteristic relaxation time of a nanoparticle system depends on the ratio of the anisotropy energy  $KV$  to the thermal energy  $k_B T$  as described in Eq. 2.10.

As concerns the Brownian relaxation mechanism, if a suspension of magnetic particles with viscosity  $\eta$  is considered, the characteristic relaxation time is given by:

$$\tau_B = \frac{3V_H\eta}{k_B T} \quad 2.11$$

where  $V_H$  is the hydrodynamic radius. Debye first derived this equation [11] for rotational polarization of molecules.

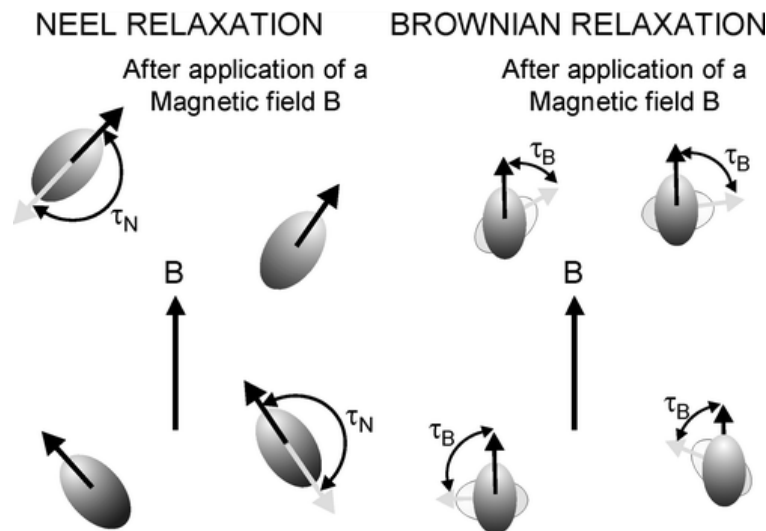


**FIG. 2.5** Illustration of the two mechanisms of the magnetic relaxation in a magnetic fluid [12].

In the general case, the faster relaxation mechanism is the dominant one and the effective relaxation time  $\tau_{eff}$  is given by:

$$\frac{1}{\tau_{eff}} = \frac{1}{\tau_N} + \frac{1}{\tau_B} \quad 2.12$$

*Interacting Superparamagnetic Systems.* In all fine-particle systems, different kinds of magnetic interparticle interactions may exist and the interaction strength varies with the volume concentration. The different types of magnetic interactions, which must be considered, are:

- *dipole-dipole interaction:* interparticle interactions may arise from dipole-dipole interactions between nanoparticles. When a capping surfactant such as oleic acid is used, the increased spacing between particles results in negligible exchange interactions (see below) and the primary interaction is considered from the dipole-dipole coupling [13].
- *Exchange interaction:* The exchange interaction is actually an effect that arises from the interplay of electromagnetism with quantum mechanics. This interaction lies at the heart of the phenomenon of long-range magnetic order. When the electrons on neighbouring magnetic atoms undergo exchange interaction, this is known as direct exchange. Hence direct exchange interaction plays a big role in nanoparticle assemblies where the surfaces of the particles are in close contact.
- *Superexchange interactions:* When the matrix is insulating, superexchange interaction can exist depending on the structure and the nature of the matrix and the bonding at the particle matrix interface. Exchange interactions are short ranged in insulating magnetic materials, but if the bonding is favorable, superexchange interactions may extend over large distances.
- *RKKY interaction:* The RKKY (Rudermann-Kittel-Kasuya- and Yosida) is an indirect exchange that couples moments over relatively large distances. It is the dominant exchange interaction in metals where there is little or no direct overlap between neighboring magnetic electrons [14].

Different models have been developed over the past years for describing the effect of interparticle interactions, and the most used are the *Shtrikman-Wohlfarth* (SW) model, developed in 1981 [15], the *Dormann-Bessais-Fiorani* (DBF) model (1998) [16], and the *Mørup-Tronc* model (1994) [17]. Both the SW and DBF models show that increase in interparticle interactions will lead to an increase in the energy barrier  $E_a$ :

$$E_a(\theta) = KV \sin^2 \theta + B_i \quad 2.13$$

where  $B_i$  is the energy term from interaction.

On the contrary the MT model indicates that increased interparticle interactions should decrease the energy barrier. On increasing the interaction strength a transition from a superparamagnetic state to a disordered collective state can be observed [18]. This state is called a superspin glass state by analogy with the disordered and frustrated magnetic state observed at low temperatures in spin glass materials [19].

Superspin glasses differ from canonical atomic spin glasses in several aspects. First, the interacting magnetic moments have very different amplitudes ( $10^2$ – $10^4 \mu_B$  for strongly coupled spins in a single-domain magnetic nanoparticle compared to a few  $\mu_B$  for an atomic spin) and the nature and range of their interactions are different (anisotropic and long range dipole/dipole interactions for magnetic nanoparticles vs shorter ranged exchange or longer range RKKY interactions for atomic spins). Additionally the characteristic time of the spin flip mechanism is very short ( $\sim 10^{-12}$ s) and nearly temperature independent in atomic spin glasses while it is much longer in superspin glasses, thermally activated and thus exponentially dependent on the ratio of the magnetic anisotropy energy  $E_a$  to the thermal energy  $k_B T$ .

Depending on the strength of the interaction one can use different magnetic models to describe the relaxation time of the ensemble. In case of interactions the *Vogel-Fulcher* model introduces in the Néel law an “ordering temperature”,  $T_0$ :

$$\tau = \tau_0 e^{-E_a/k_B(T-T_0)} \quad 2.14$$

For stronger interactions (closer distances) and if magnetic frustration and spatial randomness is present one can encounter a phase transition into a so-called superspin glass phase below a critical temperature,  $T_g$ , and  $\tau$  can be described by a power law:

$$\tau = \tau_0 \left( \frac{T_g}{T - T_g} \right)^{zv} \quad 2.15$$

where the critical exponent  $zv$  is related to the correlation length [20].

## 2.3 MRI Contrast Agents

### 2.3.1 Introduction

Most of the CAs are generally based on paramagnetic or superparamagnetic substances. The CAs used in MRI are selected to induce a shortening of the spin-lattice  $T_1$  and/or spin-spin  $T_2$  relaxation times of the hydrogen nuclei within the tissues/regions where they are delivered thus allowing a much better image contrast. Most commonly a paramagnetic CA, usually a gadolinium-based compound, is used [21,22]. Gadolinium-enhanced tissues and fluids appear extremely bright, and for this reason paramagnetic CAs are called *positive CA*.

More recently superparamagnetic (SP) CAs, based on iron oxide magnetic nanoparticles [23,24], have become commercially available. The regions where such agents are delivered appear very dark and therefore they are called *negative CA*. The big advantage of this type of CA is their sensitivity that is expected to reach single cell level [25].

As mentioned, CAs are used to provide the information at the cellular and molecular level. Increasing sensitivity and specificity proves to be the challenge for molecular and

cellular MRI. The detection of molecular or cellular events needs to exhibit *specificity* for the particular biological event. Specificity is therefore mainly reflected in the high ability of discriminating a particular molecule or cell from noise and other molecules. To achieve this high specificity, an antibody system targeting a particular antigen, for instance, will selectively bind the molecule/cell of interest [26,27]. By combining this antibody with a magnetic CA, it will be possible to provide a selective detection of the molecule or cell of interest with MRI.

The properties of the MR CA will determine its binding characteristics to the molecule of interest, its tissue penetration and circulation, and potentially its cellular uptake [28]. Modifying MR CA into multifunctional entities (e.g., optical and MR imaging simultaneously [29]) enhances their attractiveness.

Based on the functionalization of MR CAs, significant advances have been achieved in both cellular and molecular MR imaging. Notably, MR CAs can be shuttled into different types of cells *in vitro* or *in vivo* to track these by MRI [30], or they can be engineered to be attached to the particular molecules on tissues [31]. By engineering the CAs to only produce a signal change when bound to a molecule of interest [32,33], it is possible to scan the subject sooner, as there is no need to wait for unbound contrast agent to be washed out.

Among the most commonly used MR CAs (gadolinium, ferric iron, and manganese), only iron particles are ferrimagnetic and produce an effect that involves an area substantially greater than its localization [34-36]. Even small quantities of iron oxide particles can therefore be detected on MR scans. In some cases, even a single particle or cell can be detected [37-39].

At present, in most experiments iron oxide particles are the preferred agents, as they provide sufficient relaxivity to reliably detect even minute concentrations of CA. Engineering of CAs based on their physicochemical properties therefore greatly influences *in vivo* MR detection. Meticulous considerations to these characteristics will ensure significant improvements in the application of molecular imaging agents [36].

Although design and engineering of the CAs are developing, one of the greatest challenges over the coming years will be to ensure that these exciting advances find their translation into clinical applications. Not only the preclinical studies are needed to determine the feasibility and reliability of the novel CAs, but also prior to implementation in human subjects the safety of the newly engineered agents needs to be evaluated [28]. The use of CAs to visualize intracellular targets or to use them for cellular MRI especially needs to be thoroughly assessed, because they will remain localized to the compartments for considerably longer time frames compared to the current conventional MRI agents [30].

Molecular/cellular MRI is an interdisciplinary field of study that requires highly specialized expertise in CA chemistry, *MR physics*, image analysis, and biological disciplines.

### **2.3.2 Positive and Negative CAs**

Using most conventional pulse sequences,  $T_1$  agents give rise to increases in MR signal intensity and therefore they are also called *positive* contrast agents. On the other



hand,  $T_2$  agents largely increase  $1/T_2$  of tissue, hence leading to a decrease of the signal intensity and are classified as *negative* contrast agents. Paramagnetic materials increase  $1/T_1$  and  $1/T_2$  approximately equally, whereas superparamagnetic agents predominantly increase  $1/T_2$ . Paramagnetic agents include substances with one or more unpaired electrons, such as molecular nitric oxide, nitrogen dioxide, oxygen, or metal ions which have incomplete  $d$  or  $f$  orbital (mostly transition metal ions). Most of the transition metal ions alone are extremely toxic to the human body; therefore chelation of these ions with molecules such as diethylenetriamine-pentaacetic acid (DTPA) has been used to reduce their toxicity.

Fig. 2.6 shows how negative (left) and positive (right) contrast agents give a better image contrast.

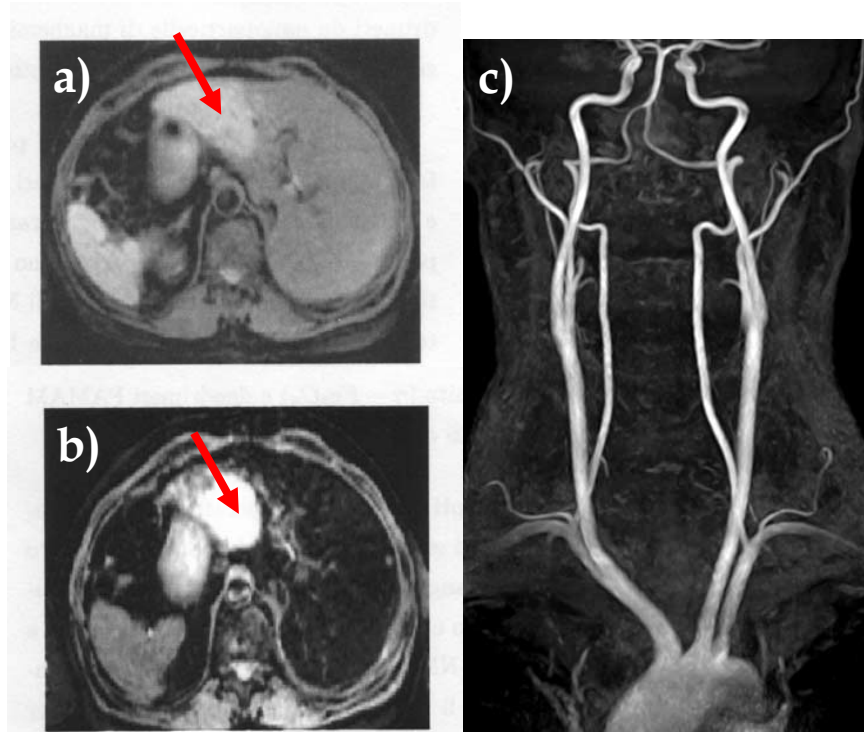


**FIG 2.6** Liver MR image (a) without and (b) with negative contrast agent. Arrows show the liver tumor. (c) an MR angiography using positive contrast agent.

Figs. 2.6a and b illustrate MRI images of liver without and with the use of magnetic CA, respectively. The arrows show the position of the tumor. As one can see, although without any CA it is possible to see the tumor, the tumor is much better defined in

presence of CA. As the CA is uptaken by the normal Kupffer cells, the signal of the normal tissues decreases and a better negative contrast is obtained. Fig. 2.6c, shows the effect of using a positive contrast agent. It is easily seen that the positive contrast agent increases the signal intensity of the vessels circuit resulting in seeing the area of interest brighter.

Gd-DTPA represents the first generation of MR contrast agents, introduced in the 1980s. This paramagnetic complex enhances predominantly the  $T_1$  relaxation rate of protons mainly through the inner sphere (see next section) relaxation [40]. Gd-DTPA has shown useful enhancement of the MR image contrast of the central nervous system [41-43]. A typical dosage required for effective contrast enhancement using this type of agents is approximately  $10^{-4}$  M. This concentration is lower than that of conventional iodinated radiographic contrast media for which  $10^{-2}$  M is an effective concentration, but higher than the effective concentration needed for radiopharmaceuticals ( $< 10^{-7}$  M).

Research on superparamagnetic pharmaceuticals, representing a second class of MR CAs, started in 1986. As already anticipated, these agents are particles with a much higher magnetic moment and they can significantly enhance the proton  $T_2$  relaxation rate (negative agents). Superparamagnetic agents include different types of inorganic iron particles which contain iron in different valence states and vary in their chemical composition, crystal structure, size and coating.

Superparamagnetic particulates have a strong effect on the spin-spin (transverse) relaxation process of the nearby protons. The relaxation mechanism of these agents is a complex process which has been the topic of several papers, and remains an active area of research.

Differently from paramagnetic chelates, the superparamagnetic particulates have a much higher magnetic moment. The large magnetic moments of these particulates in a magnetic field generate local field inhomogeneities. It is thought that as the protons diffuse near these field inhomogeneities, their Larmor frequencies lose coherence of phase, therefore causing an increase in transverse relaxation rate of protons.

A high magnetic susceptibility, i.e. the ability to cause strong inhomogeneities in the magnetic field, is desirable for a MR CA because it can significantly reduce the dosage required for sufficient contrast enhancement, thereby reducing its toxicity risk.

## 2.4 Relaxation Mechanisms of CAs

As mentioned previously, even though the intrinsic MRI contrast is much more flexible than in other clinical imaging techniques, the diagnosis of several pathologies requires the involvement of CAs that can enhance the difference between normal and diseased tissues by modifying their intrinsic parameters. This is the result of increasing (positive agents like paramagnetic CAs) or of decreasing (negative agents like superparamagnetic CAs) the signal intensity by shortening the proton relaxation times of the imaged organs and tissues. Accordingly, MR CAs are "indirect" agents because that is not the CA which becomes visible in the imaging as opposed to other imaging contrasts.

The signal produced by MRI CAs (i.e. the CAs' efficiency) depends on their spin-lattice and spin-spin *relaxivities*  $r_1$  and  $r_2$ , respectively, which are defined as the increase

of relaxation rate produced by 1 mmol per liter of magnetic center (expressed in  $s^{-1} \text{ mmol}^{-1}$ ) [44]. The  $r_1$  and  $r_2$  are the main physicochemical parameters that are considered in the development of an effective MRI CA. Relaxivity depends essentially on the size and chemical structure of a molecule and on the accessibility of water molecules to the magnetic center which is defined as:

$$r_i = [(1/T_i)_s - (1/T_i)_d] / C \quad 2.16$$

Where  $i = 1, 2$ ,  $C$  is the magnetic center concentration in the sample (in mM),  $(1/T_i)$  are the nuclear relaxation rates and the suffixes  $s$  and  $d$  stand for sample and dispersant.

It should be emphasized that the concentration of CA in the tissue is not the only parameter that contributes to its efficiency. The CA distribution within the image voxel, the proton density, the diffusion, and the chemical environment give crucial contributions to the signal enhancement/depression for  $T_1$ - or  $T_2$ -relaxing agents, respectively.

### 2.4.1 Paramagnetic Relaxation

Quantitative and heuristic theoretical models to express the nuclear relaxivity induced by paramagnetic centers have been developed. The efficiency of CAs is related to molecular motions and to intrinsic properties of the molecules (magnetic moment, gyromagnetic ratio, spin).

The paramagnetic relaxation is classically explained by two mechanisms: 1) the *inner sphere* (IS) and 2) the *outer sphere* (OS) contributions [44]. The principle of inner sphere relaxation (shown in Fig 2.7) relies on a chemical exchange during which one or several water molecules, belonging to the CA, leave the first coordination sphere of the magnetic compound and are replaced by the molecules of the bulk water (residence or exchange time  $\tau_M$ ).

This mechanism allows the propagation of the paramagnetic effect to the totality of the solvent. The IS model has been described by the Solomon-Bloembergen-Morgan theory (SBM) [45,46]. The relaxation time of water protons located in the first coordination sphere of the metal is  $T_{1M}$ . The contribution of the inner sphere mechanism is thus given by:

$$R_1^{IS} = f q \frac{1}{T_{1M} + \tau_M} \quad 2.17$$

where:

$f$  = the relative concentration of the paramagnetic complex to the water molecules;

$q$  = the number of water molecules in the first coordination sphere;

$\tau_M$  = the water residence time;

Calculation of  $T_{1M}$  is based on a model which includes the amplitude of the magnetic interaction, its temporal modulation and the effect of the strength of the external magnetic field. From a complete model (Solomon-Bloembergen equation) it was found that:

$$\frac{1}{T_{1M}} = \frac{2}{15} \left( \frac{\mu_0}{4\pi} \right)^2 \gamma_H^2 \gamma_S^2 \hbar^2 S(S+1) \frac{1}{r^6} \left[ \frac{7\tau_{c2}}{1+(\omega_S\tau_{c2})^2} + \frac{3\tau_{c1}}{1+(\omega_H\tau_{c1})^2} \right] \quad 2.18$$

With:

$$\begin{aligned} \frac{1}{\tau_{ci}} &= \frac{1}{\tau_R} + \frac{1}{\tau_M} + \frac{1}{\tau_{Si}} \\ \frac{1}{\tau_{S1}} &= \frac{1}{5\tau_{S0}} \left[ \frac{1}{1+\omega_S^2\tau_V^2} + \frac{4}{1+4\omega_S^2\tau_V^2} \right] \\ \frac{1}{\tau_{S2}} &= \frac{1}{10\tau_{S0}} \left[ 3 + \frac{5}{1+\omega_S^2\tau_V^2} + \frac{2}{1+4\omega_S^2\tau_V^2} \right] \end{aligned} \quad 2.19$$

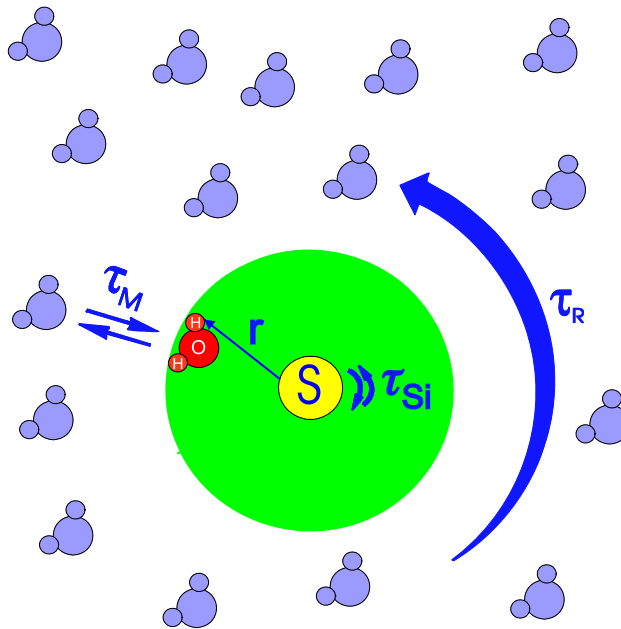


FIG. 2.7 Schematic representation of the inner sphere relaxation mechanism.

where:

$\gamma_S$  and  $\gamma_H$  = the gyromagnetic ratios of the electron (S) and of the proton (H), respectively;

$\omega_{S,H}$  = the angular frequencies of the electron and of the proton;

$r$  = the distance between coordinated water protons and unpaired electron spins;

$\tau_{c1,2}$  = the correlation times modulating the interaction;

$\tau_R$  = the rotational correlation time of the hydrated complex (due to the Brownian motion);

$\tau_{S1,2}$  = the longitudinal and transverse relaxation times of the electron;

These latter parameters are field dependent:

$\tau_{S0}$  = the value of  $\tau_{S1,2}$  at zero field;

$\tau_V$  = the correlation time characteristic of the electronic relaxation times;

The second contribution to the paramagnetic relaxation is the OS relaxation (Fig. 2.8). The main contribution to the nuclear relaxation rate increase from the OS mechanism comes from the fluctuations of the dipolar interaction acting at long-distance between the spin of the paramagnetic substance and the nuclear spin of bulk water protons. This mechanism is modulated by the translational correlation time ( $\tau_D$ ) that takes into account the relative diffusion ( $D$ ) of the paramagnetic center and the solvent molecule, as well as their distance of closest approach ( $d$ ). The OS model has been described by Freed [47], assuming that the diffusion time is given by:

$$\tau_D = \frac{d^2}{D} \quad 2.20$$

The complexity of equations describing the relaxation rate reveals the high number of parameters describing the IS and OS relaxation (eight parameters:  $\tau_M, q, \tau_R, D, r, d, \tau_V, \tau_{S0}$ ). Considering this high number of parameters, the estimation of all of them by the technique of field cycling (this technique will be explained in the next chapter) is often ambiguous. Thus, the determination of some parameters by independent methods facilitates the theoretical adjustment of the theoretical fitting of the proton nuclear magnetic relaxation dispersion (NMRD) profiles (Fig. 2.9). This curve characterizes the efficiency of CA at different magnetic fields [48-52].

The most important parameters involved in the relaxation mechanism are:

*Rotational correlation time* ( $\tau_R$ ). The rotational correlation time characterizes the relative reorientation of the electron spin vector of  $Gd^{3+}$  and the nuclear spin vector of protons of the water molecule. Generally, for a low molecular weight complex,  $\tau_R$  limits the relaxivity of the complex at imaging field. The rotational correlation time can be obtained by various methods, such as: 1) analysis of  $^{17}O$  longitudinal relaxation on Gd complexes [53,54], 2) measurement of the longitudinal relaxation rate in  $^{13}C$ -NMR [55], 3) fluorescence polarization spectroscopy [56], and 4)  $^2H$  NMR on deuterated lanthanum complexes [48].

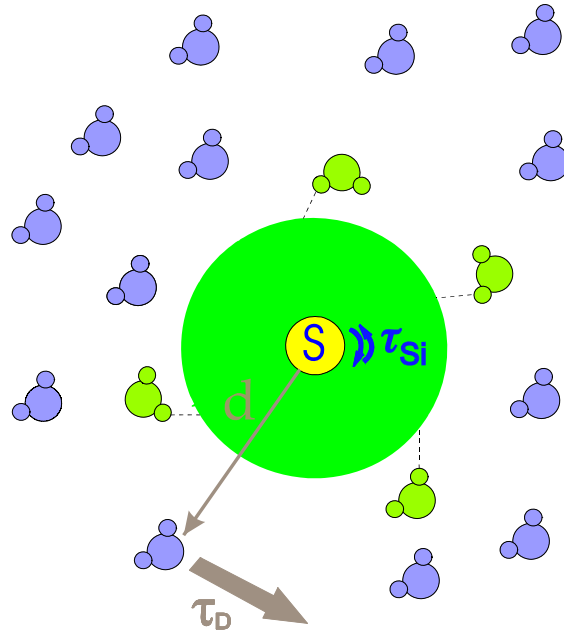


FIG. 2.8 Schematic representation of the outer sphere relaxation mechanism.

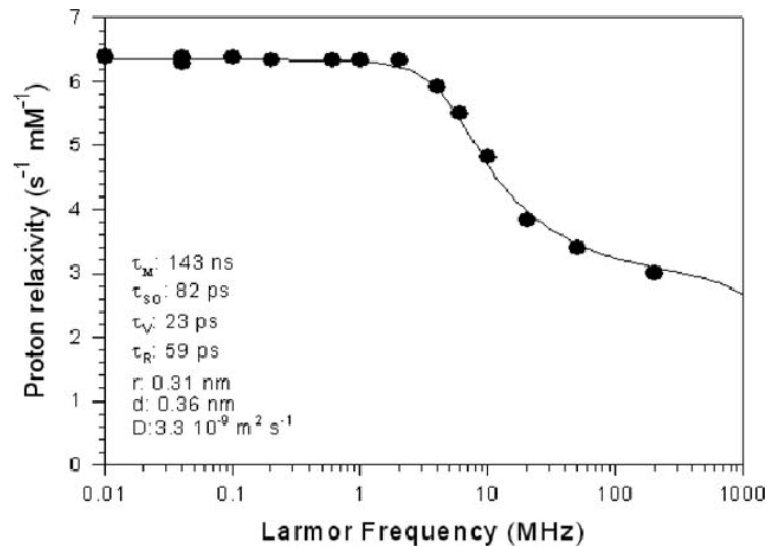


FIG. 2.9 NMRD profile of Gd-DTPA at 310 K (Laurent *et al.* 2006).

*Electronic relaxation times* ( $\tau_{S1}$  and  $\tau_{S2}$ ). Longitudinal and transverse electronic relaxation times ( $\tau_{S1}$  and  $\tau_{S2}$ , respectively) describe the process of relaxation of the magnetization associated to electrons during transitions between electronic levels of

paramagnetic center. These transitions produce fluctuations of the dipolar nuclear-electron interaction that allows the increase of the relaxation rate of protons.

*Number of coordinated water molecules ( $q$ ).* The number of coordinated water molecules strongly influences the IS contribution. For complexes like Gd-DTPA, if the number of coordinated water molecules increases from 1 to 2, the relaxivity increases by approximately 30%, but nearly all Gd-DTPA derivatives have a  $q$  value equal to 1. The value of  $q$  can be estimated either in solid phase (X-rays or neutron diffraction) or in solution [fluorescence of *Eu* or *Yb* complexes, LIS (lanthanide-induced shift) method in  $^{17}\text{O}$ -NMR].

*Proton-metal distance ( $r$ ).* In the presence of paramagnetic centers, the IS contribution relies on dipolar interactions. The efficiency of dipolar mechanism is proportional to  $1/r^6$ , where  $r$  is the metal-water proton distance. So, even a weak modification of this distance has an important impact on the complex relaxivity.

*Coordinated water residence time ( $\tau_M$ ).* The mechanism of IS relaxation is based on an exchange between bulk water molecules surrounding the complex and the water molecule(s) coordinated to the lanthanide. Consequently, the exchange rate ( $k_{ex} = 1/\tau_M$ ) is an essential parameter for transmission of the “relaxing” effect to the solvent. This parameter has been studied in many complexes to understand the influence of various factors, like the charge, the presence of amide bonds, etc. [53,54,57-62].

#### 2.4.2 Superparamagnetic Relaxation

The proton relaxation in superparamagnetic colloids like iron oxide particles occurs because of the fluctuations of the dipolar magnetic coupling between the nanocrystal magnetization  $M$  and the proton spin of the bulk water due to the diffusion motion of the water along the sample and to the fluctuations of  $M$  as a consequence of the Neel relaxation process. These two mechanisms are both weighted by the "effective" magnetic moment of the nanocrystal, i.e. the squared Langevin function whose variation with  $H$  is crucial for determining the frequency where the nuclear relaxation rate reaches its maximum. These superparamagnetic crystals of iron oxides exhibit extremely high magnetic moments due to a cooperative alignment of the electronic spins of the individual paramagnetic ions.

The nuclear relaxation is described by an OS model where the above mentioned dipolar interaction fluctuates because of both the translational diffusion process and the Neel relaxation process [63-68]. The analysis of the proton NMRD profiles (see Fig 2.10) of superparamagnetic particles gives [69]:

1. *The average hydrodynamic radius ( $r$ ):* at high magnetic fields, the relaxation rate depends only on  $\tau_D$  and the inflection point corresponds to the condition  $\omega_l \cdot \tau_D \sim 1$ . The determination of  $\tau_D$ ,  $\tau_D = r^2 / D$ , gives the crystal size.  $r$ ,  $D$  and  $\omega_l$  are the average radius of the superparamagnetic crystals, the relative diffusion coefficient, and the proton Larmor frequency, respectively.

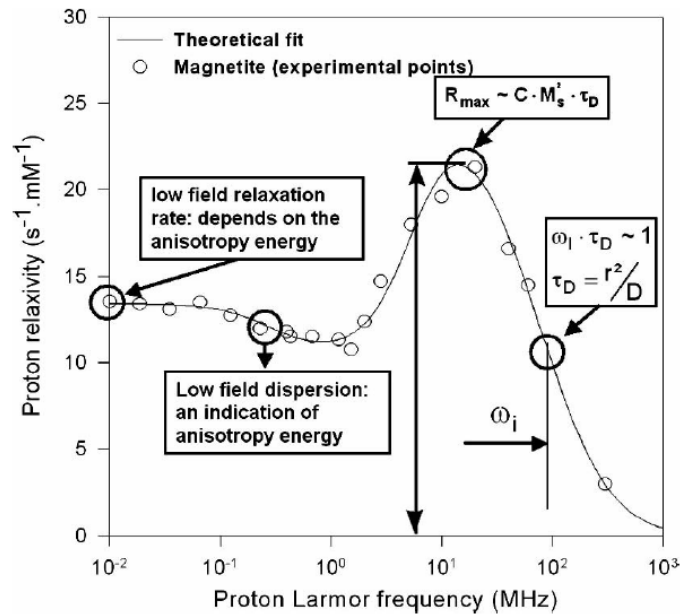


**FIG. 2.10** NMRD profile of magnetite particles in colloidal solution.

2. *The specific magnetization ( $M_s$ ):* at high magnetic fields,  $M_s$  can be obtained from the equation  $M_s \approx (R_{\max} / C \cdot \tau_D)^{1/2}$ , where  $C$  is a constant and  $R_{\max}$  the maximal relaxation rate.

3. *The crystal anisotropy energy ( $E_a$ ):* the absence or the presence of an inflection point at low fields informs about the magnitude of the anisotropy energy. For crystals characterized by a high  $E_a$  value as compared to the thermal energy  $k_B T$ , the low field dispersion disappears. This has been confirmed with cobalt ferrites [65], which are known to have high anisotropy energy.

4. *The Néel relaxation time ( $\tau_N$ ):* this correlation time characterizes the fluctuations of the total magnetization of the superparamagnetic particle. The relaxation rate at very low field  $R_0$  is governed by a “zero magnetic field” correlation time  $\tau_{C0}$ , which is equal to  $\tau_N$  if  $\tau_N \ll \tau_D$ . However, this situation is not often met, so that  $\tau_N$  is often reported as a qualitative value in addition to the crystal size and the specific magnetization, or deduced from magnetization and ac susceptibility data.

## 2.5 References

[1] E C. Stoner, and E. P. Wohlfart *Philos. Trans. London Series A* **1948**, 240, 74.



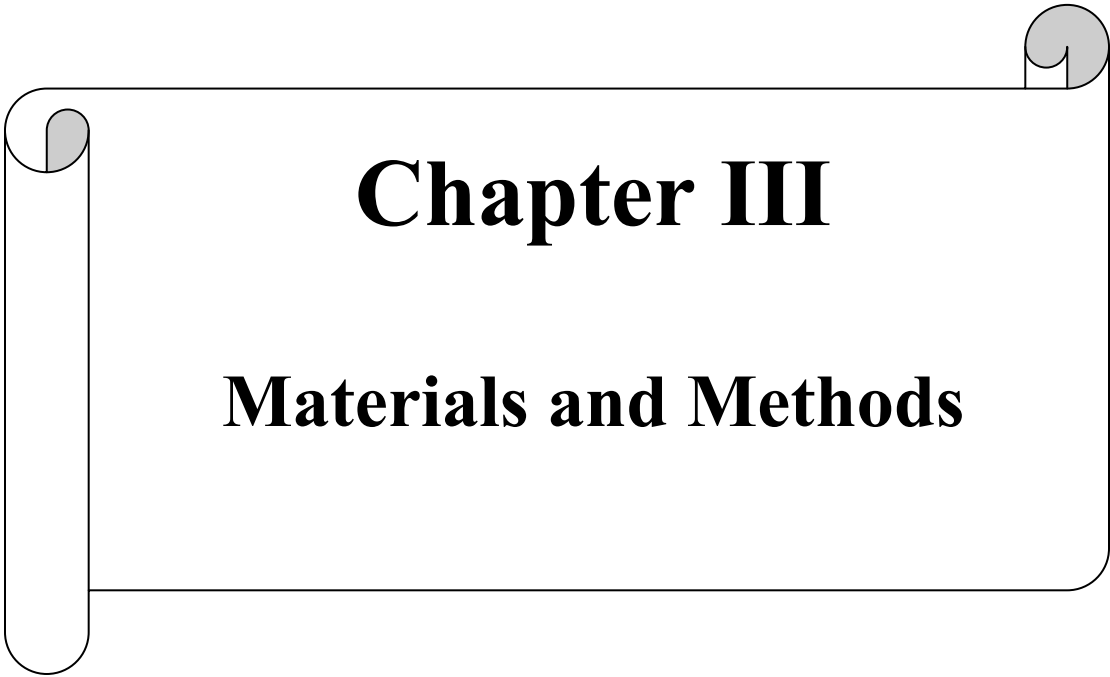
- [2] C. Kittel *Phys. Rev.* **1946**, 70, 965.
- [3] a) R.C O'Handley *Modern Magnetic Materials Principles and Application* Wiley, New-York, (2000); b) U. Jeong, X. Teng, Y. Wang, H. Yang, and Y. Xia *Adv. Mater.*, 19, 33, (2007).
- [4] E. C. Stoner, E. P. Wohlfarth *Philosophical Transaction of the Royal Society A*, 240, 599, (1948).
- [5] E. Vincent, Y. Yuan, J. Hammann, H. Hurdequint, F. Guevara *J. Magn. Magn. Mater.*, 161, 209, (1996).
- [6] J. L. Dormann *Revue Phys. Appl.*, 16, 275, (1981).
- [7] B. D. Cullity, and C.D Graham *Introduction to Magnetic Materials*, Addison-Wesley Publishing, (1972).
- [8] C. Verdes, S.M. Thompson, R.W. Chantrell, and Al. Stancu *Phys. Rev. B*, 65, 174417, (2002).
- [9] M. L Néel *Ann. Geophys.*, 5, 99, (1949).
- [10] P. C. Fannin *J. Magn. Magn. Mater.*, 258-259, 446, (2003).
- [11] S. Laurent, D. Forge, M. Port, A. Roch, C. Robic, L. V. Elst, and R. N. Muller *Chem. Rev.*, 108, 2064, (2008).
- [12] P. Debye *Polar Molecules* New York, Dover, (1929).
- [13] G. A. Held, G. Grinstein, H. Doyle, S. Sun, C. B. Murray *Phys. Rev. B*, 64, 012408, (2001).
- [14] M.A. Rudermanand, and C. Kittel *Phys. Rev.*, 96, 99, (1954).
- [15] E.C. Stoner, E.P. Wohlfarth *Phisolophical Transaction of the Royal Society A*, 240, 599, (1948).
- [16] J. L. Dormann, D. Fiorani, E. Tronc *J. Magn. Magn. Mater.*, 202, 251, (1999).
- [17] M.F Hansen, S. J. Mørup *Magn. Magn. Mater.*, 184, 262, (1998).
- [18] T. Jonsson, J. Mattsson, C. Djurberg, F. A. Khan, P. Nordblad, and P. Svedlindh *Phys. Rev. Lett.* 75, 4138, (1995).
- [19] J. A. Mydosh *Spin Glasses: An Experimental Introduction* Taylor & Francis, London, (1993).

- [20] J. J. Binney, N. J. Dowrick, A. J. Fisher and M. E. J. Newman *Theory of Critical Phenomena, An introduction to the Renormalized Group* Oxford University Press, (1992).
- [21] H. J. Weinmann, R. C. Brasch, W. R. Press, G. E. Wesbey, *American Journal of Roentgenology*, 142, 619, (1984).
- [22] M. Laniado, H.J. Weinmann, W. Schörner, R. Felix, U. Speck, *Physiological Chemistry & Physics & Medical NMR*, 16, 157, (1984).
- [23] D.J. Widder, W.L. Greif, K.J. Widder, R.R. Edelman. T.J. Brady, *American Journal of Roentgenology*, 148, 399, (1987).
- [24] R. Weissleder, G. Elizondo, J. Wittenberg, C.A Rabito, H.H. Bengel, L. Josephson, *Radiology*, 175, 489, (1990).
- [25] R. Weissleder, A. Moore, U. Mahmood, R. Bhorade, H. Benveniste, E.A. Chiocca, J.P. Basilion, *Nature Med.*, 6, 151, (2000).
- [26] Guccione, S., Li, K.C., and Bednarski, M.D., *IEEE Eng. Med. Biol. Mag.*, 23, 50–56, (2004).
- [27] Artemov, D., *Molecular magnetic resonance imaging with targeted contrast agents*, *J. Cell. Biochem.*, 90, 518–524, (2003).
- [28] Lorusso, V., Pascolo, L., Ferneti, C., Anelli, P.L., Uggeri, F., and Tiribelli, C., *Magnetic resonance contrast agents: from the bench to the patient*, *Curr. Pharm. Design*, 11, 4079–4098, (2005).
- [29] Omid Veisheh, Conroy Sun, Jonathan Gunn, Nathan Kohler, Patrik Gabikian, Donghoon Lee, Narayan Bhattarai, Richard Ellenbogen, Raymond Sze, Andrew Hallahan, Jim Olson, and Miqin Zhang, *Optical and MRI Multifunctional Nanoprobe for Targeting Gliomas*, *Nano letters*, Vol. 5, No. 6, 1003-10008, (2005).
- [30] Modo, M., Hoehn, M., and Bulte, J.W., *Cellular MR imaging*, *Mol. Imaging*, 4, 143164, (2005).
- [31] Delikatny, E.J. and Poptani, H., *MR techniques for in vivo molecular and cellular imaging*, *Radiol. Clin. N. Am.*, 43, 205–220, (2005).
- [32] Louie, A.Y., Huber, M.M., Ahrens, E. T., Rothbacher, U., Moats, R., Jacobs, R.E., Fraser, S. E., and Meade, T. J., *In vivo visualization of gene expression using magnetic resonance imaging*, *Nat. Biotechnol.*, 18, 321–325, (2000).
- [33] Li, W. H., Parigi, G., Fragai, M., Luchinat, C., and Meade, T. J., *Mechanistic studies of a calcium dependent MRI contrast agent*, *Inorg. Chem.*, 41, 4018–4024, (2002).

- [34] Bonnemain, B., Superparamagnetic agents in magnetic resonance imaging: physicochemical characteristics and clinical applications. A review, *J. Drug Target*, 6, 167–174, (1998).
- [35] Bjornerud, A. and Johansson, L., The utility of superparamagnetic contrast agents in MRI: theoretical consideration and applications in the cardiovascular system, *NMR Biomed.*, 17, 465–477, (2004).
- [36] Reichert, D.E., Lewis, J.S., and Anderson, C.J., Metal complexes as diagnostic tools, *Coordination Chem. Rev.*, 184, 3–66, (1999).
- [37] Shapiro, E.M., Sharer, K., Skrtic, S., and Koretsky, A.P., In vivo detection of single cells by MRI, *Magn. Reson. Med.*, 55, 242–249, (2006).
- [38] Heyn, C., Ronald, J.A., Mackenzie, L.T., MacDonald, I.C., Chambers, A.F., Rutt, B.K., and Foster, P.J., *In vivo* magnetic resonance imaging of single cells in mouse brain with optical validation, *Magn. Reson. Med.*, 55, 23–29, (2006).
- [39] Shapiro, E.M., Skrtic, S., Sharer, K., Hill, J.M., Dunbar, C.E., and Koretsky, A.P., MRI detection of single particles for cellular imaging, *Proc. Natl. Acad. Sci. U.S.A.*, 101, 10901–10906, (2004).
- [40] Lauffer, R. B., "Paramagnetic Metal Complexes as Water Proton Relaxation Agents for NMR Imaging: Theory and Design." *Chem. Rev.* 87: 901-927, (1987).
- [41] Weinmann, H., R. Brasch, *et al.*, "Characteristics of Gd-DTPA complex: a potential NMR contrast agent." *AJR* 142: 619-25, (1984).
- [42] Hesselink, J., M. Healey, *et al.*, "Benefits of Gd-DTPA for MR imaging of intracranial abnormalities." *J Comput Assist Tomogr* 13(2): 266-74, (1988).
- [43] Unger, E., P. McDougall, *et al.*, "Liposomal Gd-DTPA: effect of encapsulation on enhancement of hepatoma model by MRI." *Magn Reson Imaging* 7(4): 417-23, (1989).
- [44] Muller RN, Contrast agents in whole body magnetic resonance: operating mechanisms. In: *Encyclopedia of nuclear magnetic resonance*. Grant DM, Harris RK (eds.), Wiley, New York, pp 1438–1444, (1996)
- [45] Solomon I, Relaxation processes in a system of two spins. *Phys Rev* 99:559–565, (1955).
- [46] Bloembergen NJ, Proton relaxation times in paramagnetic solutions. *Chem Phys* 27: 572–573, (1957).

- [47] Freed JH, Dynamic effects of pair correlation functions on spin relaxation by translational diffusion in liquids. II. Finite jumps and independent  $T_1$  processes. *J Chem Phys* 68:4034–4037, (1978).
- [48] Vander Elst L, Maton F, Laurent S, Seghi F, Chapelle F, Muller RN, A multinuclear MR study of Gd-EOB-DTPA: comprehensive preclinical characterization of an organ specific MRI contrast agent. *Magn Reson Med* 38:604–614, (1997).
- [49] Muller RN, Raduchel B, Laurent S, Platzek J, Piérart C, Mareski P, Vander Elst L, Physicochemical characterization of MS-325, a new gadolinium complex, by multinuclear relaxometry. *Eur J Inorg Chem* 1949–1955, (1999).
- [50] Laurent S, Vander Elst L, Houzé S, Guérit N, Muller RN, Synthesis and characterization of various benzyl diethylenetriaminepentaacetic acids (DTPA) and their paramagnetic complexes: potential organ specific contrast agents for MRI. *Helv Chim Acta* 83:394–406, (2000).
- [51] Laurent S, Botteman F, Vander Elst L, Muller RN, *Magn Reson Mater Phys Biol Med* 16:235–245, (2004).
- [52] Laurent S, Botteman F, Vander Elst L, Muller RN, Relaxivity and transmetallation stability of new benzyl-substituted derivatives of gadolinium-DTPA complexes. *Helv Chim Acta* 87:1077–1089, (2004).
- [53] Micskei K, Helm L, Brucher E, Merbach AE,  $^{17}\text{O}$  NMR study of water exchange on  $[\text{Gd}(\text{DTPA})\text{H}_2\text{O}]^{2-}$  and  $[\text{Gd}(\text{DOTA})\text{H}_2\text{O}]^-$  related to NMR imaging. *Inorg Chem* 32: 3844–3850, (1993).
- [54] Micskei K, Powell DH, Helm L, Brucher E, Merbach AE, Water exchange on  $[\text{Gd}(\text{H}_2\text{O})_8]^{3+}$  and  $[\text{Gd}(\text{PDTA})(\text{H}_2\text{O})_2]^-$  in aqueous solution: a variable-pressure, -temperature and -magnetic field  $^{17}\text{O}$  NMR study. *Magn Reson Chem* 31:1011–1020, (1993).
- [55] Shukla R, Zhang X, Tweedle M., In vitro determination of correlation times independent of nuclear magnetic resonance dispersion. *Inverst Radiol* 26:S224–S225, (1991).
- [56] Helms MK, Petersen CE, Bhagavan NV, Jameson DM, Time-resolved fluorescence studies on site-directed mutants of human serum albumin *FEBS Letters*, 408:67–70, (1997).
- [57] Gonzalez G, Powell DH, Tissiéres V, Merbach AE, Water-exchange, electronic relaxation and rotational dynamics of the MRI contrast agent  $[\text{Gd}(\text{DTPA-BMA})(\text{H}_2\text{O})]$  I aqueous solution: a variable pressure, temperature, and magnetic field  $^{17}\text{O}$  NMR study. *J Phys Chem.* 98:53–59, (1994).

- [58] Aime S, Botta M, Fasano M, Terreno E, Prototropic and water-exchange processes in aqueous solutions of Gd(III) chelates. *Acc Chem Res* 32:941–949, (1999).
- [59] Zhang S, Wu K, Sherry AD, Gd<sup>3+</sup> complexes with slowly exchanging bound-water molecules may offer advantages in the design of responsive MR agents. *Invest Radiol* 36:82–86, (2001).
- [60] Toth E, Pubanz D, Vauthey S, Helm L, Merbach AE, High-pressure NMR kinetics. The role of water exchange in attaining maximum relaxivities for dendrimeric MRI contrast agents. *Chem Eur J* 2:1607–1615, (1996).
- [61] Toth E, Van Uffelen I, Helm L, Merbach AE, Ladd D, Briley-Saebo K, Kellar KE, Gadolinium-based linear polymer with temperature-independent proton relaxivities: a unique interplay between the water exchange and rotational contributions. *Magn Reson Chem* 36:S125–S134, (1998).
- [62] Toth E, Helm L, Kellar KE, Merbach AE, Gd (DTPA-bisamide) alkyl copolymers: A hint for the formation of MRI contrast agents with very high relaxivity. *Chem Eur J* 5:1202–1211, (1999).
- [63] Roch A, Muller RN, Longitudinal relaxation of water protons in colloidal suspensions of superparamagnetic crystals. *Proc. 11<sup>th</sup> Annual Meeting of the Society of Magnetic Resonance in Medicine*. 11:1447, (1992).
- [64] Roch A, Muller RN, Gillis P, Theory of proton relaxation induced by superparamagnetic particles. *J Chem Phys* 110:5403–5411, (1999).
- [65] Roch A, Gillis P, Ouakssim A, Muller RN, Proton magnetic relaxation in superparamagnetic aqueous colloids: a new tool for the investigation of ferrite crystal anisotropy. *J Magn Magn Mater* 201:77–79, (1999).
- [66] Roch A, Muller RN, Gillis P, Water relaxation by SPM particles: Neglecting the magnetic anisotropy? A caveat. *J Magn Reson Imaging* 14:94–96, (2001).
- [67] Muller RN, Roch A, Colet JM, Ouakssim A, Gillis P, Particulate magnetic contrast agents. In: *The chemistry of contrast agents in medical magnetic resonance imaging*. Merbach AE, Toth E (eds), Wiley, New York, pp 417–435, (2001).
- [68] Ouakssim A, Fastrez S, Roch A, Laurent S, Gossuin Y, Pierart C, Vander Elst L, Muller RN, Control of the synthesis of magnetic fluids by relaxometry and magnetometry. *J Magn Magn Mater* 272–276:e1711–e1713, (2004)
- [69] Carmen Burtea, Sophie Laurent, Luce Vander Elst, and Robert N. Muller, Contrast Agents: Magnetic Resonance. In: *Molecular Imaging I*. Wolfhard Semmler, Markus chwaiger (eds), Springer-Verlag Berlin Heidelberg (2008).



# **Chapter III**

## **Materials and Methods**

## Chapter III

# Materials and Methods

### *Contents*

---

|                                       |    |
|---------------------------------------|----|
| 3.1 Samples .....                     | 47 |
| 3.2 Magnetic Properties .....         | 54 |
| 3.2.1 SQUID-Based Magnetometers ..... | 54 |
| 3.2.2 NMR Relaxometers .....          | 58 |
| 3.2.3 MRI Scanner .....               | 62 |
| 3.3 References .....                  | 64 |

---

### 3.1 Samples

The revolution in nanotechnology has brought us new tools not only in analytical systems but also for human applications. One of these new tools are the magnetic nanoparticles (MNPs) [1,2]. Because of their ultrafine size, biocompatibility, and superparamagnetic properties, iron oxide nanoparticles are already approved for various biomedical applications such as enhanced contrast magnetic resonance imaging [3] and cellular labeling/cell separation [4-7] and are undergoing preclinical and clinical evaluation for applications such as drug delivery [8-14], cell and tissue targeting [15], transfection [16,17], and magnetic hyperthermia [18]. Superparamagnetic iron oxide nanoparticles (SPIONs) with a mean particle diameter of about 10 nm suspended in appropriate carrier liquids are commonly called ferrofluids and have outstanding properties. Each particle contains only a single magnetic domain and can thus be treated as a small thermally agitated magnet in the carrier liquid. The special feature of ferrofluids is the combination of normal liquid behavior with superparamagnetic

properties. This enables the use of magnetic forces for the control of properties and flow of the liquids, giving rise to numerous technical applications. Especially for in vivo applications, such as drug delivery, superparamagnetism is crucial because once the external magnetic field is removed, the magnetization disappears. Therefore, agglomeration and hence the possible embolization of the capillary vessels, can not take place [19]. However, two major shortcomings encountered in the in vivo application of superparamagnetic particles are their destabilization due to the adsorption of plasma proteins and their nonspecific uptake by the reticulo-endothelial system (RES; phagocytic cells residing in tissues forming part of the body's immune system) [20,21]. Because of the high specific surface area of the nanosized particles, plasma proteins interact with the particles, causing an increase in the particle size and often resulting in agglomeration. The particles are also considered as intruders by the innate immune system and can be readily recognized and engulfed by macrophage cells that may cause agglomeration. In both cases, the particles will be removed from the blood circulation, which will yield a decrease in their effectiveness, leading to a reduction in efficiency of nanoparticle-based diagnostics and therapeutics.

To prevent both phenomena and provide longer circulation times, the particles are usually coated with hydrophilic and biocompatible polymers/molecules such as polyethylene glycol (PEG), dextran, polyvinyl alcohol (PVA), poly(acrylic acid), chitosan, pullulan, or poly(ethyleneimine) (PEI) [22]. Furthermore, the immediate release of large amounts of the adsorbed/encapsulated drug, the so called *burst effect*, upon application into the body, an effect that is related to the high surface-to-volume ratio of nanoparticles, will cause a reduction of the amount of drug that reaches the targeted site.

The other very important and challenging issue concerning the biomedical application of nanoparticles is the possibility of getting them functionalized. This may be made using different strategies, such as the addition of specific targeting ligands, dyes or therapeutic agents. Functionalized nanoparticles will lead to design of multifunctional biomaterials for diagnostics (e.g. contrast agents in optical and MR imaging) and therapeutics (e.g. hyperthermia cancer treatment and targeted drug and gene delivery), the so called *theranostics*. Such particles would be able to identify disease states and simultaneously play the therapeutic role.

Magnetic hyperthermia has recently attracted the attention of the scientist as a new way to treat cancer. It is based on the fact that magnetic nanoparticles, when subjected to an alternating magnetic field, produce heat. As a consequence, if magnetic nanoparticles are put inside a tumor and the whole patient is placed in an alternating magnetic field of well-chosen amplitude and frequency, the tumor temperature would raise. This could kill the tumor cells by necrosis if the temperature is above 45 °C, or could improve the efficiency of chemotherapy if the temperature is raised around 42 °C. This treatment is tested on humans only in Germany, but research is in progress in several laboratories around the world to test and develop this technique [18].

Targeted drug delivery is a method of medication delivery to a patient in a manner that increases the concentration of the medication in some parts of the body relative to others. The medication is distributed throughout the body through the systemic blood circulation. For most therapeutic agents, only a small portion of the medication reaches the organ to be affected. Targeted drug delivery tries to concentrate the medication in the tissues of interest while reducing the relative concentration of the medication in the remaining



tissues. This improves the efficiency and reduce the side effects. Targeted drug delivery can be used to treat many diseases, such as the cardiovascular diseases and diabetes. However, the most important application of targeted drug delivery is to treat the cancerous tumors.

The regularly employed SPIONs in drug delivery consist of nanoparticles, nanospheres, liposomes and microspheres. In these systems, the drugs are bound to the SPIONs' surface (especially for NPs) or encapsulated in magnetic liposomes and microspheres. The most recent delivery systems are focused on anti-infective, blood clot dissolving, anti-inflammatory, anti-arthritis, photodynamic therapy, and paralysis-inducing drugs as well as on stem cell differentiating/tracking [23,24].

The surface engineered SPIONs (e.g. with targeting ligand/molecules attached to their surfaces) used together with the aid of an external magnetic field are recognized as a modern technology to introduce particles to the desired site where the drug can be released. Such a system has the potential to minimize the side effects and the required dosage of the drugs [23,25,26]. However, once the surface-derivatized nanoparticles are inside the cells, the coating is likely digested leaving the bare particles exposed to other cellular components and organelles thereby potentially influencing the overall integrity of the cells [27,28]. It is hypothesized that rigid coatings such as crosslinked PEGF could postpone this shortcoming [27].

Relying on this introduction and knowing that polymers can provide a way to avoid agglomeration and easy surface functionalisation, we have studied magnetic and relaxometric properties of two different classes of samples, both of them showing superparamagnetic behaviors and coated with the polymers. We will introduce them in the followings.

### *3.1.a Multifunctional Polymer-Based Nanostructured Bio-Ferrofluids:*

Multifunctional polymer-based nanostructured bio-ferrofluids (named samples A-D), hereafter in brief bio-ferrofluids, have been synthesized by our collaborator, *Instituto de Ciencia de Materiales de Aragón, CSIC-Universidad de Zaragoza*, in Spain (Prof. F. Palacio, Dr. A. Millan).

The synthesis of the bio-ferrofluids was performed in two steps: 1) synthesis of maghemite/polyvinylpyridine (PVP) nanocomposites, and 2) synthesis of ferrofluids (using the nanocomposites) in a buffer saline solution (PBS) medium. Maghemite/PVP nanocomposites were prepared by *in situ* precipitation from iron-PVP coordination compounds, following the procedure described in [29]. A film of iron-polymer precursor was obtained by evaporation of a 50% water:acetone solution containing 0.2g of PVP (Aldrich, 60 kD), and variable amounts of FeBr<sub>2</sub> (Aldrich) and FeBr<sub>3</sub> (Aldrich). The precursor film was treated with 20mL of 1 M NaOH solution for 1h, washed with water and dried in open air to obtain a maghemite nanocomposite. The size of the maghemite nanoparticles in the composites was tuned by using different Fe(II)/Fe(III) and Fe/N ratios. Composites for samples A-C were prepared using a Fe(II)/Fe(III) ratio of 0.5 and Fe/N ratios of 0.5, 0.625 and 1 respectively. Composite for sample D was prepared using a ratio of 1 for both Fe(II)/Fe(III) and Fe/N. The ferrofluids were prepared according to Ref. 2. The maghemite/PVP nanocomposites were dispersed in an acidic solution at pH  $\approx$

3. The resulting acidic ferrofluid was mixed with 0.18 mL of polyethyleneglycol (PEG) (MW=200D) acrylate (PEG(200)-A) (Monomer&Polymer), and 0.02g of PEG (MW=1000D) acrylate (PEG(1000)-A-COOH) (Monomer&Polymer), and was heated to 70°C during 24h. Then,  $\text{Na}_2\text{HPO}_4$  was added for a 0.01M final concentration, the pH was adjusted to 7.40 by addition of a 0.2M NaOH solution, and the ionic strength was adjusted to 0.15 by addition of NaCl and KCl. Finally, the dispersion was filtered through a 0.22 $\mu\text{m}$  membrane filter to obtain a bio-ferrofluid. Scheme of bio-ferrofluids including the carboxyl group (-COOH), for getting them functionalized, is shown in Fig. 3.1.

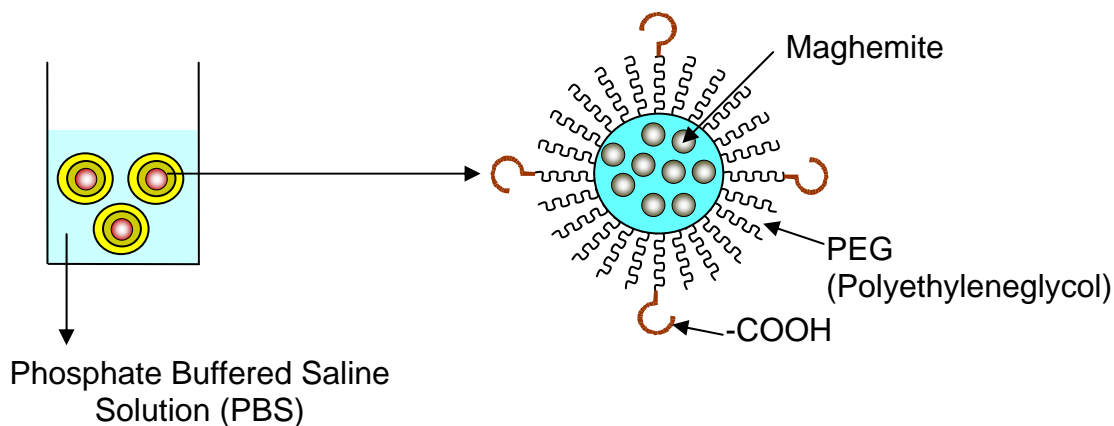


**FIG. 3.1** Scheme of bio-ferrofluids dispersed in PBS with PEG coating and carboxyl group for making them functionalized.

*In vivo toxicology experiments*, to study the effect of the bio-ferrofluids on mice, already have been done. A group of mice were injected with the maximum allowed volume of bio-ferrofluid with a concentration of 4 g/L of iron oxide. After one month, the mice did not show any anomaly and an analysis of the organs after being sacrificed did not revealed any damage nor a significant accumulation in the organs of the treated mice.

The bio-ferrofluids have been also already used in *haematology studies*. They have not shown any problems with blood. In fact they show an effect that can be beneficial, i.e. they are anticoagulants. The coagulation effects of biocompatible multifunctionalizable bio-ferrofluids designed for biomedical applications have been studied. It has been found that the bio-ferrofluids not only do not cause coagulation, but also they act as non specific circulating anticoagulant agents *in vitro* and the results are going to be confirmed *in vivo* by a Ph.D. student in Spain. Therefore, the bio-ferrofluids, in addition to their inherent biomagnetic applications, could be also useful in other biomedical applications such as anticoagulant agents.

They have also been used in *cell experiments* and low cytotoxicity in opossum kidney cells has been revealed and reported [30]. Bio-ferrofluids have been also functionalised with an optical dye (fluoresceine and rhodamine) attached to the surface of the particles which permits to track the pathway of the particles across the cellular membrane and inside the cell. It has been observed that the particles are internalized by the cells and they do not enter into organelles such as mitochondria, or ribosomes, but they accumulate in lysosomes. Thus the bio-ferrofluids could be also useful for the *optical imaging*.

The hyperthermia efficiency of the samples also has been already investigated. The measurements have been done for several frequencies, in the frequency range 2 kHz to 100 kHz, and several field intensities. The best performance has been obtained for the largest particle size (sample D) which is outstandingly larger than Endorem and substantially higher than ChemiCell (pure magnetite dispersed in water).

The main idea is to use these samples as theranostics, i.e. simultaneous diagnostic and therapeutical, agents. Thus the study of their magnetic properties and MRI efficiency is a crucial issue. This is what we will report in the next chapter.

### *3.1.b Superparamagnetic Colloidal Nano-Crystal Clusters (CNCs):*

Colloidal nano-crystal clusters (CNCs) are magnetic beads of several SPIONs with different polymer coatings. As a result of superparamagnetic behaviour, they present a large saturation magnetization, narrow size distribution, and no aggregation in solution. They have been synthesized by our collaborator, Institute for Nanoscience and Nanotechnology, Sharif University of Technology, in Iran (Dr. M. Mahmoudi).

To synthesize the CNCs, iron salts (i.e., chloride) and sodium hydroxide (NaOH), with analytical grades, purchased from Merck Inc. (Darmstadt, Germany), were used without further purification. Polyvinyl alcohol ( $M_w=30,000-40,000$ ) was obtained from Fluka. PEG diol (MW 1 kDa), fumaryl chloride, calcium hydride and propylene oxide were all purchased from Aldrich (Milwaukee, MN, USA). Ammonium per-sulfate and methylene chloride (DCM) were obtained from Merck (Germany). Fumaryl chloride was purified by distillation at 161°C under ambient pressure. Tamoxifen (TMX) was obtained from Pharma Chemie Company (Tehran, Iran). Anhydrous DCM was obtained by distillation under reflux condition for 1h in the presence of calcium hydride. Other solvents were reagent grades and used without any further purification.

*Preparation of superparamagnetic iron oxide nanoparticles (SPIONs).* SPIONs were prepared via the well known co-precipitation method, which was optimized previously [31]. Typically, iron salts (the mole fraction of  $Fe^{2+}$  to  $Fe^{3+}$  was adjusted to 1:2) were dissolved in Deionized (DI) water containing 0.5M HCL and all solutions were deoxygenated by the bubbling process with argon gas. The magnetite nanoparticles were precipitated by drop wise addition of iron salt solutions to NaOH solutions (with various molarities) under an argon atmosphere. In order to control mass transfer, which may allow particles to combine and build larger polycrystalline particles, turbulent flow was created by placing the reaction flask in an ultrasonic bath and changing the homogeneization rates during the first 2 minutes of the reaction [32]. It is notable that the stirring rate was fixed at 9000 rpm for all samples in the synthesis period (1h). Various molarities of the NaOH solutions (1, 2, 3, and 4) were examined. The particles were collected by external magnetic field and re-dispersed in DI water.

*Preparation of PVA-coated SPIONs.* A Polyvinyl Alcohol (PVA) was dissolved in DI water and was added to the alkaline solution before introducing the iron salts. Then the

same method for SPIONs preparation was employed in order to obtain coated nanoparticles.

*Preparation of poly(ethylene glycol)-co-fumarate (PEGF).* The Temenoff method was used for the preparation of PEGF macromer [32]. Commonly, 0.03 mole of PEG diol was dissolved in 100ml of anhydrous methylene chloride (DCM) in a three-necked 250ml reaction flask equipped with a reflux condenser and a magnetic stirrer. Propylene oxide was employed as a catalyst for binding to the HCl, which is produced during the polymerization. The purified fumaryl chloride was dissolved in 50 ml of DCM and added dropwise in 1h to the stirred reaction flask at  $-2^{\circ}\text{C}$  under nitrogen atmosphere. Consequently, the reaction temperature was enhanced to room temperature and run overnight. In order to remove the by-product (e.g., chlorinated propanols), the product was washed with 0.1N NaOH several times. The PEGF macromer was then obtained by rotaevaporation, dried at  $25^{\circ}\text{C}$  in vacuum for 24h, and then stored at  $-15^{\circ}\text{C}$  until further use.

*Preparation of crosslinked-PEGF-coated SPIONs.* The obtained PEGF solution was diluted in DI water and was added to the alkaline solution before introducing the iron salts. Then the same method for SPIONs preparation was employed in order to obtain coated nanoparticles. The coated-SPIONs were then collected by external magnetic field and re-dispersed in DI water in order to remove the unbounded polymers. The crosslinking of the unsaturated coating were started by Ammonium persulphate  $[(\text{NH}_4)_2\text{S}_2\text{O}_8]$  as initiator system [33] and an optimized amount of accelerator (DMAEMA) [34] via the redox polymerization. After stirring for 2h, the particles were washed several times and were kept at  $4^{\circ}\text{C}$  for future use. Schematic representative of the various synthesized magnetic nanoparticles are shown in Fig 3.2.

*Drug release.* The drug release from nanoparticles has been investigated [34]. The study revealed that by introducing a crosslinking agent to the system, the burst effect was reduced by 21%. Thus the crosslinked magnetic nanoparticles are able to control the burst effect (see the results in the next chapter).

*Biocompatibility.* To study the biocompatibility of the samples, the 3-(4,5-dimethylthiazol-2-yl)-2,5-diphenyltetrazolium bromide (MTT) assay has been made for L929 and K562 cells exposed to all the samples. All of them demonstrated acceptable levels of cell viability following exposure up to 400  $\mu\text{M}$ , with none demonstrating toxic effects at the concentrations tested. In addition, the PEGF coated samples have shown more biocompatibility than the PVA coated ones [34]. Therefore, the crosslinked-PEGF coated magnetic nanoparticles would be very promising materials for the therapeutics, i.e. targeted drug delivery, applications. The results of MTT assay are reported in the next chapter.

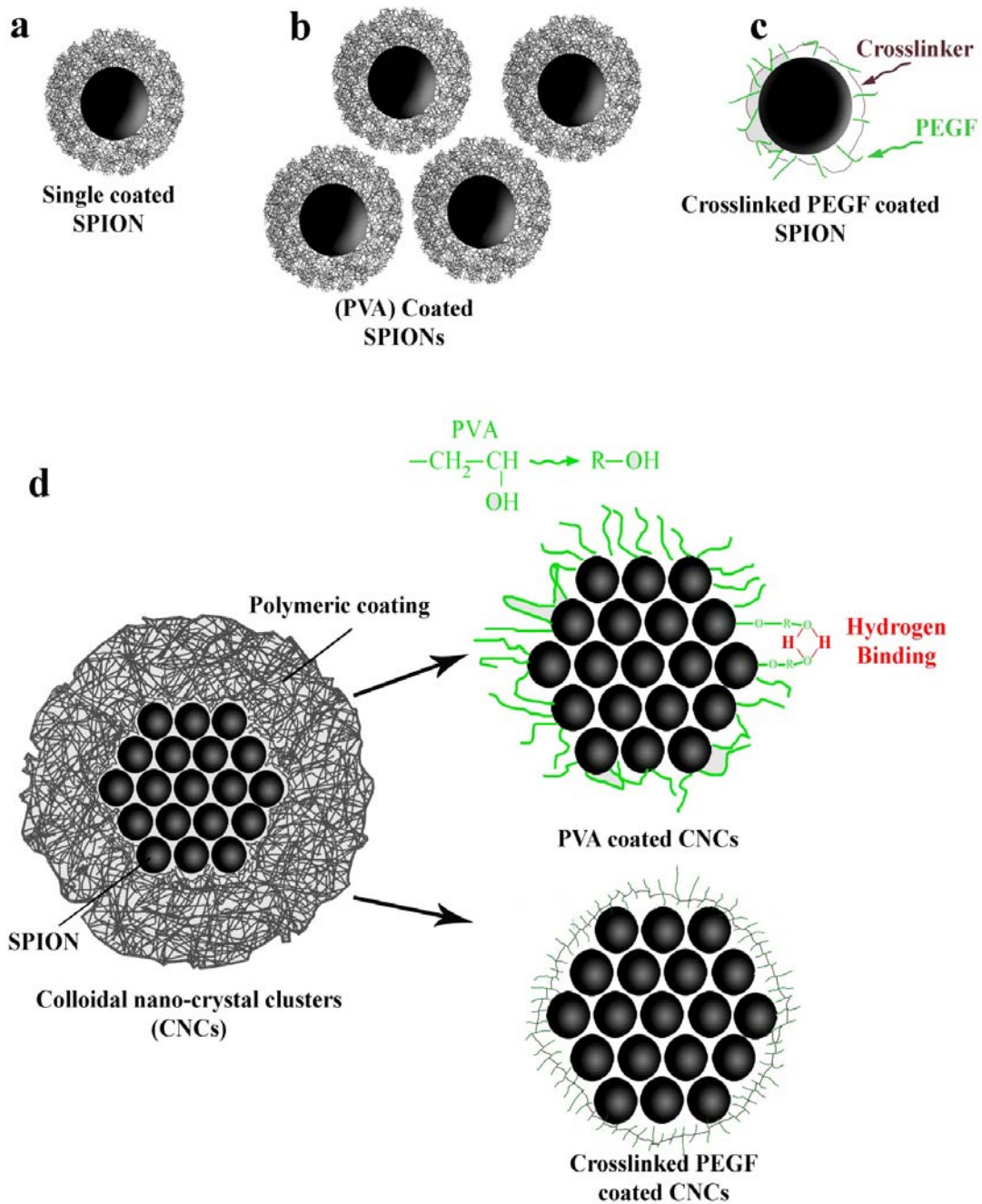


**FIG. 3.2** Schemes of the various synthesized magnetic nanoparticles including (a) single coated SPION, (b) (PVA) coated SPIONs, (c) crosslinked coated SPION, and (d) PVA- and crosslinked PEGF-coated CNCs.

To apply these materials *in vivo*, one has to be able to track them in the body. Therefore, their magnetic properties and the MRI efficiency should be studied. This is what we have investigated to see if they would be novel candidates to be introduced for the theranostics applications.

## 3.2 Magnetic Properties

### 3.2.1 SQUID-Based Magnetometers

A superconducting quantum interface device (SQUID) magnetometer combines several superconducting components, superconducting magnet, detection coils, flux transformer, and superconducting shields. To make a measurement, a sample, typically less than a few millimeters in size, is first attached to a sample rod. The sample is then moved through the center of a first- or second-order superconducting gradiometer (see Fig. 3.3).

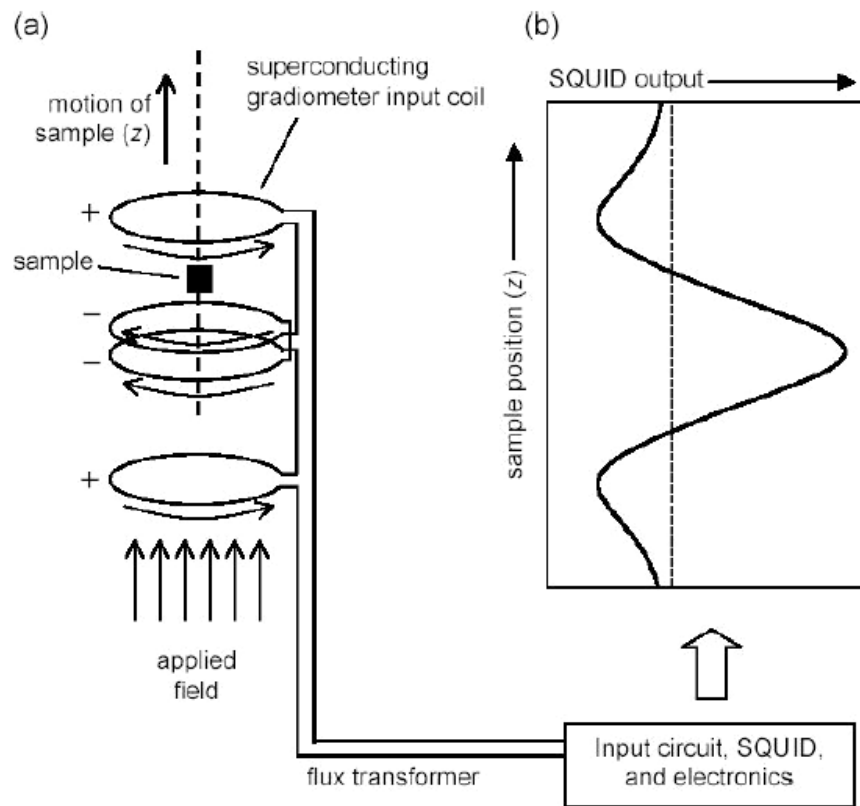


**FIG. 3.3** (a) Schematic of SQUID magnetometer, (b) Calibrated output from SQUID electronics, recorded as a function of position.

The gradiometer forms a closed flux transformer that is coupled to a SQUID and the signal from the SQUID is typically recorded as a function of sample position. The shape and magnitude of the response curve can then be analyzed using a computer to obtain a corresponding magnetic moment. The detection coils are located in the bore of a superconducting magnet by which an external static (or dynamic) magnetic field can be applied. Temperature control is made possible by placing the sample and sample rod in a sealed variable temperature insert (not shown in Fig 3.3) which is thermally isolated from the 4.2K gradiometer and magnet by an annular vacuum space.

Because a SQUID magnetometer requires a liquid helium cryostat to cool the SQUID, it is relatively little additional expense to provide a superconducting magnet system and helium gas-flow temperature control. As a result, SQUID magnetometer systems typically offer the ability to measure in applied fields of up to 7T over a temperature range from above room temperature down to below 2K.

As shown in Fig. 3.4, we have used a Magnetic Property Measurement System (MPMS) XL by Quantum Design (QD). Fig. 3.5 shows a schematic cross-section of the QD MPMS-XL. The 9-mm diameter sample chamber is cooled by liquid helium that is drawn through a pair of capillary tubes connected to the bottom of the chamber. One capillary is high-flow and thermally switched for rapid cooling. The other enables continuous-filling pumped-helium operation to below 2K. In operation, cold gas is pumped out of the top of the cryostat through the annular space between the sample chamber and the vacuum sleeve, thus cooling the sample chamber. Heaters and thermometers on the sample chamber (not shown in Fig 3.5) provide temperature control up to 400K. Lower section of the sample chamber is wrapped with the copper wires (coil-foil) for temperature uniformity in the region of the sample with minimal eddy current induction.

A linear motor attached to the sample rod at the top of the dewar is used to move the sample smoothly within the detection coils. To prevent contamination of the helium exchange gas in the sample chamber, a sliding seal is required if the motor is outside the chamber volume. An alternative is to include the motor and gearing mechanism in the vacuum space. For measuring magnetic anisotropy, a sample rotator is used to rotate the sample in situ about a horizontal axis. A different rotator is used to rotate about a vertical axis when the system is configured with optional transverse (saddle) pickup coils.

The MPMS uses an rf SQUID, operating at a 150MHz bias frequency with a modulation frequency of 100 kHz, in a flux-locked loop. Rf SQUIDs were initially selected for the first MPMS systems because they were cheaper and more readily available than dc SQUIDs. Later, MPMS systems continued to use rf SQUIDs for compatibility with the existing design and control system.



**FIG. 3.4** Magnetic Property Measurement System (MPMS) XL; (a) computer and cabinet for gas handling and all control electronics, (b) cabinet for dewar.

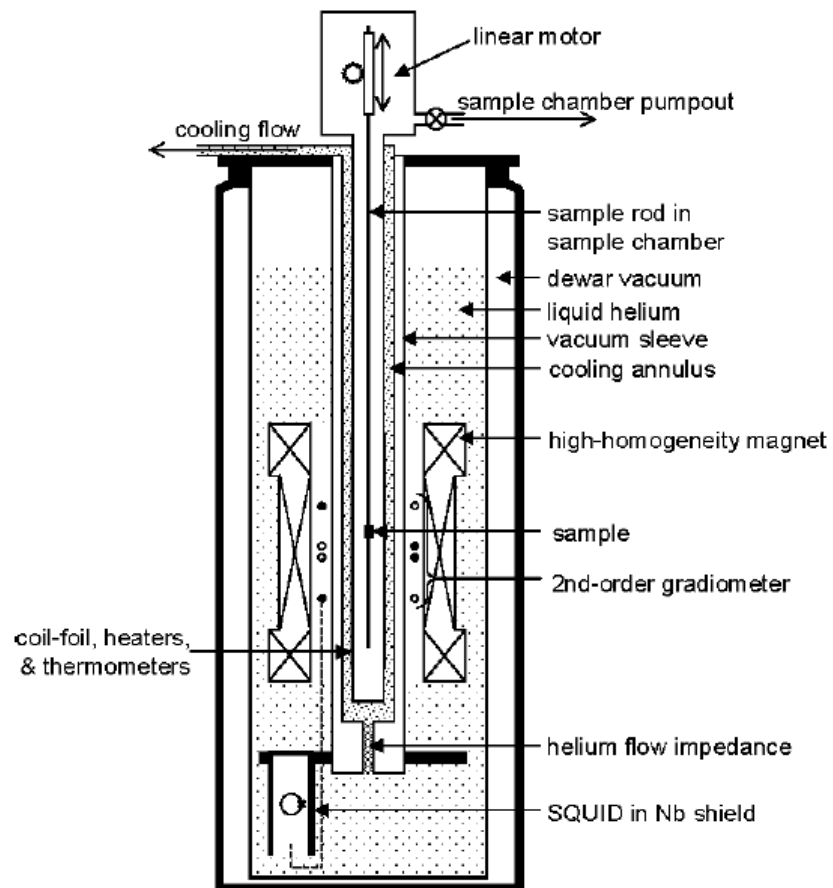


**FIG. 3.5** Schematic cross-section of the MPMS.



The design and construction of the detection coil are optimized to provide measurement sensitivity, accuracy, and noise immunity, given the mechanical constraints imposed by the other components of the system (e.g., vacuum sleeve). A second-order gradiometer design is used because it significantly reduces noise contributions from both flux motion in the magnet and from the environment with an order of magnitude improvement compared to a first-order gradiometer [35]. A longitudinal gradiometer (shown in Fig. 3.3) detects moments parallel to the applied field, while an optional transverse detection configuration is available that uses saddle coils. The magnet and gradiometer are mechanically rigid to reduce the effects from vibrations, allowing subpicotesla magnetometer sensitivity in tesla-strength fields. In the absence of a vacuum sleeve, the diameter of the detection coils could be optimized for specific sample sizes with a diameter that is small enough for good coupling and large enough that accuracy is not affected by the geometry of the sample. In the MPMS, the smallest diameter coils (20.2 mm) are used which fit on the outside of the vacuum sleeve. Once the coil diameter is determined, the baseline of the gradiometer is optimized for on-axis sensitivity while adequately rejecting field noise from the magnet and environment.

A SQUID magnetometer system is uniquely adapted to measuring static (dc) magnetization of samples. However, as a general technique for studying magnetic properties, this type of measurement is limited in that it does not directly reveal dynamical information about the magnetic properties of materials. To do that, a dynamic (ac) susceptibility measurement is generally required.

With an ac susceptometer, a small oscillating field is added to the applied field and a lock-in amplifier used to measure the complex differential susceptibility  $\chi_{ac} = dM / dH$ , where  $M$  and  $H$  are the magnetization and the total applied field, respectively. Because the measurement is narrow-band, sensitivity is greatly enhanced over a comparable dc technique. At low enough frequencies and small enough oscillation amplitudes,  $\chi_{ac}$  is real and equal to the slope of the magnetization curve. However, in general there is an imaginary part that contains dynamical information that cannot be found from measurements of the static magnetization.

Most non-SQUID magnetometer systems use mutual inductance bridges [36] and are limited to frequencies above a few hertz, because the induced signal is proportional to frequency. When configured for ac magnetization measurements, the MPMS has a flat sensitivity of  $5 \times 10^{-12} \text{ Am}^2$  down to below 0.1Hz. On the MPMS system, the ac measurement capability is provided by adding: (1) a separate excitation coil in the bore of the main magnet and (2) electronics capable of driving the excitation coil while also applying a synchronous compensation signal directly to the gradiometer feedback transformer. An oscillating applied field can be produced which ranges in amplitude from 0.1 to 400.0  $\mu\text{Tesla}$  for frequencies from 0.1 to 1000Hz, on a bias field of  $\pm 7 \text{ Tesla}$ . The compensation signal is required because measurements are performed on the most sensitive SQUID range possible. Without the compensation, the 0.1 to 0.2% gradiometer imbalance would couple too much flux directly from the excitation coil.

The system performs the following steps during an ac measurement. First, the sample is positioned in the middle of the lower side coil and the SQUID is then nulled. Nulling involves determining and setting the amplitude and phase of the 50/60Hz line compensation signal that needs to be injected into the feedback circuit. In addition, a compensation signal is determined and applied to the feedback circuit that reduces the

direct coupling of the oscillating field into the imperfect gradiometer. Next, the detected waveform is digitized. Finally, the sample is moved to the center of the gradiometer and the signal again digitized. A subtraction of the two measurements, properly weighted for the detection coil response function, removes any residual direct coupling between the drive and the detected signal [37].

Because both the drive field and detection coils are outside the sample tube and vacuum sleeve, the effects of eddy currents and the magnetic susceptibility of the tube must be considered. In the MPMS a highly resistive copper alloy with nearly temperature- and field-independent susceptibility, is used for constructing the tubes. Careful frequency-dependent calibration of amplitudes and phase shifts is still required. A further calibration is required to compensate for both field- and frequency-dependent screening of the applied field by the superconducting magnet windings and magnetoresistive effects in the surrounding materials [37].

This technique is very sensitive to differential susceptibility as a function of field and so can detect very weak phase transitions on top of weak background signals. The imaginary component reveals the time-dependent magnetic behavior of spin glasses, superparamagnetic particles, domain-wall motion in ferromagnets, flux motion in superconductors, and other dissipative phenomena in materials.

### *3.2.1.a Bio-Ferrofluids*

The magnetic properties of the bio-ferrofluids were studied by means of dc magnetization as a function of field at room temperature and ac magnetic susceptibility measurements as a function of temperature and frequency in a MPMS-XL SQUID magnetometer from Quantum Design. The results are presented in the next chapter.

### *3.2.1.b CNCs*

Magnetization measurements of CNCs have been performed on the solid (dry powder) samples using a SQUID dc magnetometer, MPMS-XL7. The temperature dependence of the magnetization has been studied in the temperature range 2-300 K by zero-field-cooling (ZFC) and field-cooling (FC) curves at  $H=10\text{mTesla}$  applied magnetic field. To investigate the behavior of the magnetization as a function of applied magnetic field, hysteresis experiments in the range of  $-5\text{Tesla} \leq H \leq +5\text{Tesla}$  have been performed at both  $T=2\text{ K}$  and  $T=300\text{ K}$ . The results are reported in the next chapter.

## **3.2.2 NMR Relaxometers**

For studying the relaxometric properties of the samples, we have measured  $T_1$  and  $T_2$  of all samples at room temperature by employing both conventional and Fast-Field-Cycling (FFC) NMR spectrometers.

The  $^1\text{H}$  NMR technique was employed to measure the longitudinal and transverse relaxivities in a wide range of frequencies covering most of the clinical imagers ( $\nu \approx 8.5$ , 21 and 63 MHz corresponding to about 0.2, 0.5 and 1.5 T respectively). For  $\nu > 10\text{ MHz}$  a Stellar Spinmaster and an Apollo-Tecmag spectrometers have been used. Standard radiofrequency excitation sequences CPMG-like and saturation-recovery were applied to determine  $T_2$  and  $T_1$  values.

For  $10 \text{ kHz} \leq \nu \leq 10 \text{ MHz}$ , the NMR data were collected with a Smartracer Stellar relaxometer using the FFC technique. The conventional spectrometers are widely used and well known to the people. In the following we will introduce briefly the principles of the FFC relaxometry.

FFC Relaxometry is a NMR technique used to determine  $T_1$  relaxation time over a range of  $B_0$ -fields spanning about 6 decades, from about  $10^{-6}$  Tesla up to  $\sim 1$  Tesla. The boundaries of this range are not well defined: the lower limit is set by the local fields; the upper limit is chiefly determined by technical choices and compromises. This enormous range should be compared with the 0.1 Tesla to 20 Tesla intervals currently covered by standard NMR superconductor magnets and electromagnets. However, studies of  $T_1$  dispersion curve with an array of standard magnets is impractical, and the usefulness of  $T_{1\rho}$  is limited by subtle differences relative to  $T_1$  and technical problems at high  $B_1$  fields (overheating of the sample, phase shifts of the transmitter during long pulses). On the other hand, FFC requires a specialized system, which does not compete with the sensitivity and resolution of most NMR spectrometers.

In practice, FFC is a convenient and, sometimes, unique method to follow over extended temperature intervals, the dynamics of "coupled" systems such as liquid crystals, polymers, biomolecules, viscous fluids and glasses, solid electrolytes and, in general, solids with "slow" or correlated motions [38,39].

A typical field cycle is schematically presented in Fig. 3.6. As one can see in Fig. 3.6, the basic field cycling experiments ideally consists of three steps:

1. The sample is polarized in a high field for a time  $t_p$  until the nuclear magnetization achieves saturation, i.e.  $t_p$  should be longer than 4 times  $T_1$  at  $B_p$  (field of polarization).
2. The magnetic field is switched to a value  $B_r$  (field of relaxation) for a time  $t_r$  during which the magnetization relaxes towards a new equilibrium value.
3. The magnetic field is switched to a value  $B_d$  (field of detection) and the equilibrium magnetization is measured with a  $90^\circ$  pulse followed by acquisition.

These steps are repeated for a set of  $t_r$  values until the  $T_1$  value at  $B_r$  is determined; then, a new  $B_r$  value is selected and the corresponding  $T_1$  is measured.

Quantitatively, the polarization field  $B_p$  should be as high as possible to increase magnetization and SNR. To analyze "fast" relaxation phenomena, we should be able to switch to  $B_r$  and to  $B_d$  in "short" times. Differently from  $B_p$  and  $B_r$ , the detection field  $B_d$  has to be "stable" and "homogeneous". Choosing the  $B_d$  as high as possible gives higher sensitivity.

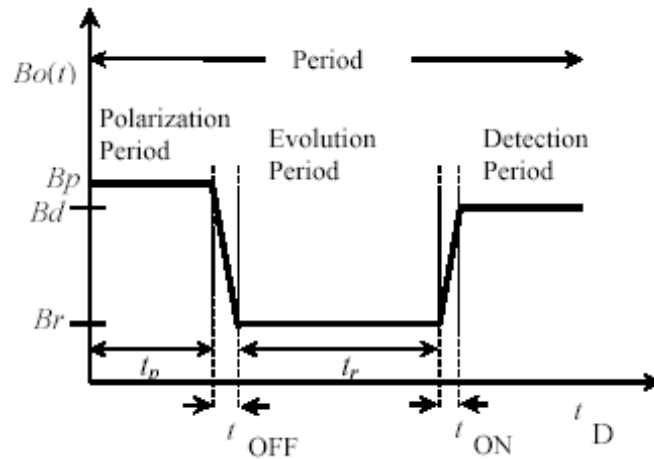


**FIG. 3.6** Schematic representation of a typical field cycle.

Due to the different requirements of these fields, it would appear reasonable to perform the experiment by adding/subtracting a time-modulated field to a stationary, and homogeneous, detection field. However, when  $B_r$  approaches zero, the time-modulated field should match the value, the homogeneity, and the stability, of the detection field. This means that, with or without a stationary field, top performances essentially require that a homogeneous field is rapidly switched between two values. Nearly universally, this goal has been achieved with a resistive solenoid connected with a suitable power supply and cooling system.

A Block diagram of a typical FFC relaxometer is shown in Fig. 3.7.

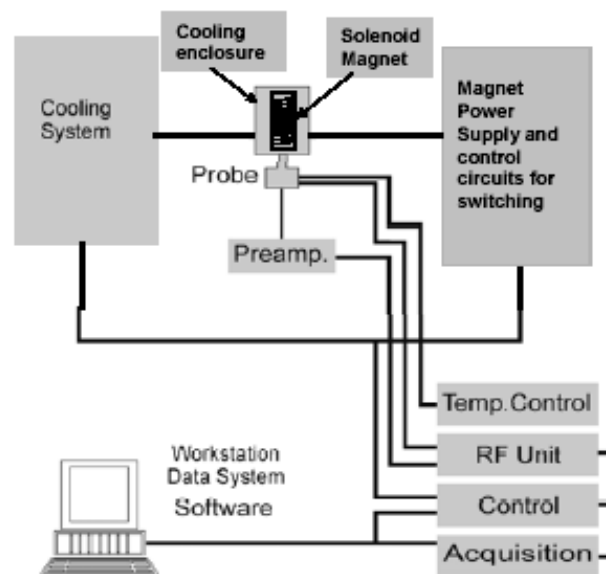


**FIG. 3.7** Block diagram of a typical FFC relaxometer.

The general FFC pulse sequence is shown in Fig. 3.8 which is suitable for the measurement when the difference of  $B_p$  and  $B_r$  is sufficiently large. For the case of high  $B_r$ , it is more favorable to start the cycle in the absence of any polarization field. Therefore, field cycling relaxometry contains basically the pre-polarized (PP) sequence for the measurements at low fields and the non-polarized (NP) sequence for the measurements at high fields (see Fig. 3.8).

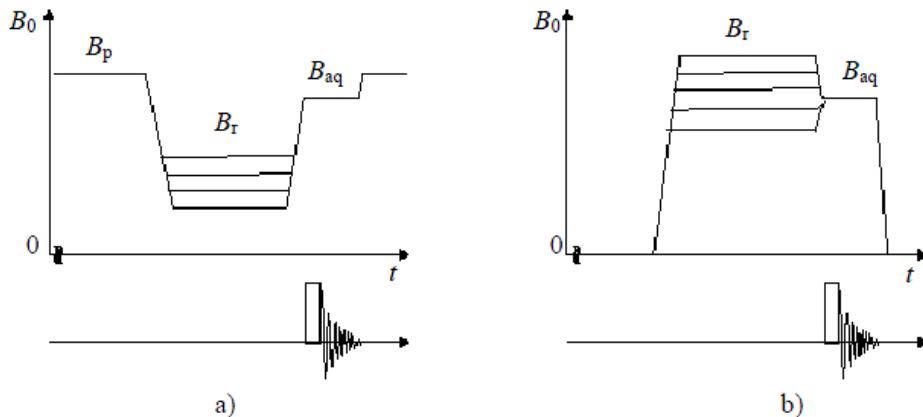


**FIG. 3.8** Two basic types of field sequences with the  $90^\circ$  rf pulse used in the field cycling measurement, a) basic pre-polarized (PP) sequence and b) basic non-polarized (NP) sequence.

For the measurements of  $T_1$  we used both PP (below 3MHz) and NP (above 3MHz) sequences. For  $T_2$  measurements, since we run the experiments for the frequencies above 4MHz, we employed NP-CPMG sequence.

### 3.2.2.a Bio-Ferrofluids

The  $^1\text{H}$  NMR technique was employed to measure the longitudinal and transverse relaxivities in a wide range of frequencies covering most of the clinical imagers ( $\nu \approx 8.5$ , 21 and 63MHz corresponding to 0.2, 0.5 and 1.5 Tesla respectively).

For  $10\text{kHz} \leq \nu \leq 10\text{MHz}$ , the NMR data were collected with a Smartracer Stellar relaxometer using the FFC technique [38,39], while for  $\nu > 10\text{MHz}$  a Stellar Spinmaster and an Apollo-Tecmag spectrometers have been used. Standard radio frequency excitation sequences CPMG-like and saturation-recovery were applied to determine  $T_2$  and  $T_1$  values, respectively.

### 3.2.2.b CNCs

The  $^1\text{H}$  NMRD profiles were determined, at room temperature, by measuring the longitudinal  $T_1$  and transverse  $T_2$  nuclear relaxation times, in the frequency range

$10\text{KHz} \leq \nu \leq 64\text{MHz}$  for  $T_1$  and  $4\text{MHz} \leq \nu \leq 64\text{MHz}$  for  $T_2$ . The frequency ranges cover the typical frequencies of the MRI clinical imagers, i.e.  $\nu \sim 8.5, 21, 63$  MHz, corresponding to the magnetic fields  $\sim 0.2, 0.5$  and  $1.5$  Tesla.

For the frequency range  $10\text{KHz} \leq \nu \leq 10\text{MHz}$ , the NMR data were collected with a Smartracer Stellar relaxometer using the FFC technique [38,39] while for  $\nu > 10\text{MHz}$  a Stellar Spinmaster spectrometer has been employed. Standard radio frequency excitation sequences CPMG-like and saturation-recovery were applied to determine  $T_2$  and  $T_1$  values, respectively.

### 3.2.3 MRI Scanner

A schematic presentation of the conventional MRI scanner is shown in Fig. 3.9. More details about the MRI technique and the magnetic field gradients are given in Appendix A.

*In vitro* MRI experiments were performed at 8.5 MHz, i.e., 0.2 Tesla, using an Artoscan Imager by Esaote S.p.A. which is presented in Fig. 3.10.

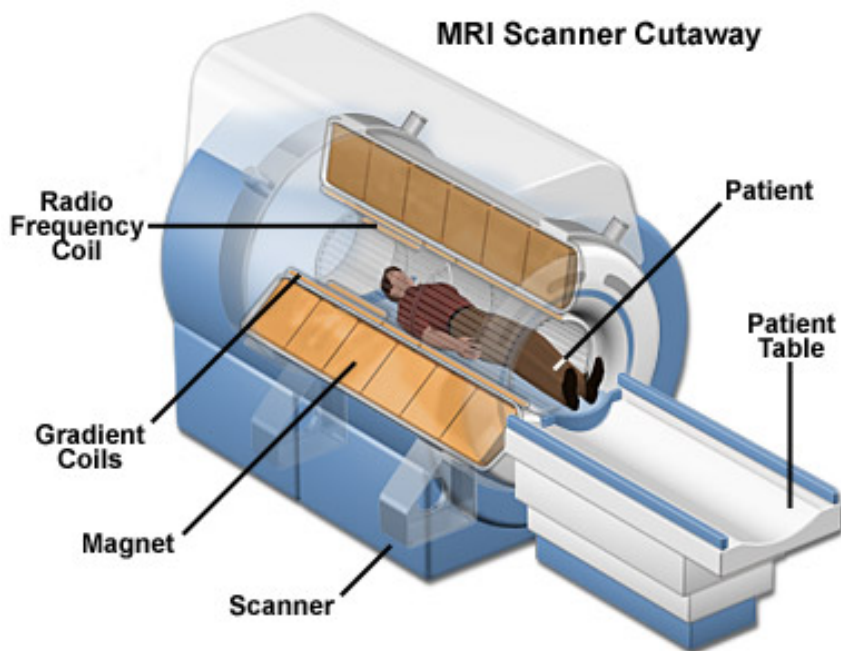


**FIG. 3.9** Schematically representation of a conventional MRI scanner.



**FIG. 3.10** Schematically representation of an Artoscan Imager by Esaote S.p.A.

For performing the experiments, we prepared Endorem and our samples with the same concentration, namely 0.02 mg/ml, and put each of them in a separate vial. The experimental parameters for each set of samples are given in the following.

### *3.2.3.a Bio-Ferrofluids*

*In vitro* MRI images for the bio-ferrofluids were performed using two pulse sequences programs: a) high resolution Gradient Echo (GE) with TR/TE/NEX=1000ms/16ms/4, matrix=256\*192, FOV=180\*180, flip angle=90°; and b) high resolution Spin Echo (SE) sequence with TR/TE/NEX=1000ms/26ms/4, matrix=192\*192, FOV=180\*180, number of slices=5 and slice thickness=5mm. The vials of samples were prepared with the same concentrations and put in the vials to perform the images. The obtained images are given in the next chapter. We remind here that TE is the distance between the first rf pulse and the echo maximum, TR is the repetition time of the sequence, NEX is the number of excitations (averages), FOV is the field of view, the matrix gives the number of sampling points in the (*xy*) plane.

### 3.2.3.b CNCs

For the CNCs *in vitro* MRI experiments, we used a Spin Echo (SE) T<sub>2</sub> pulse sequence with TR/TE/NEX=2000ms/80ms/1, matrix=256\*192, FOV=180\*180, number of slices=5, and slice thickness=4mm, as image parameters. The vials of samples were prepared with the same concentrations and put in the vials to perform the images. The obtained images are given in the next chapter.

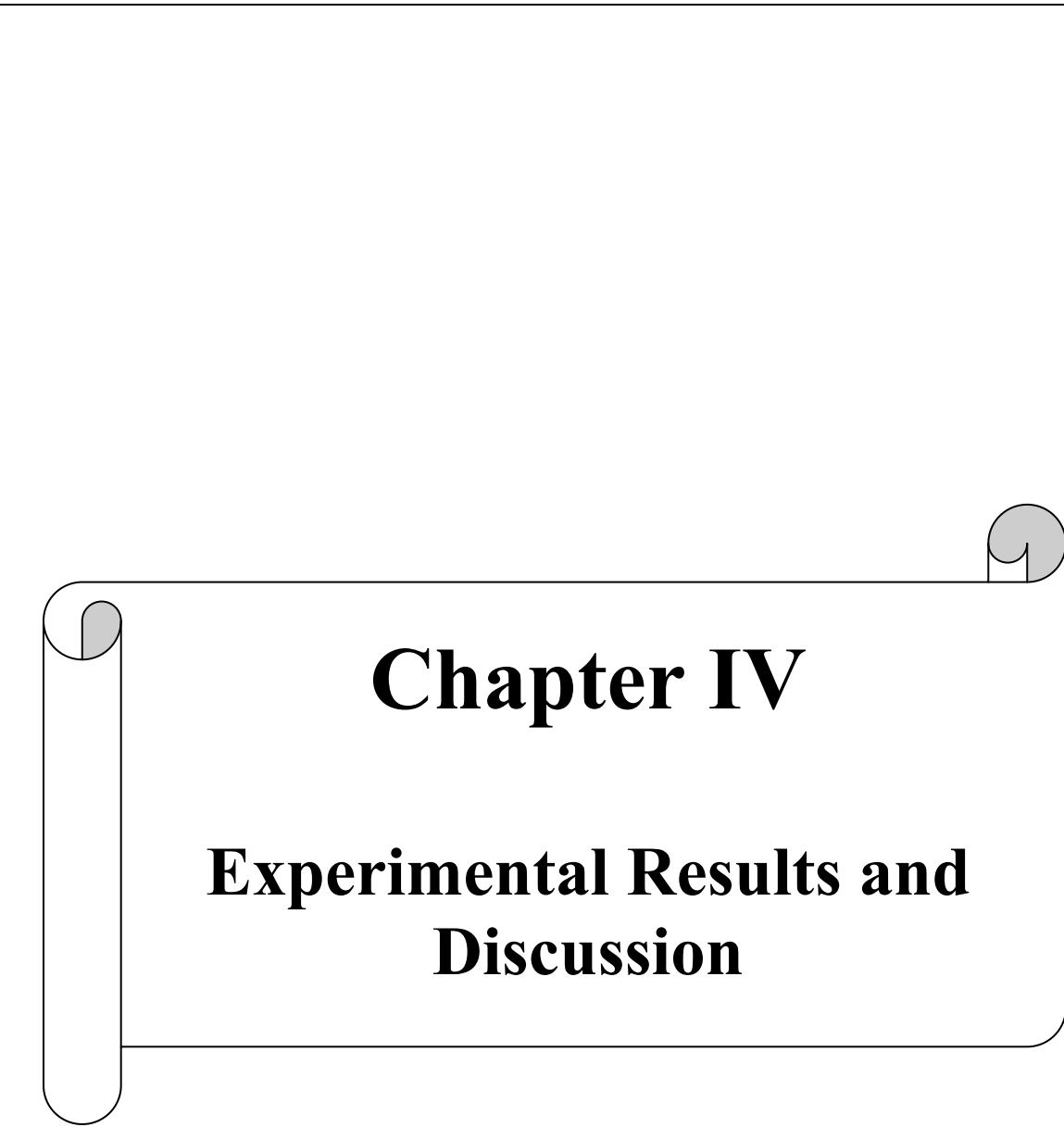
## 3.3 References

- [1] Hafeli, U. O. The MML Series; Kentus Books; London, 2006; Vol. 8, pp 77-126.
- [2] Flores, G. A.; Liu, J. Eur. Cells Mater., 3 (2), 9–11, (2002).
- [3] Tiefenauer, L. X. Nanotechnology in Biology and Medicine: Methods, DeVices, and Applications; CRC Press: Boca Raton, FL, pp 1-20, (2007).
- [4] Olsvik, O.; Popovic, T.; Skjerve, E.; Cudjoe, K. S.; Hornes, E.; Ugelstad, J.; Uhlen, M. Clin. Microbiol. ReV., 7, 43–54, (1994).
- [5] Gupta, A. K.; Curtis, A. S. G. Biomaterials, 25 (15), 3029–3040, (2004).
- [6] Gupta, A. K.; Curtis, A. S. G. Proc. 30th Annu. Symp. Controlled Release Bioact. Mater., 30, 788, (2003).
- [7] Gupta, A. K.; Berry, C.; Gupta, M.; Curtis, A. IEEE Trans. Nanobiosci., 2 (4), 256–261, (2003).
- [8] Widder, K. J.; Senyei, A. E.; Ranney, D. F. Cancer Res., 40 (10), 3512–3517, (1980).
- [9] Gupta, P. K.; Hung, C. T. Microspheres and Regional Cancer Therapy; CRC Press: Boca Raton, FL, pp 71-116, (1993).
- [10] Gallo, J. M.; Hung, C. T.; Gupta, P. K.; Perrier, D. G. J. Pharmacokinet. Biopharm., 17, 305–326, (1989).
- [11] Gallo, J. M.; Gupta, P. K.; Hung, C. T.; Perrier, D. G. J. Pharm. Sci., 78, 190–194, (1989).
- [12] Freeman, J. A.; Geer, J. C. Am. J. Dig. Dis., 10 (12), 1005–1025, (1965).



- [13] Meyers, P. H.; Nice, J.; Meckstroth, G. R.; Becker, H. C.; Moser, P. J.; Goldstein, M. *Am. J. Roentgenol. Radium Ther. Nucl. Med.*, 96 (4), 913–21, (1966).
- [14] Gupta, A. K.; Gupta, M. *Biomaterials.*, 26, 3995–4021, (2005).
- [15] Tchikov, V.; Winoto-Morbach, S.; Krohnke, M.; Kabelitz, D.; Schütze, S. *J. Magn. Magn. Mater.*, 225, 285–293, (2001).
- [16] Krotz, F.; Sohn, H. Y.; Gloe, T.; Plank, C.; Pohl, U. *J. Vasc. Res.*, 40 (5), 425–434, (2003).
- [17] Krotz, F.; de Wit, C.; Sohn, H. Y.; Zahler, S.; Gloe, T.; Pohl, U.; Plank, C. *Mol. Ther.*, 7 (5), 700–710, (2003).
- [18] Manfred Johannseni, Burghard Thiesen, Peter Wuste, and Andreas Jordan, *J. Hyperthermia*, 1–6, (2010).
- [19] Hafeli, U.; Schütt, W.; Teller, J.; Zborowski, M. Plenum Press: New York, (1997).
- [20] Berry, C. C.; Curtis, A. S. *G. J. Phys. D: Appl. Phys.*, 36, 198–206, (2003).
- [21] Moghimi, S. M.; Hunter, A. C.; Murray, J. C. *Pharm. ReV.*, 53, 283–318, (2001).
- [22] Harris, J. M.; Martin, N. E.; Modi, M. *Clin. Pharmacokinet*, (2001).
- [23] T. Neuberger, B. Schopf, H. Hofmann, M. Hofmann, B. Rechenberg, *J. Magn. and Magn. Mater.*, 293, 483–496, (2005).
- [24] E. Sykova, P. Jendelova, *Migration, Cell Death and Differentiation* 14, 1336–1342, 39–41, (2007).
- [25] A. S. Lubbe, C. Alexiou, C. Bergemann, *The Journal of Surgical Research* 95 (2), 200–206, (2001).
- [26] S. Rudge, C. Peterson, C. Vessely, J. Koda, S. Stevens, L. Catterall, *Journal of Controlled Release* 74 (1–3), 335–340, (2001).
- [27] M. Mahmoudi, A. Simchi, M. Imani, U. O. Hafeli, *Journal of Physical Chemistry C* 113 (19), 8124–8131, (2009).
- [28] A. K. Gupta, R. R. Naregalkar, V. D. Vaidya, M. Gupta, *Nanomedicine* 2 (1), 23–39, (2007).
- [29] A. Millan, F. Palacio, A. Falqui, E. Snoeck, V. Serin, A. Bhattacharjee, V. Ksenofontov, P. Gütlich, I. Gilbert, *Acta Mater.*, 55, 2201, (2007).

- [30] Villa-Bellosta R, Ibarz, Millan A, Pinol R, Ferrer-Dufol A, Palacio F, Sorribas V, *Toxicology Letters* 180, S221-S221, (2008).
- [31] M. Mahmoudi, A. Simchi, M. Imani, A. S. Milani, P. Stroeve, *Journal of Physical Chemistry B*, 112, 14470, (2008).
- [32] J. S. Temenoff, H. Shin, D. E. Conway, P. S. Engel, A. G. Mikos, *Biomacromolecules*, 4, 1605, (2003).
- [33] H. Park, J. S. Temenoff, Y. Tabata, A. Caplan, A. G. Mikos, *Biomaterials*, 28, 3217, (2007).
- [34] M. Mahmoudi, A. Simchi, M. Imani, U. O. Hafeli, *Journal of Physical Chemistry C*, 113, 8124, (2009).
- [35] Vandervoort, K. G., Griffith, G., Claus, H., and Crabtree, G. W., *Rev. Sci. Instrum.* 62, 2271–2275, (1991).
- [36] Deutz, A. F., Hulstman, R. and Kranenburg, F. J., *Rev. Sci. Instrum.* 60, 113–120, (1989).
- [37] Hibbs, A. D., Sager, R. E., Kumar, S., McArthur, J. E., Singaas, A. L., Jensen, K. G., Steindorf, M. A., Aukerman, T. A. and Schneider, H. M., *Rev. Sci. Instrum.* 65, 2644–2652, (1994).
- [38] Vamanan Satheesh, Alexander Galkin, Stan Sykora and Gianni Ferrante M Villa, P. Cofrancesco “Technical issues of Fast Field Cycling NMR Relaxometry” in *Field Cycling NMR Relaxometry Review of Technical Issues and Applications By Stelar®*.
- [39] G. Ferrante, S. Sykora, *Adv. Inorg. Chemistry*, 57, 405, (2005).



**Chapter IV**

**Experimental Results and  
Discussion**

## Chapter IV

# Experimental Results and Discussion

### *Contents*

---

|                                              |    |
|----------------------------------------------|----|
| 4.1 Bio-Ferrofluids.....                     | 67 |
| 4.1.1 TEM and X-Ray Characterizations.....   | 67 |
| 4.1.2 SQUID Magnetometry.....                | 69 |
| 4.1.3 NMR Relaxometry.....                   | 71 |
| 4.1.4 <i>In Vitro</i> MRI Experiments.....   | 76 |
| 4.2 CNCs.....                                | 76 |
| 4.2.1 Characterizations.....                 | 76 |
| 4.2.2 SQUID Magnetometry.....                | 78 |
| 4.2.3 NMR Relaxometry.....                   | 80 |
| 4.2.4 <i>In Vitro</i> MRI Experiments.....   | 84 |
| 4.2.5 Cell Endocytosis and Drug Release..... | 84 |
| 4.3 References.....                          | 86 |

---

## 4.1 Bio-Ferrofluids

### *4.1.1 TEM and X-Ray Characterizations*

The characteristics of the ferrofluids are shown in Table 4.1. Transmission electron microscopy (TEM) images (Fig. 4.1) show a uniform distribution of iron oxide nanoparticles encapsulated in a continuous polymer film. Most of the particles are spherical with an average size that increases regularly from 7.4 nm (sample A) to 15 nm

(sample D) in relation to the  $\text{Fe}_2\text{O}_3/\text{PVP}$  and  $\text{Fe(II)}/\text{Fe(III)}$  ratios selected in the synthesis (Table 4.1). Electron Diffraction (ED) patterns on these particles are consistent with a maghemite crystal structure (central image in Fig. 4.1). A small number of particles are elongated.

**TABLE 4.1** Characteristics of the ferrofluid samples.

| Sample | $\text{Fe}_2\text{O}_3/\text{PVP}^{\text{a}}$ | $\text{Fe(II)}/\text{Fe(III)}^{\text{a}}$ | $D_H$<br>(nm) <sup>b</sup> | PDI <sup>c</sup> | $D_P$<br>(nm) <sup>d</sup> | SD<br>(nm) | $T_B$<br>(K) <sup>e</sup> |
|--------|-----------------------------------------------|-------------------------------------------|----------------------------|------------------|----------------------------|------------|---------------------------|
| A      | 0.5                                           | 0.5                                       | 59                         | 0.16             | 7.4                        | 1.2        | 40                        |
| B      | 0.625                                         | 0.5                                       | 62                         | 0.18             | 8.6                        | 2.0        | 45                        |
| C      | 1                                             | 0.5                                       | 92                         | 0.15             | 10.8                       | 2.9        | 160                       |
| D      | 1                                             | 0.9                                       | 93                         | 0.14             | 15.0                       | 3.7        | 200                       |

<sup>a</sup>Molar ratios used in the preparation of the sample; <sup>b</sup>Hydrodynamic diameter; <sup>c</sup>Polydispersity index as obtained from Dynamic Light Scattering (DLS); <sup>d</sup>Maghemite particle diameter from TEM images; <sup>e</sup>Blocking temperature from AC magnetic susceptibility measurements at 30 Hz.

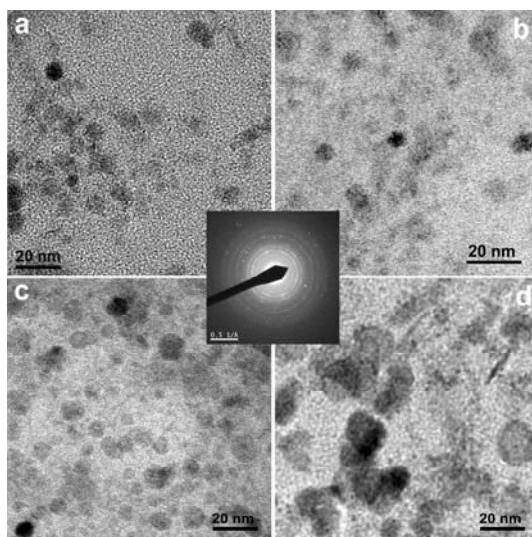


**FIG. 4.1** TEM images of samples A(a), B(b), C (c) and D (d) and a characteristic ED diffraction pattern of the particles. In sample D some of the crystals are faceted.

Distributions of the hydrodynamic sizes for the series of samples are shown in Fig. 4.2. In all cases a monomodal distribution of particle diameters was found. The average hydrodynamic diameter  $D_H$  increases with the iron oxide/polymer ratio (see Table 4.1) from 59 nm (sample A) to 92 nm (sample C), and it is hardly changing in samples with similar  $\text{Fe}_2\text{O}_3/\text{PVP}$  ratio but different particle size (samples C and D).

The average sizes of magnetic nanoparticles (MNPs) found by TEM represent about 10-15% of the average hydrodynamic sizes. Considering that at the pH of the medium (7.40) pyridine groups are hydrophobic and PEG residues are hydrophilic, then the structure of the  $\text{MNP@PVP@PEG}$  beads in suspension could be as follows: an inner part formed by a single folded PVP chain entrapping the MNPs by N-Fe coordination bonds, and an outer part formed by solvated PEG chains in a radial disposition.

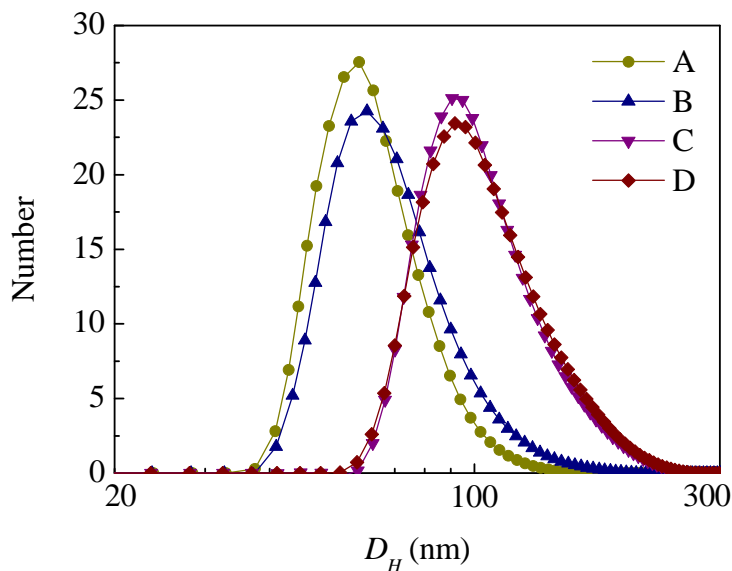


FIG. 4.2 Distribution of the hydrodynamic sizes for the series of samples.

#### 4.1.2 SQUID Magnetometry

The *ac* magnetic susceptibility as a function of temperature of samples A to D shows the characteristic behaviour of the superparamagnetic systems, with the in- and out-of-phase components ( $\chi'$  and  $\chi''$ , respectively) depending on frequency and with  $\chi''$  having a maximum at blocking temperature  $T_B$  (Fig. 4.3), which depends on the frequency of the applied magnetic field following an Arrhenius like function [1,2]. This

shows that at low temperatures the magnetic moment of the MNPs can not be reversed, i. e. it is not able to cross the anisotropy energy barrier  $E_a = KV_p$  ( $K$  is the anisotropy constant characteristic of the material and  $V_p$  is the volume of the MNPs) and follows the field. As temperature increases, the moments of the cores, i.e. MNPs, with lowest anisotropy energy start to reverse, being this process thermally activated and termed Néel relaxation. As expected from this model, at a given frequency,  $T_B$  increases with  $D_p$  (Fig. 4.4).

Below 273 K these water based bio-ferrofluids are frozen and thermal activation is the only mechanism available for reversal. At room temperature, the MNPs whose  $E$  is too high for the thermal activation to be effective (say  $E_a > k_B T$ ) have the possibility to reverse by mechanical rotation in the fluid (Brownian relaxation mechanism). The on-set of this mechanism leads to a sudden increase of  $\chi''$  in the samples with a relevant fraction of “large” nanoparticles (i. e. nanoparticles with  $E_a > k_B T$ ).

From the plot of magnetization versus applied field (Fig. 4.5) it is evident that the magnetization increases with the particle size as previously found in maghemite/PVP composites [3]. Fitting these curves to a Langevin function [4] modified by adding a linear term, it is possible to conclude that the average magnetic moment of the particles increases with the MNPs’ sizes. This model assumes that the core of the MNPs behave as a single spin (with the same value for all MNPs), and that the magnetic moments, at the MNPs’ surface, have a linear behaviour with the field in the studied field range [3]. The linear term also accounts for the diamagnetic contribution of polymer coating and the fluid.

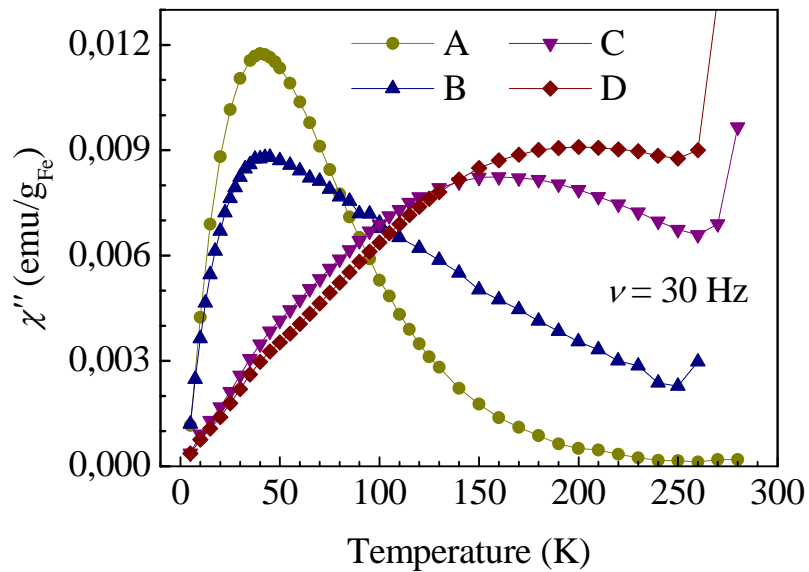


**FIG. 4.3**  $\chi''$  vs. temperature for samples A to D. The  $T_B$  increases with increasing average sizes.

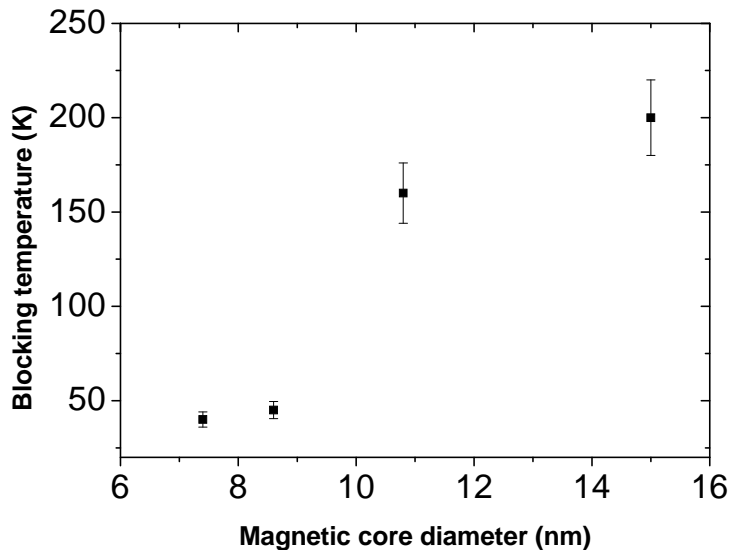


**FIG. 4.4** Blocking temperature as a function of magnetic core size. The  $T_B$  increases with increasing average sizes.

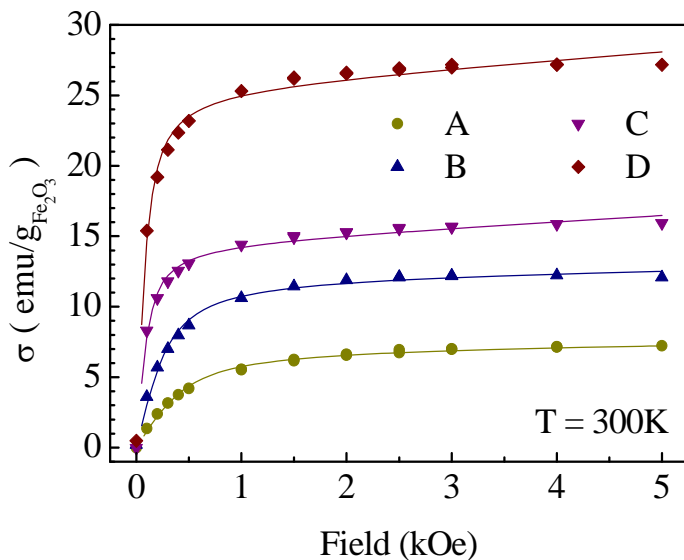


**FIG. 4.5** Magnetization per gram of iron oxide for the series of bio-ferrofluids. Lines correspond to fitting to a modified Langevin function.

### 4.1.3 NMR Relaxometry

To evaluate the MRI contrast efficiency of the samples, the nuclear longitudinal and transverse relaxivities ( $r_1$  and  $r_2$ , respectively) were obtained from the spin-lattice  $T_1$  and



the spin-spin  $T_2$  relaxation times measured at room temperature. It is notable that for the bio-ferrofluids, PBS (at physiological pH) is the diamagnetic host solution.

Endorem<sup>®</sup> (Feridex in the USA) is one of the well-known commercial superparamagnetic iron oxide MRI contrast agents coated with dextran for intravenous administration for the detection of liver lesions. The NMRD profiles for samples A to D and the Endorem<sup>®</sup> are shown in Fig 4.6. The dashed lines indicate the most clinical operating frequencies.

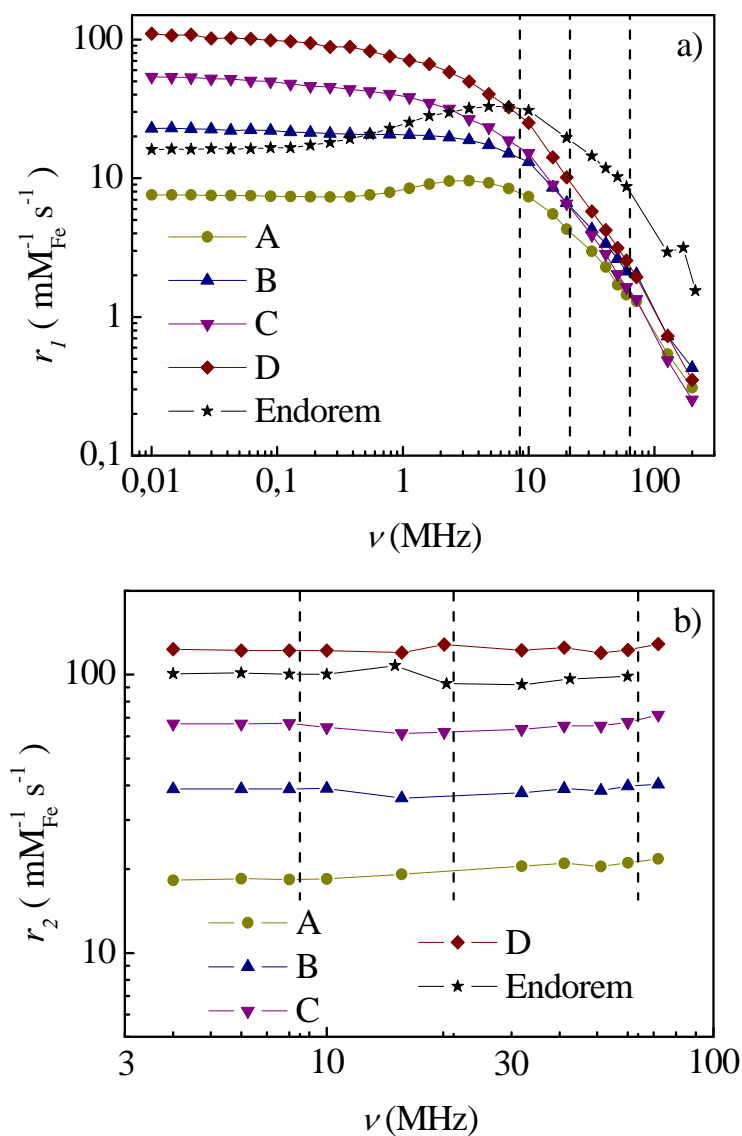


**FIG. 4.6** a) longitudinal  $r_1$  and b) transverse  $r_2$  relaxivities vs. frequency for samples A to D and the commercial CA, Endorem. Dashed lines indicate the operating frequencies of most clinical imagers ( $\nu \approx 8.5, 21$  and  $63$  MHz).

The SPIONs are negative contrast agents and they decrease the signal intensity. The most important parameter to determine their contrast efficiency is the transverse relaxivity  $r_2$ . As one can see in Fig 4.6, the transverse relaxivity of the samples is increasing with the particle core size and the best efficiency is obtained for the biggest particles, i.e. sample *D*.

The  $r_1$  value gives us the information about the physical phenomena responsible for the nuclear relaxation such as diffusion, anisotropy, etc. For our samples, the longitudinal relaxivity curves are constant for low frequencies. In the range from 1 to ~10MHz  $r_1(\nu)$  shows a maximum for sample *A* and Endorem that have similar  $D_p$  (see Table 4.1), which is not present for the rest of the samples; apparently in our system there is a threshold in the particle size around 8nm over which this maximum is no longer present. The  $r_1(\nu)$  rapidly decreases for higher frequencies. The transverse relaxivity has a linear behaviour in the studied frequency range with a slope very close to zero.

Regarding the mechanisms that induce nuclear longitudinal relaxation in SP particles, it is worth to remind that the main mechanisms are [5,6]: (i) for  $\nu < 1-5$  MHz, the Neel relaxation of the particle magnetization, giving a correlation time related to the magnetic anisotropy barrier, and an associated reversal time,  $\tau_N$ , that follows the Arrhenius law; (ii) for  $\nu > 1-5$  MHz, the Curie relaxation, which takes into account the sample magnetization through the squared Langevin function weighted by the spectral density function  $J^F(\omega_D)$ , where  $\omega_D = 1/\tau_D$ ,  $\tau_D$  being the correlation time related to the diffusion of the water. While the mechanism (i) gives a flattening of  $r_1(\nu)$  at frequencies  $\nu < 1-5$  MHz, the mechanism (ii) is responsible of the maximum in  $r_1(\nu)$  at higher frequencies  $\nu > 1-5$  MHz, see Endorem and sample *A* in Fig. 4.6a. In addition, for particles characterized by a distance  $< 5$ nm between the magnetic core and the hydrogen nuclei of the bulk water (eventually permeating the coating), “dispersion” at intermediate frequencies occurs [5]. As said above, no high-frequency maximum is observed in most of our samples. This fact can be tentatively attributed to the dominant role of the magnetic anisotropy that “covers” the high frequency feature arising from Curie relaxation, possibly depressed by a scarce contribution of the diffusion process to  $r_1(\nu)$ . This experimental evidence suggests also that the bulk water does not penetrate the MNPs coating and so does not diffuse close to the magnetic cores.

A detailed discussion on the frequency dependence of longitudinal relaxivity in our system would require further experimental and theoretical investigations that we are currently undertaking. Here, we will restrict to an analysis of the variation of  $(1/T_1)_s = R_1(\nu)$  and  $(1/T_2)_s = R_2(\nu)$  at low frequencies for different particle sizes. Roch and Muller proposed a theoretical model that relates  $R_1$  and  $R_2$  to the energy levels of a magnetic particle of spin  $S$  obtained from a simplified Hamiltonian accounting for (magnetic) anisotropy energies [6]. This model is computer-time-consuming and, as such, inapplicable to large particles with a high total spin,  $S$ . To overcome these limitations, the authors suggested an alternative heuristic model where  $R_1$  and  $R_2$  are expressed (Eqs. 31 and 32 in Ref. [6]) as the sum of two contributions corresponding to the limits of zero and high anisotropy in the complete theory, respectively. The expressions of  $R_1$  and  $R_2$  can be simplified (the Langevin term in particular) for low frequencies, and still reproducing the increase of the absolute values of  $R_1$  and  $R_2$  with particle size in this frequency range, as follows:

$$R_1 = \frac{1}{3}C_1 \times \left\{ 7PJ^F[\Omega(\omega_s, \omega_0), \tau_D, \tau_N] + [7Q + 3] \times J^F(\omega_H, \tau_D, \tau_N) \right\} \quad (1)$$

$$R_2 = \frac{1}{3}C_2 \times \left\{ 13PJ^F[\Omega(\omega_s, \omega_0), \tau_D, \tau_N] + 7J^F(\omega_H, \tau_D, \tau_N) + 6J^F(0, \tau_D, \tau_N) + 3[3J^F(\omega_H, \tau_D, \tau_N) + 4J^F(0, \tau_D, \tau_N)] \right\} \quad (2)$$

$$C_1 = \left( \frac{32\pi}{135000} \right) \gamma_H^2 \mu_{SP}^2 \left( \frac{N_{SP}}{RD} \right) = \frac{32}{16} C_2 \quad (3)$$

where  $\mu_{SP}$  is the magnetic moment of the nanoparticle,  $\gamma_H$  the gyromagnetic ratio of protons,  $N_{SP}$  the number of particles per litre,  $R$  the particle radius,  $D$  the diffusion coefficient,  $\tau_D$  the diffusion correlation time of the water molecules,  $\tau_N$  the Néel relaxation time,  $\omega_s$  and  $\omega_H$  the electron and proton Larmor angular frequencies, and  $J^F$  is a spectral density function accounting for the proton diffusion in the non uniform magnetic field created by  $\mu_{SP}$ , and its fluctuation around its mean value;  $\omega_0$  is an adjustable parameter that considers the anisotropy field in the electron Larmor angular frequency ( $\omega_0 < \omega_s$ ), and  $P$  and  $Q$  ( $P+Q \leq 1$ ) are weighting factors for functions corresponding to zero and high anisotropy cases, respectively. Fig. 4.7 shows that this approximation is valid up to 1 MHz.

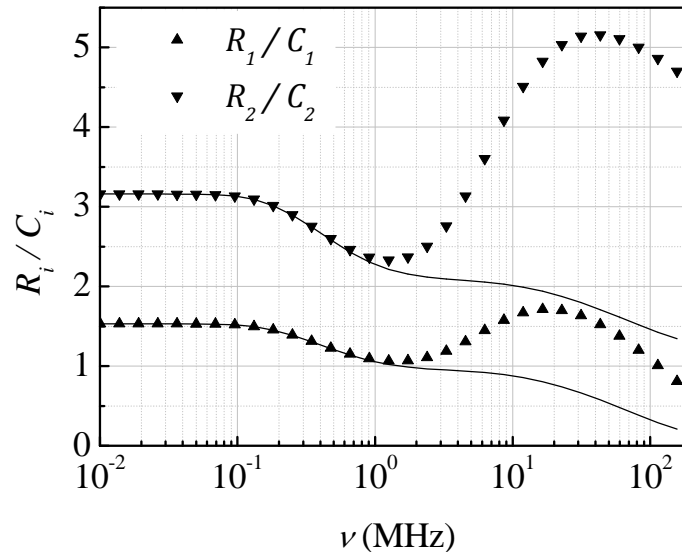


**FIG 4.7.** Theoretical frequency dependence of longitudinal and transverse relaxivities and their low field approximation (lines) divided by  $C_i$  using the same parameters as in Fig. 8 of ref. [6].

As the absolute values of the terms in brackets multiplying  $C_1$  and  $C_2$  in Eq. 1 and 2 hardly change with the magnetic core diameter  $D_p$ , in the low frequency range the most important contribution to the size dependence of  $R_1$  and  $R_2$  comes from the term  $\mu_{SP}^2 N_{SP}/R$ . It is important to note that the iron concentration, commonly used to normalize the NMRD curves of different samples, is implicit in the particle density or number of particles per litre ( $N_{SP}$ ) so that, for a fixed iron concentration, the particle density differs among samples with different particle size.

Fig. 4.8 shows that  $r_1$  and  $r_2$  absolute values at low frequency increase quite linearly with  $\mu_{SP}^2(N_{SP}/R)$ . Therefore, the main reason for the increase with size of  $r_1$  and  $r_2$  along the series of samples is caused by an increment of  $\mu_{SP}$ .

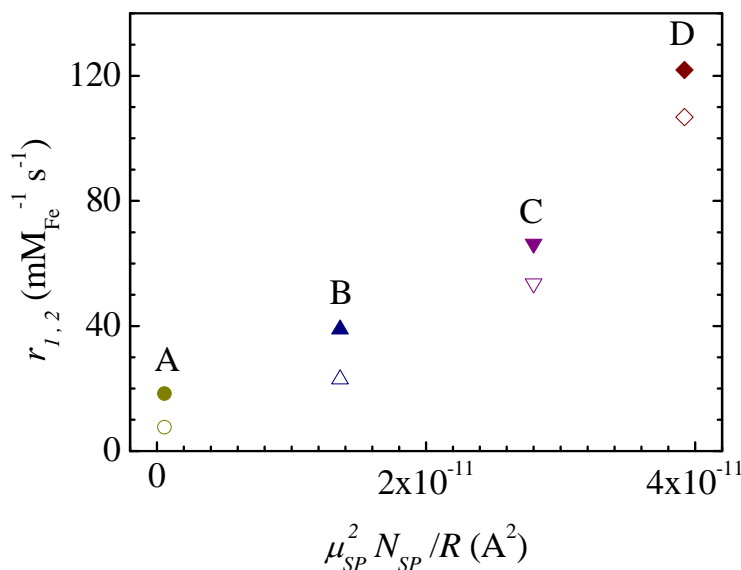


**FIG. 4.8.** Low frequency  $r_1$  (open symbols) and  $r_2$  (full symbols) absolute values as a function of  $\mu_{SP}^2(N_{SP}/R)$  for samples A to D.  $\mu_{SP}$  and  $N_{SP}$  are extracted from the fit of  $\sigma$  vs.  $H$  in Fig. 4.5.

On the other hand, for the contrast enhancement of magnetic spheres, different regimes are predicted [8,9]. The first one, which is called “*motional averaging regime*” (MAR) or “*motional narrowing regime*” describes the transverse relaxation for relatively small particles that are homogeneously dispersed in solution. This theory implies that water diffusion between particles occurs on a much faster time scale than the resonance frequency shift (and predicts identical values for  $R_2(=1/T_2)$  and  $R_2^*(=1/T_2^*)$ ). In this regime, the transverse relaxivity increases with increasing particle size. For larger particles, this theory breaks down. In this case, the relaxation rates are given by the “*static dephasing regime*” (SDR) theory. The SDR, first introduced by Yablonskiy and Haacke [10], implies that a large magnetic perturber produces strong dipolar fields in its surroundings, the result of which is the fact that, in contrast to the MAR, diffusion has a

minimal influence on nuclear magnetic resonance signal decay. The SDR places an absolute limit in the transverse relaxation rate: increasing the perturber size will not result in higher relaxation rates.

We found that our bio-ferrofluids, which are homogeneously dispersed nanoparticles, satisfy MAR theory because transverse relaxivity  $r_2$  increases with increasing core size.

Actually, for a further increase in size of the superparamagnetic core of polymer-coated particles, the increase in  $R_2$  and  $R_2^*$  should be violated at some point due to the decreasing influence of diffusion and thus reaching the SDR condition.

#### **4.1.4 In Vitro MRI Experiments**

To confirm the relaxivity results, according to the NMRD profiles, samples *C* and *D* with the highest  $r_2$  values at 8.5 MHz (see Fig. 4.6b) were selected for MRI experiments. To this aim, an Artoscan S.p.A imager was employed. Prior to imaging, the iron concentration of all samples together with the Endorem<sup>®</sup> was carefully fixed at 0.02 mg/mL.

In Fig 4.9 images of three vials containing samples *C*, *D* and Endorem<sup>®</sup>, are presented using two different pulse sequences a) high resolution Gradient Echo with TR/TE/NEX=1000ms/16ms/4, matrix=256\*192, FOV=180\*180, flip angle=90°; and b) high resolution Spin Echo sequence with TR/TE/NEX=1000ms/26ms/4, matrix=192\*192, FOV = 180\*180. For both sequences we selected five slices with the thickness of 5mm.

It is apparent for both sequences that the signal of sample *D* is darker than Endorem<sup>®</sup> and therefore shows a better performance to decrease the transverse relaxation time  $T_2$  as a negative contrast agent at the imager operating frequency, i.e. 8.5MHz. These results are consistent with what we found from relaxivity experiments.

## **4.2 CNCs**

### **4.2.1 Characterizations**

TEM of the bare SPIONs, show that uncoated SPIONs have the mean diameter of 5 nm in the absence of surfactants (Fig 4.10a).

By increasing the alkalinity of the solution (NaOH molarity from 1 to 4) in the presence of PVA, the magnetite nanoparticles spontaneously aggregate to form CNCs, as shown in the representative TEM images in Fig 4.10b-e. It is noted that the single coated SPIONs were formed in the lowest base molarity (i.e. 1). According to the TEM images, these monodisperse PVA coated CNCs are made up of superparamagnetic magnetite nanoparticles with the size of 5 nm. The hydrodynamic size of the obtained monodispersed CNCs is about 50 nm and increases by simply increasing the molarity of NaOH while keeping all other parameters fixed. The same behavior was detected for the CNCs which were synthesized by using a high-temperature hydrolysis reaction in the presence of polyacrylic acid [11,12]. The average size of synthesized samples, measured by X-ray diffraction (XRD), TEM, and DLS, is given in Table 4.2. In order to define the

polydispersity of the various coated SPIONs, we calculated the variance over 20 particles in the TEM images using the standard formula

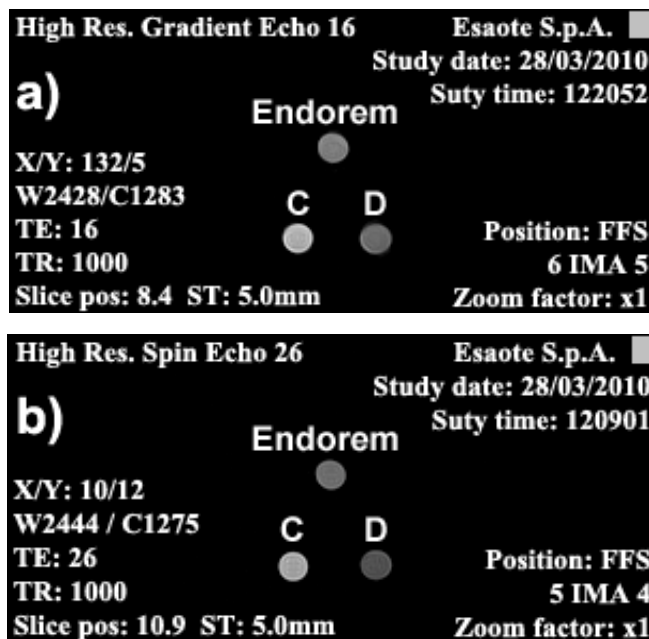


**FIG. 4.9** MRI images of vials containing bio-ferrofluids C, D and Endorem<sup>®</sup> with the same concentrations (0.02 mg/ml) obtained by Artoscan S.p.A imager at 8.5MHz: a) high resolution Gradient Echo with TR/TE/NEX=1000ms/16ms/4, matrix=256\*192, FOV=180\*180, flip angle=90°; and b) high resolution Spin Echo sequence with TR/TE/NEX=1000ms/26ms/4, matrix=192\*192, FOV = 180\*180.

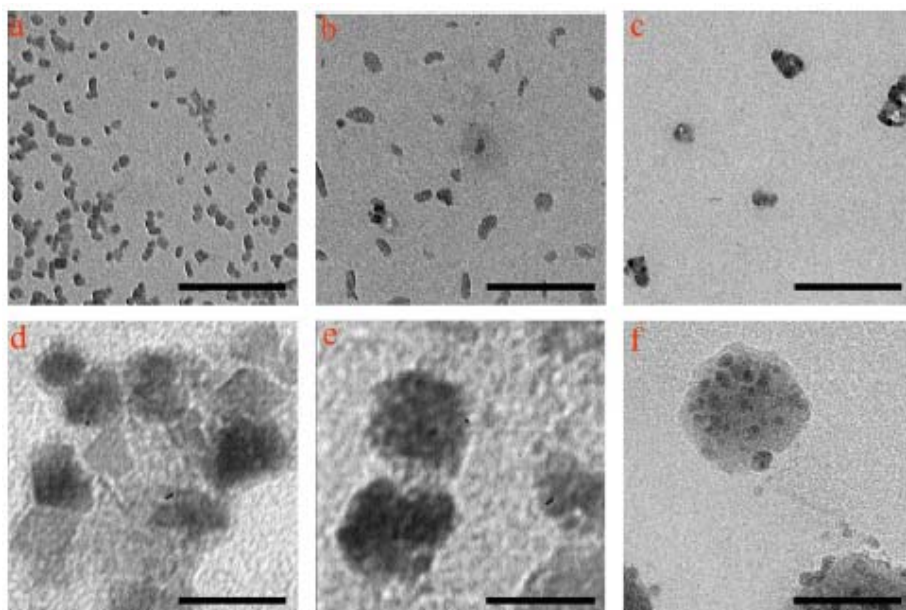


**FIG. 4.10** TEM images of (a) the bare SPIONs, and magnetite CNCs obtained from the solutions with the molarity of (b) 1, (c) 2, (d) 3, and (e) 4 in the presence of PVA; (f) TEM image of the crosslinked-PEGF coated CNCs prepared from the solution with the molarity of 4. The scale bar is 50nm.

**TABLE 4.2** Average size of SPIONs and CNCs, measured by X-ray diffraction (XRD), TEM, and DLS.

| Sample           | Remark                                 | Average Core Size of SPIONs <sup>a</sup> (nm) | Average Hydrodynamic Size <sup>b</sup> (nm) | Average Hydrodynamic Size <sup>c</sup> (nm) |
|------------------|----------------------------------------|-----------------------------------------------|---------------------------------------------|---------------------------------------------|
| Bare SPIONs      | No surfactant in the synthesis medium. | 5                                             | 5 ±1.1 (core size)                          | -----*                                      |
| PVA-Coated CNCs  | Synthesis base molarity: 1             | 5                                             | 10.5±1.7                                    | 12.5                                        |
|                  | Synthesis base molarity: 2             | 4.5                                           | 21±2.3                                      | 23                                          |
|                  | Synthesis base molarity: 3             | 5                                             | 33±3.1                                      | 41.5                                        |
|                  | Synthesis base molarity: 4             | 4.5                                           | 48±4.9                                      | 55.1                                        |
| PEGF-Coated CNCs | Polymeric shell: Cross-linked          | 5                                             | 52±5.6                                      | 56.5                                        |

<sup>a</sup> measured by XRD, <sup>b</sup> measured by TEM, <sup>c</sup> measured by DLS, \* since bare SPIONs are very eager to reduce their surface energy in the absence of surfactants, severe agglomeration may occurred; hence, their DLS data is not reliable.

It is well recognized that the saturation magnetization of the CNCs is enhanced by increasing their size; hence we employed the CNCs which were synthesized in basic molarity of 4, for crosslinkable PEGF coating.

#### 4.2.2 SQUID Magnetometry

It is well known that the magnetic magnetization of SPIONs strongly depends on the way how the cooling of the system is done before or during the measurements [13]. Typically there are two types of magnetization, zero-field-cooled (ZFC) magnetization and field-cooled (FC) magnetization. In the case of the ZFC magnetization, the system is cooled in the absence of an external magnetic field (H) from high temperatures well above a freezing temperature  $T_B$  (blocking temperature) to the lowest temperature well below  $T_B$ . After H is applied at the lowest temperature, the ZFC magnetization is measured with increasing temperature (T). In contrast, the FC magnetization is measured in the presence of H with decreasing T from high temperatures well above  $T_B$  to the lowest temperature well below  $T_B$ . For SPIONs [14], the ZFC magnetization exhibits a peak at the blocking temperature  $T_B$ , while the FC magnetization monotonically increases with decreasing T, showing no anomaly at  $T_B$ .

Sample solutions of CNCs were dried to solid form and the magnetization experiments were performed using a dc SQUID (Quantum Design MPMS XL) magnetometer. The temperature-dependence magnetization of the CNCs has been greatly different between the ZFC and FC measurements, as expected. In a ZFC measurement, the sample was cooled from  $T=300\text{K}$  to  $T=2\text{K}$  without applying any external magnetic field. Once reaching  $T=2\text{K}$ , a magnetic field of  $H=10\text{ mTesla}$  was applied and the magnetization of the sample was measured while the temperature was increasing. The magnetization increased as the temperature raised from  $2\text{K}$  (see Fig. 4.11) and started to decrease after reaching a maximum corresponding to the blocking temperature. In the FC measurement, the sample was cooled to  $2\text{K}$  under a  $10\text{ mTesla}$  applied magnetic field and the magnetization was measured while cooling down. The FC magnetization steadily increased as the temperature decreased.

The ZFC-FC curves and the relevant parameters are shown in Fig 4.11 and Table 4.3, respectively. The curves represent the typical behaviour of superparamagnetic nanoparticles. The blocking temperatures  $T_B$ , corresponding to the maximum in the ZFC curves, are all placed in the temperature range  $145\text{-}180\text{K}$ . Below  $T_B$ , the spins freeze and the system enters the blocked regime with typical out-of-equilibrium behaviour [15-17].

The difference in the blocking temperature for different samples is related to the different coatings. When the inter-particle separation increases, the magnetic dipole-dipole interaction reduces and the blocking temperature decreases. This result is typical for coated nanoparticles where the coating reduces the magnetic interaction. Kim *et al.* [18] showed similar effects for iron oxide particles covered with an oleate layer and Tartaj *et al.* [19] showed similar effects for  $\gamma\text{-Fe}_2\text{O}_3$  particles dispersed in silica.

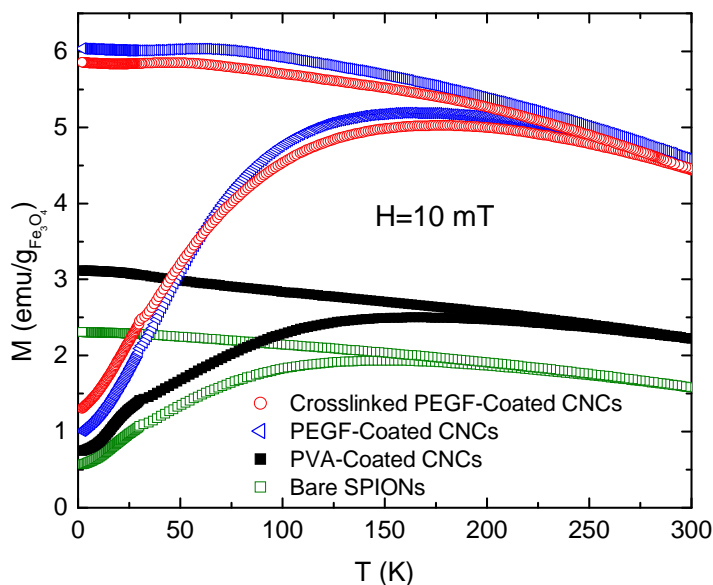


**FIG. 4.11** ZFC and FC magnetization measurements of dry powder of the CNCs using a dc SQUID magnetometer. The applied magnetic field is  $H=10\text{mTesla}$  and the data are reported per gram of magnetite.



**TABLE 4.3** Magnetic parameters extracted from ZFC/FC curves and hysteresis loops.

| Sample                       | Bare SPIONs | PVA-Coated CNCs | PEGF-Coated CNCs | Crosslinked-Coated CNCs |
|------------------------------|-------------|-----------------|------------------|-------------------------|
| $T_B$ (K)                    | 148.54      | 166.54          | 161.26           | 178.34                  |
| $H_c$ (mT)                   | 53.8        | 56.1            | 53.0             | 54.9                    |
| $M_r$ (emu / $g_{Fe_3O_4}$ ) | 5.31        | 7.16            | 16.27            | 14.73                   |

We have not observed a sharp blocking transition (as expected for a monodisperse system with a very tight size) but rather have a broad transition which is realized in polydisperse nanoparticles with a broader size distribution. In other words, the broad maximum may indicate that the agglomeration is inhomogeneous and the different aggregates are becoming blocked at varied temperatures, creating the distribution of blocking temperatures. It is also notable that there is a difference in magnitudes for the CNCs with different coatings. The PEGF- and crosslinked PRGF- coated CNCs have greater magnetization which might be explained by their coating effect which improves the spin-ordering at the surface. That is, bare SPIONs and PVA-coated CNCs have a high degree of spin-disorder.

To further characterize particle behavior and to confirm that the particles were in fact superparamagnetic, hysteresis curves were analyzed. Magnetic domains of ferromagnetic materials have a magnetic memory where once aligned in an applied field, they do not return to their original state without energy expense. This dependency on recent history traces a hysteresis loop and energy loss is measured by the area of the loop.

Superparamagnetic materials at high temperature have no permanent magnetic moment and, hence, no hysteresis. Instead at low temperature, where the spins are frozen, when it is possible to individuate an axis of anisotropy and to measure  $M$  along such axis on a single crystal, opening of the hysteresis can be observed. The degree of opening depends on sample's properties and, in powders, average over different directions. To test the magnetic behavior of the CNCs, the temperature was held constant at  $T=2K$  and  $300K$  for hysteresis measurements in the applied field ranges  $\pm 5T$ esla (Fig. 4.12). The low temperature hysteresis (Fig 4.12a) are slightly open with small coercive fields in the range  $53mT < H_c < 57mT$  and a small remanent magnetization,  $5emu / g_{Fe_3O_4} < M_r < 17emu / g_{Fe_3O_4}$ , while the high temperature hysteresis curves (Fig 4.12b) are not open, as expected for SPIONs and superparamagnetic CNCs [20-26]. The extracted data are given in Table 4.3.

### 4.2.3 NMR Relaxometry

As mentioned before, the efficiency of an MRI CA is determined by measuring the  $^1H$  nuclear longitudinal  $r_1$  and transverse  $r_2$  relaxivities. The NMRD profiles for all samples and for the commercial compound Endorem<sup>®</sup> are shown in Figs. 4.13a and 4.11b.

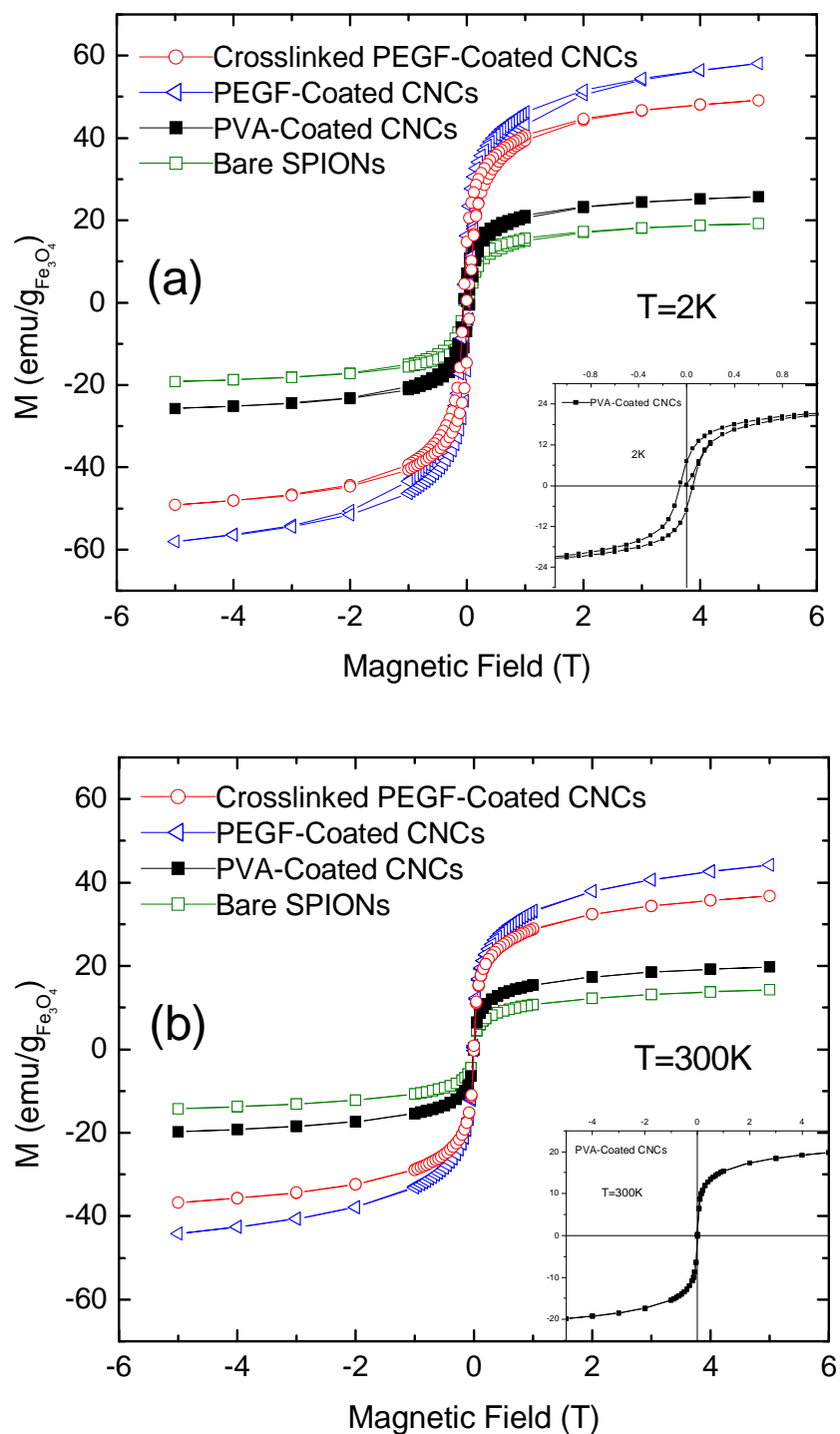


**FIG. 4.12** Magnetization vs. magnetic field at (a) 2K and (b) 300K for all the CNCs; the insets are zooms on the curves of PVA-coated CNCs with the same axis units.

Fig. 4.13a shows that the longitudinal relaxivity values of the PEGF-coated and the PVA-coated CNCs at very low frequencies are comparable with Endorem<sup>®</sup> while for higher frequencies all the samples have lower values. Looking at Figs. 4.13a, one simply can see that there is a decrease in the longitudinal relaxivity of CNCs compared to Endorem<sup>®</sup>. This decrease in the relaxivity is related to the agglomeration of the CNCs which are made of the ensembles of the SPIONs.

Particles containing only one ferrite crystal behave different from those having relatively larger particles containing several magnetic crystals within the same flake of permeable coating. For the former ones, a theoretical approach assuming a uniform distribution of the magnetic crystals within the solvent is rather realistic and allows the calculation of the nuclear magnetic relaxation rate [27-29]. This assumption is no longer valid for the clusters such as our systems, i.e. CNCs, which contain several ferrite crystals per particle.

Generally, the effects arising from the aggregation of magnetic grains can be divided in two: on one hand, those related to the global structure of the cluster and to the magnetic field distribution around it, and on the other hand, those limited to the inner part of the aggregate. While the former ones essentially affect  $T_2$  and  $T_2^*$  [28,30], the latter ones govern  $T_1$ .

The cluster itself may be considered as a large magnetized sphere whose total magnetic moment increases according to the Langevin's law. The global magnetization of the agglomerate is always aligned with the external field. Its effect on relaxation is characterized by a long correlation time, because of its large size, so that its contribution mainly affects the secular term of the relaxation rate. This contribution is given by the outer sphere diffusion theory, provided the motional averaging condition is fulfilled  $\Delta\omega\tau_{Da} < 1$ , where  $\Delta\omega$  is the difference in angular frequency between the local field experienced by a proton at the cluster surface and in the bulk;  $\tau_{Da}$  is the translational diffusion time around the cluster ( $\tau_{Da} = R_a^2 / D$ ,  $R_a$  being the cluster radius and  $D$  the water diffusion coefficient) [31].

It has been shown [32] that accounting for agglomeration is mandatory for explaining the relaxation properties of superparamagnetic colloids and the published models [27-29] do not incorporate such a feature: they only apply to non-agglomerated suspensions, where each flake does not generally contain more than one ferrite crystal. Agglomeration modifies relaxivities.

Longitudinal relaxation undergoes quite different modifications under agglomeration: NMRD profiles become flatter, because of an important decrease of the relaxation rates. This effect is interpreted as the result of a virtual exchange between the water inside the agglomerates, rapidly relaxed, and the waters within the bulk, relaxing much slower. In such cases, the time spent by the water molecules within the agglomerate is not simply given by the usual diffusion time  $\tau_{Da} = R_a^2 / D$ , it is instead deduced from the exact solution of the diffusion equation in a finite spherical space, producing an ensemble of decaying modes each characterized by its own decay time. These modes play the same role as binding sites with a short relaxation time, and with a residence time corresponding to the decay time of the diffusion modes.

Fig. 4.13b shows that the transverse relaxivities of all the samples are approximately constant in the frequency range of study. The transverse relaxivities of PEGF-coated,

PVA-coated, and crosslinked PEGF-coated CNCs are almost comparable to Endorem<sup>®</sup>. As the  $r_2$  value is the crucial parameter for a negative contrast agent (the higher  $r_2$ , the better the MRI contrast), the CNCs can be in principle usefully employed in MRI.

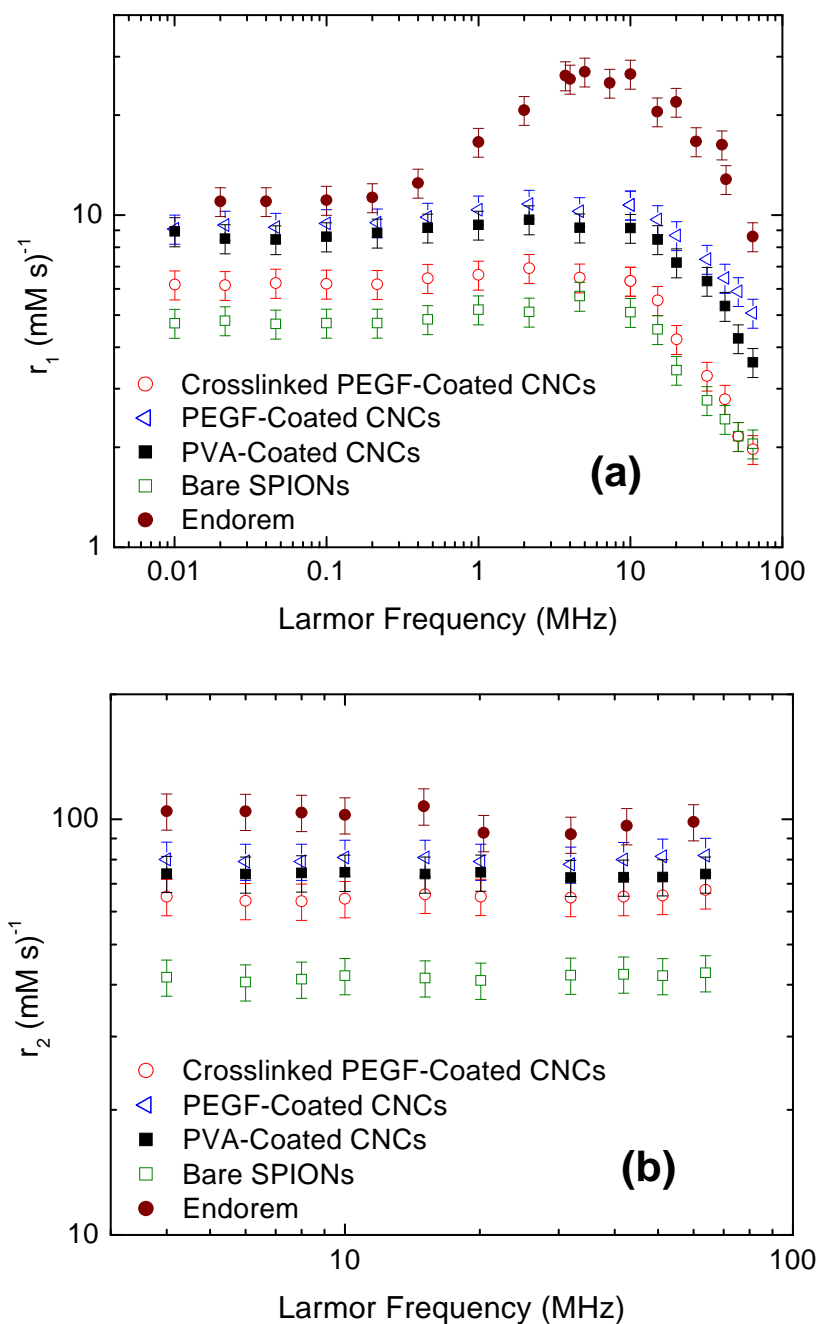


**FIG. 4.13** (a) Longitudinal  $r_1$  and (b) transverse  $r_2$  relaxivities vs. Larmor frequency for all CNCs together with the commercial CA, Endorem<sup>®</sup>.

#### 4.2.4 *In Vitro MRI Experiments*

In order to investigate the efficiency of CNCs at the level of *in vitro* MRI, we collected images at  $\sim 8.5$  MHz. To do that, five vials containing 4 of our samples and Endorem<sup>®</sup> have been prepared with the same concentration  $c=0.02$  mg/mL and placed in the MRI Imager. The obtained image, using a Spin Echo T<sub>2</sub> pulse sequence and TR/TE/NEX=2000ms/80ms/1, matrix=256\*192, and FOV=180\*180 as imaging parameters, is shown in Fig. 4.14. As one can see, PEGF-coated, PVA-coated, and crosslinked PEGF-coated CNCs show a contrast nicely comparable with Endorem<sup>®</sup>. Fig. 4.14 shows that the signal intensity is the lowest (i.e. the maximum efficiency) for PEGF-coated particles and increases going to PVA-coated, crosslinked PEGF-coated CNCs and bare SPIONs. As we know that the higher  $r_2$  the lower the signal, these results are fully consistent with the relaxometry data (see Fig. 4.13b).

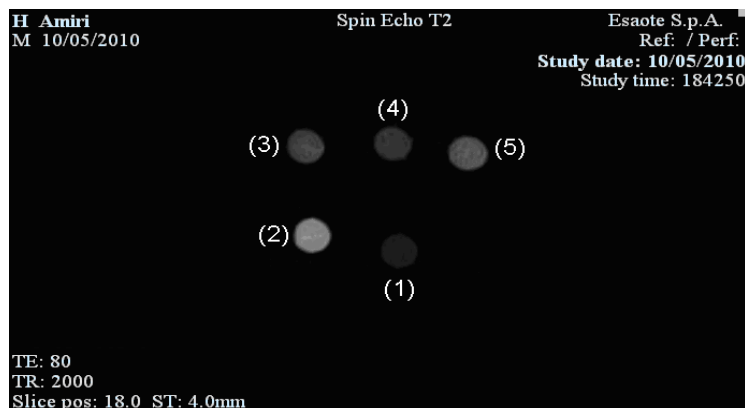


**FIG. 4.14** MRI image of vials containing different CNC samples with the same iron concentrations (0.02 mg/ml) obtained by Artoscan S.p.A. imager at  $H=0.2T$ . (1) Endorem, (2) bare SPIONs, (3) PVA-Coated CNCs, (4) PEGF-coated CNCs, (5) Crosslinked PEGF-Coated CNCs. Image parameters: TR/TE/NEX=2000ms/80ms/1, matrix=256\*192, and FOV=180\*180.

#### 4.2.5 *Cell Endocytosis and Drug Release*

The biocompatibility of PVA- and PEGF- coated SPIONs using the 3-(4,5-dimethylthiazol-2-yl)-2,5-diphenyltetrazolium bromide (MTT) assay, has been already confirmed [33,34].

Here, TEM has been employed to investigate the possibility of entrance of the coated CNCs inside the L929 cells through a mechanism of uptake induced by their hydrophilic and biocompatible coatings; the uptake of these CNCs are essential for the cellular drug delivery and imaging purposes. As shown in Figs 4.15b and 4.14c, both the PVA-coated and crosslinked PEGF-coated CNCs are accumulated within the cells. This

is likely due to the electrostatic interactions between the negatively charged membranes and the positively charged surface-saturated PVA-coated CNCs and crosslinked PEGF-coated CNCs (9.5 and 11 mV, respectively), resulting in the uptake of the CNCs by the cells. The TEM observations show that the CNCs were present in the membrane-bound multivesicle bodies, having entered the cells as larger aggregates. Little organelle damage following exposure to both the PVA-coated and crosslinked PEGF-coated CNCs, is also evident. The levels of damage in the cells, exposed to the coated CNCs, were negligible, confirming the biocompatibility of magnetic CNCs. The nuclei and organelles in the control cells remained intact.

On the other hand, the CNCs, once accumulated inside the desired tissue/cells as a drug delivery system, should be able to release their drug payload at an optimal rate. However, it is observed that the majority of the drug payload is quickly released upon injection into the *in vivo* environment (the so-called *burst effect*), since the drug is loaded on the surface of CNCs. Consequently, very small (inadequate) amount of the drug reach the specific site after e.g., proper antigene-antibody targeting.

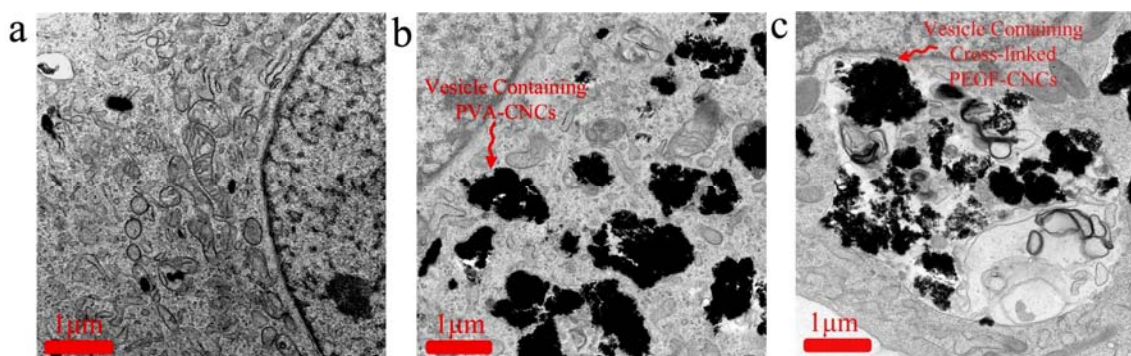


**FIG. 4.15** (a) TEM image of the control L929 cells. (b) TEM image of the L929 cells exposed to the PVA-coated CNCs. (c) TEM image of the L929 cells exposed to the cross-linked PEGF-coated CNCs.

Fig. 4.16 illustrates drug release from PEGF- and crosslinked PEGF- coated single nanoparticles and PVA-, PEGF- and crosslinked PEGF- coated CNCs over 12 days. According to the results, the crosslinking of the PEGF hydrogel caused a significant decrease in the burst effect not only for the coated CNCs but also for the single coated SPIONs; thus, as predicted, the crosslinked system have a great potential to control the burst effect even in this very simple drug loading system. Here, the drug was trapped in the crosslinked shell, consequently the barriers, for the reduction of the drug-gradient concentration, are gradually increased due to the existence of the crosslinked shell; hence its release (due to the lower diffusion process) has been kinetically controlled. More specifically, the TMX burst effect of the single PEGF coated SPIONs and PEGF coated CNCs reduced from 73% to 52% and from 61% to 41%, respectively. The crosslinked PEGF-coated CNCs have the lower burst effect compared to the single coated

nanoparticles: the reason is the lower chemical activity of CNCs in comparison to the single nanoparticles. Additionally, PVA coated CNCs have a burst effect similar to non-crosslinked PEGF one. It should be noted that a better control over burst effect could be obtained using more sophisticated drug loading methods, like e.g. conjugating the drug to the crosslinked PEGF CNCs.

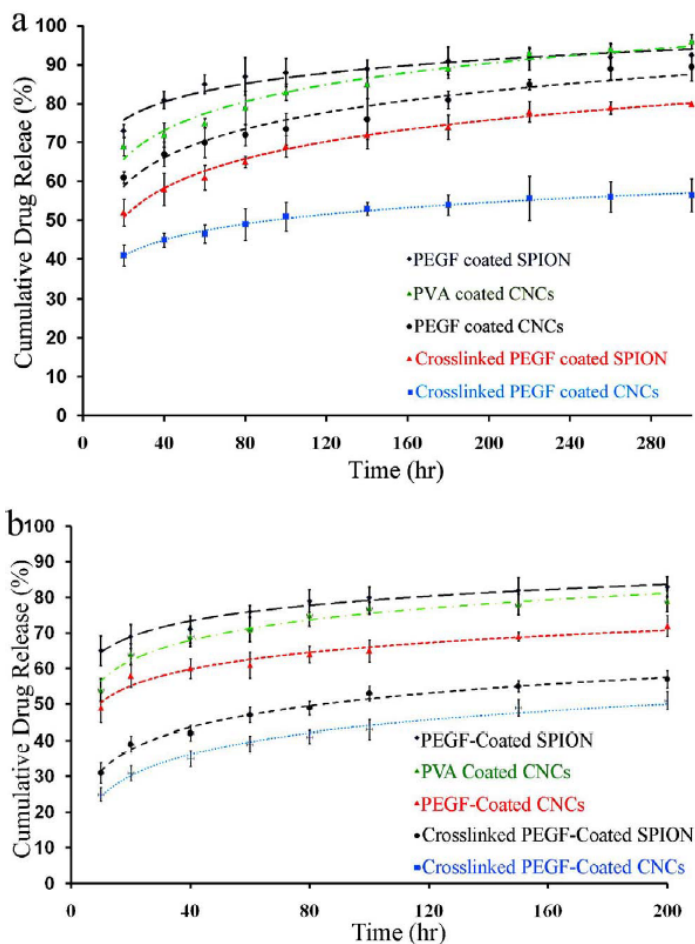


**FIG. 4.16** Release profile of (a) TMX and (b) DOX from PEGF- and crosslinked PEGF- coated single nanoparticles; and PVA- (obtained by the base molarity of 4), PEGF- and crosslinked PEGF- coated CNCs over 300 and 200 hours, respectively.

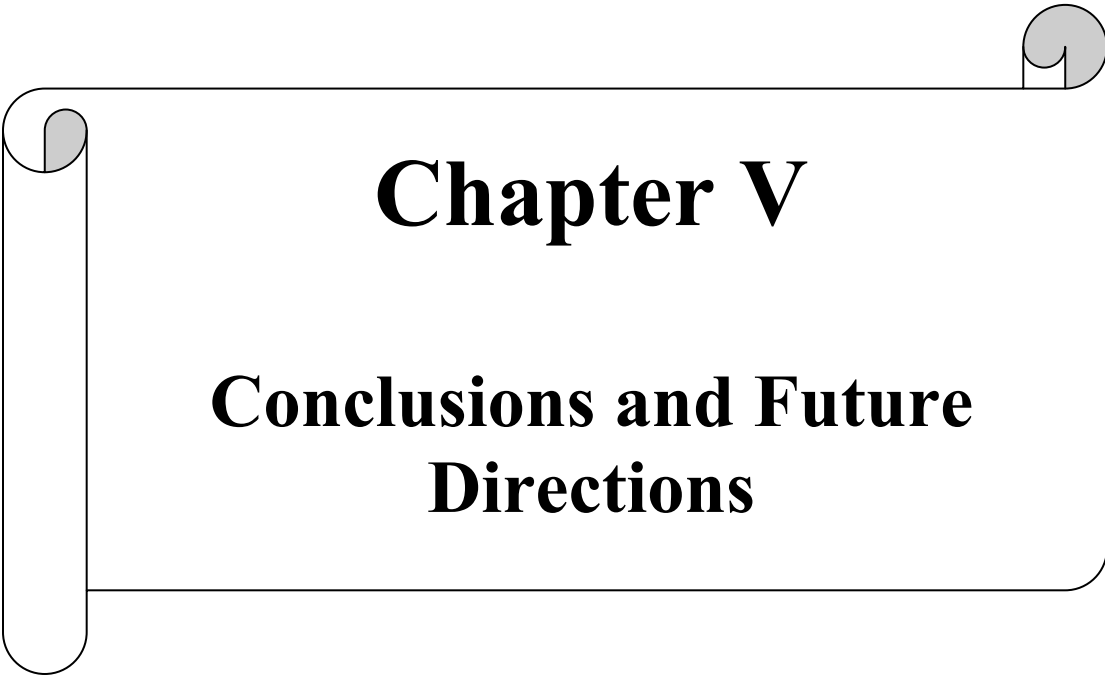
### 4.3 References

- [1] L. Néel, *Ann. Geophys.*, 5, 99, (1949).
- [2] W. F. Brown Jr., *Phys. Rev.*, 130, 1677, (1963).

- [3] A. Millan, A. Urtizberea, N. J. O. Silva, F. Palacio, V. S. Amaral, E. Snoeck, V. Serin, *J. Magn. Magn. Mater.*, 312, L5, (2007).
- [4] P. Langevin, *Annales de Chimie et de Physique*, 5, 70, (1905).
- [5] S. Laurent, D. Forge, M. Port, A. Roch, C. Robic, L. Vander Elst, R. N. Muller, *Chem. Rev.* 108, 2064 (2008).
- [6] A. Roch, R. N. Muller, P. Gillis, *J. Chem. Phys.*, 110, 5403, (1999).
- [7] A. Roch, R.N. Muller, P. Gillis, *J. Chem. Phys.*, 110, 5403, (1999).
- [8] Gillis, P.; Moiny, F.; Brooks, R. A. *Magn. Reson. Med.*, 47, 257-263, (2002).
- [9] Brooks, R. A.; Moiny, F.; Gillis, P. *Magn. Reson. Med.*, 45, 1014-1020, (2001).
- [10] Yablonskiy, D. A.; Haacke, E. M. *Magn. Reson. Med.*, 32, 749-763, (1994).
- [11] J. Ge, Y. Hu, M. Biasini, W. P. Beyermann, Y. Yin, *Angew. Chem.*, 119, 4420. (2007).
- [12] J. Ge, Y. Hu, Y. Yin, *Angew. Chem. Int. Ed.*, 46, 7428, (2007).
- [13] J. A. Mydosh, *Spin Glasses: An Experimental Introduction*, Taylor & Francis, London, (1993).
- [14] T. Bitoh, K. Ohba, M. Takamatsu, T. Shirane, S. Chikazawa, *J. Phys. Jpn.* 64 1305, (1995).
- [15] U. Jeong, X. Teng, Y. Wang, H. Yang, Y. Xia, *AdV. Mater.*, 19, 33, (2007).
- [16] R. H. Kodama, *J. Magn. Magn. Mater.*, 200, 359, (1999).
- [17] J. L. Dormann, D. Fiorani and E. Tronc, in "Magnetic relaxation in fine particle systems", from *Advances in Chemical Physics*, Vol. XCVIII, eds. I. Prigogine and S.A. Rice, J. Wiley and sons, (1997).
- [18] Kim DK, Zhang Y, Voit W, Rao KV, Muhammed M. *J. Magn. Magn. Mater.*, 225:30–36, (2001).
- [19] Tartaj S, Gonzalez-Carreno T, Serna CJ. *J Phys Chem B*, 107:20–24, (2003).
- [20] M. Corti, A. Lascialfari, M. Marinone, A. Masotti, E. Micotti, F. Orsini, G. Ortaggi, G. Poletti, C. Innocenti, C. Sangregorio, *J. Magn. Magn. Mater.*, 320, 316, (2008).



- [21] A. Boni, M. Marinone, C. Innocenti, C. Sangregorio, M. Corti, A. Lascialfari, M. Mariani, F. Orsini, G. Poletti, M.F. Casula, *J. Phys. D: Appl. Phys.*, 41, 134021, (2008).
- [22] L. Lartigue, K. Oumzil, Y. Guari, J. Larionova, C. GueLrin, J.-L. Montero, V. Barragan-Montero, C. Sangregorio, A. Caneschi, C. Innocenti, T. Kalaivani, P. Arosio, A. Lascialfari, *Organic Letters*, 11, 2992, (2009).
- [23] M. F. Casula, P. Floris, C. Innocenti, A. Lascialfari, M. Marinone, M. Corti, R. A. Sperling, W. J. Parak, C. Sangregorio, *Chem. Mater.*, 22, 1739, (2010).
- [24] E. Taboada, E. Rodriguez, A. Roig, J. Oro, A. Roch, R. N. Muller, *Langmuir*, 23, 4583, (2007).
- [25] U.I. Tromsdorf, N.C. Bigall, M.G. Kaul, O.T. Bruns, M.S. Nikolic, B. Mollwitz, R.A. Sperling, R. Reimer, H. Hohenberg, W.J. Parak, S. Forster, U. Beisiegel, G. Adam, H. Weller, *NanoLett.*, 7, 2422, (2007).
- [26] J.-F. Berret, N. Schonbeck, F. Gazeau, D. El Kharrat, O. Sandre, A. Vacher, M. Airiau, *J. Am. Chem. Soc.*, 128, 1755, (2006).
- [27] Roch, A., and Muller, R. N., *Proceedings of the 11th Annual Meeting of the Society of Magnetic Resonance in Medicine, Works in Progress*, p. 1447, (1992).
- [28] Roch, A., Muller, R. N., and Gillis, P., *J. Chem. Phys.* 110, 5403-5411, (1999).
- [29] Roch, A., Muller, R.N., and Gillis, P., *J. Magn. Reson. Imaging*, 14(1):94-6, (2001).
- [30] Moiny, F., Gillis, P., Roch, A., and Muller, R. N., *Proceedings of the 11th Annual Meeting of the Society of Magnetic Resonance in Medicine*, p. 1431, (1992).
- [31] Ayant, Y., Belorizky, E., Alizon, J., and Gallice, J., *J. Phys.* 36, 991-1004, (1975).
- [32] Alain Rocha, Yves Gossuinb, Robert N. Mullera, Pierre Gillis, *J. Magn. and Magn. Mater.* 293, 532–539, (2005).
- [33] M. Mahmoudi, A. Simchi, M. Imani, A. S. Milani, P. Stroeve, *Nanotechnology*, 20, (2009).
- [34] M. Mahmoudi, A. Simchi, M. Imani, U. O. Hafeli, *Journal of Physical Chemistry C*, 113, 8124, (2009).



# **Chapter V**

## **Conclusions and Future Directions**

## Chapter V

# Conclusions and Future Directions

### *Contents*

---

|                             |    |
|-----------------------------|----|
| 5.1 Conclusions.....        | 89 |
| 5.2 Future Directions ..... | 92 |
| 5.3 References.....         | 92 |

---

## 5.1 Conclusions

In this thesis we investigated the magnetic and relaxometric properties of two novel classes of superparamagnetic nanoparticles with polymer coatings and capability of being functionalized. The effect of core size and the type of coating has been studied. Obviously, to use a compound for the biomedical applications, one of the most important parameters is its biocompatibility which was a great motivation to study the present biocompatible systems. The advantages of investigated samples that motivated our research can be summarized as follows:

1) *Multifunctional polymer-based nanostructured bio-ferrofluids, in brief bio-ferrofluids*: These bio-ferrofluids represent a class of multifunctional maghemite/polymer composites, made of fully biocompatible ingredients. Previously, some very important characteristics and properties of these samples have been established, i.e.:

1. They have not shown any *in vivo* toxicity: after one month, the mice did not show any anomaly and an analysis of the organs, after being sacrificed, did not reveal neither any damage nor a significant accumulation of the bio-ferrofluids.
2. Haematology studies of the samples revealed no problem with the blood. That is, no anomalies in morphology and number of erythrocytes, leukocytes and platelets and observing normal size curves for all of them; no aggregation; no change in the haemoglobin concentration; and no haemolysis. Moreover, as an additional interesting effect, they are anticoagulant. Therefore, besides the bio-

magnetic applications, these materials could be also useful in other biomedical applications where anticoagulant agents are requested.

3. In cell experiments, low cytotoxicity (opossum kidney cells) has been reported.
4. Bio-ferrofluids have been also functionalised with an optical dye (fluoresceine and rhodamine), attached to the surface, which permits to track the pathway of the particles across the cellular membrane and inside the cell. It has been observed that the particles are internalized by the cells and they do not enter into organelles such as mitochondria, or ribosomes, but they accumulate in lysosomes. This allows suggesting them also for optical imaging.
5. In order to study the efficiency of the samples for the therapeutic applications, the hyperthermia efficiency has been investigated. The measurements have been performed for several frequencies, in the frequency range 2 kHz to 100 kHz, at several intensities of ac magnetic fields. The best performance has been obtained for the largest particle size (sample D) which is outstandingly larger than Endorem and substantially larger than ChemiCell (pure magnetite dispersed in water).

Since the main idea of these samples is to use them for theranostics, i.e. simultaneous diagnosis and therapeutics applications, one had to study also their magnetic and relaxometric properties. We studied the efficiency of bio-ferrofluids as MRI contrast agent versus particle sizes. Both longitudinal and transverse relaxivities show a strong increase with the particle size in relation to the increase of the magnetic moment. The best efficiency (i.e. the transverse relaxivity, the main parameter for superparamagnetic contrast agents) is reached for the maximum magnetic core diameter  $d \sim 15\text{nm}$ , sample *D*. This is in accordance with the predictions of the theoretical model by A. Roch and R. N. Muller [1]. Remarkably, sample *D* has demonstrated a MRI efficiency superior to a well-known commercial product, i.e. Endorem<sup>®</sup>, both in transverse relaxivity measurements and *in vitro* MRI experiments. From fundamental physics point of view, for the bio-ferrofluids we found that in the relaxation process the magnetic anisotropy role is dominant and the bulk water does not penetrate the MNPs coating and so does not diffuse close to the magnetic cores. Moreover, we found that our bio-ferrofluids, which are homogeneously dispersed nanoparticles, satisfy MAR theory because transverse relaxivity  $r_2$  increases with increasing magnetic core size. The presented multifunctional bio-ferrofluids have thus proven to be very interesting model systems for both fundamental studies of nuclear relaxation induced by superparamagnetic nanoparticles and clinical MRI. Particularly, sample D has the best MRI efficiency which couples to its very good hyperthermia efficiency and gives a system for therapy and diagnostics applications, as it was hoped at the beginning of the research.

## 2) *Superparamagnetic colloidal nano-crystal clusters (CNCs), in brief CNCs:*

CNCs are a class of PVA-, PEGF- and crosslinked PEGF-coated colloidal nanocrystals with a magnetic core of magnetite. The following properties of CNCs have been previously established:

1. The biocompatibility of the CNCs has been proved by the 3-(4,5-dimethylthiazol-2-yl)-2,5-diphenyltetrazolium bromide (MTT) assay and all of them have demonstrated acceptable levels of cell viability following exposure up

to 400mM, with none showing toxic effects at the concentrations tested. The PEGF coated samples showed better biocompatibility than the PVA coated ones.

2. In order to investigate if these systems could be useful for the targeted drug delivery, the drug release from CNCs has been studied. The study revealed that by introducing a crosslinking agent to the system, the burst effect was reduced by 21%. Thus the crosslinked magnetic nanoparticles are able to reduce the burst effect.

The aforementioned points are strong evidences for suggesting the CNCs for biomedical applications and due to their superparamagnetic properties; it is possible to track them in the body using the magnetic field. The magnetic properties and the MRI efficiency have been investigated to state if they can be novel candidates for theranostics applications. Differently from bio-ferrofluids presented above, the CNCs play their theranostic role in releasing a drug, while still the diagnosis is thought to be obtained through MRI.

The efficiency of our systems, to contrast suitably the MR images has been demonstrated by the relatively high values (comparable to the commercial compound Endorem<sup>®</sup>) of the transverse relaxivity  $r_2$  in the PEGF-coated, crosslinked PEGF-coated and PVA-coated CNCs, at frequencies of clinical applications. The efficiency of the compounds has been confirmed by the MRI *in vitro* experiments. Summarizing, the CNCs (and specially the crosslinked ones) are biocompatible, show a relatively controlled burst effect (meaning that are good candidates for the targeted drug delivery), and behave like good negative MRI contrast agents. Therefore, this novel class of magnetic nanoparticles could be introduced for the theranostics (MRI + drug release) applications.

From fundamental physics point of view, Fig. as 4.13a shows, the longitudinal relaxivity values of the PEGF-coated and the PVA-coated CNCs at very low frequencies are comparable with Endorem<sup>®</sup> while for higher frequencies all the samples have lower values. Looking at Figs. 4.13a, one simply can see that there is a decrease in the longitudinal relaxivity of CNCs compared to Endorem<sup>®</sup>. This decrease in the relaxivity is related to the agglomeration of the CNCs which are made of the ensembles of the SPIONs. Particles containing only one ferrite crystal behave different from those having relatively larger particles containing several magnetic crystals within the same flake of permeable coating. For the former ones, a theoretical approach assuming a uniform distribution of the magnetic crystals within the solvent is rather realistic and allows the calculation of the nuclear magnetic relaxation rate [2-4]. This assumption is no longer valid for the clusters such as our systems, i.e. CNCs, which contain several ferrite crystals per particle.

Generally, the effects arising from the aggregation of magnetic grains can be divided in two: on one hand, those related to the global structure of the cluster and to the magnetic field distribution around it, and on the other hand, those limited to the inner part of the aggregate. While the former ones essentially affect  $T_2$  and  $T_2^*$  [3,5], the latter ones govern  $T_1$ .

## 5.2 Future Directions

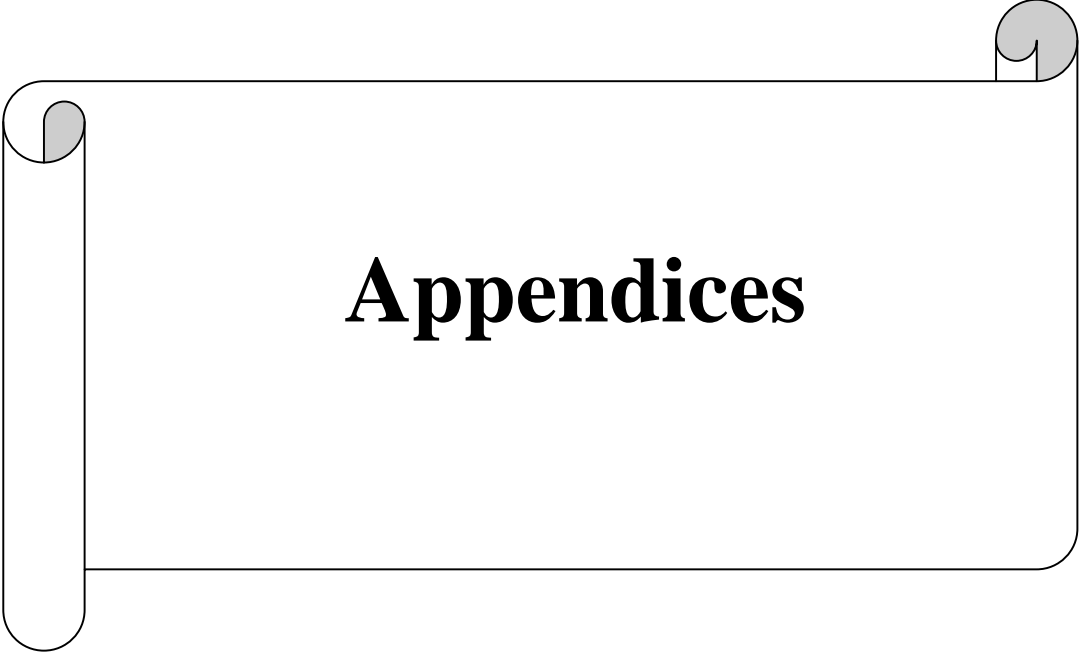
We studied two different superparamagnetic systems for biomedical applications.

The bio-ferrofluids with the largest core size have been demonstrated to be very good for both hyperthermia and MRI. Since their cytotoxicity has been also proved to be small, in next future it is planned to test them *in vivo* and possibly study their efficiency in clinical diagnosis and therapy. First, we will perform MRI *in vivo* experiments, looking at the contrast and the nanoparticles uptaking by the normal cancerous tissues. Secondly, we'll perform *in vivo* hyperthermia experiments trying to reduce the tumor growth/size with applying a magnetic field for a certain time interval and of proper strength and frequency. The MRI will allow us to follow the tumor evolution before and after the magnetic hyperthermia treatment.

The results for the CNCs are also very promising for theranostics applications. So far, it has been shown that the drug release in the crosslinked compounds is very effective and they are good candidates as negative MRI contrast agent. Therefore, both diagnostics and therapeutics are possible. It has been planned to look for a specific tumor sensitive to the doxorubicin and to inject a physiological solution of drug-loaded CNCs with well established concentration in an *in vivo* model of tumor. The tumor is expected to regress upon the action of the drug and its regression will be followed with time by MRI experiments.

## 5.3 References

- [1] A. Roch, R. N. Muller, P. Gillis, J. Chem. Phys., 110, 5403 (1999).
- [2] Roch, A., and Muller, R. N., Proceedings of the 11th Annual Meeting of the Society of Magnetic Resonance in Medicine, Works in Progress, p. 1447, (1992).
- [3] Roch, A., Muller, R. N., and Gillis, P., J. Chem. Phys. 110, 5403-5411, (1999).
- [4] Roch, A., Muller, R.N., and Gillis, P., J. Magn. Reson. Imaging, 14(1):94-6, (2001).
- [5] Moiny, F., Gillis, P., Roch, A., and Muller, R. N., Proceedings of the 11th Annual Meeting of the Society of Magnetic Resonance in Medicine, p. 1431, (1992).



# Appendices

# Appendix A

## Some Details About MRI

### *Contents*

---

|                                                           |    |
|-----------------------------------------------------------|----|
| A.1 Magnetic Field Gradients.....                         | 94 |
| A.2 k-Space and Pulse Sequences .....                     | 96 |
| A.3 Steady State and T <sub>1</sub> -Weighted Images..... | 97 |
| A.4 Multi-Slice 2D Imaging .....                          | 98 |
| A.5 3D Volume Imaging.....                                | 98 |

---



### A.1 Magnetic Field Gradients

To produce an image of a specific tissue placed at a certain point, the presence of a gradient field, varying linearly across the sample, is an important issue. Therefore one will be able to encode the signal of the spins in space. Fig. A.1 shows how the gradient coils are positioned to produce the gradient fields.

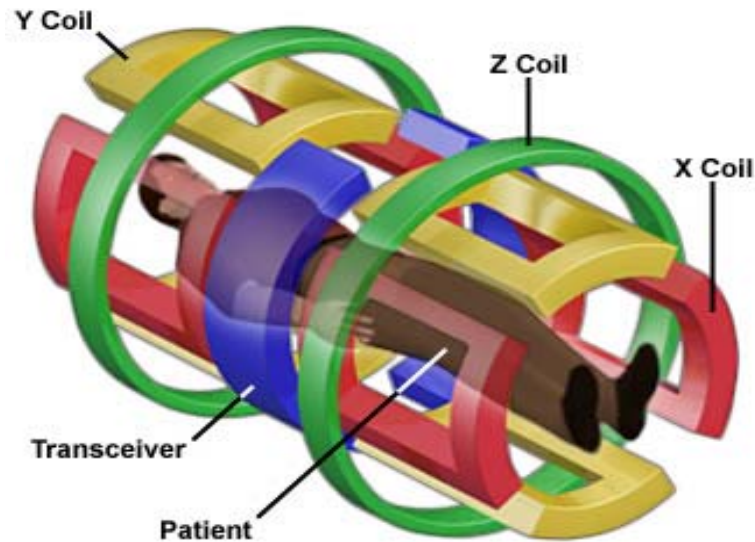


FIG. A.1 MRI scanner gradient coils.

Two-dimensional (2D) *Fourier Imaging* is one of the most common imaging techniques; that uses three perpendicular pulsed gradients in order to obtain the spatially magnetic resonance information. These three gradient fields, so called *slice selection*, *phase encoding* and *frequency encoding*, play very important roles and will be explained below.

1. *Slice Selection*. Slice selection (or selective excitation) is performed by applying a magnetic field gradient during the rf excitation. Often, the direction of the slice selective gradient is chosen along  $z$  (the direction of the applied magnetic field,  $B_0$ ) so, for the sake of simplicity, here we will consider only this case, referring to the slice selection gradient as  $G_z$ , where:

$$G_z = \frac{\partial B_0}{\partial z} \quad \text{A.1}$$

It should be noted that only the magnitude of the applied field is affected by the gradients and the direction of  $\mathbf{B}_0$  remains constant all over the sample.

In presence of  $G_z$ , the Larmor frequency becomes a function of  $z$ , that is:

$$\omega(z) = -\gamma(B_0 + G_z z) \quad \text{A.2}$$

By exciting the sample with an rf pulse of  $\omega_{rf}$ , only the spins located at  $z = -(\omega_{rf} + \gamma B_0) / (\gamma G_z)$  will be placed into the  $xy$ -plane, contributing to the final signal, thus selecting a plane of the sample perpendicular to  $\mathbf{B}$ . For a rectangular rf pulse of duration  $\tau$ , there will be a spread of frequencies described by the *Fourier Transform* (FT) of a rectangular window function, i.e., a sinc function centered on  $\omega_{rf}$ , with a bandwidth proportional to  $1/\tau$ . The width of the selected slice can be written:

$$\Delta z \sim \frac{1}{\gamma G_z \tau} \quad \text{A.3}$$

The main parameter to control the slice thickness is the rf pulse duration. A slice profile that is a sinc function however is not ideal, as it produces substantial excitation in the lobes away from the selected slice. Improved slice profiles can be obtained by using excitation pulses of different shapes such as Gaussian.

*2. Frequency and Phase Encoding.* Once the slice volume is selected, to determine an exact and precise tissue, we will need to apply another two gradients to have each single magnetic moment at a certain place and with a certain frequency and phase. Usually, a magnetic field gradient is applied along  $x$ -direction,  $G_x$ , which is switched on during the signal acquisition. Therefore the Larmor frequency of each spin will be a function of  $x$ , so called *frequency encoding*:

$$\omega(x) = -\gamma(B_0 + G_x x) \quad \text{A.4}$$

and the slice is cut into strips of constant Larmor frequency. Ignoring the  $T_2$  decay, an area  $dx dy$  in the selected slice gives a contribution  $dS(t)$  to the total signal:

$$dS(t) = \rho(x, y) e^{-i\gamma(B_0 + G_x x)t} dx dy \quad \text{A.5}$$

where  $\rho$  is the proton density function and the time origin is set at the  $G_x$  activation (i.e., at the beginning of the signal acquisition).

Demodulating the signal, to remove the carrier frequency  $B_0$ , and integrating over the slice, one obtains the following expression for the total receiving signal:

$$S(t) = \int \underbrace{\int \rho(x, y) dy}_{y\text{-projection of } \rho} e^{-i\gamma G_x x t} dx \quad \text{A.6}$$

where we recognize the  $\rho$  projection along the  $y$ -axis. The  $\rho$  projection along  $y$  can be resolved applying, for a certain amount of time, a gradient along  $y$ , immediately following the selective excitation and just before signal acquisition. By briefly turning on the  $G_y$  field gradient, the precessional phases of the rotating macroscopic magnetization can be manipulated as follows.  $G_y$  induces a variation of the Larmor frequency along the  $y$ -direction, according to:

$$\omega(y) = -\gamma(B_0 + G_y y) \quad \text{A.7}$$

If  $G_y$  is now turned off after a time  $\tau_y$ ,  $\mathbf{M}$  returns to the constant frequency  $\omega_0$ , but having accumulated a phase shift,  $\phi$ , as a function of  $y$  (phase encoding), i.e.,

$$\phi(y) = \gamma G_y y \tau_y \quad \text{A.8}$$

If now we turn on the frequency encoding gradient and acquire the signal, then the FID will be a function of  $t$  and  $\tau_y$  i.e.,

$$\begin{aligned} S(t, \tau_y) &= \iint \rho(x, y) e^{-i[\gamma G_x x t + \phi(y)]} dx dy \\ &= \iint \rho(x, y) e^{-i[\gamma G_x x t + G_y y \tau_y]} dx dy \end{aligned} \quad \text{A.9}$$

Using  $G_x$  and  $G_y$  we have indexed each nutated macroscopic magnetic moment in the selected slice, that is, each  $(x, y)$  position, with an unique combination of Larmor frequency and Larmor phase,  $(\omega, \phi)$ .

## A.2 $k$ -Space and Pulse Sequences

Eq. A.9 can be conveniently rewritten as:

$$S(k_x, k_y) = \iint \rho(x, y) e^{-i(k_x x + k_y y)} dx dy \quad \text{A.10}$$

Where;

$$k_x = \gamma G_x t \quad \text{A.11}$$

$$k_y = \gamma G_y t \quad \text{A.12}$$

The plane defined by the  $\mathbf{k} = (k_x, k_y)$  points is called  $k$ -space, and plays an important role in the interpretation of MRI experiments.

In Eq. A.10 we can note that  $S(k_x, k_y)$  and  $\rho(x, y)$  are FT-pairs. The proton density over the slice (i.e., the image, in absence of relaxations) can thus be obtained by taking the inverse  $2D$  FT of the demodulated FID over the  $k$ -space.  $k_y$  is varied by stepping through different values of  $G_y$ , whereas  $k_x$  is sampled by holding on the frequency encoding gradient while sampling the signal discretely.

The acquisition of each line of the  $k$ -space (i.e.,  $\{\forall(k_x, k_y): k_y = \text{const}\}$ ) implies at least an rf pulse (the excitation), a series of gradient pulses, and the signal acquisition.

The time course between two subsequent excitation rf pulses is called *repetition time* (TR). The complex sequence of time delays, gradients and rf pulses is known as *pulse sequence*. The total acquisition time of a slice,  $T_{\text{acq}}$  is thus given by:

$$T_{\text{acq}} = N_y (TR) \quad \text{A.13}$$

where  $N_y$  is the number of  $k_y$  steps.

From the properties of the FT, we know that the signal acquired at each  $k$ -space location contains information about the whole image, but the type of information varies across the  $k$ -space. Most of the contrast of the final image is encoded at the center of the  $k$ -space (small  $k_x$  and  $k_y$ ), while its peripheral part accounts mainly for the high frequency contributes to the image, that is, resolution of details and noise.

The trajectory of the vector  $\mathbf{k}$  during the pulse sequence can be written as:

$$\mathbf{k}(t) = \gamma \int_0^t \mathbf{G}(t') dt' \quad \text{A.14}$$

where the time origin is now at the beginning of the sequence and  $\mathbf{G}(t)$  is the general function describing orientation, shape and duration of the magnetic field gradients applied during the MRI experiment. The  $\mathbf{k}(t)$  formalism is of great help in interpreting complex pulse sequences.

### A.3 Steady State and $T_1$ -Weighted Images

It should be noted that after each acquisition one should wait (TR), at least five times  $T_1$ , in order to let the longitudinal magnetization recovers completely. Therefore the maximum signal will be obtained. This is actually impractical for in-vivo imaging, due to the resulting too long acquisition time (see Eq. A.13). In fact, TR is always set  $\leq T_1$ . After a few pulses, the recovered value of  $M_z$  reaches a steady state, depending upon the  $T_1$  of the sample, but always lower than  $M_0$ .

The longitudinal magnetization after the  $n$ -th TR interval is given by:

$$\begin{aligned} M_z^{(n)} &= M_z^{(n-1)} \cos \alpha + (1 - E)(M_0 - M_z^{(n-1)} \cos \alpha) \\ &= (1 - E)M_0 + K M_z^{(n-1)} \end{aligned} \quad \text{A.15}$$

where  $\alpha$  is the FA of the excitation pulse, and we define:

$$E = e^{-TR/T_1} \quad \text{A.16}$$

$$K = E \cos \alpha \quad \text{A.17}$$

Writing Eq. A.15 as a sequence we have:

$$\begin{aligned}
M_z^{(n)} &= (1-E)M_0(1+K+K^2+\dots+K^n) + K^n e^{-TR/T_1} M_0 \\
&= (1-E)M_0 \frac{1-K^{n+1}}{1-K} + K^n E M_0
\end{aligned}
\tag{A.18}$$

and, since  $K < 1$ , for  $n \rightarrow \infty$ , the steady state value is:

$$M_z^{n \rightarrow \infty} = M_z^{steady} = \frac{(1-E)M_0}{1-K} \tag{A.19}$$

A short TR, together with reducing  $T_{acq}$ , can thus be used to induce a contrast between two regions of the sample having the same proton density, but different  $T_1$  ( $T_1$ -weighted image).

#### A.4 Multi-Slice 2D Imaging

The coverage of a 3D volume is accomplished through the multi-slice approach, by applying a sequence of rf pulses, exciting different slices, within a single TR. During each TR, one  $k$ -space line is acquired for all the slices, thus keeping the same  $T_{acq}$  of the single-slice acquisition. On the other hand, TR has to be set long enough to allow for the pulse sequence of each slice being executed.

Because of imperfect rf profiles, the immediate neighborhood of an excited slice is also partly excited (slice cross-talk effect). In multi-slice imaging, this region cannot be included in the following slice since the spins do not have time to recover toward equilibrium. To overcome the problem, it is common either to leave a gap between slices or to excite the odd number of slices first and the even numbered ones afterwards (*interleaved acquisition*).

#### A.5 3D Volume Imaging

As an alternative to the 2D multi-slice approach for imaging 3D volumes, the 2D coverage of  $k$ -space can be generalized to 3D.

The excitation pulse is used to select a thick slab of the sample, and then the 3D  $k$ -space is discretely sampled in both  $k_y$  and  $k_z$  directions, through phase encoding. The read sampling along the  $x$ -direction is carried out, as in 2D, with measurements at finite time steps  $\Delta t$  during the continuous application of a gradient  $G_x$ . The associated step in the  $k_x$  direction is:

$$\Delta k_x = \gamma G_x \Delta t \tag{A.20}$$

The  $(k_x, k_z)$  position of each acquisition line is determined by applying the orthogonal gradients  $G_y$  and  $G_z$ , for the  $\tau_y$  and  $\tau_z$  time intervals, respectively. The corresponding steps in  $k$ -space are:

$$\Delta k_y = \gamma \Delta G_y \tau_y \quad \text{A.21}$$

$$\Delta k_z = \gamma \Delta G_z \tau_z \quad \text{A.22}$$

where  $\Delta G_y$  is the difference in  $G_y$  intensity between two consecutive read lines, and analogously for  $\Delta G_z$ .

Under 3D imaging conditions, the signal from a single rf excitation of the whole sample can be written as a 3D FT of the proton density:

$$S(\mathbf{k}) = \int \rho(\mathbf{r}) e^{-i\mathbf{k}\cdot\mathbf{r}} d\mathbf{r} \quad \text{A.23}$$

3D imaging has several advantages compared to the multi-slice imaging:

1. The ability to change the number of the  $N_z$  phase encoding steps over the excited slab, of thickness  $TH$ , gives the control over the size of the partition thickness  $\Delta z = TH / N_z$  without any limitation on the rf amplitude or duration. In general, higher  $z$  resolutions are obtainable.
2. The Signal-to-Noise Ratio (SNR) can be enhanced, thanks to the higher flexibility in setting the pulse program parameters available in 3D imaging, but achieving this may come at the expense of increased imaging time.
3. Consecutive slices may be adjacent without cross-talk effects.
4. Shorter TR is usable if necessary, since only one  $k$ -space line has to be acquired for each repetition.

On the other hand, the total acquisition time for 3D imaging is given by:

$$T_{acq} = N_y N_z TR \quad \text{A.24}$$

where  $N_y$  and  $N_z$  denote the number of phase encoding steps along  $y$  and  $z$ . One can simply realize from Eqs. A.13 and A.24 that 3D imaging takes more time compared to the 2D imaging.

An immediate consequence is the capability of acquiring more 2D than 3D images within the same time, thus allowing a higher temporal resolution, in dynamic studies.

A more indirect effect is due to the capability (but also the necessity) of setting longer TR, given a certain  $T_{acq}$ , in multi-slice imaging. A longer TR implies a higher steady-state value of the longitudinal magnetization, thus giving a higher SNR.

# Appendix B

## **Presentations & Publications**

### *Contents*

---

|                        |     |
|------------------------|-----|
| A. Presentations ..... | 101 |
| B. Publications .....  | 102 |
| C. Papers .....        | 103 |

---

## A. Presentations

1. **H. Amiri**, M. Mahmoudi, and A. Lascialfari, “*Novel superparamagnetic nano-crystal clusters for the theranostic applications*”, Nano2010 - X International Conference on Nanostructured Materials, September 13-17, Rome, Italy, 2010.
2. **H. Amiri**, P. Arosio, M. Corti, A. Lascialfari, R. Bustamante, A. Millán, N. J. O. Silva, R. Piñol, L. Gavilondo, F. Palacio, “*Magnetic properties and MRI contrast efficiency of novel ferrofluid-based nanoparticles*”, ESF Conference, Nanomedicine: Reality Now and Soon, October 23-28, Sant Feliu de Guixols, Spain, 2010.
3. Purificacion Sánchez, Elsa Valero, Natividad Gálvez, José M. Dominguez-Vera, Massimo Marinone, Alessandro Lascialfari, Giulio Poletti, Maurizio Corti, **Houshang Amiri**, “*Investigation of a New Class of Gd-Based Nanoparticles for Magnetic Resonance Imaging*” The 6<sup>th</sup> Conference on Field Cycling NMR Relaxometry, June 4-6, 2009, Torino, Italy.
4. **H. Amiri**, M. Mariani, F. Borsa, A. Lascialfari, G. A. Timco, R. E. P. Winpenny, “*Investigation of magnetic properties and spin dynamics of  $Cr_7Fe^{2+}$  nanomagnet by means of  $^1H$  NMR*”, International Conference on Magnetism (ICM 2009), 26-31 July, 2009, Karlsruhe, Germany.
5. **H. Amiri**, M. Mariani, F. Borsa, A. Lascialfari, G. A. Timco, R. E. P. Winpenny, “*A NMR Approach to study a nanomagnetic structure:  $Cr_7Fe^{2+}$  Nanomagnet*”, European Conference on Molecular Magnetism (ECMM 2009), 4-7 October, 2009, Wroclaw, Poland.
6. **H. Amiri**, M. Mariani, F. Borsa, A. Lascialfari, G. A. Timco, R. E. P. Winpenny, “*Spin dynamics study of the heterometallic  $(C_4H_9)_2NH_2Cr_7Fe^{2+}F_8(O_2CCMe_3)_{16}$  nanomagnet by means of  $^1H$  NMR*”, The 11<sup>th</sup> International Conference on Molecular-based Magnets (ICMM), September 21-24, 2008, Florence, Italy.
7. Purificacion Sánchez, Elsa Valero, Natividad Gálvez, José M. Dominguez-Vera, Massimo Marinone, Alessandro Lascialfari, Giulio Poletti, Maurizio Corti, **H. Amiri**, “*MRI Relaxation Properties of Water-Soluble Apoferritin-encapsulated Gadolinium Oxide/Hydroxide Nanoparticles*”, The 11<sup>th</sup> International Conference on Molecular-based Magnets (ICMM), September 21-24, 2008, Florence, Italy.
8. Purificacion Sánchez, Elsa Valero, Natividad Gálvez, José M. Dominguez-Vera, Massimo Marinone, Alessandro Lascialfari, Giulio Poletti, Maurizio Corti, **Houshang Amiri** “*Relaxation Properties Study of Water-Soluble Gadolinium Oxide Nanoparticles as a Novel Class of MRI Contrast Agents*”, The First Transalpine Conference on Nanoscience and Nanotechnologies, October 27-29, 2008, Lyon, France.



**B. Publications**

1. **H. Amiri**, M. Mariani, A. Lascialfari, F. Borsa, G. A. Timco, F. Tuna, and R. E. P. Winpenny, “*Magnetic properties and spin dynamics in the Cr<sub>7</sub>Fe nanomagnet: A heterometallic antiferromagnetic molecular ring*”, Phys. Rev. B, **81**, 104408, 2010.
2. **H. Amiri**, A. Lascialfari, Y. Furukawa, F. Borsa, G. A. Timco, and R. E. P. Winpenny, “*Comparison of the magnetic properties and the spin dynamics in heterometallic antiferromagnetic molecular rings*”, Phys. Rev. B, **82**, 144421, 2010.
3. **Houshang Amiri**, Morteza Mahmoudi, and Alessandro Lascialfari, “*Superparamagnetic Colloidal Nano-crystal clusters coated with Polyethylene Glycol Fumarate: a possible novel theranostic agent*”, Nanoscale, in press.
4. **Houshang Amiri**, Rodney Bustamante, Angel Millán, N. J. O. Silva, R. Piñol, L. Gavilondo, Fernando Palacio, Paolo Arosio, Maurizio Corti and Alessandro Lascialfari, “*Multifunctional polymer-based nanostructured bio-ferrofluids: novel MRI contrast agents*”, Small, under review.

## C. Papers

PHYSICAL REVIEW B 81, 104408 (2010)

**Magnetic properties and spin dynamics in the Cr<sub>7</sub>Fe nanomagnet:  
A heterometallic antiferromagnetic molecular ring**H. Amiri,<sup>1,2,\*</sup> M. Mariani,<sup>2</sup> A. Lascialfari,<sup>1,2,3</sup> F. Borsa,<sup>2</sup> G. A. Timco,<sup>4</sup> F. Tuna,<sup>4</sup> and R. E. P. Winpenny<sup>4,5</sup><sup>1</sup>Department of Molecular Sciences Applied to Biosystems, DISMAB, Università degli Studi di Milano, I-20134 Milan, Italy<sup>2</sup>Department of Physics "A. Volta" and CNISM-INFN unit, Università di Pavia, I-27100 Pavia, Italy<sup>3</sup>Centro S3, CNR-Istituto di Nanoscienze, I-41125 Modena, Italy<sup>4</sup>The Lewis Magnetism Laboratory, School of Chemistry, The University of Manchester, Oxford Road, Manchester M13 9PL, United Kingdom<sup>5</sup>The Photon Science Institute, The University of Manchester, Oxford Road, Manchester M13 9PL, United Kingdom

(Received 14 December 2009; revised manuscript received 18 February 2010; published 15 March 2010)

We present magnetic susceptibility, <sup>1</sup>H nuclear magnetic resonance (NMR) spectra, spin-spin- and spin-lattice-relaxation rates data, collected in the temperature range 1.65 < *T* < 300 K at two applied magnetic fields *H* = 0.35 and 1.5 T, on a single crystal of Cr<sub>7</sub>Fe heterometallic molecular nanomagnet. From a simple analysis of the magnetic susceptibility data, we deduce that the ring has a magnetic total spin *S<sub>T</sub>* = 1/2 ground state and Cr-Cr antiferromagnetic (AFM) exchange interactions comparable to similar Cr<sub>7</sub>M heterometallic rings. The proton NMR data indicate that the main coupling between nuclei and electronic moments is of dipolar origin. The spin-lattice-relaxation rate behavior is qualitatively explained by a model which assumes a single-correlation time as used previously for homometallic AFM rings. The direct comparison of the relaxation data in Cr<sub>7</sub>Fe and Cr<sub>8</sub> shows a substantial change in the spin dynamics as the result of Fe replacing one Cr ion. The difference is attributed to the change in the elastic properties of the sample with Fe substitution and/or to the multi-Lorentzian behavior of the spin-spin correlation function resulting from the presence of inequivalent ions in the heterometallic ring.

DOI: 10.1103/PhysRevB.81.104408

PACS number(s): 76.60.Es, 75.50.Xx

## I. INTRODUCTION

The discovery of transition-metal complexes (magnetic molecules) which act as individual nanomagnets has opened a new field of research in the physics community.<sup>1-3</sup> In a nanomagnet the magnetic core of the individual molecules is shielded from each other by a shell of bulky organic ligands so that the intermolecular magnetic interactions (usually dipolar) are very weak compared to the intramolecular exchange interactions.<sup>3</sup> Therefore, measurements in these crystalline samples reflect the magnetic properties of one isolated molecule. As a result, these zero-dimensional nanomagnetic systems have become a unique platform for studying spin dynamical effects.

Antiferromagnetic (AFM) rings are magnetic molecules comprising an even number (*N*) of uniformly spaced paramagnetic metal ions arranged as a planar ring. If the ring contains just one type of magnetic ion then it is called homometallic (homonuclear), e.g., Cr<sub>8</sub>, which is characterized by a singlet zero-field ground state with total spin *S<sub>T</sub>* = 0.<sup>4</sup> Recently it has been recognized that the substitution in the ring of one paramagnetic ion with a nonmagnetic ion or with an ion with different magnetic moment can generate heterometallic AFM rings, which reveal new interesting physics both in the static and in the dynamical magnetic properties.<sup>5</sup> One obvious consequence is the change in the ground state from a singlet with *S<sub>T</sub>* = 0 to a magnetic state with *S<sub>T</sub>* ≠ 0. Furthermore, the local spin moment in the ground state becomes redistributed in a staggered and nonuniform way.<sup>6</sup> Finally the ground state of these heterometallic AFM rings could be used for implementation of qubits for quantum computation and the synthesis of heterometallic rings con-

taining coupled molecules could lead to quantum entanglement.<sup>7,8</sup> The investigation of the magnetic properties and particularly of the spin dynamics which can affect the quantum coherence or decoherence in these heterometallic rings is thus of paramount importance.

Nuclear magnetic resonance (NMR) has been proved to be an efficient local probe of both static and dynamic properties of magnetic molecules<sup>9</sup> and used in combination with thermodynamic magnetization measurements can give a good characterization of the magnetic properties and the spin dynamics in the heterometallic rings. In this paper we investigate the heterometallic molecular magnetic ring of formula (C<sub>4</sub>H<sub>9</sub>)<sub>2</sub>NH<sub>2</sub>Cr<sub>7</sub>Fe<sup>2+</sup>F<sub>8</sub>(O<sub>2</sub>CCMe<sub>3</sub>)<sub>16</sub>, in brief Cr<sub>7</sub>Fe. In the ground state, this ring is characterized by a total spin *S<sub>T</sub>* = 1/2 resulting from AFM interactions *J* and *J'* between two Cr<sup>3+</sup>, *s* = 3/2, ions and between Cr<sup>3+</sup> and Fe<sup>2+</sup>, *s* = 2, ions, respectively.

The paper is organized as follows. In Sec. II we summarize briefly the synthesis of the compounds and their crystal structure. In Sec. III we present the experimental results and data analysis for the magnetization. In Sec. IV we present in separate sections the static and the dynamic NMR results with their analysis. Section V contains a comparison between the heterometallic ring Cr<sub>7</sub>Fe and the homometallic ring Cr<sub>8</sub> and a discussion of the results obtained with the different techniques and the relevant conclusions. We will show that the spin dynamics in the heterometallic ring Cr<sub>7</sub>Fe differs substantially from the one of homometallic Cr<sub>8</sub>.

## II. SYNTHESIS AND STRUCTURE

The homometallic ring, [Cr<sub>8</sub>F<sub>8</sub>(O<sub>2</sub>CCMe<sub>3</sub>)<sub>16</sub>], has been widely studied,<sup>10</sup> both because of its magnetic properties<sup>11</sup>

AMIRI *et al.*

PHYSICAL REVIEW B 81, 104408 (2010)

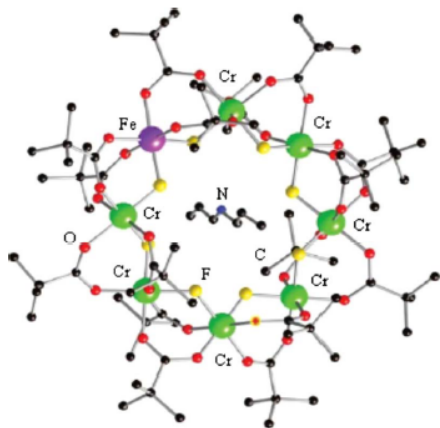


FIG. 1. (Color online) Structure of  $(C_4H_9)_2NH_2Cr_7Fe^{2+}F_8(O_2CCMe_3)_{16}$  nanomagnet, in brief  $Cr_7Fe$ .

and because it can act as a host for heterometallic substitution.<sup>12</sup> In order to prepare a heterometallic ring one of the chromium ions should be substituted with a metallic ion.<sup>5</sup> For this,  $CrFe_3 \cdot 4H_2O$  (5.0 g, 27.6 mmol), di-*n*-butylamine (1.43 g, 11.1 mmol), and pivalic acid (14.0 g, 137.1 mmol) were heated to 140 °C while stirring for 1.5 h in an open teflon flask. Then the following procedures were performed under nitrogen atmosphere. The  $FeCl_2 \cdot 4H_2O$  (1.5 g, 7.5 mmol) was added to the mixture and the temperature was increased to 160 °C for 5 h, at which point a green crystalline product had formed. The flask was cooled to room temperature and acetone (50 mL) was added while stirring. The product was collected by filtration, washed with a large quantity of acetone, then dried *in vacuo* and then purified by column chromatography on silica gel using as the eluent toluene. The compound  $(C_4H_9)_2NH_2Cr_7Fe^{2+}F_8(O_2CCMe_3)_{16}$  elutes as the second fraction then crystallized by evaporation of the toluene. Yield: 6.04 g (66%, based on Cr). Elemental analysis calculated (%) for  $C_{88}H_{164}Cr_7F_8FeNO_{32}$ : Cr 15.69, Fe 2.41, C 45.56, H 7.12, N 0.60, and F 6.55; found: Cr 15.35, Fe 2.37, C 46.88, H 7.10, N 0.52, and F 6.51. Electrospray-MS (THF/MeOH)  $m/z$ :  $-2188[Cr_7FeF_8(O_2CCMe_3)_{16}]^-$ ;  $+2320[M^+]$ ;  $+2342[M+Na]^+$ .

The schematic structure of  $Cr_7Fe$  ring is shown in Fig. 1. The position of protons in the molecule is important for our  $^1H$  NMR study. Around each Cr there are three closest  $CH_3$  groups. For each  $CH_3$  there are three Cr-H distances: (i) shortest, fall in the range of 4.07–4.32 Å, (ii) middle, fall in the range of 4.48–4.93 Å, and (iii) longest, fall in the range of 5.47–5.57 Å. Other protons are located even further away from Cr ions.

### III. MAGNETIC SUSCEPTIBILITY

Measurements of magnetic susceptibility, i.e.,  $\chi \approx (M/H)_{H \rightarrow 0}$  ( $\equiv M/H$  for paramagnets, like our case) have been performed with a superconducting quantum interference device (SQUID) magnetometer on  $Cr_7Fe$  single crys-

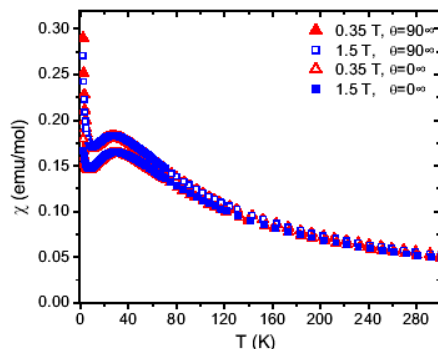


FIG. 2. (Color online) Magnetic susceptibility vs temperature in a single-crystal sample of  $Cr_7Fe$  at the same external magnetic fields used in NMR, both parallel (angle between  $H$  and  $c$  axis:  $\theta = 0^\circ$ ) and perpendicular ( $\theta = 90^\circ$ ) to the molecular axis.

als, at two different external magnetic fields  $H = 0.35$  and  $1.5$  T, applied parallel and perpendicular to the molecular  $c$  axis. The  $c$  axis is perpendicular to the plane formed by the magnetic ions, i.e., to the plane of the ring. The results, corrected for the small single-ion diamagnetism ( $5.8 \times 10^{-4}$  emu/mol), are shown in Fig. 2. The results should be analyzed in terms of a Heisenberg Hamiltonian including the AFM coupling  $J$  between the seven nearest-neighbor  $Cr^{3+}$  ( $s = 3/2$ ) and a different coupling  $J'$  between the two pairs of  $Cr^{3+}$ - $Fe^{2+}$  where  $Fe^{2+}$  carries a spin  $s = 2$ . Small single-ion anisotropy may be also present as revealed by the susceptibility data collected at two orientations of the external field (see Fig. 2).

For a detailed and complete characterization of the magnetic structure and properties, neutron-scattering data would be necessary as in the case of  $Cr_7Ni$  (Ref. 13). A preliminary simplified analysis is, however, sufficient for the purpose of the present work which is mostly focused on the spin dynamics obtained by NMR measurements. For this purpose we show in Fig. 3 a plot of the effective Curie constant  $C = \chi T$  as a function of temperature.

Both in Figs. 2 and 3 there appear to be a small difference in the susceptibility between the parallel and the perpendicular orientations of the external magnetic field. We will neglect this anisotropy in the analysis which follows. The upper dashed line ( $C = 16.32$ ) in Fig. 3 corresponds to the value of the Curie constant  $C = Ng^2\mu_B^2[s(s+1)]/3k_B$  where it was assumed for the gyromagnetic ratio  $g = 2$  for both  $Cr^{3+}$  and  $Fe^{2+}$  ions while the spin  $s$  is  $3/2$  and  $2$ , respectively. The experimental data in Fig. 3 lie below the high- $T$  limit as expected in presence of AFM coupling but seem to bend towards the limit calculated for noninteracting ions with the given spin  $s$  value and negligible single-ion anisotropy ( $g = 2$ ). The low-temperature dashed line represents the Curie constant for a single spin,  $S_7 = 1/2$ , with  $g = 2$ . Again the agreement is good indicating that the ground state is a magnetic state,  $S_7 = 1/2$ , with small anisotropy.

In Fig. 4 we plot the inverse susceptibility vs temperature in order to derive an estimate of the AFM coupling constants  $J$  and  $J'$  between nearest-neighbor magnetic ions in the ring.

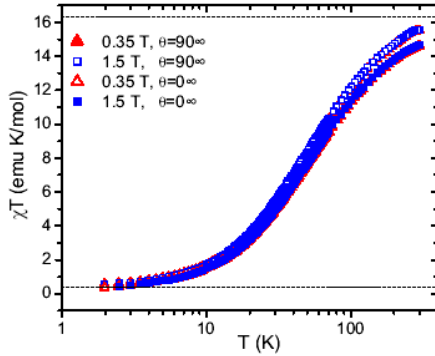


FIG. 3. (Color online) The product of the susceptibility times temperature plotted vs temperature in  $\text{Cr}_7\text{Fe}$  at two external magnetic fields both parallel ( $\theta=0^\circ$ ) and perpendicular ( $\theta=90^\circ$ ) to the molecular axis. The dashed lines are the limiting behaviors at high and low temperatures, respectively, expected for a simple AFM ring model (see text).

The high-temperature results can be fitted reasonably well by using a Curie-Weiss law for the susceptibility, i.e.,  $1/\chi = [T + \Theta]/C$ , with  $C=16.32$  as calculated above for the high- $T$  limit in Fig. 3 and choosing the only fitting parameter to be  $\Theta = -32 \pm 2$  K.

Assuming that the dominant contribution to the Curie-Weiss temperature  $\Theta$  comes from the more abundant  $\text{Cr}^{3+}$  ions and using the molecular field approximation expression  $\Theta = [2zs(s+1)J]/3k_B$ , with the number of nearest neighbors of a given moment being  $z=2$ , one gets an AFM coupling constant  $J/k_B = -6.4 \pm 0.4$  K.

The exchange constant  $J$  derived above corresponds to a Hamiltonian for the Heisenberg model written as  $\sum_{i>j} -2J_{ij}\vec{S}_i \cdot \vec{S}_j$ . Since the values of  $J$  given in molecular nanomagnets are normally referred to a Hamiltonian written as  $\sum_{i>j} J_{ij}\vec{S}_i \cdot \vec{S}_j$ , we multiply our value by two and change sign in order to compare it with the  $J$  constants given in the literatures for AFM rings. For other heterometallic rings such as  $\text{Cr}_7\text{Zn}$ ,  $\text{Cr}_7\text{Ni}$ , and  $\text{Cr}_7\text{Mn}$  as well as for the homometallic

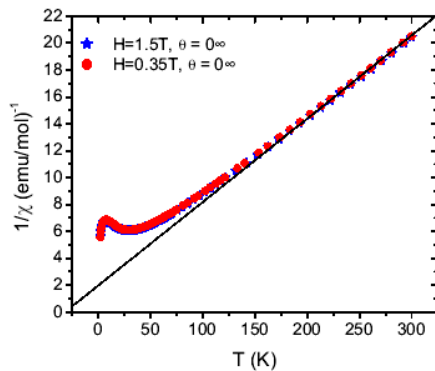


FIG. 4. (Color online) Inverse susceptibility vs  $T$  in  $\text{Cr}_7\text{Fe}$  with the external magnetic fields parallel ( $\theta=0^\circ$ ) to the molecular axis; the solid line is a fit according to the Curie-Weiss law (see text).

ring  $\text{Cr}_8$  (Refs. 13 and 14) the exchange constant between adjacent Cr ions is found to be approximately the same, namely,  $J_{\text{Cr-Cr}} = 17 \pm 0.5$  K. The value estimated above from the high-temperature Curie-Weiss law for  $\text{Cr}_7\text{Fe}$  is smaller, i.e.,  $J = 13 \pm 1$  K, but this can be due to the neglecting of Cr-Fe exchange coupling, which could be smaller than the Cr-Cr one, and to the approximate model we have used for the susceptibility.

#### IV. NMR EXPERIMENTAL RESULTS AND ANALYSIS

Proton NMR measurements on  $\text{Cr}_7\text{Fe}$  powder sample (single crystals are too small to give detectable signals) including nuclear spin-lattice-relaxation time ( $T_1$ ) and spin-spin-relaxation time ( $T_2$ ) were performed using a standard TecMag Fourier transform pulse NMR spectrometer with short  $\pi/2$ - $\pi/2$  radio frequency pulses (1.9–2.2  $\mu\text{s}$ ) in the temperature range  $1.65 < T < 300$  K at two applied magnetic fields:  $H=0.35$  and  $1.5$  T. In order to study the temperature dependence of the relaxation times, we used two different cryostats: (a) a continuous flow cryostat in the temperature range  $4.2 < T < 300$  K and (b) a bath cryostat in the temperature range  $1.65 < T < 4.2$  K. Fourier transform of half of the echo spin signal yields the NMR spectrum in the case where the whole line could be irradiated with one radio frequency (rf) pulse.

The nuclear spin-lattice-relaxation rate  $T_1^{-1}$  was determined by monitoring the recovery of the longitudinal nuclear magnetization measured by the spin echo amplitude obtained with  $\pi/2$ - $\pi/2$  Hahn echo reading sequence, following a saturating comb of rf pulses. The length of the rf saturation comb was chosen to ensure the best initial saturation conditions, which vary depending on temperature and resonance frequency.

To perform the spin-spin-relaxation time experiments, a standard solid echo ( $\pi/2$ - $\pi/2$ ) pulse sequence was used. For all temperatures a monoexponential behavior was observed so that a well-defined spin-spin-relaxation time parameter  $T_2$  was extracted from the decay of the transverse proton magnetization.

On the other hand the recovery after saturation of the longitudinal component of the nuclear magnetization was found to follow a nonexponential law. Thus we obtained  $T_1$  values using the slope of the tangent at the origin of the semilogarithmic recovery plot of the nuclear magnetization. This corresponds to measure the average value of the relaxation rate  $T_1^{-1}$  over all the nuclei irradiated.<sup>9</sup> The recovery of the nuclear magnetization below 3.8 K displays an initial fast recovery followed by a very slow recovering tail. In view of the difficulty in interpreting the recovery curve we decided not to include in the presentation the very low-temperature data.

##### A. Proton NMR spectra

The proton NMR linewidth full width at half maximum (FWHM) or  $\Delta\nu$  is shown in Fig. 5(a) as a function of temperature at two values of the external magnetic field. The shape and width of the proton NMR spectrum are determined



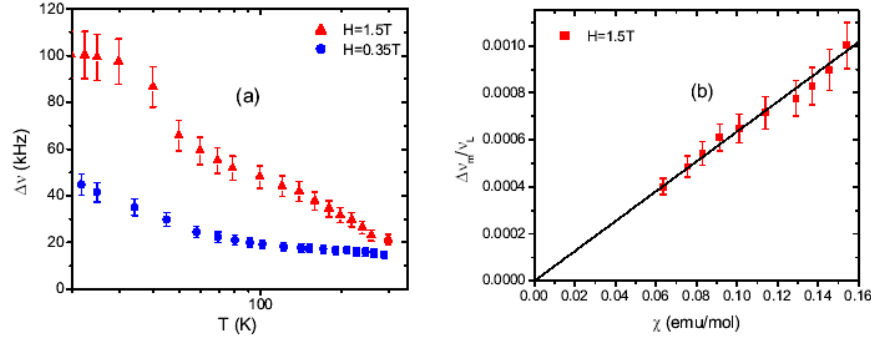


FIG. 5. (Color online) (a) Proton linewidth vs temperature in  $\text{Cr}_7\text{Fe}$  at two different external magnetic fields; (b) inhomogeneous part of the linewidth, extracted as explained in the text, plotted vs magnetic susceptibility with temperature as implicit parameter.

by two main interactions: (i) the nuclear-nuclear dipolar interaction and (ii) the hyperfine interaction of the proton with the neighboring magnetic ions. The first interaction generates a temperature- and field-independent broadening, which depends on the hydrogen distribution in the molecule and is thus similar in all molecular magnets independently of their magnetic properties.<sup>9</sup>

The hyperfine field resulting from the interaction of protons with local magnetic moments of  $\text{Cr}^{3+}$  ( $\text{Fe}^{2+}$ ) may contain contributions from both the classical dipolar interaction and from a direct contact term due to the hybridization of proton  $s$ -wave function with the  $d$ -wave function of magnetic ions. The dipolar contribution has tensorial character and is thus responsible for the inhomogeneous width of the line due to the random distribution of orientations in a powder sample and to the many nonequivalent proton sites in the single crystal. The contact interaction, on the other hand, has scalar form and it can generate a shift of the line for certain groups, each one constituted by equivalent protons in the molecule. Since we have not observed any measurable shift of the proton NMR line from the Larmor frequency, we can conclude that the dominant hyperfine interaction is of dipolar origin.

In the usual simple Gaussian approximation for the NMR line shape, the linewidth is proportional to the square root of the second moment, which in turn is given by the sum of the second moments due to the two interactions described above<sup>15</sup>

$$\text{FWHM} \propto \sqrt{\langle \Delta\nu^2 \rangle_d + \langle \Delta\nu^2 \rangle_m}, \quad (1)$$

where  $\langle \Delta\nu^2 \rangle_d$  is the intrinsic second moment due to nuclear-nuclear dipolar interactions, and  $\langle \Delta\nu^2 \rangle_m$  is the second moment of the local frequency-shift distribution (due to nearby electronic moments) at the different proton sites of all molecules. The proportionality constant in Eq. (1) is of the order of one depending on the exact shape of the spectrum. We will assume it to be one for simplicity. The relation between  $\langle \Delta\nu^2 \rangle_m$  and the local  $\text{Cr}^{3+}$ ,  $\text{Fe}^{2+}$  electronic moments for a simple dipolar interaction is given by<sup>9,15</sup>

$$\begin{aligned} \langle \Delta\nu^2 \rangle_m &= \frac{1}{N} \sum_R \left( \sum_{i \in R} \langle \nu_{R,i} - \nu_0 \rangle_{\Delta t} \right)^2 \\ &= \frac{\gamma^2}{N} \sum_R \left[ \sum_{i \in R} \sum_{j \in R} \frac{A(\theta_{i,j})}{r_{i,j}^3} \langle m_{z,j} \rangle_{\Delta t} \right]^2, \end{aligned} \quad (2)$$

where  $R$  labels different molecules,  $i$  and  $j$  span different protons and  $\text{Cr}^{3+}$  ions within each molecule, and  $N$  is the total number of probed protons. In Eq. (2),  $\nu_{R,i}$  is the NMR resonance frequency of nucleus  $i$  and  $\nu_L = (\gamma/2\pi)H = \gamma H$  is the bare Larmor resonance frequency. The difference between the two resonance frequencies represents the shift for nucleus  $i$  due to the local field generated by the nearby moments  $j$ . The angular-dependent dipolar coupling constant between nucleus  $i$  and electronic moment  $j$  is  $A(\theta_{i,j})$  and  $r_{i,j}$  is the corresponding distance.  $\langle m_{z,j} \rangle$  is the component of the Cr (Fe) moment  $j$  in the direction of the applied field, averaged over the NMR data acquisition time. In a simple paramagnet one expects  $\langle m_{z,j} \rangle = \frac{\chi}{N_A} H$  with  $\chi$  the SQUID susceptibility in emu/mole,  $N_A$  Avogadro's number, and  $H$  the applied field.<sup>16</sup>

We can thus write approximately

$$\sqrt{\langle \Delta\nu^2 \rangle_m} = A'_z \chi H = A'_z \chi \nu / \gamma = A_z \chi \nu / N_A, \quad (3)$$

where  $A'_z$  and  $A_z$  are the dipolar coupling constants averaged over all protons and all orientations expressed in different units and  $\nu$  is the resonance frequency. The experimental results for the magnetic contribution to the linewidth are plotted as a function of the magnetic susceptibility in Fig. 5(b) for  $\text{Cr}_7\text{Fe}$ . The linear relation predicted by Eq. (3) is well verified. In the fit of Fig. 5(b) we have neglected the nuclear dipolar contribution in Eq. (1) since at 1.5 T the inhomogeneous contribution to the width is already dominant. The values obtained from the fit for the average dipolar coupling is  $A'_z = 27 \text{ Hz}/(\text{G emu mol})$  corresponding to an hyperfine constant  $A_z = (N_A/\gamma)A'_z = 3.82 \times 10^{21} \text{ cm}^{-3}$ . This hyperfine constant corresponds to the dipolar interaction of a nucleus of  $^1\text{H}$  with the electronic moment of a  $\text{Cr}^{3+}$  ion located at a distance of  $r = 5 \text{ \AA}$  or more. This distance is on the order of magnitude of the longest distances between protons and Cr ions in the molecule as seen from the structural data

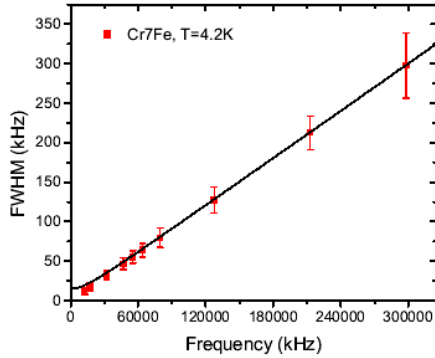


FIG. 6. (Color online) Proton NMR linewidth vs resonance frequency in  $\text{Cr}_7\text{Fe}$  at liquid Helium temperature. The full line is a fit according to Eqs. (1) and (3) as explained in the text.

in Sec. II. This agrees with the notion that the NMR signal arises mainly from the protons furthest away and thus least magnetically coupled to the Cr(Fe) magnetic moments.

On lowering the temperature one expects a slowing down of the local moment fluctuations and for temperatures sufficiently low a freezing of the local moment on the time scale of the NMR hyperfine interactions which is on the order of  $10^{-5}$  s. When this freezing occurs, one expects that the NMR width is no longer proportional to the external applied field.<sup>9</sup> In order to check the existence or not of freezing of the local moment at low temperature we have measured the field dependence of the linewidth at  $T=4.2$  K. The results are shown in Fig. 6.

As can be seen from the Fig. 6 the linewidth is still proportional to the external field at Helium temperature, as predicted by Eq. (3), indicating that the fluctuations are still fast and the system behaves as a normal paramagnet. The data can be fitted using Eqs. (1) and (3) with  $\langle \Delta \nu^2 \rangle_H = 15$  KHz and  $A'_z \chi / \gamma = 0.001$  Hz/G. By using the value of the susceptibility at 4.2 K from Fig. 2, i.e.,  $\chi = 0.15$  emu/mol, one gets  $A'_z = 28$  Hz/(G emu mol) corresponding to  $A_z = (N_A / \gamma) A'_z = 3.9 \times 10^{21}$  cm<sup>-3</sup> in good agreement with the value obtained from the fit of the data in Fig. 5, as expected since the hyperfine interaction should be almost temperature independent.

### B. Temperature dependence of $T_2^{-1}$ and wipe-out effect

The temperature dependence of the proton transverse relaxation rate as a function of temperature is shown in Fig. 7. As seen in the figure,  $T_2^{-1}$  increases on lowering the temperature. The shortening of  $T_2$  is accompanied by a loss of signal intensity due to the limit of detectability of the NMR signal for short  $T_2$  values (wipe-out effect) as is discussed below. The apparent maximum observed around 7–8 K is due to the fact that below 10 K the signal loss is severe and the measured  $T_2$  is not representative of all nuclei but only of a small fraction having longer  $T_2$  values.

The signal loss observed on lowering the temperature is described in Fig. 8. The wipe-out effect is a rather general phenomenon in NMR and has been observed previously in

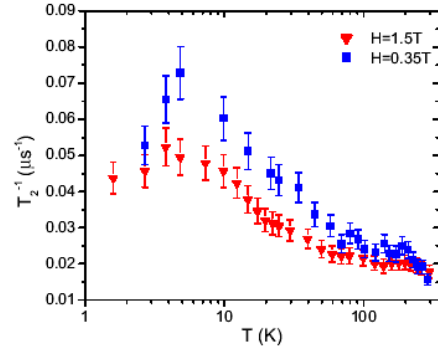


FIG. 7. (Color online) Proton spin-spin-relaxation rate  $T_2^{-1}$  as a function of temperature at two values of the external magnetic field for a polycrystalline sample of  $\text{Cr}_7\text{Fe}$ .

other systems such as spin glasses,<sup>17</sup> stripe-ordered cuprates,<sup>18</sup> and colossal magnetic resistance manganites.<sup>19</sup> In particular a loss of  $^1\text{H}$  NMR signal on lowering the temperature has been observed previously in other molecular nanomagnets with a magnetic ground state and in that case also the wipe-out effect is correlated to an enhancement of the spin-spin-relaxation rate as in the present case.<sup>9,20</sup>

A quantitative analysis of the wipe-out effect was done successfully in  $\text{Mn}_6$ ,  $\text{Fe}_4$ , and  $\text{Fe}_{19}$  molecular clusters<sup>20</sup> by using a simple and intuitive model which captures the main physical characteristics of the problem. We are going to analyze the wipe-out effect in  $\text{Cr}_7\text{Fe}$  by using the same model, which we summarize briefly in the following.

We assume that the dominant contribution to  $T_2^{-1}$  is coming from the dephasing due to the hyperfine interactions with the exchange coupled magnetic ions. In the weak collision, fast-motion approximation, the relaxation rate can be expressed in terms of the spectral density of the fluctuating hyperfine field at zero frequency as<sup>15,21</sup>

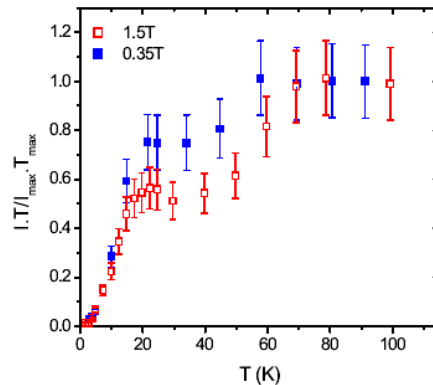


FIG. 8. (Color online) Proton NMR signal intensity multiplied by temperature plotted as a function of temperature for two external magnetic fields in polycrystalline  $\text{Cr}_7\text{Fe}$ . The decrease from the maximum value indicates that the observed signal at lower temperatures does not arise from all the nuclei present in the sample.

$$T_2^{-1} = \gamma_N^2 \langle \delta H_z^2 \rangle \tau(T) \propto \gamma_N^2 \frac{\langle \delta \mu_c^2 \rangle}{r^6} \tau(T), \quad (4)$$

where  $\delta H_z$  is the local longitudinal fluctuating field originating from a magnetic moment at a distance  $r$  from the proton spin, and  $\tau$  gives the correlation time, which is solely determined by the dynamics of the exchange coupled magnetic ions and can thus be temperature dependent. The central idea is that, on lowering the temperature, the correlation time  $\tau(T)$  becomes progressively longer and thus the relaxation rate  $T_2^{-1}$  becomes shorter [see Eq. (4)] until eventually it reaches the limiting value  $\tau_d = 10^{-5}$  s, which we estimate to be the limit of detectability of the NMR signal in our experimental setup. Since the dipolar hyperfine field and thus  $T_2$  depends on the distance  $r$  from the magnetic ions, the limiting value  $\tau_d$  is reached progressively by all protons, with the ones closer being wiped out first.

To describe the wipeout we assume one central ion surrounded by a large number of protons homogeneously distributed at distances up to a maximum value  $R^*$ , the number density being  $\rho = n_0 / [(4\pi/3)(R^*)^3]$ , where  $n_0$  is the total number of protons in each molecule. Being in the regime of the wipe-out effect, and for a given temperature or value of the correlation time  $\tau(T)$ , there is a number of protons having a  $T_2^{-1}$  value larger than the critical value of  $10^5$  s $^{-1}$ . These protons are enclosed within a notional sphere of radius  $r_c(T)$  and do not contribute to the measured signal intensity. On the other hand, the protons located outside this sphere can be detected and their number  $n(T)$  can be written as

$$n(T) = n_0 \left[ 1 - \left( \frac{r_c}{R^*} \right)^3 \right]. \quad (5)$$

The value of the critical radius  $r_c$  in Eq. (5) can be obtained from Eq. (4) by setting  $T_2^{-1} = \tau_d^{-1}$ . Then one can express  $n(T)$  in terms of the temperature-dependent correlation time  $\tau(T)$  as

$$\frac{n(T)}{n_0} = 1 - \frac{\gamma_N \sqrt{\langle \delta \mu_c^2 \rangle} \sqrt{\tau_d}}{(R^*)^3 \sqrt{\tau(T)}}. \quad (6)$$

In order to use Eq. (6) to fit the data in Fig. 8 one has to make some educated guess about the functional form of the temperature dependence of the correlation time  $\tau(T)$ . Previous NMR studies in a series of AFM rings have shown that the temperature dependence of the correlation time (extracted from the spin-lattice-relaxation data) has the form of a power law  $\tau(T) = cT^{-3.5}$  for all the rings.<sup>22</sup> Therefore we adopt the same expression to fit the wipe-out data also for Cr<sub>7</sub>Fe in Fig. 9, using Eq. (6). The two fitting parameters are the constant  $c = 4 \times 10^{-6}$  s/rad and  $\sqrt{\langle \delta \mu_c^2 \rangle} (R^*)^{-3} = 300$  G. The result of the fit is shown in Fig. 9 for the low-field data in which the wipe-out effect is more pronounced.

In view of the crudeness of the model the agreement appears satisfactory since the theoretical curve reproduces well the sudden drop in intensity occurring below 20 K. A qualitative confirmation of the model and of the fitting parameters used here will come from the analysis of the spin-lattice-relaxation rate  $T_1^{-1}$  presented in the next section. Finally it should be noted that the assumption of a single correlation

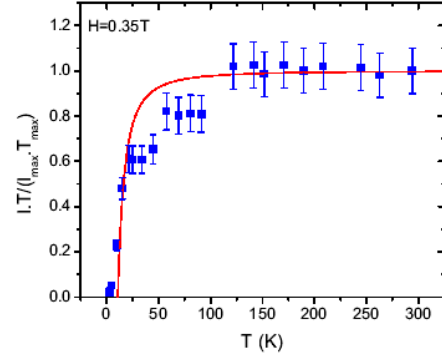


FIG. 9. (Color online) Fit of the wipe-out effect in Cr<sub>7</sub>Fe using Eq. (6) with the following fitting parameters:  $c = 4 \times 10^{-6}$  s/rad and  $\sqrt{\langle \delta \mu_c^2 \rangle} (R^*)^{-3} = 300$  G.

time and of the consequent temperature-dependence law for  $\tau(T)$  may be an approximation in heterometallic rings worse than in homometallic rings and clusters since in the first case one expects multiexponential behavior of the electron spin-correlation function due to the size distribution of local moments in the ring.

### C. Temperature dependence of $T_1^{-1}$

The temperature dependence of the proton average spin-lattice-relaxation rate is shown in Fig. 10 for two values of the external magnetic field. The main qualitative feature is the presence of a field-dependent peak at low temperature. This peak is typical of all molecular magnetic homometallic rings and clusters.<sup>9,22</sup> A quantitative theoretical explanation of the peak was given before in terms of the relaxation of the magnetization due to spin-phonon interactions.<sup>23</sup> A subsequent theoretical analysis has provided an explanation for the origin of the universal behavior of the slowing down of the magnetization fluctuations, which is responsible for the observed peak.<sup>24</sup> In this experimental paper we analyze the data

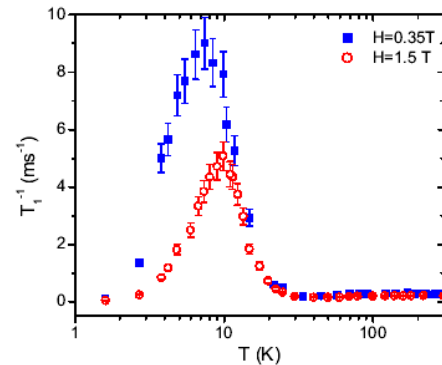


FIG. 10. (Color online) Proton average spin-lattice-relaxation rate plotted vs temperature for two external magnetic fields in a Cr<sub>7</sub>Fe powder sample.

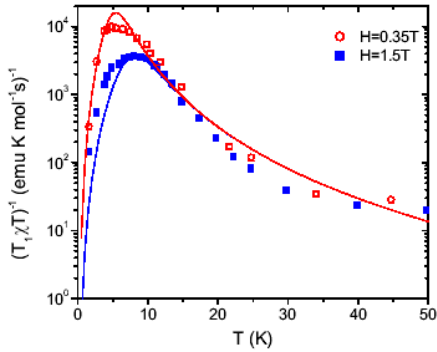


FIG. 11. (Color online) Proton spin-lattice-relaxation rate divided by  $\chi T$  vs temperature for  $\text{Cr}_7\text{Fe}$  at two values of the external field. The curves are fitted using Eq. (7) with  $A=3.0 \times 10^9 \text{ (ms}^{-1} \text{ rad)}^2$ , a fitting parameter obtained from the high field data, and  $\omega_c=2.5 \times 10^3 T^{3.5}$  as obtained from the fit of the wipe-out effect in FIG. 9.

in a phenomenological way using a single-correlation frequency to describe the electronic spin dynamics in the same way as done in Ref. 22. This will allow us to capture the relevant changes occurring in the spin dynamics when comparing the results in the heterometallic ring  $\text{Cr}_7\text{Fe}$  with the homometallic one  $\text{Cr}_8$ .

In order to fit the data in Fig. 10 we refer to the simple expression for the relaxation rate, which can be obtained from the original Moriya theory of nuclear relaxation in paramagnets<sup>15,21</sup> under some simplifying assumptions, the main one being that the electronic spin dynamics is dominated by a single-correlation frequency, which drives the longitudinal electron spin fluctuations.<sup>22,23</sup> The expression is

$$\frac{1}{T_1} = A' \frac{\omega_c(T)}{\omega_c^2(T) + \omega_L^2} = A\chi T \frac{\omega_c(T)}{\omega_c^2(T) + \omega_L^2}, \quad (7)$$

where  $A\chi T$  is the average square of the fluctuating transverse hyperfine field,  $\omega_L$  is the proton Larmor frequency,  $\omega_c(T) = 1/\tau(T)$  is the characteristic frequency, and  $\chi$  is the uniform magnetic susceptibility expressed in emu/mole. The temperature dependence of  $\chi T$  (see Fig. 3) represents the amplitude of the local effective moments. Thus in order to extract the dynamics, it is best to plot  $(T_1\chi T)^{-1}$  versus temperature, as shown in Fig. 11. The data can now be fitted with two fitting parameters:  $A$  which represents the average square of the nuclear electron hyperfine fluctuations and  $\omega_c(T)$  which can be assumed to be of the form  $\omega_c(T) = \tau(T)^{-1} = c^{-1}T^{3.5}$  to be consistent with the wipe-out analysis of the previous paragraph and the results in other AFM rings.<sup>22</sup>

As one can see in Fig. 11, the theoretical curve given by Eq. (7) reproduces qualitatively the relaxation data by using only one single fitting parameter, namely,  $A=3.0 \times 10^9 \text{ (ms}^{-1} \text{ rad)}^2$  while for the correlation frequency we used the value obtained from the analysis of the wipe-out effect. One should note that a good fit for temperatures less than 10 K is impossible anyway since the data at low temperature are affected by the wipe-out effect and thus they do

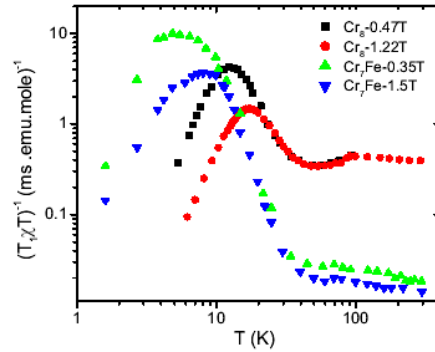


FIG. 12. (Color online) Comparison of the proton relaxation data in  $\text{Cr}_7\text{Fe}$  with the published data in homometallic ring  $\text{Cr}_8$  (Ref. 22).

not represent an average relaxation rate over all protons of the molecule. The value of the squared hyperfine interaction  $A$  can be compared with the hyperfine interaction obtained from the fit of the linewidth data in Figs. 5 and 6. To do so one has to convert the units by recalling that  $A_{\pm}^2 = A/4\pi(\hbar\gamma_n\gamma_e)^2 = 1.44 \times 10^{44} \text{ cm}^{-6}$  corresponding to  $A_{\pm} = 1.2 \times 10^{22} \text{ cm}^{-3}$ . This value for the transverse hyperfine field,  $A_{\pm}$ , compares well with the value obtained from the linewidth for the longitudinal hyperfine field  $A_z$ . This is a confirmation that both the temperature-dependent inhomogeneous broadening and the spin-lattice-relaxation are driven by the nuclear electron dipolar interaction.

As anticipated in the previous section, it must be remarked that two assumptions made here, based on previous work in homometallic AFM rings, could be subject to criticism. One regards the assumption of a single-correlation function since it was found that in heterometallic rings, particularly in the temperature region of the peak in  $T_1^{-1}$ , the spin-spin-correlation function shows a multi-Lorentzian regime.<sup>25,26</sup> The second assumption is the one leading to the proportionality of  $T_1^{-1}$  to  $\chi T$  [see Eq. (7)]. Both effects are the consequence of a nonuniform distribution of the local magnetic moments in the heterometallic rings.

## V. DISCUSSION AND CONCLUSIONS

One of the aims of the present work is to study the effect of the heterometallic substitution on the spin dynamics in the AFM ring. The strong effect on the spin dynamics as the result of the heterometallic substitution of one Cr atom with a Fe atom in the ring can be seen directly by comparing the proton relaxation rates in  $\text{Cr}_7\text{Fe}$  and in  $\text{Cr}_8$  at similar values of the external magnetic fields, as shown in Fig. 12. As can be seen from the figure, at comparable values of the external magnetic field, the relaxation in heterometallic rings displays a maximum shifted by several degrees towards lower temperature compared with the data in the homometallic ring. Furthermore the results at high temperature ( $T > 40 \text{ K}$ ) differ by more than one order of magnitude.

Another more quantitative way to compare the spin dynamics in heterometallic and homometallic ring can be done



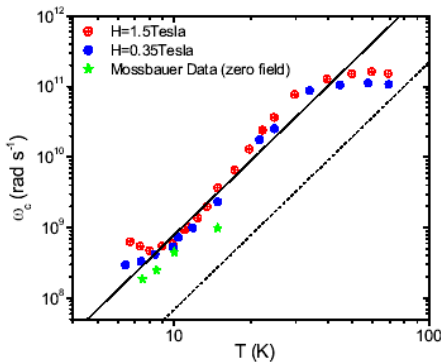


FIG. 13. (Color online) Correlation frequencies for  $\text{Cr}_7\text{Fe}$  extracted from the NMR experimental data compared with the ones obtained from Mossbauer data, Ref. 27, plotted vs temperature. The full line corresponds to the behavior  $\omega_c(T) = 2.5 \times 10^5 T^{3.5}$  rad/s obtained from the relaxation and wipe-out effect (see FIG. 11). The dashed line corresponds to the behavior found in  $\text{Cr}_8$ , i.e.,  $\omega_c(T) = 2.2 \times 10^4 T^{3.5}$  rad/s (Ref. 20).

By extracting the temperature dependence of the correlation frequency  $\omega_c(T)$  from the experimental NMR relaxation data  $T_1 \chi T^{-1}$  in Fig. 11 and using Eq. (7). As shown in Fig. 13 this correlation frequency follows rather well the power-law temperature dependence in the intermediate temperature range. At low temperature the results are not reliable because of the wipe-out effect while at high temperature the deviation is probably due to additional relaxation mechanisms not included in Eq. (7). The two important points are first, that our results obtained from proton NMR are in good agreement with the results obtained from the temperature dependence of the width of the Mossbauer spectrum<sup>27</sup> and second, that the correlation frequency in  $\text{Cr}_7\text{Fe}$  seems to be one order of magnitude higher than in  $\text{Cr}_8$  (dashed line in Fig. 13). This last point is important because it indicates that the heterometallic substitution has a strong effect on the spin dynamics.

By concluding we can say that the magnetic-susceptibility measurements show that the heterometallic ring  $\text{Cr}_7\text{Fe}$  displays a magnetic ground state with  $S_T = 1/2$ . The Cr-Cr exchange interaction as derived from the high-temperature magnetization data is found to be comparable to the one found in other heterometallic rings and in  $\text{Cr}_8$ , while the exchange interaction Cr-Fe cannot be determined from our data alone. The proton NMR inhomogeneous linewidth and the spin-lattice-relaxation rates are driven by the dipolar interaction of nuclei with the magnetic moment of the paramagnetic ion. The NMR results, including the wipe-out effect, can all be explained qualitatively with the known theoretical formula and in terms of a single temperature-dependent correlation frequency, which characterizes the spin dynamics in the AFM rings. The spin dynamics appears to be faster by one order of magnitude in  $\text{Cr}_7\text{Fe}$  with respect to  $\text{Cr}_8$ . This is a central result of the present work. According to previous theoretical work,<sup>23,24</sup> the correlation frequency for the electron spin fluctuations should be driven by spin-phonon interaction. It is remarked again that the simple description in terms of a single-correlation frequency [see Eq. (7)] may be inadequate in presence of a distribution of different sizes of local moments as expected in heterometallic rings. A refined theoretical analysis, now in progress, will take into account the exact expression of the hyperfine fluctuations, the different dominating correlation times and the changes in elastic properties with respect to homometallic rings.<sup>26</sup>

#### ACKNOWLEDGMENTS

The authors are grateful to P. Santini, S. Carretta, and G. Amoretti for useful discussions and suggestions. Thanks are also due to L. Cianchi, M. Lantieri, and G. Spina for discussions and making available the Mossbauer data before publication. The present work was done with financial support from the NoE-MAGMANET network of the European community and PRIN-200609518 project of the Italian Ministry of Research.

Corresponding author; houshang.amiri@unipv.it

<sup>1</sup>O. Kahn, *Molecular Magnetism* (VCH, Berlin, 1990); D. Gatteschi, R. Sessoli, and J. Villain, *Molecular Nanomagnets* (Oxford University Press, New York, 2006).

<sup>2</sup>I. S. Tupitsyn and B. Barbara, in *Magnetism: Molecules to Materials III*, edited by J. Müller and M. Drillon (Wiley, New York, 2002).

<sup>3</sup>E. del Barco, A. D. Kent, S. Hill, J. M. North, N. S. Dalal, E. M. Rumberger, D. N. Hendrickson, N. Chakov, and G. Christou, *J. Low Temp. Phys.* **140**, 119 (2005); W. Wernsdorfer, *Adv. Chem. Phys.* **99**, 118 (2001).

<sup>4</sup>M. Affronte, T. Guidi, R. Caciuffo, S. Carretta, G. Amoretti, J. Hinderer, I. Sheikin, A. G. M. Jansen, A. A. Smith, R. E. P. Winpenny, J. van Slageren, and D. Gatteschi, *Phys. Rev. B* **68**, 104403 (2003).

<sup>5</sup>F. K. Larsen, E. J. L. McInnes, H. ElMkami, J. Overgaard, S.

Piligkos, G. Rajaraman, E. Rentschler, A. A. Smith, G. M. Smith, V. Boote, M. Jennings, G. A. Timco, and R. E. P. Winpenny, *Angew. Chem., Int. Ed.* **42**, 101 (2003).

<sup>6</sup>E. Micotti, Y. Furukawa, K. Kumagai, S. Carretta, A. Lascialfari, F. Borsa, G. A. Timco, and R. E. P. Winpenny, *Phys. Rev. Lett.* **97**, 267204 (2006).

<sup>7</sup>F. Troiani, M. Affronte, S. Carretta, P. Santini, and G. Amoretti, *Phys. Rev. Lett.* **94**, 190501 (2005); F. Troiani, A. Ghirri, M. Affronte, S. Carretta, P. Santini, G. Amoretti, S. Piligkos, G. Timco, and R. E. P. Winpenny, *ibid.* **94**, 207208 (2005).

<sup>8</sup>G. A. Timco, S. Carretta, F. Troiani, F. Tuna, R. J. Pritchard, E. J. L. McInnes, A. Ghirri, A. Candini, P. Santini, G. Amoretti, M. Affronte, and R. E. P. Winpenny, *Nat. Nanotechnol.* **4**, 173 (2009).

<sup>9</sup>F. Borsa, A. Lascialfari, and Y. Furukawa, in *Novel NMR and EPR Techniques*, edited by J. Dolinsek, M. Viflan, and S. Zumer

MAGNETIC PROPERTIES AND SPIN DYNAMICS IN...

PHYSICAL REVIEW B **81**, 104408 (2010)

- (Springer, New York, 2006).
- <sup>10</sup>N. V. Gerbelev, Yu. T. Struchkov, G. A. Timco, A. S. Batsanov, K. M. Indrichan, and G. A. Popovich, *Dokl. Akad. Nauk SSSR* **313**, 1459 (1990).
- <sup>11</sup>J. van Slageren, R. Sessoli, D. Gatteschi, A. A. Smith, M. Hellwig, R. E. P. Winpenny, A. Comia, A.-L. Barra, A. G. M. Jansen, G. A. Timco, and E. Rentschler, *Chem.-Eur. J.* **8**, 277 (2002).
- <sup>12</sup>M. Affronte, A. Ghirri, S. Carretta, G. Amoretti, S. Piligkos, G. A. Timco, and R. E. P. Winpenny, *Appl. Phys. Lett.* **84**, 3468 (2004).
- <sup>13</sup>A. Bianchi, S. Carretta, P. Santini, G. Amoretti, Y. Furukawa, K. Kiuchi, Y. Ajiro, Y. Narumi, K. Kindo, J. Lago, E. Micotti, P. Arosio, A. Lascialfari, F. Borsa, G. Timco, and R. E. P. Winpenny, *J. Magn. Magn. Mater.* (to be published).
- <sup>14</sup>R. Caciuffo, T. Guidi, G. Amoretti, S. Carretta, E. Livioti, G. Amoretti, S. Piligkos, G. Timco, C. A. Muryn, and R. E. P. Winpenny, *Phys. Rev. B* **71**, 174407 (2005).
- <sup>15</sup>C. P. Slichter, *Principles of Magnetic Resonance* (Springer-Verlag, Berlin, 1996).
- <sup>16</sup>P. Khuntia, M. Mariani, M. C. Mozzati, L. Sorace, F. Orsini, A. Lascialfari, F. Borsa, C. Maxim, and M. Andruh, *Phys. Rev. B* **80**, 094413 (2009).
- <sup>17</sup>D. A. Levitt and R. E. Walstedt, *Phys. Rev. Lett.* **38**, 178 (1977).
- <sup>18</sup>A. W. Hunt, P. M. Singer, K. R. Thurber, and T. Imai, *Phys. Rev. Lett.* **82**, 4300 (1999).
- <sup>19</sup>G. Papavassiliou, M. Belesi, M. Fardis, and C. Dimitropoulos, *Phys. Rev. Lett.* **87**, 177204 (2001).
- <sup>20</sup>M. Belesi, A. Lascialfari, D. Procissi, Z. H. Jang, and F. Borsa, *Phys. Rev. B* **72**, 014440 (2005).
- <sup>21</sup>T. Moriya, *Prog. Theor. Phys.* **16**, 23 (1956).
- <sup>22</sup>S. H. Baek, M. Luban, A. Lascialfari, E. Micotti, Y. Furukawa, F. Borsa, J. van Slageren, and A. Comia, *Phys. Rev. B* **70**, 134434 (2004).
- <sup>23</sup>P. Santini, S. Carretta, E. Livioti, G. Amoretti, P. Carretta, M. Filibian, A. Lascialfari, and E. Micotti, *Phys. Rev. Lett.* **94**, 077203 (2005).
- <sup>24</sup>I. Rousochatzakis, A. Lauchli, F. Borsa, and M. Luban, *Phys. Rev. B* **79**, 064421 (2009).
- <sup>25</sup>A. Bianchi, S. Carretta, P. Santini, G. Amoretti, J. Lago, M. Corti, A. Lascialfari, P. Arosio, G. Timco, and R. E. P. Winpenny (unpublished); A. Bianchi *et al.*, *J. Magn. Magn. Mater.* (to be published).
- <sup>26</sup>P. Santini *et al.* (unpublished).
- <sup>27</sup>M. Lantieri, L. Cianchi, F. Del Giallo, P. Moretti, G. Spina, and G. Timco, *J. Phys.: Conf. Ser.* (to be published); (private communication).

H. Amiri,<sup>1,2,\*</sup> A. Lascialfari,<sup>1,2,3</sup> Y. Furukawa,<sup>4</sup> F. Borsa,<sup>2,4</sup> G. A. Timco,<sup>5</sup> and R. E. P. Winpenny<sup>5,6</sup>

<sup>1</sup>*Department of Molecular Sciences Applied to Biosystems, Università degli Studi di Milano, I-20134 Milan, Italy*

<sup>2</sup>*Department of Physics "A. Volta" and CNISM, Università di Pavia, I-27100 Pavia, Italy*

<sup>3</sup>*Centro S3, CNR-Istituto di Nanoscienze, I-41125 Modena, Italy*

<sup>4</sup>*Ames Laboratory and Department of Physics and Astronomy, Iowa State University, Ames, Iowa 50011, USA*

<sup>5</sup>*The Lewis Magnetism Laboratory, School of Chemistry, The University of Manchester, Oxford Road, Manchester M13 9PL, United Kingdom*

<sup>6</sup>*The Photon Science Institute, The University of Manchester, Oxford Road, Manchester M13 9PL, United Kingdom*

(Received 19 July 2010; published 12 October 2010)

We present a comparison of the results obtained in the antiferromagnetic (AFM) homometallic ring  $\text{Cr}_8$  with the results in three heterometallic rings with a Cr ion replaced by Cd, Ni, and Fe ions, i.e.,  $\text{Cr}_7\text{Cd}$ ,  $\text{Cr}_7\text{Ni}$ , and  $\text{Cr}_7\text{Fe}$ , respectively. The experimental results include magnetic susceptibility,  $^1\text{H}$  nuclear-magnetic-resonance (NMR) spectra, spin-spin and spin-lattice relaxation rates data, collected in the temperature range  $1.65 < T < 300$  K at two applied magnetic fields. The data include both new results and previously published data. The static magnetic properties derived from susceptibility and  $^1\text{H}$  NMR linewidth can be analyzed in a simple way in terms of the properties of the individual ions constituting the ring and their nearest-neighbor antiferromagnetic exchange coupling. The nuclear-spin-lattice relaxation rate at low temperature can be described phenomenologically by a model, which assumes a single-correlation time for the relaxation of the magnetization, as used previously for homometallic AFM rings. The correlation frequencies obtained from the fit of the data, increase by as much as two orders of magnitude in the  $\text{Cr}_7\text{Ni}$  and  $\text{Cr}_7\text{Fe}$  rings with respect to the homometallic ring  $\text{Cr}_8$  and the diamagnetically substituted  $\text{Cr}_7\text{Cd}$  ring. This result can be explained qualitatively in terms of a change in spin-phonon coupling due to the enhancement of crystal-field effects in the heterometallic rings. For a more quantitative analysis one should take into account the multi-Lorentzian behavior of the spin-spin correlation function for which detailed theoretical calculations are required. At temperatures higher than the magnetic exchange energy  $J/k_B$ , the mechanism for nuclear-spin-lattice relaxation changes since the fluctuations of the moments of the magnetic ions become weakly correlated. We find a fluctuation frequency much higher in the heterometallic rings as a result of the perturbation introduced by the substituted magnetic ion.

DOI: [10.1103/PhysRevB.82.144421](https://doi.org/10.1103/PhysRevB.82.144421)

PACS number(s): 75.50.Xx, 75.75.Fk, 76.60.Es

## I. INTRODUCTION

Molecular nanomagnets have opened the possibility to investigate new interesting phenomena in magnetism.<sup>1-3</sup> In molecular nanomagnets, investigation of the magnetic properties and of the spin dynamics of a single molecule is possible because the magnetic cores of the individual molecules are isolated from each other by a shell of bulky organic ligands so that the intermolecular magnetic interactions (usually dipolar) are very weak compared to the intramolecular exchange interactions.<sup>3</sup>

A specific type of nanomagnets are the antiferromagnetic (AFM) molecular rings, i.e., magnetic molecules with an even number of uniformly spaced paramagnetic metal ions arranged as a planar ring and interacting via strong nearest-neighbor antiferromagnetic exchange interactions. If the ring contains just one type of magnetic ion, then it is called homometallic (e.g.,  $\text{Cr}_8$  which is characterized by a singlet zero-field ground state with total spin  $S_T=0$ ).<sup>4</sup> On the other hand by substituting one of the paramagnetic ions with a nonmagnetic ion (e.g., Cd) or with an ion with different magnetic moment (e.g.,  $\text{Fe}^{2+}$  and  $\text{Ni}^{2+}$ ) one obtains a heterometallic AFM ring with a magnetic ground state  $S_T \neq 0$  and with different static and dynamical magnetic properties.<sup>5</sup> Of particular interest are the effects of redistribution of the local

magnetic moment density in the heterometallic rings<sup>6</sup> and the changes in the spin dynamics. Since the ground state of these heterometallic AFM rings could be used for implementation of qubits for quantum computation, and the synthesis of heterometallic rings containing coupled molecules could lead to quantum entanglement,<sup>7,8</sup> the investigation of the magnetic properties and particularly of the spin dynamics which can affect the quantum coherence or decoherence in these heterometallic rings is of great relevance.

Nuclear magnetic resonance (NMR) has been proved to be an efficient local probe of both static and dynamic properties of magnetic molecules<sup>9</sup> and used in combination with thermodynamic magnetization measurements can give a good characterization of the magnetic properties and the spin dynamics in the heterometallic rings. In this paper we will compare the results in the homometallic AFM ring  $\text{Cr}_8$  with the results in three heterometallic rings with a Cr ion replaced by Cd, Ni, and Fe ions, i.e.,  $\text{Cr}_7\text{Cd}$ ,  $\text{Cr}_7\text{Ni}$ , and  $\text{Cr}_7\text{Fe}$ , respectively. In the ground state, these rings are characterized by a total spin  $S_T=0$ ,  $1/2$ ,  $1/2$ , and  $3/2$ , for the  $\text{Cr}_8$ ,  $\text{Cr}_7\text{Fe}$ ,  $\text{Cr}_7\text{Ni}$ , and  $\text{Cr}_7\text{Cd}$ , respectively, resulting from AFM interactions  $J$  between nearest-neighbor  $\text{Cr}^{3+}$  ( $s=3/2$ ) ions and  $J'$  between  $\text{Cr}^{3+}$  and the substituted ions:  $\text{Fe}^{2+}$  ( $s=2$ ),  $\text{Ni}^{2+}$  ( $s=1$ ), and  $\text{Cd}^{2+}$  ( $s=0$ ). The paper is organized as follows. In Sec. II we summarize briefly the synthesis of the compounds

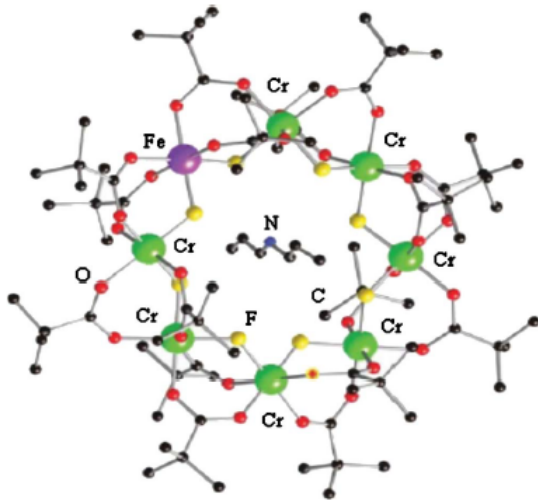
AMIRI *et al.*PHYSICAL REVIEW B **82**, 144421 (2010)

FIG. 1. (Color online) Structure of  $(C_4H_9)_2NH_2Cr_7Fe^{2+}F_8(O_2CCMe_3)_{16}$  molecular nanomagnet, in brief  $Cr_7Fe$ .

and their crystal structure. In Sec. III the experimental results and data analysis for the magnetization will be presented. In Sec. IV we present in separate sections the static and the dynamic NMR results with their analysis. Sec. V contains a summary of the results and the conclusions.

## II. SYNTHESIS AND STRUCTURE

The homometallic ring  $Cr_8$ ,  $[Cr_8F_8(O_2CCMe_3)_{16}]$ , has been widely studied,<sup>10,11</sup> both because of its magnetic properties<sup>11</sup> and because it can act as a host for heterometallic substitution.<sup>12</sup> In order to prepare a heterometallic ring one of the chromium ions should be substituted with a metallic ion. In our case the Cr ion is replaced with Cd, Ni, and Fe. Using the same amine as a template for  $Cr_7M$  ( $M=Cd$ , Ni, and Fe) rings will give us the isostructural  $Cr_7Cd$ ,  $Cr_7Ni$ , and  $Cr_7Fe$  rings with the same bond length within the ring. Although the lattices parameters may vary slightly, the structure will be the same. The nearest-neighbor exchange interaction between Cr ions is almost independent from the substituting ion while the exchange interaction between the Cr ion and the substituting ion depends on the type of heterometallic substitution as will be discussed further on. The synthesis procedure for all of them has been reported in Ref. 5.

The schematic structure of a heterometallic ring, for the case that one Cr is replaced with a Fe ion, is shown in Fig. 1. The position of protons in the molecule is important for our  $^1H$  NMR study. Around each Cr there are three closest  $CH_3$  groups. For each  $CH_3$  there are three Cr-H distances: (i) shortest, in the range 4.07–4.32 Å, (ii) middle, in the range 4.48–4.93 Å, and (iii) longest, in the range of 5.47–5.57 Å. Other protons are located even further away from Cr ions.

## III. MAGNETIC SUSCEPTIBILITY

Measurements of magnetic susceptibility

$$\chi = \lim_{H \rightarrow 0} M/H,$$

which for paramagnets far from saturation can be approximated by  $M/H$ , have been performed with a superconducting quantum interference device (SQUID) magnetometer on different rings, at two different external magnetic fields. The data for  $Cr_8$  were taken in polycrystalline powder sample while in the other three rings the data were taken on single crystals with  $H$  oriented perpendicular to the molecular  $c$  axis which is perpendicular to the plane formed by the magnetic ions, i.e., to the plane of the ring. In the temperature and field interval measured here the susceptibility is found to be isotropic, within the experimental error.

For a straightforward comparison of the results in the four rings, we show in Fig. 2 the susceptibility times temperature vs temperature, which corresponds to the plot of the effective Curie constant as a function of temperature. The data for  $Cr_7Fe$  are from a previous publication.<sup>13</sup> All other data are new although partial susceptibility data have been published earlier for  $Cr_7Ni$  (Ref. 14) and  $Cr_8$  (Refs. 9, 15, and 16).

The upper dashed lines in Fig. 2 correspond to the value of the Curie constant  $C = Ng^2\mu_B^2[s(s+1)]/3k_B$ , where it was assumed for the  $g$  factor  $g=2$  for both  $Cr^{3+}$  and the substituted ions while the spin  $s$  for  $Cr^{3+}$  is  $3/2$  and for the  $Fe^{2+}$ ,  $Ni^{2+}$ , and Cd is 2, 1, and 0, respectively. The experimental data in Fig. 2 lie below the high- $T$  limit as expected in presence of AFM coupling but seem to bend toward the limit calculated for noninteracting ions with the given spin  $s$  value and negligible single ion anisotropy ( $g=2$ ). The low-temperature dashed-dotted lines represent the Curie constant for a single total spin,  $S_T=0, 1/2, 1/2,$  and  $3/2$ , for the  $Cr_8$ ,  $Cr_7Fe$ ,  $Cr_7Ni$ , and  $Cr_7Cd$ , respectively, with  $g=2$ . The agreement is good indicating that at low temperature the rings occupy a collective ground state characterized by a total spin value as given above. The calculated Curie constants for both high- and low-temperature limits are summarized in Table I.

For temperatures above 100 K the magnetic ions are weakly correlated and their susceptibility can be described, in the molecular-field approximation, in terms of the nearest-neighbor  $Cr^{3+}-Cr^{3+}$  interaction  $J$  and the interaction  $J'$  between  $Cr^{3+}$  ions and the substituted ion.

In Fig. 3 we have plotted the inverse susceptibility vs temperature for the four rings. The high-temperature (above 100 K) results can be fitted reasonably well by using a Curie-Weiss law for the susceptibility, i.e.,  $1/\chi = [T - \Theta]/C$ , with  $C$  values calculated above for the high- $T$  limit (see Table I) and by choosing  $\Theta$  as the only fitting parameter. The  $\Theta$  values obtained from the fits for different rings are listed in Table I. Assuming that the dominant contribution to the Curie-Weiss temperature  $\Theta$  comes from the more abundant  $Cr^{3+}$  ions and using the molecular-field approximation expression  $\Theta = [2zs(s+1)J]/3k_B$ , with the number of nearest neighbors of a given moment being  $z=2$ , we have obtained the AFM coupling constants  $Cr_7Cd$  for all the rings.

The exchange constants derived above correspond to a Hamiltonian for the Heisenberg model written as  $\sum_{i>j} -2J_{ij}\vec{S}_i \cdot \vec{S}_j$ . Since the values of  $J$  given in the molecular nanomagnets are normally referred to a Hamiltonian written as



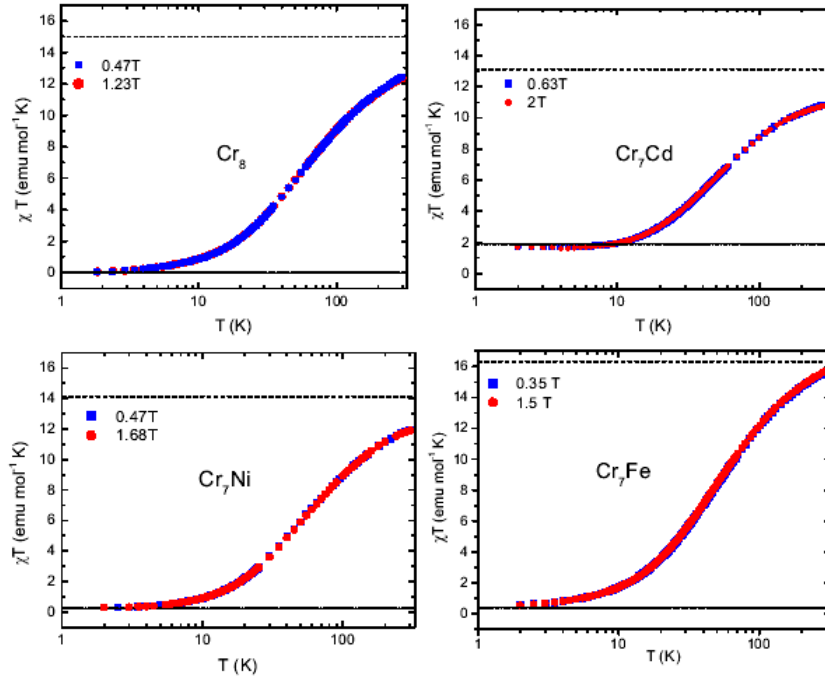


FIG. 2. (Color online) The susceptibility times temperature plotted vs temperature in different magnetic rings at two external magnetic fields. The dashed and dashed-dotted lines are the limiting behaviors at high and low temperatures, respectively, expected for a simple paramagnetic model of the AFM rings (see text).

$\sum_{i>j} J_{ij} \vec{S}_i \cdot \vec{S}_j$ , we multiply our value by two and change sign in order to compare it with the  $J$  constants given in the literatures for AFM rings. The values obtained for  $J$  are reported in Table I. The values of  $J$  are very similar for all rings except  $\text{Cr}_7\text{Fe}$  for which the value is smaller, i.e.,  $J = 13 \pm 1$  K, indicating a stronger magnetic perturbation of the exchange couplings in the ring as also evident in the dynamic properties discussed in the following section.

The oversimplified analysis presented above is justified by the desire to have a quick comparison of the magnetic properties of the four rings and is in reasonable agreement with more rigorous fits of the susceptibility and analysis of the coupling constants published for some of the rings.<sup>17</sup>

TABLE I. High- and low-temperature limits  $C_{\text{high-}T \text{ limit}}$  and  $C_{\text{low-}T \text{ limit}}$ , respectively, the Curie-Weiss temperature  $\Theta$ , and the AFM coupling constants for all the investigated rings.

| Molecule               | $C_{\text{high-}T \text{ limit}}$ | $C_{\text{low-}T \text{ limit}}$ | $\Theta$<br>(K) | $J/k_B$<br>(K) |
|------------------------|-----------------------------------|----------------------------------|-----------------|----------------|
| $\text{Cr}_8$          | 15.005                            | 0                                | -64             | 25.6           |
| $\text{Cr}_7\text{Cd}$ | 13.13                             | 1.875                            | -58             | 23.2           |
| $\text{Cr}_7\text{Ni}$ | 14.13                             | 0.249                            | -55             | 22             |
| $\text{Cr}_7\text{Fe}$ | 16.32                             | 0.374                            | -32             | 13             |

#### IV. NMR EXPERIMENTAL RESULTS AND ANALYSIS

Proton NMR measurements including nuclear-spin-lattice relaxation time ( $T_1$ ) and spin-spin relaxation time ( $T_2$ ) were performed using a standard TecMag Fourier-transform pulse NMR spectrometer with short  $\pi/2$ - $\pi/2$  radio frequency (rf) pulses (1.9–2.2  $\mu\text{s}$ ) in the temperature range  $1.65 < T < 300$  K. In order to study the temperature dependence of the relaxation times, we used two different cryostats: (a) a continuous flow cryostat in the temperature range  $4.2 < T < 300$  K and (b) a bath cryostat in the temperature range  $1.65 < T < 4.2$  K. Fourier transform (FT) of half of the echo spin signal yields the NMR spectrum in the case where the whole line could be irradiated with one rf pulse.

The nuclear-spin-lattice relaxation rate  $T_1^{-1}$  was determined by monitoring the recovery of the longitudinal nuclear magnetization measured by the spin-echo amplitude obtained with  $\pi/2$ - $\pi/2$  pulse sequence, following a saturating comb of rf pulses. The length of the rf saturation comb was chosen to insure the best initial saturation conditions which vary depending on temperature and resonance frequency. The recovery of the nuclear magnetization was found to follow a multiexponential law. The effective relaxation rate was determined as described further on.

To perform the spin-spin relaxation time experiments, a standard solid echo ( $\pi/2$ - $\pi/2$ ) pulse sequence was used. For all temperatures a single exponential decay of the transverse

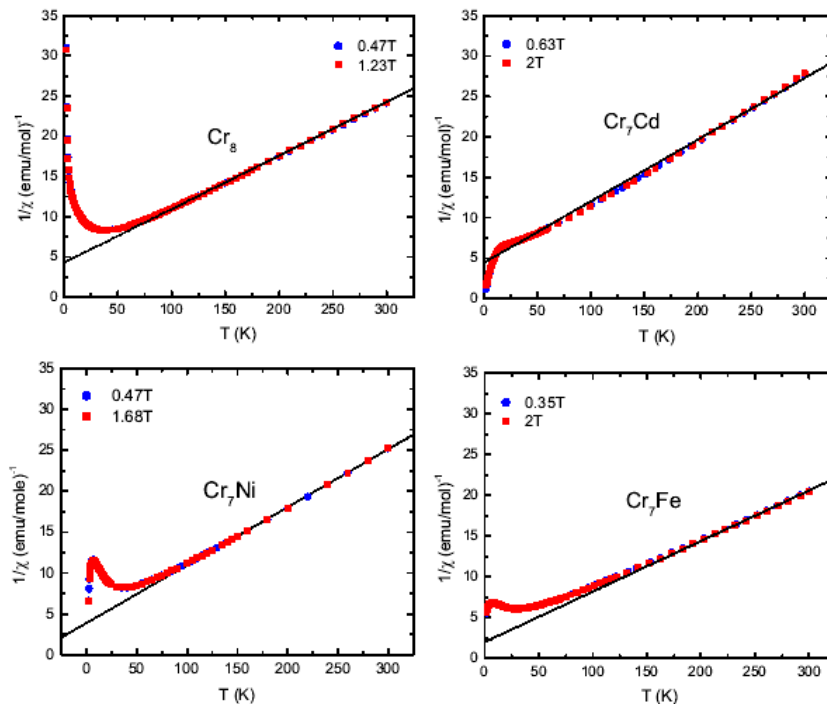


FIG. 3. (Color online) Inverse susceptibility vs temperature in different rings at two external magnetic fields; the solid lines are fits according to the Curie-Weiss law (see text).

nuclear magnetization was observed so that a well-defined spin-spin relaxation time parameter  $T_2$  can be defined.

#### A. Proton NMR spectra

The proton NMR linewidth full width at half maximum (FWHM) or  $\Delta\nu$  for all the rings is shown in Fig. 4 as a function of temperature at two values of the external magnetic field. The magnitude and the temperature dependence of the linewidth are similar in all the rings reflecting the fact that the broadening has the same origin in all of them. In fact the shape and width of the proton NMR spectrum is determined by two main interactions: (i) the nuclear-nuclear dipolar interaction and (ii) the hyperfine interaction of the proton with the neighboring magnetic ions. The first interaction generates a temperature- and field-independent broadening which depends on the hydrogen distribution in the molecule and is thus the same in all molecular magnets independently of their magnetic properties.<sup>9</sup>

The hyperfine field resulting from the interaction of protons with local magnetic moments of  $\text{Cr}^{3+}$  ( $\text{Fe}^{2+}$  and  $\text{Ni}^{2+}$ ) may contain contributions from both the classical dipolar interaction and from a direct contact term due to the hybridization of proton  $s$ -wave function with the  $d$ -wave function of magnetic ions. The dipolar contribution has tensorial character and is thus responsible for the inhomogeneous width of the line due to the random distribution of orientations in a powder sample of the vector joining the nucleus to the elec-

tronic moment and to the many nonequivalent proton sites in the single crystal. The contact interaction, on the other hand, has scalar form and it can generate a shift of the line for certain groups, each one constituted by equivalent protons in the molecule. Since we have not observed any measurable shift of the proton NMR line from the Larmor frequency, we can conclude that the dominant hyperfine interaction is of dipolar origin.

In the usual simple Gaussian approximation for the NMR line shape, the linewidth is proportional to the square root of the second moment, which in turn is given by the sum of the second moments due to the two interactions described above,<sup>18</sup>

$$\text{FWHM} \propto \sqrt{\langle \Delta\nu^2 \rangle_d + \langle \Delta\nu^2 \rangle_m}, \quad (1)$$

where  $\langle \Delta\nu^2 \rangle_d$  is the intrinsic second moment due to nuclear-nuclear dipolar interactions and  $\langle \Delta\nu^2 \rangle_m$  is the second moment of the local frequency-shift distribution (due to the nearby electronic moments) at the different proton sites of all molecules. The proportionality constant in Eq. (1) is on the order of one depending on the exact shape of the spectrum. We will assume it to be one, for simplicity. The relation between  $\langle \Delta\nu^2 \rangle_m$  and the local  $\text{Cr}^{3+}$ ,  $\text{Fe}^{2+}$ , and  $\text{Ni}^{2+}$  electronic moments for a simple dipolar interaction is given by<sup>9,18</sup>

COMPARISON OF THE MAGNETIC PROPERTIES AND THE...

PHYSICAL REVIEW B 82, 144421 (2010)

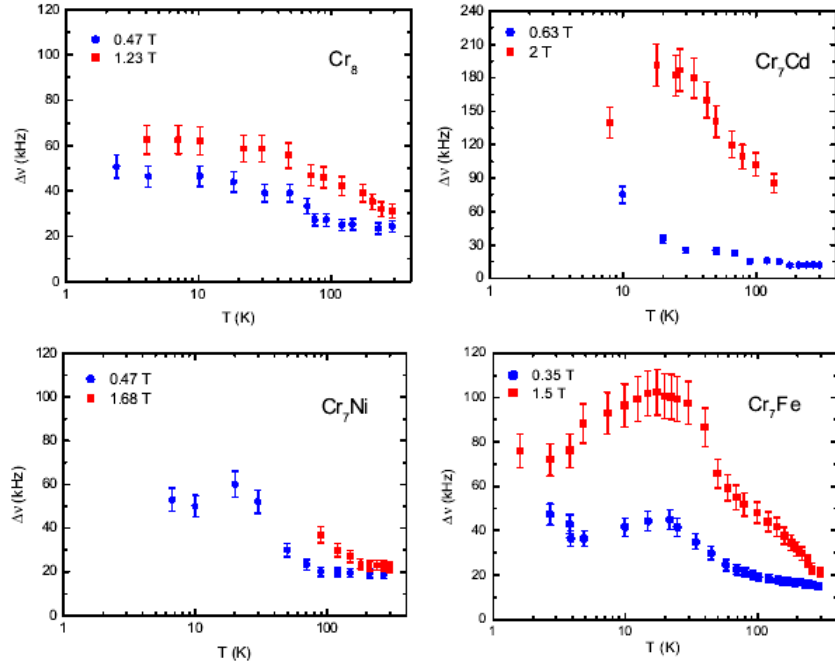


FIG. 4. (Color online) Proton linewidth vs temperature in all the molecular rings at two different external magnetic fields.

$$\begin{aligned} \langle \Delta \nu^2 \rangle_m &= \frac{1}{N} \sum_R \left( \sum_{i \in R} \langle \nu_{R,i} - \nu_L \rangle_{\Delta t} \right)^2 \\ &= \frac{\gamma^2}{N} \sum_R \left[ \sum_{i \in R} \sum_{j \in R} \frac{A(\theta_{i,j})}{r_{i,j}^3} \langle m_{z,j} \rangle_{\Delta t} \right]^2, \end{aligned} \quad (2)$$

where  $R$  labels different molecules,  $i$  and  $j$  span different protons and  $\text{Cr}^{3+}$  ions within each molecule,  $N$  is the total number of probed protons. In Eq. (2),  $\nu_{R,i}$  is the NMR resonance frequency of nucleus  $i$  and  $\nu_L = (\gamma/2\pi)H = \gamma H$  is the bare Larmor resonance frequency. The difference between the two resonance frequencies represents the shift for nucleus  $i$  due to the local field generated by the nearby moments  $j$ . The angular-dependent dipolar coupling constant between nucleus  $i$  and electronic moment  $j$  is  $A(\theta_{i,j})$  and  $r_{i,j}$  is the corresponding distance.  $\langle m_{z,j} \rangle$  is the component of the Cr (Fe and Ni) moment  $j$  in the direction of the applied field, averaged over the NMR data acquisition time. In a simple paramagnet one expects  $\langle m_{z,j} \rangle = (\chi/N_A)H$  with  $\chi$  the SQUID susceptibility in electromagnetic unit/mole,  $N_A$  Avogadro's number, and  $H$  the applied field.<sup>19</sup> We can thus write

$$\langle \Delta \nu^2 \rangle_m = A_z' (\chi H)^2 = A_z' \left( \chi \frac{\nu_L}{\gamma} \right)^2 = A_z \left( \chi \frac{\nu_L}{N_A} \right)^2, \quad (3)$$

where  $A_z$  and  $A_z'$  are the square dipolar coupling constants averaged over all protons and all orientations expressed in different units.

The experimental results for the magnetic contribution to the linewidth are plotted as a function of the magnetic susceptibility in Fig. 5 for all the molecular rings. As one can

see the linear relation, predicted by Eqs. (1) and (3), is well verified. In the fit of Fig. 5 we have neglected the nuclear dipolar contribution in Eq. (1) since at such fields the inhomogeneous contribution to the width is already dominant. The values obtained from the fit are summarized in Table II.

The average square dipolar coupling constants (see Table II) are practically the same in all the rings as expected in view of the same crystal structure and thus the same proton-ion distance. The smaller values for the Ni and Fe substituted rings are probably due to slightly larger distances not revealed by x-ray analysis.

### B. NMR signal intensity: Wipe-out effect

The wipe-out effect consists in a progressive loss of measurable NMR signal intensity normally observed in magnetic systems as the temperature is lowered. There is a general consensus that the effect has to be ascribed to a shortening of the spin-spin nuclear relaxation time  $T_2$  (which follows a correspondent shortening of the spin-lattice relaxation time  $T_1$ ) whereby the shortening of  $T_2$  produces a decay of the transverse nuclear magnetization in a time shorter than the detection time of the spectrometer. The wipe-out results from a combination of a strong hyperfine coupling of nuclei to the electron spin and a slowing down of the fluctuations of the magnetic moment of the ions. Thus the wipe-out effects contains useful information about both the hyperfine coupling and the electron spin dynamics. The effect is a rather general phenomenon in NMR and has been observed previously in other systems such as spin glasses,<sup>20</sup> stripe-ordered cuprates,<sup>21</sup> and colossal magnetic resistance manganites.<sup>22</sup> In

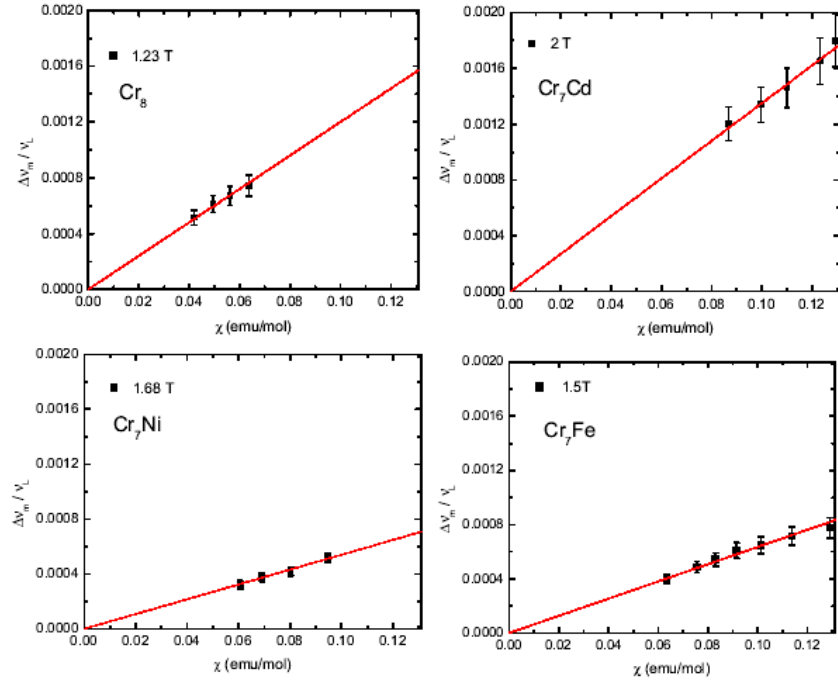


FIG. 5. (Color online) Inhomogeneous part of the linewidth, extracted as explained in the text, plotted vs magnetic susceptibility with temperature as implicit parameter.

particular, a loss of  $^1\text{H}$  NMR signal on lowering the temperature has been observed previously in other molecular nanomagnets with a magnetic ground state.<sup>9,23</sup>

A quantitative analysis of the wipe-out effect was done successfully in  $\text{Mn}_6$ ,  $\text{Fe}_4$ , and  $\text{Fe}_{10}$  molecular clusters<sup>23</sup> by using a simple and intuitive model which captures the main physical characteristics of the problem. The model allows for a semiquantitative determination of the relevant fluctuation frequency of the electron spin moment. In the following we present a summary of the wipe-out effect in the different heterometallic rings from which one can deduce a relative comparison of the spin dynamics in the different systems. The data of  $\text{Cr}_7\text{Fe}$  (Ref. 13) and partly  $\text{Cr}_7\text{Ni}$  (Ref. 14) have been published before while the data in  $\text{Cr}_8$  and  $\text{Cr}_7\text{Cd}$  are new. We are going to analyze the wipe-out effect in our cases ( $\text{Cr}_7\text{Fe}$ ,  $\text{Cr}_8$ ,  $\text{Cr}_7\text{Cd}$ , and  $\text{Cr}_7\text{Ni}$ ) by using the same model used before<sup>23</sup> which we summarize briefly in the following.

TABLE II. The average square dipolar coupling constant in Eq. (3) determined from the fits in Fig. 5 for the different rings.

| Molecule               | $A_z'$<br>(Hz mol/G emu) <sup>2</sup> | $A_z$<br>(cm <sup>-6</sup> ) |
|------------------------|---------------------------------------|------------------------------|
| $\text{Cr}_8$          | 2600                                  | $5 \times 10^{43}$           |
| $\text{Cr}_7\text{Cd}$ | 3250                                  | $6.4 \times 10^{43}$         |
| $\text{Cr}_7\text{Ni}$ | 530                                   | $0.9 \times 10^{43}$         |
| $\text{Cr}_7\text{Fe}$ | 730                                   | $0.9 \times 10^{43}$         |

We assume that the dominant contribution to  $T_2^{-1}$  is coming from the dephasing due to the hyperfine interactions with the exchange coupled magnetic ions. In the weak collision, fast motion approximation, the relaxation rate can be expressed in terms of the spectral density of the fluctuating hyperfine field at zero frequency as<sup>18,24</sup>

$$T_2^{-1} = \gamma_N^2 \langle \delta H_z^2 \rangle \tau(T) \propto \gamma_N^2 \frac{\langle \delta \mu_z^2 \rangle}{r^6} \tau(T), \quad (4)$$

where  $\delta H_z$  is the local longitudinal fluctuating field originating from a magnetic moment at a distance  $r$  from the proton spin, and  $\tau$  gives the correlation time, which is solely determined by the dynamics of the exchange coupled magnetic ions and can thus be temperature dependent. The central idea is that, on lowering the temperature, the correlation time  $\tau(T)$  becomes progressively longer and thus the relaxation time  $T_2$  becomes shorter [see Eq. (4)] until eventually it reaches the limiting value  $\tau_d = 10^{-5}$  s which we estimate to be the limit of detectability of the NMR signal in our experimental setup. Since the dipolar hyperfine field and thus  $T_2$  depends upon the distance  $r$  from the magnetic ions, the limiting value  $\tau_d$  is reached progressively by all protons, with the ones closer being wiped-out first. To describe the wipe out we assume one central ion surrounded by a large number of protons homogeneously distributed at distances up to a maximum value  $R^*$ , the number density being  $\rho = n_0 / [(4\pi/3)(R^*)^3]$ , where  $n_0$  is the total number of protons in each molecule. Being in the regime of the wipe-out effect,



COMPARISON OF THE MAGNETIC PROPERTIES AND THE...

PHYSICAL REVIEW B 82, 144421 (2010)

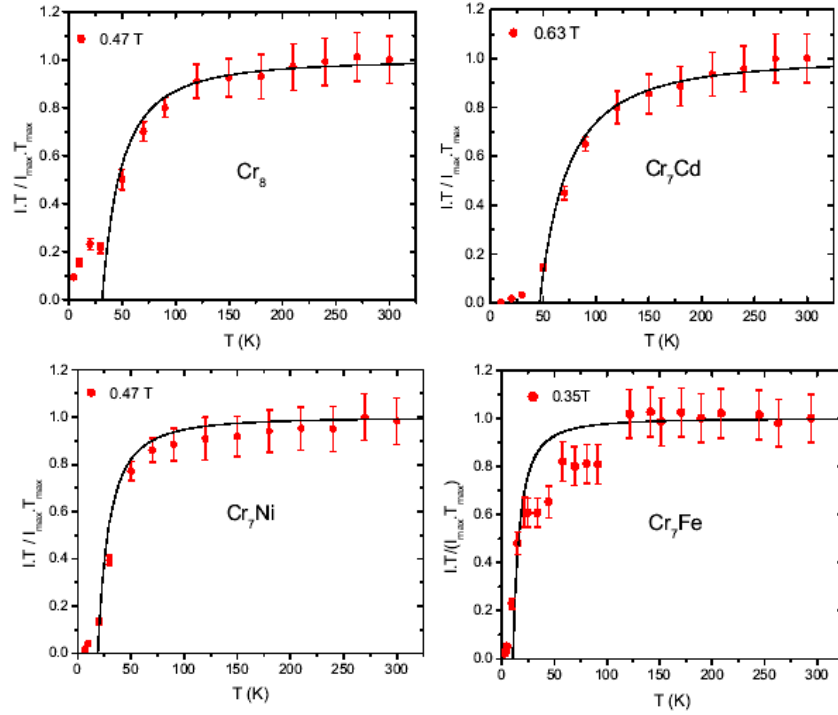


FIG. 6. (Color online) Signal intensity times the temperature normalized to the room-temperature value plotted vs temperature for the four rings. Without signal loss the plot should be temperature independent. The full lines are fits of the wipe-out effect using Eq. (6) with the fitting parameters given in Table II.

and for a given temperature or value of the correlation time  $\tau(T)$ , there is a number of protons having a  $T_2^{-1}$  value larger than the critical value of  $10^5 \text{ s}^{-1}$ . These protons are enclosed within a notional sphere of radius  $r_c(T)$  and do not contribute to the measured signal intensity. On the other hand, the protons located outside this sphere can be detected and their number  $n(T)$  can be written as

$$n(T) = n_0 \left[ 1 - \left( \frac{r_c}{R^*} \right)^3 \right]. \quad (5)$$

The value of the critical radius  $r_c$  in Eq. (5) can be obtained from Eq. (4) by setting  $T_2^{-1} = \tau_d^{-1}$ . Then one can express  $n(T)$  in terms of the temperature-dependent correlation time  $\tau(T)$  as

$$\frac{n(T)}{n_0} = 1 - \frac{\gamma_N \sqrt{\langle \delta \mu_e^2 \rangle} \sqrt{\tau_d}}{(R^*)^3 \sqrt{\tau(T)}}. \quad (6)$$

In order to use Eq. (6) to fit the data, one has to make some educated guess about the functional form of the temperature dependence of the correlation time  $\tau(T)$ .

Previous NMR studies in a series of AFM rings have shown that the temperature dependence of the correlation time (extracted from the spin-lattice relaxation data) has the form of a power law  $\tau(T) = cT^{-3.5}$  for all the rings.<sup>25</sup> Therefore we adopt the same expression to fit the wipe-out data also for our samples in Fig. 6, using Eq. (6). The two fitting

parameters for different rings, i.e.,  $c$  and  $\sqrt{\langle \delta \mu_e^2 \rangle} (R^*)^{-3}$ , are given in Table III and the results of the fits are shown in Fig. 6 for the low-field data in which the wipe-out effect is more pronounced.

The theoretical curve reproduces well the sudden drop in intensity occurring at low temperature although a good fit over the whole temperature range is impossible due to the crudeness of the model. This is particularly evident in  $\text{Cr}_7\text{Fe}$  where the big drop in signal intensity occurs at lower temperature leaving an intermediate temperature range where the fit is poor. Thus the values of the fitting parameters in Table III have to be considered only indicative. The values of the coupling parameter  $\sqrt{\langle \delta \mu_e^2 \rangle} (R^*)^{-3}$  are of the same order in all rings and are mainly due to the dipolar coupling of the protons with the magnetic moment of the ions. On the other

TABLE III. The two fitting parameters, i.e.,  $c$  and  $\sqrt{\langle \delta \mu_e^2 \rangle} (R^*)^{-3}$ , for different rings according to Eq. (6).

| Molecule               | $c$<br>(srad)         | $\sqrt{\langle \delta \mu_e^2 \rangle} (R^*)^{-3}$<br>(G) |
|------------------------|-----------------------|-----------------------------------------------------------|
| $\text{Cr}_8$          | $0.66 \times 10^{-4}$ | 600                                                       |
| $\text{Cr}_7\text{Cd}$ | $1.33 \times 10^{-4}$ | 850                                                       |
| $\text{Cr}_7\text{Ni}$ | $1.6 \times 10^{-5}$  | 500                                                       |
| $\text{Cr}_7\text{Fe}$ | $4 \times 10^{-6}$    | 300                                                       |

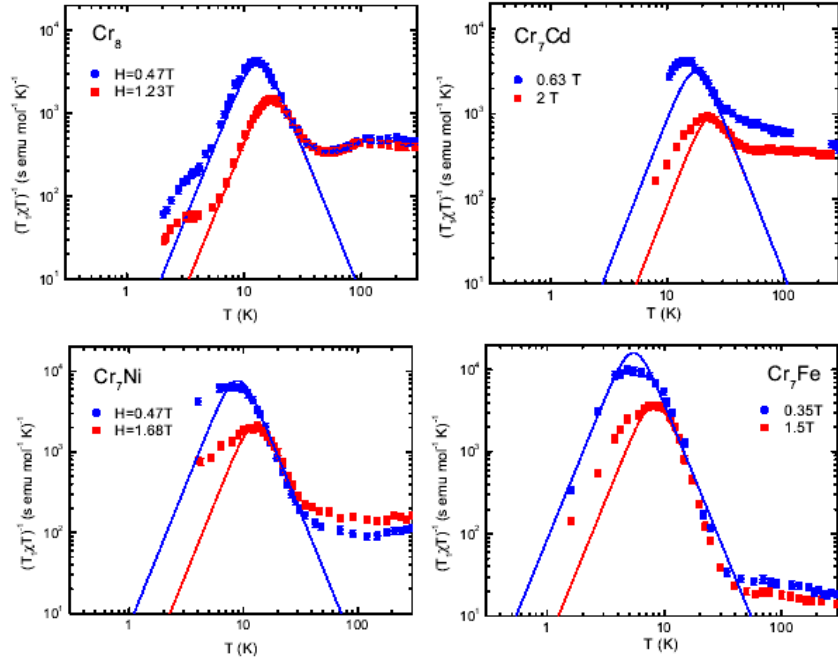


FIG. 7. (Color online) Proton spin-lattice relaxation rate divided by  $\chi^2$  vs temperature for different rings at two values of the external field. The curves are fitted using Eq. (7) with two fitting parameters:  $A$  obtained from the high-field data, and  $\omega_c$  obtained from the fit of the wipe-out effect in Fig. 6. The fitting parameters are given in Table IV.

hand the constant  $c$  which determines the correlation time  $\tau(T) = cT^{-3.5}$  is more than one order of magnitude shorter in the Fe (and Ni) substituted ring with respect to the homometallic ring  $\text{Cr}_8$ . This effect of magnetic ion substitution on the spin dynamics in the ring will be confirmed in next section where it is shown that with the same correlation frequency, used to explain the wipe-out effect, we can fit the low-temperature peak in the spin-lattice relaxation rate  $T_1^{-1}$ .

### C. Spin-lattice relaxation at low temperature

The temperature dependence of the proton spin-lattice relaxation rate is characterized by a strong peak centered at around 10–20 K and dependent on the external magnetic field as shown in Fig. 7 for the four rings at two values of the external magnetic field. This peak is typical of all molecular magnetic homometallic rings and clusters.<sup>9,15</sup> A qualitative explanation can be given which is related to the wipe-out effect. The slowing down of the fluctuation frequency  $\omega_c = \tau^{-1} = c^{-1} T^{3.5}$ , which is responsible for the shortening of  $T_2$  as discussed in the previous paragraph, is also responsible for the shortening of  $T_1$ . However, while  $T_2$  keeps shortening until  $\omega_c$  becomes on the order of the static nucleus-electron coupling energy which, in frequency units, is in the kilohertz range,  $T_1^{-1}$  reaches a maximum when the correlation frequency  $\omega_c$  becomes on the order of the nuclear Larmor frequency (in the megahertz range).<sup>18</sup> A rigorous theoretical approach has shown that at low temperature the fluctuations of the hyperfine field at the nuclear site are due to the relaxation

of the macroscopic magnetization of the ring, not to the fluctuations of the individual spin at the ion sites. This relaxation is dominated by a single correlation frequency which we identify with  $\omega_c$  and is due to spin-phonon interactions.<sup>16</sup> A subsequent theoretical analysis has provided an explanation for the origin of the universal behavior of the slowing down of the magnetization fluctuations which is responsible for the observed peak.<sup>25</sup> In this experimental paper we analyze the data in a phenomenological way using a single correlation frequency to describe the electronic spin dynamics in the same way as done in Ref. 15. This will allow us to capture the relevant changes occurring in the spin dynamics when comparing the results in the heterometallic rings with the homometallic one  $\text{Cr}_8$ .

The simple expression for the relaxation rate can be obtained from the original Moriya theory of nuclear relaxation in paramagnets<sup>18,24</sup> under some simplifying assumptions, the main one being that the hyperfine field at the nuclear site is modulated by a dominant single correlation frequency which drives the relaxation and fluctuation of the ring magnetization.<sup>14,16,25</sup> The expression is

$$\frac{1}{T_1} = A' \chi^2 \frac{\omega_c(T)}{\omega_c^2(T) + \omega_L^2}, \quad (7)$$

where  $A' \chi^2$  is the average square of the transverse fluctuating hyperfine field in frequency units,  $\omega_L$  is the proton Larmor frequency,  $\omega_c(T) = 1/\tau(T)$  is the characteristic frequency, and  $\chi$  is the uniform magnetic susceptibility ex-

COMPARISON OF THE MAGNETIC PROPERTIES AND THE...

PHYSICAL REVIEW B 82, 144421 (2010)

TABLE IV. Correlation frequency  $\omega_c$ , the average square of the nuclear electron hyperfine fluctuation  $A'$ , and the hyperfine field  $A$  for different molecular rings.

| Molecule           | $\omega_c$<br>(rad/s)      | $A'$<br>(rad <sup>2</sup> mol/s <sup>2</sup> emu K) | $A$<br>(cm <sup>-6</sup> ) |
|--------------------|----------------------------|-----------------------------------------------------|----------------------------|
| Cr <sub>8</sub>    | $1.5 \times 10^4 T^{3.5}$  | $1 \times 10^{12}$                                  | $4.5 \times 10^{43}$       |
| Cr <sub>7</sub> Cd | $0.75 \times 10^4 T^{3.5}$ | $1 \times 10^{12}$                                  | $4.5 \times 10^{43}$       |
| Cr <sub>7</sub> Ni | $6 \times 10^4 T^{3.5}$    | $1.9 \times 10^{12}$                                | $9 \times 10^{43}$         |
| Cr <sub>7</sub> Fe | $2.5 \times 10^5 T^{3.5}$  | $3 \times 10^{12}$                                  | $14.4 \times 10^{43}$      |

pressed in electromagnetic unit/mole. The temperature dependence of  $\chi T$  (see Fig. 2) represents the amplitude of the local effective moments. Thus in order to isolate the dynamics from the static effects, we have plotted  $(T_1 \chi T)^{-1}$  versus temperature as shown in Fig. 7. The data can now be fitted with two fitting parameters:  $A'$  related to the average square of the nuclear electron hyperfine fluctuations and  $\omega_c(T)$  which can be assumed to be of the form  $\omega_c(T) = \tau(T)^{-1} = c^{-1} T^{3.5}$  to be consistent with the wipe-out analysis of the previous paragraph and the results in other AFM rings.<sup>15</sup> The fitting parameters are given in Table IV.

As one can see in Fig. 7, the theoretical curves given by Eq. (7) reproduce qualitatively the relaxation data by using only one single fitting parameter, namely,  $A'$  while for the correlation frequency we used the values obtained from the analysis of the wipe-out effect. One should note that a good fit for temperatures less than 10 K is impossible anyway since the data at low temperature are affected by the wipe-out effect and thus they do not represent an average relaxation rate over all protons of the molecule.

From the value of  $A'$ , one can obtain the square hyperfine interaction  $A$  in units of inverse volume using the following equation:

$$A = \frac{A'}{4\pi(\hbar\gamma_n\gamma_e)^2}. \quad (8)$$

$\gamma_n$  and  $\gamma_e$  are the gyromagnetic ratios for the nuclear and the electron, respectively.

The obtained values of the  $A$  for different molecular rings are also given in Table IV. The hyperfine field  $A$  corresponds essentially to the  $(1/r^3)^2$  term in the nuclear-electron dipolar interaction. The obtained values are all of the same order of magnitude reflecting the fact that the average distance between protons and magnetic ions is very similar in all rings. Furthermore the values of the hyperfine coupling constant obtained from relaxation data (Table IV) are of the same order of magnitude as the ones obtained from linewidth data (Table II) indicating that in both cases the dominant interaction is the nuclear-ion dipolar interaction.

On the other hand, the correlation frequency  $\omega_c$  is much higher in the Ni and Fe substituted rings. This can be seen well in Fig. 8 where we show the correlation frequency extracted from Eq. (7) with the experimental data for the nuclear-spin-lattice relaxation and by using the values of  $A'$  in Table IV. The results are shown in Fig. 8 together with the

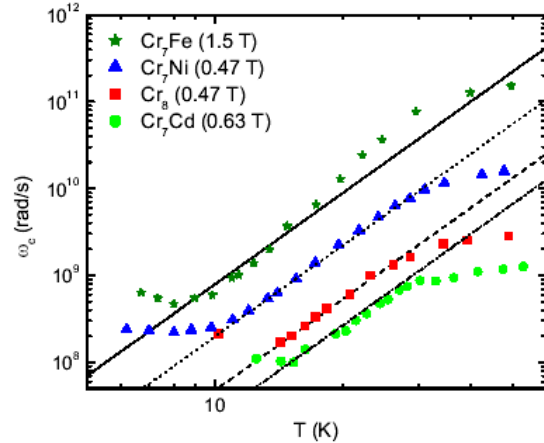


FIG. 8. (Color online) Correlation frequencies for different molecular magnets extracted from the NMR experimental data plotted vs temperature. The solid, dot, dashed, and dashed-dotted lines correspond to the behavior of  $\omega_c(T)$  for Cr<sub>7</sub>Fe, Cr<sub>7</sub>Ni, Cr<sub>8</sub>, and Cr<sub>7</sub>Cd, respectively, which are obtained from the relaxation and wipe-out effect (see Table IV).

lines representing the best fit for the  $T$  dependence of  $\omega_c$  given in Table IV.

The dramatic effect of the ion substitution in the ring on the relaxation spin dynamics at low temperature is a central finding of this paper. Since the relaxation of the ring magnetization at low temperature is believed to be due to spin phonon interaction<sup>16,25</sup> the much higher correlation frequency in the Ni and Fe substituted rings must be associated to much stronger crystal-field effects in the latter heterometallic rings. It should be remarked, however, that two assumptions made here, based on previous work in homometallic AFM rings, could be subject to criticism. One regards the assumption of a single correlation function (CF) since it was found that in heterometallic rings, particularly in the temperature region of the peak in  $T_1^{-1}$ , the spin-spin correlation function shows a multi-Lorentzian regime.<sup>14,26</sup> The second assumption is the one leading to the proportionality of  $T_1^{-1}$  to  $\chi T$  [see Eq. (7)]. Both effects are the consequence of a nonuniform distribution of the local magnetic moments in the heterometallic rings. These effects should be taken into consideration in a detailed theoretical explanation of the present data, which is outside the scope of the present paper.

#### D. Spin-lattice relaxation at high temperature

As can be seen in Fig. 7 the temperature dependence of the proton spin-lattice relaxation rate changes for all the rings at temperatures above about 30–40 K. Above this temperature and up to room temperature,  $(T_1 \chi T)^{-1}$  is weakly temperature and field dependent and it departs completely from the behavior predicted by Eq. (7) with the fitting parameters in Table IV. The changeover of behavior of the nuclear relaxation rate is most likely related to the changeover from a correlated spin dynamics at low temperature,

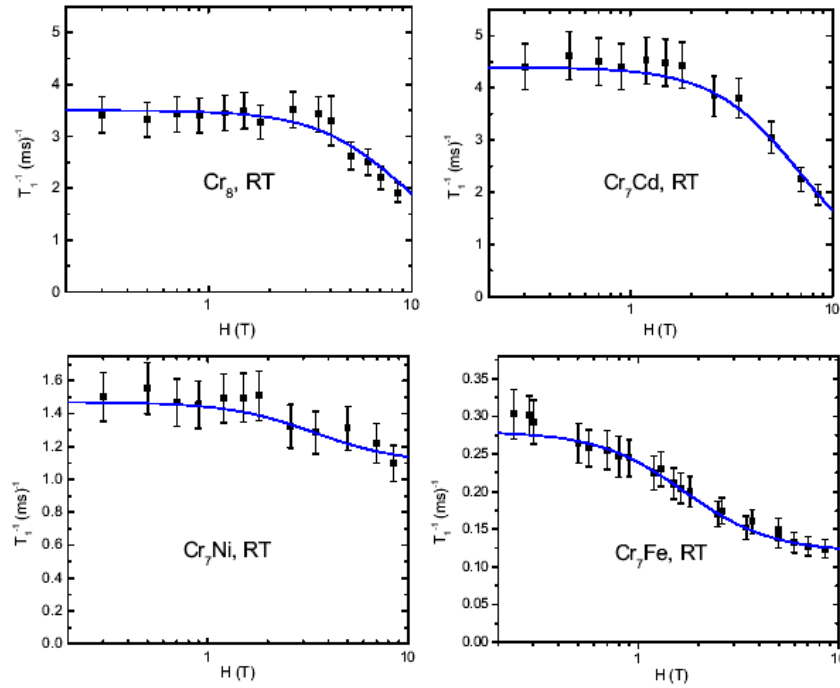


FIG. 9. (Color online) Proton spin-lattice relaxation rate vs external magnetic field at RT for the four investigated rings. Note, in comparing, that for  $\text{Cr}_7\text{Ni}$  and  $\text{Cr}_7\text{Fe}$  the vertical scale is magnified. The full lines are fitting curves as explained in the text.

whereby the local spin dynamics is driven by the relaxation of the macroscopic magnetization to a high-temperature spin dynamics. For the  $k_B T \gg J$  the local spins of the magnetic ions fluctuate almost independently from each other. Another important effect to be noted is that above 40 K the magnitude of  $(T_1 \chi T)^{-1}$  is much smaller for the Ni and Fe heterometallic rings with respect to the homometallic ring  $\text{Cr}_8$  as well as the diamagnetically substituted ring  $\text{Cr}_7\text{Cd}$  (see Fig. 7). To explore more quantitatively this effect, we have performed a series of measurements of  $T_1^{-1}$  as a function of external magnetic field at room temperature (RT) for four rings. The results are shown in Fig. 9 for all the rings.

To explain the high-temperature data we refer to the original Moriya theory of nuclear relaxation in paramagnetic materials.<sup>24</sup> In the weak collision approximation one can write

$$T_1^{-1} \alpha \sum_{ij} \alpha_{ij} J_{\pm}^{ij}(\omega_e) + \sum_{ij} \beta_{ij} J_{\pm}^{ij}(\omega_N), \quad (9)$$

where  $i$  and  $j$  number the electronic spins,  $\omega_e$  and  $\omega_N$  are the Larmor frequencies of the electron and of the nucleus, respectively,  $\alpha_{ij}$  and  $\beta_{ij}$  are geometrical factors of the nuclear-electron dipolar interaction, and  $J_{\pm}^{ij}$  and  $J_z^{ij}$  are the transverse and longitudinal spectral densities of the spin fluctuations, respectively. In Eq. (9), the spectral density  $J_{\pm,z}^{ij}(\omega)$  can be expressed by the FT of the spin CF,

$$J_{\pm,z}^{ij}(\omega) = \int G_{\alpha}^{ij}(r,t) e^{i\omega t} dt, \quad (10)$$

where  $\alpha = \pm, z$  corresponds to the transverse and longitudinal components, respectively.

For uncorrelated spins, namely,  $T \gg J/k_B$ , one can assume that the CF decays as a Gaussian or an exponential<sup>24</sup> with a correlation frequency which is due to the rapid exchange of energy between adjacent electronic spins with an exchange frequency given approximately by<sup>24</sup>

$$\Gamma_{exc} = (2\pi J/\hbar)[S(S+1)]^{1/2}. \quad (11)$$

Thus in the simplest approximation one can write for the relaxation rate

$$T_1^{-1} = K \left\{ \frac{1}{2} A^{\pm} [\Gamma_{exc}/(\omega_e^2 + \Gamma_{exc}^2) + A^{\mp} \Gamma_{exc}/(\omega_N^2 + \Gamma_{exc}^2)] \right\} \\ \cong K \left\{ \frac{1}{2} A^{\pm} [\Gamma_{exc}/(\omega_e^2 + \Gamma_{exc}^2) + A^z/\Gamma_{exc}] \right\}, \quad (12)$$

where we assumed  $\omega_N \ll \Gamma_{exc}$  and the constants  $A^{\pm}$  and  $A^z$  are averages over all protons in the molecule of the products of the hyperfine dipolar tensor components  $\alpha_{ij}$  and  $\beta_{ij}$ , respectively [see Eq. (9)]. The constant  $K$ , which has been factored out from the dipolar tensor coefficients, is given by  $K = (\hbar \gamma_N \gamma_e)^2 / 4\pi = 1.94 \times 10^{-32} (\text{s}^{-2} \text{cm}^6)$  where the electronic and nuclear gyromagnetic ratios are defined by the Larmor relation  $\omega_e = \gamma_e H$  and  $\omega_N = \gamma_N H$ , respectively. For both  $\text{Cr}_8$  and  $\text{Cr}_7\text{Cd}$ , Eq. (12) should hold and the data in Fig. 9 can be fitted (solid lines) with the following choice of parameters:  $\Gamma_{exc} = 1.6 \times 10^{12} (\text{rad Hz})$ ;  $A^{\pm} = 4.7 \times 10^{47} \text{ cm}^{-6}$ ; and  $A^z = 4.9$



$\times 10^{46}$  cm $^{-6}$  for the Cr $_8$ , and  $\Gamma_{exc}=1.2 \times 10^{12}$ (rad Hz);  $A^\pm = 5.2 \times 10^{47}$  cm $^{-6}$ ;  $A^z=1.9 \times 10^{46}$  cm $^{-6}$  for the Cr $_7$ Cd.

The value of the exchange frequency is indeed of the order predicted by Eq. (11) for the appropriate  $J$  coupling of the ring and the dipolar coupling coefficients are consistent with the proton-ion distance in the ring. It should be noted that for an isotropic Heisenberg exchange system of identical electronic spins, the CF of the transverse spin components  $S_\pm(t)$  contains a term randomly varying multiplied by a coherent electronic Larmor precession around the external magnetic field.<sup>24</sup> Thus the CF in Eq. (10) contains a term  $G_\pm$  proportional to  $\langle S'_\pm(t)S'_\pm(0) \rangle e^{-i\omega_e t}$ . When one takes the FT, according to the Eq. (10), one obtains a spectral density  $J_\pm(\omega)$  centered at  $\omega_e \pm \omega_N \cong \omega_e$ , as it appears in the first term of Eq. (9). If the spin system is no longer isotropic and/or is made up of nonequivalent moments, i.e., there is a symmetry breaking in the plane perpendicular to the magnetic field as in the case of the heterometallic rings, one expects that the coherent electronic Larmor precession is damped. Consequently, the term of Eq. (10) containing the transverse CF, should probe the spectral density at  $\omega_N$ , as for the longitudinal fluctuations. This observation is of paramount importance to explain the difference in magnitude of  $T_1^{-1}$  for the different rings (see Figs. 7 and 9).

In the two rings with magnetic substitution, i.e., Cr $_7$ Ni and Cr $_7$ Fe, one expects a breakdown of the assumption of isotropic Heisenberg exchange between equivalent magnetic moments and thus Eq. (12) should be replaced by

$$\begin{aligned} T_1^{-1} &= K \left\{ \frac{1}{2} A^\pm [\Gamma_{exc}^\pm / (\omega_N^2 + \Gamma_{exc}^{\pm 2}) + A^z / \Gamma_{exc}^z] \right\} \\ &= K \left[ \frac{1}{2} A^\pm (1/\Gamma_{exc}^\pm) + A^z / \Gamma_{exc}^z \right], \end{aligned} \quad (13)$$

where we assumed  $\omega_N \ll \Gamma_{exc}$  and the exchange frequencies may be different from the isotropic case and different for transverse ( $\Gamma_{exc}^\pm$ ) and longitudinal ( $\Gamma_{exc}^z$ ) fluctuations.

The contributions described by Eqs. (12) and (13) refer to homometallic and heterometallic rings, respectively. These two equations lead, in agreement with the results in Fig. 7, to a temperature-independent behavior of  $(T_1 \chi T)^{-1}$ , since the exchange frequency is  $T$  independent. The field dependence observed in the data in Fig. 9 for Cr $_8$  and Cr $_7$ Cd arise from the term  $\omega_e = \gamma_p H$  present in Eq. (12). On the other hand Eq. (13), valid for the heterometallic rings Cr $_7$ Ni and Cr $_7$ Fe, predict no field dependence while it is clear that the field dependence is present also in the heterometallic rings (see Fig. 9). In order to explain the field dependence in Cr $_7$ Ni and Cr $_7$ Fe, one should thus postulate an additional contribution to the proton relaxation arising from the interaction of the protons with the heterometallic ion. This additional contribution can be put in the form,

$$T_1^{-1} = K A_h^z \frac{\Gamma_T}{\omega_N^2 + \Gamma_T^2}, \quad (14)$$

which is the expression of the nuclear relaxation due to a paramagnetic ‘‘impurity’’ with correlation frequency  $\Gamma_T$ . The dipolar coupling constant  $A_h^z$  is expected to be smaller than

the constants  $A^\pm$  and  $A_z$  in Eq. (12) because on the average the protons are further away from the Fe $^{2+}$  (Ni $^{2+}$ ) moments. Thus the data in Fig. 9 for Cr $_7$ Ni and Cr $_7$ Fe can be tentatively fitted by an expression of the form,

$$T_1^{-1} = K \left[ \frac{1}{2} A^\pm (1/\Gamma_{exc}^\pm) + A^z / \Gamma_{exc}^z \right] + K A_h^z \frac{\Gamma_T}{\omega_N^2 + \Gamma_T^2}. \quad (15)$$

The full curves in Fig. 9 for Cr $_7$ Ni and Cr $_7$ Fe correspond to Eq. (15) with the following fitting parameters:  $K[A^\pm/2\Gamma_{exc}^\pm + A^z/\Gamma_{exc}^z] = 1100$  s $^{-1}$ ;  $A_h^z = 1.7 \times 10^{43}$  cm $^{-6}$ ; and  $\Gamma_T = 9 \times 10^8$  rad Hz for Cr $_7$ Ni, and  $K[A^\pm/2\Gamma_{exc}^\pm + A^z/\Gamma_{exc}^z] = 120$  s $^{-1}$ ;  $A_h^z = 3.8 \times 10^{42}$  cm $^{-6}$ ; and  $\Gamma_T = 4.6 \times 10^8$  rad Hz for Cr $_7$ Fe.

Regarding the first term in Eq. (15), one can observe that it corresponds to what expected on the basis of the same coupling constants  $A^\pm$  and  $A^z$ , derived above for Cr $_8$  and Cr $_7$ Cd, and exchange frequencies,  $\Gamma_{exc}^\pm$  and  $\Gamma_{exc}^z$ , almost one order of magnitude larger for Cr $_7$ Fe. This is not surprising since in the heterometallic rings the damping process of the precession of the spin due to inequivalency of the adjacent moments and/or the anisotropy can speed up the decay of the electronic correlation function. On the other hand, the energy conserving exchange fluctuations are not allowed for the Fe $^{2+}$  (Ni $^{2+}$ ) moments since they are different from the nearest-neighbor Cr $^{3+}$  moments. Thus only longitudinal spin-lattice fluctuations are allowed for the substituted ion. The value of the correlation frequency  $\Gamma_T$  for the longitudinal fluctuations of the Fe $^{2+}$  (Ni $^{2+}$ ) moment, is consistent with a slow fluctuation of the impurity spin due to the spin-lattice relaxation. The consistency of the small coupling constants  $A_h^z$  is more difficult to be determined in view of the semi-quantitative model adopted.

## V. SUMMARY AND CONCLUSIONS

We have presented and compared susceptibility and NMR data in three heterometallic rings with the corresponding homometallic ring Cr $_8$ . The singlet ground state,  $S=0$ , of the antiferromagnetic coupled ring Cr $_8$  is modified into a magnetic ground state with total spin  $S=3/2$  for Cr $_7$ Cd,  $S=1/2$  for Cr $_7$ Ni and Cr $_7$ Fe. The nearest-neighbor magnetic exchange coupling remains antiferromagnetic in all rings with a small change in the value of the effective  $J$ . Regarding the spin dynamics we have found that the proton relaxation rate is driven by a mechanism different at low temperature from the one at high temperature. For  $T < J/k_B$  the magnetic moments of the ions are strongly correlated and the nuclear relaxation is due to the modulation of the hyperfine field by the relaxation process of the total magnetization of the ring.<sup>15,16,25</sup> The relaxation process of the magnetization is dominated in AFM rings by a single correlation frequency  $\omega_c$  which is driven by spin-phonon interaction and is thus strongly temperature dependent.<sup>14,16,25</sup> This single correlation frequency can be extracted from nuclear relaxation measurements via a simple model.<sup>15</sup> By using here this simple model we were able to compare the spin dynamics in homometallic and heterometallic rings whereby we found a much higher correlation frequency for Cr $_7$ Ni and even higher for Cr $_7$ Fe.

AMIRI *et al.*PHYSICAL REVIEW B **82**, 144421 (2010)

This is a clear evidence of enhanced spin-phonon interaction in the heterometallic rings due most likely to the strong single ion anisotropy of, e.g.,  $\text{Fe}^{2+}$  as also found in Mossbauer measurements.<sup>27</sup> For  $T > J/k_B$  the magnetic moments of the ions become weakly correlated and the proton relaxation is dominated by the fluctuations of the individual paramagnetic moments. In this high-temperature region we have observed a drastic difference in the values of the  $T_1^{-1}$  in  $\text{Cr}_8$  and  $\text{Cr}_7\text{Cd}$  when compared to  $\text{Cr}_7\text{Ni}$  and  $\text{Cr}_7\text{Fe}$ . We have interpreted the effect as due to the change in the electron spin correlation function, whereby in the homometallic  $\text{Cr}_8$  and weakly perturbed  $\text{Cr}_7\text{Cd}$  rings the coherent precession of the spin around the applied field predicted for the transverse components in the isotropic Heisenberg model is allowed, while in the strongly perturbed  $\text{Cr}_7\text{Ni}$  and more so in  $\text{Cr}_7\text{Fe}$  this precession is completely overdamped. This agrees with the notion that in  $\text{Cr}_7\text{Ni}$  and  $\text{Cr}_7\text{Fe}$  the spin dynamics is perturbed by the substituted magnetic ion and that the distribution of spin density in the ring is nonuniform. The local spin-density redistribution in the ring could be obtained, in principle, from NMR measurements. As a matter of fact the local distribution of the spin density at the different ion sites in the ground state was measured in a previous publication in  $\text{Cr}_7\text{Cd}$  by  $^{57}\text{Cr}$  NMR and found to remain rather uniform

over the ring.<sup>6</sup> We have attempted to measure the spin density in the other heterometallic rings but the NMR signal of  $^{53}\text{Cr}$ ,  $^{57}\text{Fe}$ , and  $^{61}\text{Ni}$  could not be detected down to 1.4 K due to the combination of poor signal to noise ratio and very short  $T_2$ . A recent Mossbauer investigation of  $\text{Cr}_7\text{Fe}$  has shown a reduction in the expectation value of the  $\text{Fe}^{2+}$  ( $s=2$ ) spin moment to  $\langle s \rangle = 0.9$  and a strong magnetic single-ion anisotropy.<sup>27</sup> Thus measurements of NMR at the  $^{53}\text{Cr}$  site appear to be essential and will be attempted again at very low temperature by the use of a dilution refrigerator. Indirect evidence of a strong perturbation of the Cr spin density by insertion of Fe and Ni ions is inferred indirectly from the spin dynamics as discussed above.

## ACKNOWLEDGMENTS

The authors are grateful to P. Santini, S. Carretta, and G. Amoretti for useful discussions and suggestions. The present work was done with financial support from the NoE-MAGMANET network of the European community and PRIN-2008 project of the Italian Ministry of Research. Work at the Ames Laboratory was supported by the Department of Energy, Basic Energy Sciences, under Contract No. DE-AC02-07CH11358.

\*Corresponding author; houshang.amiri@unipv.it

<sup>1</sup>O. Kahn, *Molecular Magnetism* (VCH, Berlin, 1990); D. Gatteschi, R. Sessoli, and J. Villain, *Molecular Nanomagnets* (Oxford University Press, New York, 2006).

<sup>2</sup>I. S. Tupitsyn and B. Barbara, in *Magnetism: Molecules to Materials III*, edited by J. Miller and M. Drillon (Wiley-VCH, Weinheim, Germany, 2002).

<sup>3</sup>E. del Barco, A. D. Kent, S. Hill, J. M. North, N. S. Dalal, E. M. Rumberger, D. N. Hendrickson, N. Chakov, and G. Christou, *J. Low Temp. Phys.* **140**, 119 (2005); W. Wernsdorfer, *Adv. Chem. Phys.* **99**, 118 (2001).

<sup>4</sup>M. Affronte, T. Guidi, R. Caciuffo, S. Carretta, G. Amoretti, J. Hinderer, I. Sheikin, A. G. M. Jansen, A. A. Smith, R. E. P. Winpenny, J. van Slageren, and D. Gatteschi, *Phys. Rev. B* **68**, 104403 (2003).

<sup>5</sup>F. K. Larsen, E. J. L. McInnes, H. Eimkani, J. Overgaard, S. Piligkos, G. Rajaraman, E. Rentschler, A. A. Smith, G. M. Smith, V. Boote, M. Jennings, G. A. Timco, and R. E. P. Winpenny, *Angew. Chem., Int. Ed.* **42**, 101 (2003).

<sup>6</sup>E. Micotti, Y. Furukawa, K. Kumagai, S. Carretta, A. Lascialfari, F. Borsa, G. A. Timco, and R. E. P. Winpenny, *Phys. Rev. Lett.* **97**, 267204 (2006).

<sup>7</sup>F. Troiani, M. Affronte, S. Carretta, P. Santini, and G. Amoretti, *Phys. Rev. Lett.* **94**, 190501 (2005); F. Troiani, A. Ghirri, M. Affronte, S. Carretta, P. Santini, G. Amoretti, S. Piligkos, G. Timco, and R. E. P. Winpenny, *ibid.* **94**, 207208 (2005).

<sup>8</sup>G. A. Timco, S. Carretta, F. Troiani, F. Tuna, R. J. Pritchard, E. J. L. McInnes, A. Ghirri, A. Candini, P. Santini, G. Amoretti, M. Affronte, and R. E. P. Winpenny, *Nat. Nanotechnol.* **4**, 173 (2009).

<sup>9</sup>F. Borsa, A. Lascialfari, and Y. Furukawa, in *Novel NMR and*

*EPR Techniques*, edited by J. Dolinsek, M. Vilfan, and S. Zumer (Springer, New York, 2006).

<sup>10</sup>N. V. Gerbelev, Yu. T. Struchkov, G. A. Timco, A. S. Batsanov, K. M. Indrichan, and G. A. Popovich, *Dokl. Akad. Nauk SSSR* **313**, 1459 (1990).

<sup>11</sup>J. van Slageren, R. Sessoli, D. Gatteschi, A. A. Smith, M. Hellwell, R. E. P. Winpenny, A. Cornia, A.-L. Barra, A. G. M. Jansen, E. Rentschler, and G. A. Timco, *Chem.-Eur. J.* **8**, 277 (2002).

<sup>12</sup>M. Affronte, A. Ghirri, S. Carretta, G. Amoretti, S. Piligkos, G. A. Timco, and R. E. P. Winpenny, *Appl. Phys. Lett.* **84**, 3468 (2004).

<sup>13</sup>H. Amiri, M. Mariani, A. Lascialfari, F. Borsa, G. A. Timco, F. Tuna, and R. E. P. Winpenny, *Phys. Rev. B* **81**, 104408 (2010).

<sup>14</sup>A. Bianchi, S. Carretta, P. Santini, G. Amoretti, Y. Furukawa, K. Kiuchi, Y. Ajiro, Y. Narumi, K. Kindo, J. Lago, E. Micotti, P. Arosio, A. Lascialfari, F. Borsa, G. Timco, and R. E. P. Winpenny, *J. Magn. Mater.* **322**, 1262 (2010); A. Bianchi *et al.* (unpublished).

<sup>15</sup>S. H. Baek, M. Luban, A. Lascialfari, E. Micotti, Y. Furukawa, F. Borsa, J. van Slageren, and A. Cornia, *Phys. Rev. B* **70**, 134434 (2004).

<sup>16</sup>P. Santini, S. Carretta, E. Livioti, G. Amoretti, P. Carretta, M. Filibian, A. Lascialfari, and E. Micotti, *Phys. Rev. Lett.* **94**, 077203 (2005).

<sup>17</sup>M. Affronte *et al.*, *Polyhedron* **24**, 2562 (2005).

<sup>18</sup>C. P. Slichter, *Principles of Magnetic Resonance* (Springer-Verlag, New York, 1996).

<sup>19</sup>P. Khuntia, M. Mariani, M. C. Mozzati, L. Sorace, F. Orsini, A. Lascialfari, F. Borsa, C. Maxim, and M. Andruh, *Phys. Rev. B* **80**, 094413 (2009).

COMPARISON OF THE MAGNETIC PROPERTIES AND THE ...

PHYSICAL REVIEW B 82, 144421 (2010)

- <sup>20</sup>D. A. Levitt and R. E. Walstedt, *Phys. Rev. Lett.* **38**, 178 (1977).
- <sup>21</sup>A. W. Hunt, P. M. Singer, K. R. Thurber, and T. Imai, *Phys. Rev. Lett.* **82**, 4300 (1999).
- <sup>22</sup>G. Papavassiliou, M. Belesi, M. Fardis, and C. Dimitropoulos, *Phys. Rev. Lett.* **87**, 177204 (2001).
- <sup>23</sup>M. Belesi, A. Lascialfari, D. Procissi, Z. H. Jang, and F. Borsa, *Phys. Rev. B* **72**, 014440 (2005).
- <sup>24</sup>T. Moriya, *Prog. Theor. Phys.* **16**, 23 (1956); **28**, 371 (1962).
- <sup>25</sup>I. Rousochatzakis, A. Lauchli, F. Borsa, and M. Luban, *Phys. Rev. B* **79**, 064421 (2009).
- <sup>26</sup>P. Santini *et al.* (unpublished).
- <sup>27</sup>L. Cianchi, F. Del Giallo, M. Lantieri, P. Moretti, G. Spina, G. Timco, and R. Winpenny, *Solid State Commun.* **150**, 903 (2010).

## Superparamagnetic colloidal nanocrystal clusters coated with polyethylene glycol fumarate: a possible novel theranostic agent†

Houshang Amiri,<sup>ab</sup> Morteza Mahmoudi<sup>\*c</sup> and Alessandro Lascialfari<sup>†ad</sup>

Received 17th August 2010, Accepted 2nd November 2010

DOI: 10.1039/c0nr00603c

We report cell endocytosis, drug release, NMR relaxometry and *in vitro* MRI studies on a novel class of superparamagnetic colloidal nanocrystal clusters (CNCs) with various biocompatible coatings. It is shown that the transverse relaxivity  $r_2$ , the parameter representing the MRI efficiency in negative contrast agents, for the PVA-coated, PEGF-coated, and crosslinked PEGF-coated CNCs, is high enough to contrast suitably the magnetic resonance images. The same samples have shown a good ability also in drug releasing (particularly the crosslinked PEGF-coated compound), thus finally allowing us to propose this class of compounds for future applications in theranostics.

### 1. Introduction

Due to its possibility of noninvasive, three-dimensional examination of biological events in living organisms and its capability to formulate diagnosis and follow treatments, magnetic resonance imaging (MRI) has been recognized as a powerful technique in medicine.<sup>1–4</sup> In order to increase the contrast of the MRI images, which is essential for a better and more precise detection, contrast agents (CAs) can be used.<sup>5,6</sup> The gadolinium chelates are the most common compounds used as CAs: they are characterized by a strong paramagnetism due to the seven unpaired electrons, thus giving a source of shortening of the longitudinal  $T_1$  and transverse  $T_2$  nuclear relaxation times. However, the recently acquired good control in the synthesis of superparamagnetic (SP) compounds<sup>7–9</sup> gave new perspectives to the use of low-toxicity novel and possibly multifunctional CAs. The ideal multifunctional SP-based compound should be able to have applications not only in the MR Molecular Imaging but also in magnetic moving and separation, optical detection by fluorescence, magnetic hyperthermia (for local release of heat) and so on.<sup>7–10</sup> In this regard, superparamagnetic iron oxide nanoparticles (SPIONs) are the most promising candidate, not only for their efficacy in enhancing magnetic resonance image contrast but also to their high biocompatibility.<sup>11,12</sup> In order to increase the targeting ability of the SPIONs at cellular/nanoscale (e.g. cells, protein and biomolecules), in recent years a big effort has been done to label SPIONs with targeting molecules,<sup>13–15</sup> in the direction of the so-called Molecular Imaging.

SPIONs are commercially produced. Endorem® (by Guerbet Group, Feridex in the USA) is one of the most known commercial MRI contrast agents and it is constituted by a magnetic core (diameter ~6 to 7 nm) of mixed  $\gamma$ - $\text{Fe}_2\text{O}_3$  and  $\text{Fe}_3\text{O}_4$  oxides coated with dextran, giving a nanoparticle which has an average ~150 nm

hydrodynamic diameter. Despite the undoubted efficacy of Endorem®, problems of reproducibility of the MR images are often encountered, possibly because the nanoparticles present high polydispersity and different batches of sample possess different mix of the two iron oxides. The limited reproducibility together with the necessity of obtaining systems with better controlled microscopic properties, motivated many research groups to synthesize new monodispersed SPIONs families.

A fundamental ingredient for using SPIONs in MRI is the high value of the saturation magnetization that induces the shortening of  $T_2$  and, consequently, a better contrast in the image.<sup>16,17</sup> There are three ways for increasing the saturation magnetization of the nanoparticles *i.e.* the size enhancement, the uni-direction growth of magnetite nanoparticles and the synthesis of colloidal nanocrystal clusters (CNCs) starting from a collection of SPIONs.<sup>18</sup> Increasing the size of nanoparticles enhances the saturation magnetization and a particular ability is requested to not generate an unstable colloidal dispersion of nanoparticles that easily can agglomerate, precipitate and provoke a possible embolization of the capillary vessels.<sup>19–21</sup> On the other hand, it was shown that the polyvinyl alcohol (PVA) molecules act as a template in hot water (e.g. 70 °C), leading to the oriented growth of  $\text{Fe}_3\text{O}_4$  nanorods<sup>18</sup> although the saturation magnetization of the prepared nanorods was significantly increased, these systems were not fully stable. In order to overcome the problem, post-synthesis process (e.g. freezing/thawing technique) should be applied to fabricate stable nanorods with rigid walls.

The CNCs approach allows creation of a very stable colloidal dispersion with high saturation magnetization and superparamagnetic properties.<sup>16</sup> In addition, these CNCs have been used as colloidal photonic crystals with magnetically tunable stop bands covering the entire visible spectrum; they were prepared by hydrolyzing  $\text{FeCl}_3$  with the addition of a base agent (NaOH) at around 220 °C in a solution containing polyacrylic acid as a surfactant in diethylene glycol.<sup>16,22</sup>

Several synthesis methods for SPIONs have been suggested. However, due to their scale up capability and to the ability of controlling size, shape and surface characteristics, the chemical routes (co-precipitation, microemulsions, hydrothermal, solvent and solvent free thermal decomposition, sol-gel, polyol, sonochemical, and electrochemical deposition) are highly preferred by

<sup>a</sup> Department of Molecular Sciences Applied to Biosystems, Università degli Studi di Milano, I-20134 Milano, Italy

<sup>b</sup> Department of Physics "A. Volta", Università degli Studi di Pavia, I-27100 Pavia, Italy

<sup>c</sup> National Cell Bank, Pasteur Institute, Tehran, Iran

<sup>d</sup> Centro S3, CNR-Istituto di Nanoscienze, I-41125 Modena, Italy

† Electronic supplementary information (ESI) available: [DETAILS]. See DOI: 10.1039/c0nr00603c



the scientific community.<sup>3,17</sup> Among chemical routes, the co-precipitation is used widely due to its easy, efficient chemical pathway and the possibility to achieve both type of iron oxide nanoparticles *i.e.* magnetite ( $\text{Fe}_3\text{O}_4$ ) and maghemite ( $\gamma\text{-Fe}_2\text{O}_3$ ) through the forced hydrolysis of iron salt (*i.e.*  $\text{Fe}^{2+}$  and  $\text{Fe}^{3+}$ ) solutions (*e.g.* in deionized (DI) water) in the presence of the base. The main problem of the co-precipitation method is its poor size, shape and monodispersity control.<sup>20</sup> In order to overcome the problem, Mahmoudi *et al.*<sup>19</sup> employed a novel design of experimental methodology, in agreement also with the resulting 3-D response surfaces, it was shown that optimum regions for stirring rate and molarity could be obtained to synthesize coated SPIONs with desirable size, purity, magnetization and shape. It must be remarked that particles with diameter bigger than 50 nm are mainly captured by the reticuloendothelial system, making them suitable for, but confining themselves to, liver or spleen imaging/therapy.<sup>24</sup>

The aim of the present work is the synthesis and first efficiency tests for biomedical purposes of highly water dispersible and biocompatible coated magnetite CNCs (composed of several single magnetite crystallites approximately 5 nm in size) with high saturation magnetization and superparamagnetic properties, using an easy and optimized-co-precipitation method. The CNCs are coated with crosslinked poly(ethylene glycol)-co-fumarate (PEGF); the first use of this hydrogel on the surface of CNCs, which have the potential to decrease the protein interaction and to reduce the drug burst effect (*i.e.* quick release of drugs upon injection), has been reported by Mahmoudi and co-workers.<sup>25–27</sup> The potentialities of the samples here investigated in drug release and MRI contrast are evidenced. As it will be shown, the obtained crosslinked-coated SPIONs are ideal candidates for ‘*theranostics*’ (*i.e.* therapy and diagnostics applications with the same compound), tracing the pathway for targeted drug delivery and imaging.

## 2. Materials and methods

### 2.1. Materials

Iron salts (*i.e.* chloride) and sodium hydroxide (NaOH), with analytical grades, were purchased from Merck Inc. (Darmstadt, Germany) and used without further purification. Polyvinyl alcohol ( $M_w = 30\,000\text{--}40\,000$ ) was obtained from Fluka. PEG diol ( $M_w = 1\text{ kDa}$ ), fumaryl chloride, calcium hydride and propylene oxide were all purchased from Aldrich (Milwaukee, MN, USA). Ammonium persulfate and methylene chloride (DCM) were obtained from Merck (Germany). Fumaryl chloride was purified by distillation at 161 °C under ambient pressure. Tamoxifen (TMX) and Doxorubicin (DOX) were obtained from Pharma Chemie Company (Tehran, Iran). Anhydrous DCM was obtained by distillation under reflux condition for 1 h in the presence of calcium hydride. Other solvents were reagent grades and used without any further purification.

### 2.2. Preparation of SPIONs

SPIONs were prepared *via* the well known co-precipitation method, which was optimized previously.<sup>19</sup> Typically, iron salts (the mole fraction of  $\text{Fe}^{2+}$  to  $\text{Fe}^{3+}$  was adjusted to 1 : 2) were dissolved in DI water containing 0.5 M HCl and all solutions

were deoxygenated by the bubbling process with argon gas. The magnetite nanoparticles were precipitated by dropwise addition of iron salt solutions to NaOH solutions (with various molarities) under an argon atmosphere. In order to control mass transfer, which may allow particles to combine and build larger polycrystalline particles, turbulent flow was created by placing the reaction flask in an ultrasonic bath and changing the homogenization rates during the first 2 minutes of the reaction.<sup>19</sup> It is notable that the stirring rate was fixed at 9000 rpm for all samples in the synthesis period (1 h). Various molarities of the NaOH solutions (1, 2, 3, and 4) were examined. The obtained  $\text{Fe}_3\text{O}_4$  nanoparticles were collected by external magnetic field and re-dispersed in DI water.

### 2.3. Preparation of PVA-coated SPIONs

PVA was dissolved in DI water and was added to the alkaline solution before introducing the iron salts. Then the method, which is given in Section 2.2, was employed in order to obtain coated nanoparticles.

### 2.4. Preparation of PEGF

The Temenoff method was used for the preparation of PEGF macromer.<sup>28</sup> Commonly, 0.03 mole of PEG diol was dissolved in 100 ml of anhydrous methylene chloride (DCM) in a three-necked 250 ml reaction flask equipped with a reflux condenser and a magnetic stirrer. Propylene oxide was employed as a catalyst for binding to the HCl, which is produced during the

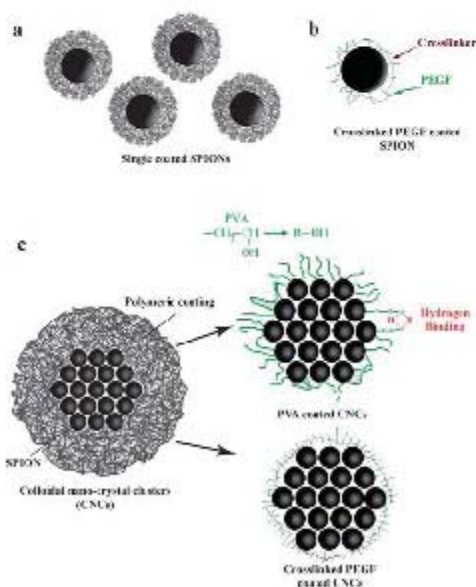


Fig. 1 Schemes of the various synthesized magnetic nanoparticles including (a) single coated SPIONs, (b) crosslinked coated SPION, and (c) PVA- and crosslinked PEGF-coated CNCs.

polymerization. The purified fumaryl chloride was dissolved in 50 ml of DCM and added dropwise in 1 h to the stirred reaction flask at  $-2\text{ }^{\circ}\text{C}$  under nitrogen atmosphere. Consequently, the reaction temperature was enhanced to room temperature and run overnight. In order to remove the by-product (e.g. chlorinated propanols), the product was washed with 0.1 N NaOH several times. The PEGF macromer was then obtained by rotoevaporation, dried at  $25\text{ }^{\circ}\text{C}$  in vacuum for 24 h, and then stored at  $-15\text{ }^{\circ}\text{C}$  until further use.

### 2.5. Preparation of crosslinked-PEGF-coated SPIONs

The synthesis stages and parameters of PEGF were fully described in a previous report.<sup>26</sup> The obtained PEGF solution was diluted in DI water and was added to the alkaline solution before introducing the iron salts. Then the method, which is

given in Section 2.2., was employed in order to obtain coated nanoparticles. The coated-SPIONs were then collected by external magnetic field and re-dispersed in DI water in order to remove the unbound polymers. The crosslinking of the unsaturated coating was started with ammonium persulfate  $[(\text{NH}_4)_2\text{S}_2\text{O}_8]$  as initiator system<sup>29</sup> and an optimized amount of accelerator (DMAEMA)<sup>26</sup> via the redox polymerization. After stirring for 2 h, the particles were washed several times and were kept at  $4\text{ }^{\circ}\text{C}$  for future use. A schematic representation of the various synthesized magnetic nanoparticles is shown in Fig. 1.

### 2.6. Drug loading of CNCs

Tamoxifen citrate (TMX), which is an anti-oestrogen drug for treatment of breast cancer,<sup>30</sup> and doxorubicin (DOX), an anti-cancer drug which has therapeutic index of 1.2–1.4 and gives

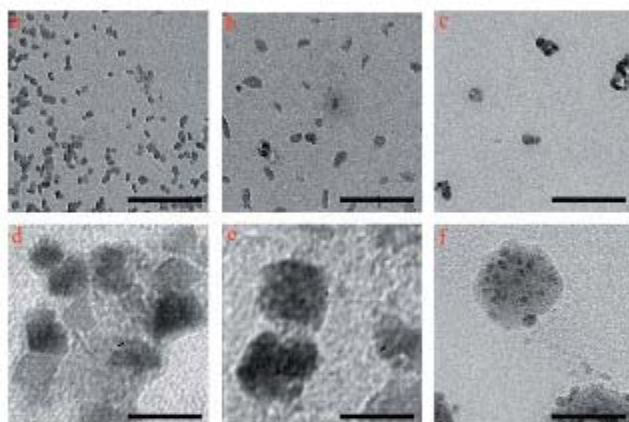


Fig. 2 TEM images of (a) the bare SPIONs, and magnetic CNCs obtained from the solutions with the molarity of (b) 1, (c) 2, (d) 3, and (e) 4 in the presence of PVA; (f) TEM image of the crosslinked-PEGF coated CNCs prepared from the solution with the molarity of 4. The scale bar is 50 nm.

Table 1 Average diameter size of SPIONs and CNCs, measured by XRD (see Fig. 4), TEM, and DLS

| Sample           | Remark                                          | Average size of magnetic cores measured by XRD/nm | Average hydrodynamic size measured by TEM/nm | Average hydrodynamic size measured by DLS/nm |
|------------------|-------------------------------------------------|---------------------------------------------------|----------------------------------------------|----------------------------------------------|
| Bare SPIONs      | There was no surfactant in the synthesis medium | 5                                                 | $5(\text{core size}) \pm 1.1$                | — <sup>a</sup>                               |
| PVA-coated CNCs  | Synthesis base molarity was 1                   | 5                                                 | $10.5 \pm 1.7$                               | 12.5                                         |
|                  | Synthesis base molarity was 2                   | 4.5                                               | $21 \pm 2.3$                                 | 23                                           |
|                  | Synthesis base molarity was 3                   | 5                                                 | $33 \pm 3.1$                                 | 41.5                                         |
|                  | Synthesis base molarity was 4                   | 4.5                                               | $48 \pm 4.9$                                 | 55.1                                         |
| PEGF-coated CNCs | Polymeric shell has been cross-linked           | 5                                                 | $52 \pm 5.6$                                 | 56.5                                         |

<sup>a</sup> Since bare SPIONs are very eager to reduce their surface energy in the absence of surfactants, severe agglomeration may occur; hence, their DLS data are not reliable.



good activity on solid tumor,<sup>41</sup> were selected as a model drug. The same amounts of PVA-, non-cross-linked PEGF- and cross-linked PEGF-coated CNCs, which are defined by atomic absorption, were dried in vacuum at 40 °C. Phosphate Buffered Saline (PBS) with pH of 7.4 containing 1 mg drug per ml was added to the dried CNCs and a stable colloidal suspension is formed by dispersion of the CNCs with both ultrasonic probe and homogenization. Due to their hydrogel properties, PVA and PEGF adsorbed the PBS containing drugs on their structures. After 10 h of incubation, the CNCs were collected using external magnetic field and re-dispersed in fresh PBS. In this case, the drug is going to be released from the polymeric shells due to their high-gradient concentration compared to the fresh PBS. Drug release data were collected for the duration of 200 and 300 hours for TMX and DOX, respectively. Two millilitre of each sample was centrifuged at selected times and the drug concentration measured in the supernatant using an ultraviolet (UV) spectrometer (Milton Roy Spectronic 601) at 277 and 498 nm for TMX and DOX, respectively. The calibration curves of drugs were drawn and their concentrations in PBS solution were measured before and after interaction with CNCs by UV spectrometry, in order to define the approximated amount of drug which is adsorbed at the surface of the CNCs. Consequently, the differences between the obtained amounts were taken as drug uptake by the CNCs. All release and adsorption measurements were done in triplicates and the standard deviations calculated.

### 2.7. Cell endocytosis assessments

Mouse fibroblast adhesive cells (L929) were obtained from the National Cell Bank of Iran (NCBI) at the Pasteur Institute of Iran. The seeded-cells (after 24 h) cultured in DMEM (Gibco, USA) supplemented with 10% fetal bovine serum (FBS) (Gibco, USA) and 1% streptomycin-penicillin (Gibco, USA) at 37 °C in a 5% CO<sub>2</sub> atmosphere were exposed to the surface-saturated<sup>42</sup> PVA-coated CNCs and cross-linked PEGF-coated CNCs with the iron concentration of 100 µg ml<sup>-1</sup>; it is notable that the iron concentrations of various CNCs were defined and fixed by atomic absorption.

### 2.8. Experimental methods

**2.8.1. Samples characteristics.** Morphology and size of the nanoparticles were investigated by Transmission Electron Microscope (TEM) (ZEISS, EM-10C, Germany) operating at 100 kV and Scanning Electron Microscope (SEM) (Philips-XL30) after placing and drying a drop of the suspension on a copper grid. X-Ray Diffraction (XRD) analysis to characterize the phases was carried out on a Siemens D5000 X-ray diffractometer using filtered Cu K $\alpha$  ( $\lambda = 1.54062$  Å) radiation. The average size of the nanoparticles was calculated from the broadening of the characteristic XRD peak (*i.e.* (311)) using the Scherrer formula. Mean size of nanoparticles was determined by Dynamic Light Scattering (DLS; Zetasizer model ZEN 1600, nano laser 633 nm). Furthermore, the surface charge on the nanoparticles was measured through the  $\zeta$  potential using phase-analysis light scattering (ZetaPALS) (Brookhaven Instruments Corporation, Holtsville, NY).

For the TEM analysis, the cells were fixed with 2.5% pentane-1,5-dial in a 0.1 M sodium cacodylate buffer (pH = 7.4) and post-fixed in 1% osmium tetroxide. After a final wash with the sodium cacodylate buffer, the specimens were dehydrated through a graded series of alcohol baths (30–100%) and then embedded in Epon resin. Ultrathin sections were cut using a Reichert-Jung Ultracut E ultramicrotome, transferred onto 200-mesh Cu TEM grids with formvar support film, and stained with uranyl acetate and lead citrate (see Fig. S2 in the ESI†). The samples were imaged with an FEI Tecnai 12 TEM equipped with a Gatan CCD Camera Model 792 at an accelerating voltage of 120 kV.

**2.8.2. SQUID magnetometry.** Magnetization measurements have been performed on the solid (dry powder) samples using a Quantum Design Superconducting Quantum Interference Device (SQUID) MPMS-XL7 magnetometer. The temperature dependence of the magnetization has been studied in the temperature range 2–300 K by collecting zero-field-cooling (ZFC) and field-cooling (FC) curves at  $H = 10$  mTesla applied magnetic field. To investigate the behavior of the magnetization as a function of applied magnetic field, hysteresis experiments in the range of  $-5 \text{ Tesla} \leq H \leq +5 \text{ Tesla}$  have been performed at both  $T = 2 \text{ K}$  and  $T = 300 \text{ K}$ .

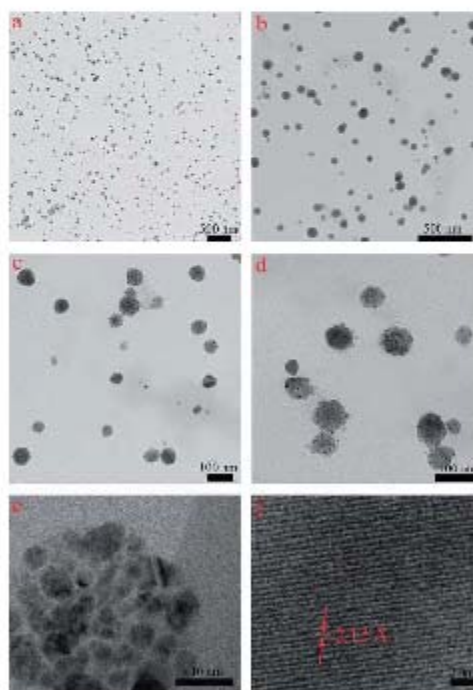
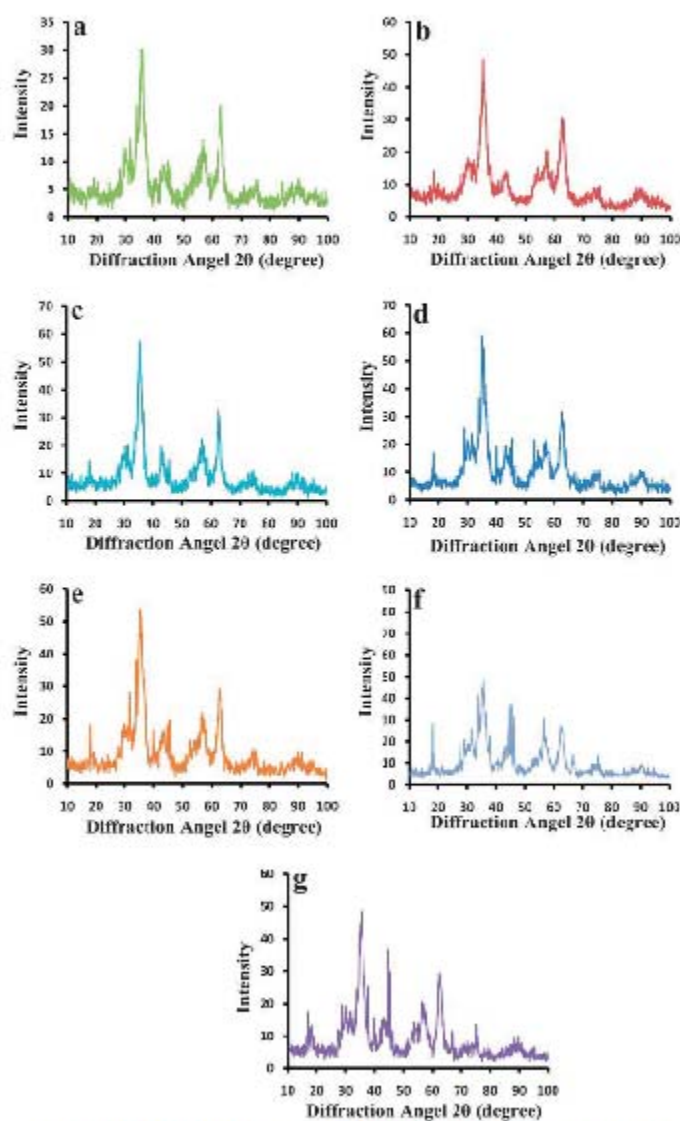


Fig. 3 (a–e) TEM images of crosslinked PEGF-coated CNCs with various magnifications; (f) high resolution TEM showing the lattice fringes of single SPION core.

**2.8.3. NMR relaxometry.** The  $^1\text{H}$  nuclear magnetic resonance dispersion (NMR-D) profiles were determined, at room temperature, by measuring the longitudinal  $T_1$  and transverse  $T_2$  nuclear relaxation times, in the frequency range  $10\text{ kHz} \leq \nu \leq 64\text{ MHz}$  for  $T_1$  and  $4\text{ MHz} \leq \nu \leq 64\text{ MHz}$  for  $T_2$ . The frequency ranges cover the typical frequencies of the MRI clinical imagers,

*i.e.*  $\nu = 8.5, 21,$  and  $63\text{ MHz}$ , corresponding to the magnetic fields  $\sim 0.2, 0.5$  and  $1.5\text{ T}$ .

For the frequency range  $10\text{ kHz} \leq \nu \leq 10\text{ MHz}$ , the NMR data were collected with a Smartracer Stellar relaxometer using the Fast-Field-Cycling technique<sup>27</sup> while for  $\nu > 10\text{ MHz}$  a Stellar Spinmaster spectrometer has been employed. Standard radio



**Fig. 4** XRD patterns of (a) the bare SPIONs and the PVA coated CNCs obtained from the solutions with the molarity of (b) 1, (c) 2, (d) 3, and (e) 4; (f) and (g) XRD patterns of PEGF coated CNCs and crosslinked PEGF coated CNCs, respectively.



frequency excitation sequences CPMG-like and saturation-recovery were applied to determine  $T_2$  and  $T_1$  values, respectively.

**2.8.4. *In vitro* MRI experiments.** *In vitro* MRI experiments were performed at 8.5 MHz using a 0.2 Tesla Artoscan Imager by Esaote S.p.A. Vials of the samples were placed in the scanner and coronal images were acquired. We used a Spin Echo (SE) pulse sequence with the following imaging parameters: repetition time (TR)/echo time (TE)/number of excitations (NEX) = 2000 ms/80 ms/1, matrix =  $256 \times 192$ , and field of view (FOV) =  $180 \times 180$ .

### 3. Results and discussion

#### 3.1. Electron microscopy and XRD characterizations of CNCs

TEM of the bare SPIONs showed uncoated SPIONs with the mean diameter of 5 nm in the absence of surfactants (Fig. 2a). By increasing the alkalinity of the solution (NaOH molarity from 1 to 4) in the presence of PVA, the magnetite nanoparticles spontaneously aggregate to form CNCs, as shown in the representative TEM images in Fig. 2b–e. It is noted that the single

coated SPIONs were formed in the lowest base molarity (*i.e.* 1). According to the TEM images, these monodisperse PVA-coated CNCs consist of superparamagnetic magnetite nanoparticles with the size of 5 nm. The hydrodynamic size of the obtained monodispersed CNCs is about 50 nm and increases by simply increasing the molarity of NaOH while keeping all the other parameters fixed. The same behavior was detected for the CNCs which were synthesized by using a high-temperature hydrolysis reaction in the presence of polyacrylic acid.<sup>6,22</sup>

In order to define the polydispersity of the various coated SPIONs, we calculated the variance over 20 particles in the TEM images using the standard formula (data reported in Table 1).<sup>24</sup>

It is well recognized that the saturation magnetization of the CNCs is enhanced by increasing their size; hence we employed the CNCs, which were synthesized in basic molarity of 4, for crosslinkable PEGF coating. TEM and SEM images of cross-linked magnetite CNCs revealed the existence of a rigid shell on the surface of iron oxide nanoparticle clusters (Fig. 2g and h). From Fig. 2g and h and 3a–f it can be concluded that PEGF has been crosslinked on the surface of the CNCs. The XRD patterns of the samples are illustrated in Fig. 4. The average size of the nanoparticles was calculated from the broadening of the XRD peaks (the full width at half maximum (FWHM) of the (311) reflection) using the Scherrer formula:  $d = 0.9\lambda/(w - w_i) \cos(\theta)$ , where  $d$  is the crystal diameter,  $w$  and  $w_i$  are the half-intensity width of the relevant diffraction peak and the instrument broadening, respectively,  $\lambda$  is the X-ray wavelength, and  $\theta$  is the angle of diffraction. The XRD spectra for all samples match well with magnetite ( $\text{Fe}_3\text{O}_4$ , reference JCPDS No. 82-1533), indicating that the samples have a cubic crystal system.

#### 3.2. Magnetic characterization of CNCs

**3.2.1. SQUID magnetometry.** ZFC and FC magnetization curves collected on different CNCs at  $H = 10$  mT are shown in Fig. 5. The curves display the typical behaviour of superparamagnetic nanoparticles. The blocking temperatures  $T_B$ , corresponding to the maximum in the ZFC curves, fall in the temperature range 145–180 K. Below  $T_B$ , the spins freeze and the

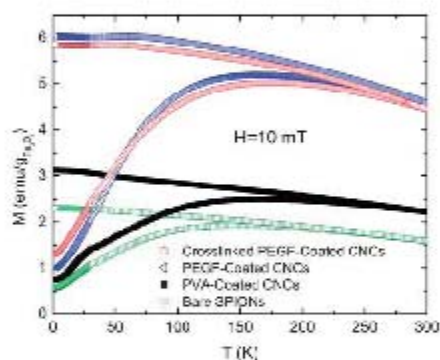


Fig. 5 ZFC and FC magnetization measurements of dry powder of CNCs. The data are reported per gram of magnetite.

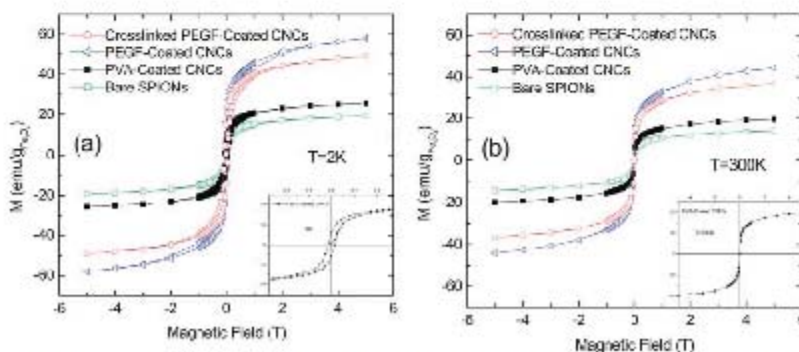


Fig. 6 Magnetization vs. magnetic field at (a) 2 K and (b) 300 K for all the CNCs; the insets (with the same units) are zooms on the curves of PVA-coated CNCs.

**Table 2** Magnetic parameters extracted from ZFCFC curves and hysteresis loops

| Compound                    | Bare SPIONs | PVA-coated CNCs | PEGF-coated CNCs | Crosslinked PEGF-coated CNCs |
|-----------------------------|-------------|-----------------|------------------|------------------------------|
| $T_g/K$                     | 148.54      | 166.54          | 161.26           | 178.34                       |
| $H_c/mT$                    | 53.8        | 56.1            | 53.0             | 54.9                         |
| $M_r/emu$ per $g_{Fe_3O_4}$ | 5.31        | 7.16            | 16.27            | 14.73                        |

system enter the blocked regime with typical out-of-equilibrium behaviour.<sup>34-36</sup>

In Fig. 6a and b the hysteresis curves, collected at  $T = 2$  K and 300 K, are reported. The low temperature curves (Fig. 6a) are slightly open with small coercive fields in the range 53 mTesla  $< H_c < 57$  m Tesla and a small remanent magnetization, 5 emu per  $g_{Fe_3O_4}$ ,  $< M_r < 17$  emu per  $g_{Fe_3O_4}$ , while the high temperature ones (Fig. 2c) are not open, as observed for SPIONs and superparamagnetic CNCs with the dimensions of the magnetic core similar to our samples.<sup>20,23,37-41</sup> The extracted data are given in Table 2.

**3.2.2. NMR relaxometry.** The efficiency of a MRI CA is determined by measuring the  $^1H$  nuclear longitudinal  $r_1$  and transverse  $r_2$  relaxivities defined as:<sup>23</sup>

$$r_i = [(1/T_i)_c - (1/T_i)_d] / c \quad (i = 1, 2) \quad (1)$$

where  $(1/T_i)_c$  is the measured value on the sample, with iron concentration  $c$  (in mM), and  $(1/T_i)_d$  refers to the diamagnetic host solution (in our case PBS at physiological pH).

Once  $r_1$  and  $r_2$  are measured as a function of frequency, the NMR-D profiles are obtained. The NMR-D profiles for all samples and for the commercial compound Endorem® are shown in Fig. 7a and b. Fig. 7a shows that the longitudinal relaxivity values of the PEGF-coated and the PVA-coated CNCs at very low frequencies are comparable with Endorem® while for higher frequencies all the samples have lower values. Fig. 7b shows that the transverse relaxivities of all the samples are approximately constant in the frequency range of study. The transverse relaxivities of PEGF-coated, PVA-coated, and

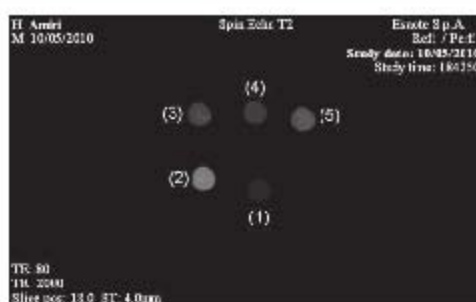


**Fig. 8** MRI image of vials containing different samples with the same iron concentrations ( $0.02 \text{ mg ml}^{-1}$ ) obtained by Arioscan S.p.A. imager at  $H = 0.2$  T. (1) Endorem®, (2) bare SPIONs, (3) PVA-coated CNCs, (4) PEGF-coated CNCs, (5) crosslinked PEGF-coated CNCs. Image parameters are given in the text.

crosslinked PEGF-coated CNCs are almost comparable to Endorem®. As the  $r_2$  value is the crucial parameter for a negative contrast agent (the higher  $r_2$ , the better the MRI contrast), our samples can be in principle usefully employed in MRI.

**3.2.3. In vitro MRI experiments.** In order to investigate the efficiency of our samples at the level of *in vitro* MRI, we collected images at  $\sim 8.5$  MHz. Five vials containing four of our samples plus Endorem® have been prepared with the same iron concentration  $c = 0.02 \text{ mg ml}^{-1}$  and placed in the MRI Imager. The obtained image, using a Spin Echo (SE) pulse sequence, is shown in Fig. 8. The other experimental parameters were reported in Section 2.8.4. As one can see, PEGF-coated (4), PVA-coated (3), and crosslinked PEGF-coated (5) CNCs show a contrast nicely comparable with Endorem®. Fig. 8 shows that the signal is the lowest (*i.e.* maximum efficiency) for PEGF-coated particles and increases going to PVA-coated, crosslinked PEGF-coated CNCs and bare SPIONs. As we know that the higher the  $r_2$  the lower the signal, these results are fully consistent with the relaxometry data (see Fig. 7b).

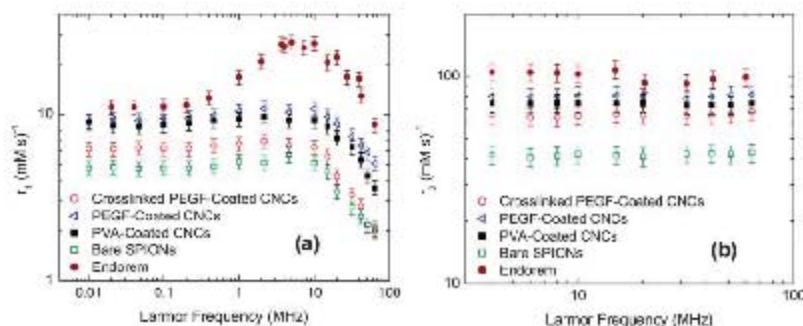


**Fig. 7** (a) Longitudinal  $r_1$  and (b) transverse  $r_2$   $^1H$  NMR relaxivities vs. Larmor frequency for all CNCs together with the commercial CA, Endorem®.



### 3.3. Cell endocytosis and drug release studies

Previous studies confirmed the biocompatibility of PVA- and PEGF-coated SPIONs using the 3-(4,5-dimethylthiazol-2-yl)-2,5-diphenyltetrazolium bromide (MTT) assay.<sup>26,27</sup> Here, TEM was employed to investigate the possibility of entrance of the coated CNCs inside the L929 cells through a mechanism of uptake induced by their hydrophilic and biocompatible coatings; the uptake of these CNCs are essential for the cellular drug delivery and imaging purposes. As shown in Fig. 9b and c, both the PVA-coated CNCs and cross-linked PEGF-coated CNCs accumulated within the cells. This is likely to be due to electrostatic interactions between the negatively charged membranes and the positively charged surface-saturated PVA-coated CNCs and cross-linked PEGF-coated CNCs (9.5 and 11 mV, respectively), resulting in the uptake of the CNCs by the cells. The TEM observations show that the CNCs were present in the membrane-bound multivesicular bodies, having entered the cells as larger aggregates. Little organelle damage following exposure to both the PVA-coated CNCs and crosslinked PEGF-coated CNCs is also evident. The level of damage in the cells exposed to the coated CNCs was negligible, confirming the biocompatibility of magnetic CNCs. The nuclei and organelles in the control cells remained intact.

Fig. 10 illustrates drug releases from PEGF- and crosslinked PEGF-coated single nanoparticles, PVA-, PEGF- and cross-linked PEGF-coated CNCs over 12 days. According to the results, the crosslinking of the PEGF hydrogel caused a significant decrease in the burst effect not only for the coated CNCs but also for the single coated SPION; thus, as predicted, the cross-linked system has a great potential to control the burst effect even in this very simple drug loading system. Here, the drug was trapped in the crosslinked shell and consequently the barriers, for the reduction of the drug-gradient concentration, are gradually

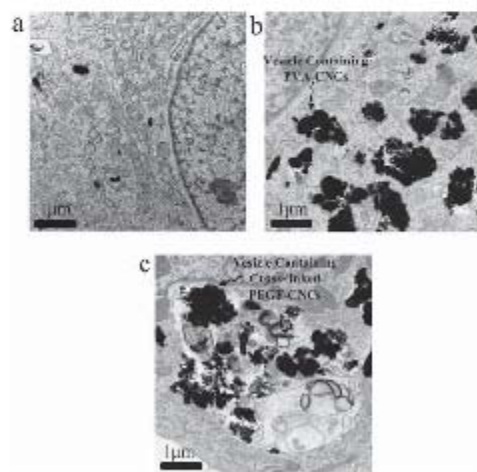


Fig. 9 (a) TEM image of the control L929 cells. (b) TEM image of the L929 cells exposed to the PVA-coated CNCs. (c) TEM image of the L929 cells exposed to the cross-linked PEGF-coated CNCs.

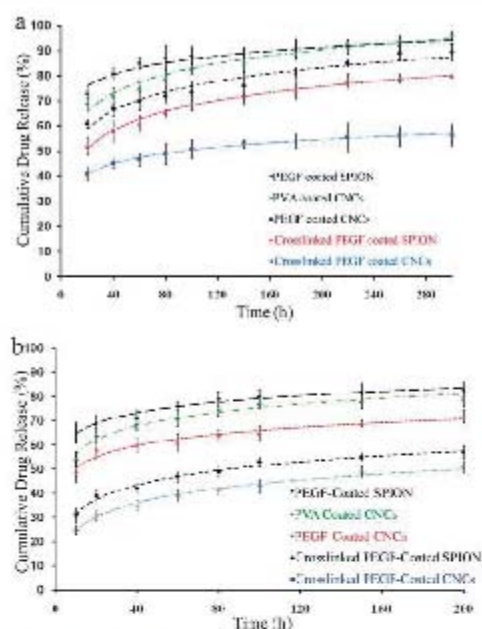


Fig. 10 Release profile of (a) TMX and (b) DOX from PEGF- and crosslinked PEGF-coated single nanoparticles; and PVA- (obtained by the base molarity of 4), PEGF- and crosslinked PEGF-coated CNCs over 300 and 200 hours, respectively.

increased because of the existence of the crosslinked shell; hence its release (due to the lower diffusion process) has been kinetically controlled. More specifically, the TMX burst effect of the single PEGF coated SPIONs and PEGF coated CNCs reduced from 73% to 52% and from 61% to 41%, respectively. The crosslinked PEGF-coated CNCs have the lower burst effect compared to the single coated nanoparticles; the reason is the lower chemical activity of CNCs in comparison to single nanoparticle one. Additionally, PVA coated CNCs have a burst effect similar to non-crosslinked PEGF one. It should be noted that a better control over burst effect could be obtained using more sophisticated drug loading methods, like *e.g.* conjugating the drug to the crosslinked PEGF CNCs.

### 4. Conclusions

We have synthesized a class of PVA-, PEGF- and cross-linked PEGF-coated colloidal nanocrystals with a magnetic core of magnetite. In these systems the drug burst effect and thus the drug release can be obtained in a massive way. In addition, the efficiency of our systems as MRI contrast agents has been demonstrated by the relatively high values (almost comparable to the commercial compound Endorem®) of the <sup>1</sup>H NMR transverse relaxivity  $r_2$  in the PEGF-coated, crosslinked PEGF-coated and PVA-coated CNCs, at frequencies of clinical application. This efficiency has been confirmed by MRI *in vitro*

experiments. The ability of our PEGF-coated, PVA-coated and crosslinked PEGF-coated systems in both releasing drug and contrasting MR images, open the way to the synthesis of a well controlled novel class of theranostic agents.

### Acknowledgements

The SQUID and NMR/MRI experiments have been performed with the funds from PUR2008 project from Università degli Studi di Milano. M. Corti is gratefully acknowledged for his help in experimental measurements.

### References

- 1 E. M. Haacke, R. W. Brown, M. R. Thompson and R. Venkatesan, in *Magnetic Resonance Imaging. Physical Principles and Sequence Design*, Wiley-Liss, 1999.
- 2 M. V. Yigit, D. Mazumdar and Y. Lu, *Bioconjugate Chem.*, 2008, **19**, 412-417.
- 3 J. Lee, M. J. Zylka, D. J. Anderson, J. E. Burdette, T. K. Woodruff and T. J. Meade, *J. Am. Chem. Soc.*, 2005, **127**, 13164-13166.
- 4 L. Frullano, B. Tejerina and T. J. Meade, *Inorg. Chem.*, 2006, **45**, 8489-8491.
- 5 See various contributions in *The Chemistry of Contrast Agents in Medical Magnetic Resonance Imaging*, ed. A. E. Merbach and E. Toth, J. Wiley and sons, 2001.
- 6 M. Mahmoudi, M. Hosseinkhani, S. Laurent, A. Simchi, H. Hosseinkhani, W. S. Journey, K. Subramani and S. Broutry, *Chem. Rev.*, 2010, accepted.
- 7 A. G. Roa, R. Costo, A. F. Rebollo, S. Veintemillas-Verdaguer, P. Tartaj, T. Gonzalez-Carreno, M. P. Morales and C. J. Serna, *J. Phys. D: Appl. Phys.*, 2009, **42**, 224002.
- 8 Q. A. Pankhurst, J. Connolly, S. K. Jones and J. Dobson, *J. Phys. D: Appl. Phys.*, 2003, **36**, R167-R181.
- 9 Q. A. Pankhurst, N. K. T. Thanh, S. K. Jones and J. Dobson, *J. Phys. D: Appl. Phys.*, 2009, **42**, 224001.
- 10 C. C. Berry, *J. Phys. D: Appl. Phys.*, 2009, **42**, 224003.
- 11 L. Josephson, J. Lewis, P. Jacobs, P. F. Hahn and D. D. Stark, *Magn. Reson. Imaging*, 1988, **6**, 647-653.
- 12 M. Mahmoudi, S. Sant, B. Wang and T. Sen, *Adv. Drug Delivery Rev.*, 2010, DOI: 10.1016/j.addr.2010.05.006.
- 13 N. Nitin, L. E. W. LaCombe, O. Zarkiya, X. Hu and G. Bao, *JBIC J. Biol. Inorg. Chem.*, 2004, **9**, 706-712.
- 14 M. Lewin, N. Carlesso, C.-H. Tung, X.-W. Tang, D. Cory, D. T. Scadden and R. Weissleder, *Nat. Biotechnol.*, 2000, **18**, 410-414.
- 15 L. Josephson, C.-H. Tung, A. Moore and R. Weissleder, *Bioconjugate Chem.*, 1999, **10**, 186-191.
- 16 J. Ge, Y. Hu, M. Biasini, W. P. Beyermann and Y. Yin, *Angew. Chem.*, 2007, **119**, 4420-4423.
- 17 M. Mahmoudi, M. A. Shokrgozar, A. Simchi, M. Imani, A. S. Milani, P. Stroeve, H. Vali, U. O. Hafeli and S. Bonakdar, *J. Phys. Chem. C*, 2009, **113**, 2322-2331.
- 18 M. Mahmoudi, A. Simchi, M. Imani, P. Stroeve and A. Sohrabi, *Thin Solid Films*, 2010, **518**, 4281-4289.
- 19 M. Mahmoudi, A. Simchi, M. Imani, A. S. Milani and P. Stroeve, *J. Phys. Chem. B*, 2008, **112**, 14470-14481.
- 20 A. Boni, M. Marinone, C. Innocenti, C. Sangregorio, M. Corti, A. Lascialfari, M. Mariami, F. Orsini, G. Poletti and M. F. Casula, *J. Phys. D: Appl. Phys.*, 2008, **41**, 134021.
- 21 M. Corti, A. Lascialfari, M. Marinone, A. Masotti, E. Micotti, F. Orsini, G. Ortaggi, G. Poletti, C. Innocenti and C. Sangregorio, *J. Magn. Magn. Mater.*, 2008, **320**, 316.
- 22 J. Ge, Y. Hu and Y. Yin, *Angew. Chem., Int. Ed.*, 2007, **46**, 7428-7431.
- 23 S. Laurent, D. Forge, M. Port, A. Roch, C. Robic, L. Vander Elst and R. N. Muller, *Chem. Rev.*, 2008, **108**, 2064-2110.
- 24 M. Arruebo, R. Fernandez-Pacheco, M. R. Ibarra and J. Santamaria, *Nano Today*, 2007, **2**, 22-32.
- 25 M. Mahmoudi, M. Imani and A. Simchi, *US Pat.*, pending, 2010.
- 26 M. Mahmoudi, A. Simchi, M. Imani and U. O. Hafeli, *J. Phys. Chem. C*, 2009, **113**, 8124-8131.
- 27 M. Mahmoudi, A. Simchi, M. Imani, A. S. Milani and P. Stroeve, *Nanotechnology*, 2009, **20**.
- 28 J. S. Temenoff, H. Shin, D. E. Conway, P. S. Engel and A. G. Mikos, *Biomacromolecules*, 2003, **4**, 1605-1613.
- 29 H. Park, J. S. Temenoff, Y. Tabata, A. Caplan and A. G. Mikos, *Biomaterials*, 2007, **28**, 3217-3227.
- 30 V. C. Jordan, *Br. J. Pharmacol.*, 2006, **147**, S269-S276.
- 31 A. Di Marco, M. Gaetani and B. Scarpinato, *Cancer Chemother. Rep.*, 1969, **53**, 33.
- 32 M. Mahmoudi, A. Simchi, M. Imani, M. A. Shokrgozar, A. S. Milani, U. Hafeli and P. Stroeve, *Colloids Surf., B*, 2010, **78**, 300-309.
- 33 W. E. Biles and J. J. Swain, *Optimization and Industrial Experimentation*, Wiley, New York, 1980.
- 34 U. Jeong, X. Teng, Y. Wang, H. Yang and Y. Xia, *Adv. Mater.*, 2007, **19**, 33.
- 35 R. H. Kodama, *J. Magn. Magn. Mater.*, 1999, **200**, 359.
- 36 J. L. Dormann, D. Fiorani and E. Tronc, Magnetic Relaxation in Fine Particle Systems, in *Advances in Chemical Physics, vol. XCIII*, ed. I. Prigogine and S. A. Rice, J. Wiley and sons, 1997.
- 37 L. Larigue, K. Oumzil, Y. Guari, J. Larionova, C. Guelrin, J. L. Montero, V. Barragan-Montero, C. Sangregorio, A. Caneschi, C. Innocenti, T. Kalavani, P. Arosio and A. Lascialfari, *Org. Lett.*, 2009, **11**, 2992.
- 38 M. F. Casula, P. Floris, C. Innocenti, A. Lascialfari, M. Marinone, M. Corti, R. A. Sperling, W. J. Parak and C. Sangregorio, *Chem. Mater.*, 2010, **22**, 1739.
- 39 E. Taboada, E. Rodriguez, A. Roig, J. Oro, A. Roch and R. N. Muller, *Langmuir*, 2007, **23**, 4583.
- 40 U. I. Tromsdorf, N. C. Bigall, M. G. Kaul, O. T. Bruns, M. S. Nikolic, B. Mollwitz, R. A. Sperling, R. Reimer, H. Hohenberg, W. J. Parak, S. Forster, U. Beisiegel, G. Adam and H. Weller, *Nano Lett.*, 2007, **7**, 2422.
- 41 J.-F. Berret, N. Schonbeck, F. Gazeau, D. El Kharrai, O. Sandre, A. Vacher and M. Airiau, *J. Am. Chem. Soc.*, 2006, **128**, 1755.



NANO MICRO  
Submitted to **small**

## Multifunctional Polymer-based Nanostructured Bio-ferrofluids: Novel MRI Contrast Agents

*Houshang Amiri, Rodney Bustamante, Angel Millán, Nuno J.O. Silva, Rafael Piñol, Lierni Gabilondo, Fernando Palacio, Paolo Arosio, Maurizio Corti, and Alessandro Lascialfari\**

[\*] Prof. A. Lascialfari Corresponding-Author,<sup>§##</sup> Dr. H. Amiri,<sup>§#</sup> Dr. P. Arosio,<sup>§+</sup> Prof. M. Corti<sup>##+</sup>

<sup>§</sup>Dipartimento di Scienze Molecolari Applicate ai Biosistemi, Università degli studi di Milano, and Consorzio INSTM, Milano Unit. Milano, I-20134 (Italy)

<sup>#</sup>Dipartimento di Fisica “A. Volta”, Università degli studi di Pavia. Pavia, I-27100 (Italy)

<sup>+</sup>Centro S3, CNR-Istituto di Nanoscienze. I-41125, Modena (Italy)

E-mail: [alessandro.lascialfari@unipv.it](mailto:alessandro.lascialfari@unipv.it)

Prof. F. Palacio, Dr. R. Bustamante,<sup>§</sup> Dr. A. Millán, Dr. R. Piñol, Dr. L. Gabilondo  
Instituto de Ciencia de Materiales de Aragón, CSIC-Universidad de Zaragoza. Zaragoza,  
50009 (Spain)

<sup>§</sup> On leave from Centro de Estudios Avanzados de Cuba, Habana, Cuba.

Dr. N. J.O. Silva

Departamento de Física and CICECO, Universidade de Aveiro. Aveiro, 3810-193,  
(Portugal)

Keywords: MRI, contrast agents, ferrofluids, relaxometry, multifunctional magnetic nanoparticles

We have investigated the MRI contrast efficiency of novel maghemite/polymer composite ferrofluids that contain anchoring groups for biofunctionalization, can incorporate fluorescent dyes and have shown low cellular toxicity in previous studies. We have determined that the magnetic core size for reaching the best MRI contrast efficiency is  $d \sim 15$  nm. Our experimental results allow us to propose first a set of optimal microstructural parameters for multifunctional superparamagnetic ferrofluids to be used in MRI medical diagnosis.

### 1. Introduction

The use of magnetic nanoparticles (MNPs) may lead to exciting new developments in biomedicine.<sup>[1-3]</sup> Attaching MNPs to a biological entity (e.g., cell, protein, enzyme,

antibody, drug, DNA, etc.) permits to perform a variety of operations (i.e., moving, fixing, counting, heating, locating, etc.) with minimal interaction, thus leading to a large number of applications.<sup>[4]</sup> For biomedical uses in general, physical performances are always subordinated to biocompatibility. Materials that have shown excellent magnetic properties can find severe validation difficulties for clinical applications. Another desirable feature is multifunctionality. The nanoparticles will be far more useful when they are provided with anchoring sites for biological vectors, luminescent labels, drugs, etc.<sup>[5]</sup> The ferrofluids used here have been designed ad hoc for biomedical applications taking into account these requisites in the following way:<sup>[6-8]</sup> a) the magnetic core is maghemite, one of the most biocompatible magnetic compounds,<sup>[9]</sup> the coating is made of biocompatible polymers, polyvinylpyridine (PVP) and polyethylenglycol (PEG), and the dispersing media is a phosphate buffer saline solution (PBS) with pH=7.4; b) they incorporate anchoring groups (-COOH) for biological vectors and luminescent dyes for live cell studies; (c) they have shown low toxicity in cells cultures, human blood, and *in vivo* experiments;<sup>[8]</sup> and (d) they are stable for years.<sup>[8]</sup>

A good applicative example of the use of MNPs is magnetic resonance imaging (MRI), which is one of the best non-invasive diagnostic techniques in medicine.<sup>[10]</sup> Despite the relatively high number of degrees of freedom for obtaining good MR images of the soft tissues of living beings, in some cases it is not possible to have enough image contrast to show the tissue anatomy or pathology of interest. In such cases, one has to use contrast agent (CA), generally based on paramagnetic or superparamagnetic substances. The CAs used in MRI are selected to induce a shortening of the spin-lattice  $T_1$  and/or spin-spin  $T_2$  relaxation times of the hydrogen nuclei within the tissues/regions where they are delivered, thus allowing a much better image contrast. Most commonly a paramagnetic CA, usually a gadolinium-based compound, is used.<sup>[11,12]</sup> Gadolinium-doped tissues and fluids appear extremely bright in MR images, and for this reason paramagnetic CAs are called positive CA. More recently superparamagnetic (SP) CAs, based on iron oxide MNPs,<sup>[13,14]</sup> have become commercially available. The regions where such agents are delivered appear darker and, therefore, they are called negative CA. The big advantage of this type of CA is their higher sensitivity that is expected to reach single cell level.<sup>[15]</sup>

In order to exploit the full potential of MNPs in MRI, it is necessary to determine the structure/performance relations that would lead to the optimal product. In fact, despite the great interest in synthesizing novel more efficient CAs, the influence of microstructural parameters like the kind of magnetic ion, the kind and thickness of the coating, the dimensions of the magnetic core and of the nanoparticle on the MRI efficiency, has been scarcely studied.<sup>[16]</sup> Studies of such kind on ferrites-based CA with different magnetic core dimensions and an amphiphilic polymer or micelles coatings have been reported.<sup>[17-20]</sup> In particular, an optimum magnetic core diameter,  $d \approx 8-12$  nm, has been suggested for particles having the same coating but with a thickness slightly dependent on the magnetic core size. Other authors have shown that the kind and thickness of coating have a marked influence on the relaxivity, as deduced from preliminary studies on Mn-ferrites-based compounds.<sup>[21]</sup>

Here we examine the relation between particle size, magnetic properties and CA efficiency in a polymer-based MNP system that, as described above, is biocompatible and suitable for *in vivo* applications, and has low cellular toxicity and a high capacity for multifunctionalization. We measured the  $^1\text{H}$  Nuclear Magnetic Resonance (NMR)

longitudinal  $r_1$  and transverse  $r_2$  nuclear relaxivities, these parameters measuring the increase of the nuclear relaxation rates per unit of magnetic center. In some of the investigated samples the transverse relaxivity, which is the most significant parameter for the efficiency of negative CAs, resulted comparable with or higher than commercial contrast agents. In order to confirm the MRI efficiency of our samples, we also performed some MRI *in vitro* experiments at  $\nu=8.5$  MHz using a low-field Imager.

This work has been carried out in parallel with similar studies about magnetic hyperthermia performances and toxicology. Thus, this is a first part of a general study aiming to develop a MNP system optimised for simultaneous diagnosis and therapy applications, the so-called theranostics.<sup>[22]</sup>

## 2. Results and Discussion

The characteristics of our ferrofluids are shown in Table 1. TEM images (Figure 1) show a uniform distribution of iron oxide nanoparticles encapsulated in a continuous polymer film. Most of the particles are rounded with an average size that increases regularly from 7.4 nm (sample A) to 15 nm (sample D) in relation to the  $\text{Fe}_2\text{O}_3/\text{PVP}$  and  $\text{Fe(II)}/\text{Fe(III)}$  ratios selected in the synthesis (Table 1). ED patterns on these particles are consistent with a maghemite crystal structure (central image in Figure 1). A small number of particles are elongated.

**Table 1.** Characteristics of the ferrofluid samples.

| Sample | $\text{Fe}_2\text{O}_3/\text{PVP}^a$ | $\text{Fe(II)}/\text{Fe(III)}^a$ | $D_H$<br>(nm) <sup>b</sup> | PDI <sup>c</sup> | $D_P$<br>(nm) <sup>d</sup> | SD<br>(nm) | $T_B$<br>(K) <sup>e</sup> |
|--------|--------------------------------------|----------------------------------|----------------------------|------------------|----------------------------|------------|---------------------------|
| A      | 0.5                                  | 0.5                              | 59                         | 0.16             | 7.4                        | 1.2        | 40                        |
| B      | 0.625                                | 0.5                              | 62                         | 0.18             | 8.6                        | 2.0        | 45                        |
| C      | 1                                    | 0.5                              | 92                         | 0.15             | 10.8                       | 2.9        | 160                       |
| D      | 1                                    | 0.9                              | 93                         | 0.14             | 15.0                       | 3.7        | 200                       |

[a] Molar ratios used in the preparation of the sample; [b] Hydrodynamic diameter; [c] Polydispersity index as obtained from DLS; [d] Maghemite particle diameter from TEM images; [e] Blocking temperature from AC magnetic susceptibility measurements at 30 Hz.

Histograms of the hydrodynamic sizes for the series of samples are shown in Figure 2. In all cases a monomodal distribution of particle diameters was found. The average hydrodynamic diameter  $D_H$  increases with the iron oxide/polymer ratio (Table 1) from 59 nm (sample A) to 92 nm (sample C), and it is hardly changing in samples with similar  $\text{Fe}_2\text{O}_3/\text{PVP}$  ratio but different particle size (samples C and D).

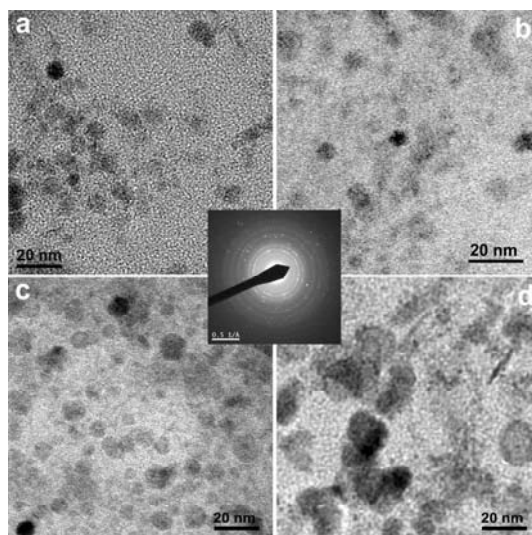


**Figure 1.** TEM images of samples A(a), B(b), C (c) and D (d) and a characteristic ED diffraction pattern of the particles. In sample D some of the crystals are faceted.

The average sizes of MNPs found by TEM represent about 10-15% of the average hydrodynamic sizes. Considering that at the pH of the medium (7.40) pyridine groups are hydrophobic and PEG residues are hydrophilic, then the structure of the MNP@PVP@PEG beads in suspension could be as follows: an inner part formed by a single folded PVP chain entrapping the MNPs by N-Fe coordination bonds, and an outer part formed by solvated PEG chains in a radial disposition.

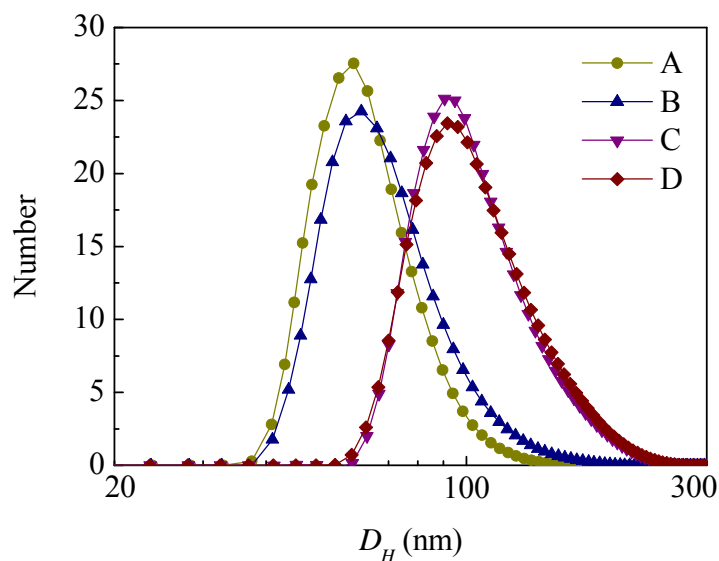


**Figure 2.** Histograms of the hydrodynamic sizes for the series of samples. Colour online.

The AC magnetic susceptibility as a function of temperature of samples A to D shows the characteristic behaviour of the superparamagnetic systems, with the in- and out-of-phase components ( $\chi'$  and  $\chi''$ , respectively) depending on frequency and with  $\chi''$  having a maximum at blocking temperature ( $T_B$ ), which depends on the frequency of the applied

field following an Arrhenius like function.<sup>[23,24]</sup> This shows that at low temperatures the magnetic moment of the magnetic nanoparticles can not be reversed, i. e. it is not able to cross the anisotropy energy  $E=KV_p$  ( $K$  is the anisotropy constant characteristic of the material and  $V_p$  is the volume of the magnetic nanoparticles) and follow the field. As temperature increases, the moments of the nanoparticles with lowest anisotropy energy start to reverse, being this process thermally activated and termed Néel relaxation. As expected from this model, at a given frequency,  $T_B$  increases with  $D_p$  (Figure 3).

Below 273 K these water based ferrofluids are frozen and thermal activation is the only mechanism available for reversal. At room temperature, the nanoparticles whose  $E$  is too high for the thermal activation to be effective (say  $E > k_B T$ ) have the possibility to reverse by mechanical rotation in the fluid (Brownian relaxation mechanism). The on-set of this mechanism leads to a sudden increase of  $\chi''$  in the samples with a relevant fraction of “large” nanoparticles (i. e. nanoparticles with  $E > k_B T$ ).

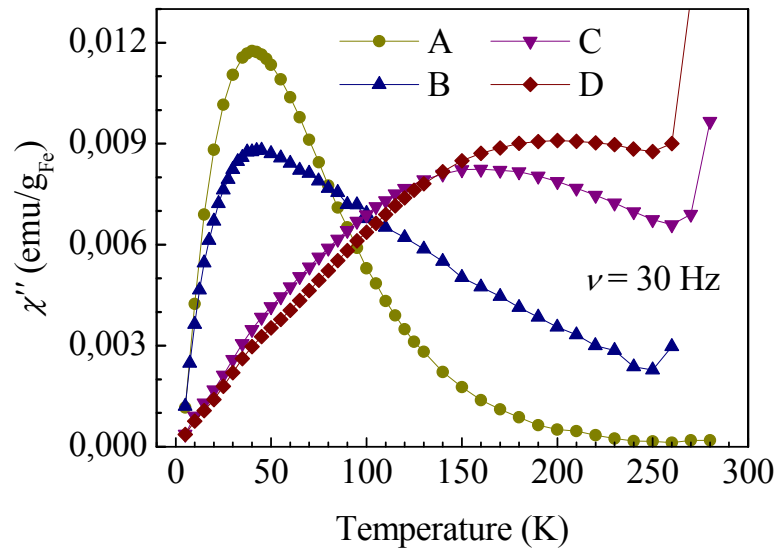


**Figure 3.**  $\chi''$  vs. temperature for samples A to D. The  $T_B$  increases with increasing average sizes. Colour online.

From the plot of magnetization versus applied field (Figure 4) it is evident that the magnetization increases with increasing particle size as previously found in maghemite/PVP composites.<sup>[25]</sup> Fitting these curves to a Langevin function<sup>[26]</sup> modified by adding a linear term, it is possible to conclude that the average magnetic moment of the particles increases with the MNPs size. This model assumes that the core of the MNPs behaves as a single spin (with the same value for all MNPs), and that the magnetic moments, at the MNPs' surface, have a linear behaviour with the field in the studied field range.<sup>[25]</sup> The linear term also accounts for the diamagnetic contributions of the polymer coating and the fluid.

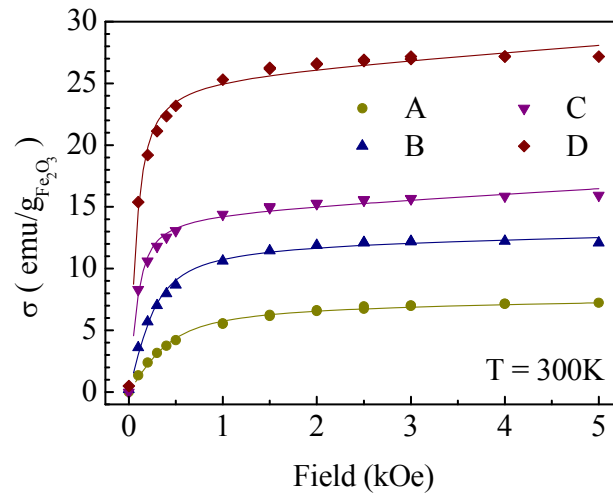


**Figure 4.** Magnetization per gram of iron oxide for the series of samples. Lines correspond to fitting to a modified Langevin function. Colour online.

To evaluate the MRI contrast efficiency of the samples, the nuclear longitudinal and transverse relaxivities ( $r_1$  and  $r_2$ , respectively) were obtained from the spin-lattice  $T_1$  and the spin-spin  $T_2$  relaxation times measured at room temperature for each frequency, as:<sup>[10,16]</sup>

$$r_i = \left[ (1/T_i)_s - (1/T_i)_d \right] / c$$

Where  $i = 1, 2$ , and  $c$  is the iron concentration in the sample (in mM),  $(1/T_i)$  are the nuclear relaxation rates and the suffixes  $s$  and  $d$  stand for sample and dispersant (in our samples PBS at physiological pH), respectively.

The NMR-dispersion profiles for samples A to D and the commercial compound Endorem are shown in Figure 5. The longitudinal relaxivity curves are constant for low frequencies. In the range from 1 to  $\sim 10$  MHz  $r_1(\nu)$  shows a maximum for sample A and Endorem, with similar  $D_p$  (see Table 1), which is not present for the rest of the samples; apparently in our system there is a threshold in the particle size around 8 nm over which this maximum is no longer present.  $r_1(\nu)$  rapidly decreases for higher frequencies. The transverse relaxivity has a linear behaviour in the studied frequency range with a slope very close to zero.

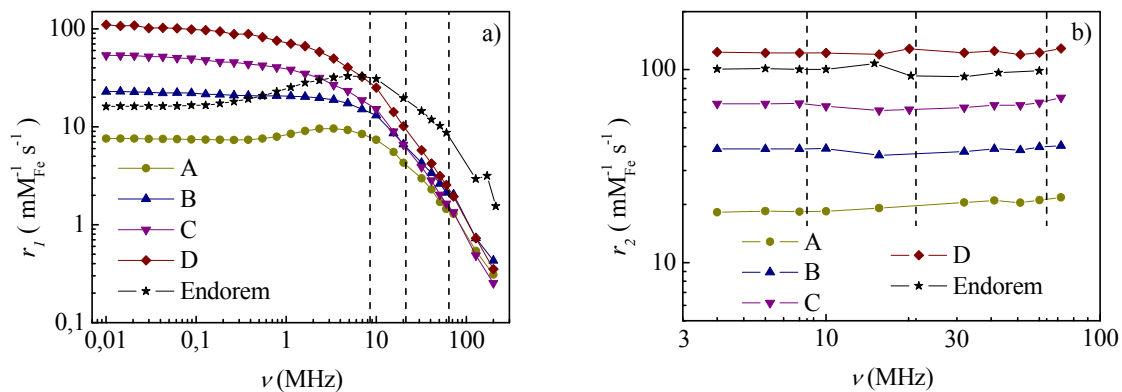


**Figure 5.** a) longitudinal  $r_1$  and b) transverse  $r_2$  relaxivities vs. frequency for samples A to D and the commercial CA, Endorem. Dashed lines indicate the operating frequencies of most clinical imagers ( $\nu \approx 8.5, 21$  and  $63$  MHz). Colour online.

Regarding the mechanisms that induce nuclear longitudinal relaxation in SP particles, it is worth to remind that the main mechanisms are:<sup>[16,27]</sup> (a) for  $\nu < 1 \div 5$  MHz, the Neel relaxation of the particle magnetization, giving a correlation time related to the magnetic anisotropy barrier, and an associated reversal time,  $\tau_N$ , that follows the Arrhenius law; (b) for  $\nu > 1 \div 5$  MHz, the Curie relaxation, which takes into account the sample magnetization through the (square of) Langevin function weighted by the spectral density function  $J^F(\omega_D)$ , where  $\omega_D = 1/\tau_D$ ,  $\tau_D$  being the correlation time related to the diffusion of the water. While the mechanism (a) gives a flattening of  $r_1(\nu)$  at frequencies  $\nu < 1 \div 5$  MHz, the mechanism (b) is responsible of the maximum in  $r_1(\nu)$  at higher frequencies  $\nu > 1 \div 5$  MHz, see Endorem and sample B in Figure 5a. In addition, for particles characterized by a distance  $< 5$  nm between the magnetic core and the hydrogen nuclei of the bulk water (eventually permeating the coating), a “dispersion” at intermediate frequencies occurs.<sup>[16,27]</sup> As said above, no high-frequency maximum is observed in most of our samples. This fact can be tentatively attributed to the dominant role of the contribution coming from the magnetic anisotropy that “covers” the high frequency feature arising from Curie relaxation, possibly depressed also by a scarce contribution of the diffusion process to  $r_1(\nu)$ .

A detailed discussion on the frequency dependence of longitudinal relaxivity in our system would require further experimental and theoretical investigations that we are currently undertaking. Here, we will restrict to an analysis of the variation of  $(1/T_1)_s = R_1(\nu)$  and  $(1/T_2)_s = R_2(\nu)$  at low frequencies for different particle sizes. Roch and Muller proposed a theoretical model that relates  $R_1$  and  $R_2$  to the energy levels of a magnetic particle of spin  $S$  obtained from a simplified Hamiltonian accounting for (magnetic) anisotropy energies.<sup>[27]</sup> This model is computer-time-consuming and, as such, inapplicable to large particles with a high total spin,  $S$ . To overcome these limitations, the authors suggested an alternative heuristic model where  $R_1$  and  $R_2$  are expressed (Eqs. 31 and 32 in Ref. [27]) as the sum of two contributions corresponding to the limits of zero and high anisotropy in the complete theory, respectively. The expressions of  $R_1$  and  $R_2$  can be simplified (the Langevin term in particular) for low frequencies, and still reproducing the increase of the absolute values of  $r_1$  and  $r_2$  with particle size in this frequency range, as follows:

$$R_1 = \frac{1}{3} C_1 \times \{7PJ^F[\Omega(\omega_S, \omega_0), \tau_D, \tau_N] + [7Q + 3] \times J^F(\omega_H, \tau_D, \tau_N)\} \quad (1)$$

$$R_2 = \frac{1}{3} C_2 \times \{13PJ^F[\Omega(\omega_S, \omega_0), \tau_D, \tau_N] + 7J^F(\omega_H, \tau_D, \tau_N) + 6J^F(0, \tau_D, \tau_N) + 3[3J^F(\omega_H, \tau_D, \tau_N) + 4J^F(0, \tau_D, \tau_N)]\} \quad (2)$$

$$C_1 = \left( \frac{32\pi}{135000} \right) \gamma_H^2 \mu_{SP}^2 \left( \frac{N_{SP}}{RD} \right) = \frac{32}{16} C_2 \quad (3)$$

where  $\mu_{SP}$  is the magnetic moment of the nanoparticle,  $\gamma_H$  the gyromagnetic ratio of protons,  $N_{SP}$  the number of particles per litre,  $R$  the particle radius,  $D$  the diffusion coefficient,  $\tau_D$  the diffusion correlation time of the water molecules,  $\tau_N$  the Néel relaxation time,  $\omega_S$  and  $\omega_H$  the electron and proton Larmor angular frequencies, and  $J^F$  is a spectral density function accounting for the proton diffusion in the non uniform magnetic field created by  $\mu_{SP}$ , and its fluctuation around its mean value;  $\omega_0$  is an

adjustable parameter that considers the anisotropy field in the electron Larmor angular frequency ( $\omega_0 < \omega_S$ ), and  $P$  and  $Q$  ( $P+Q \leq 1$ ) are weighing factors for functions corresponding to zero and high anisotropy cases, respectively. Figure 6 shows that this approximation is valid up to 1 MHz.

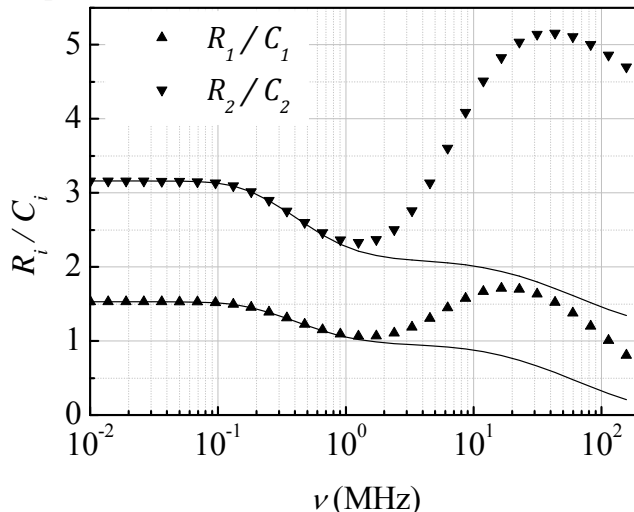


**Figure 6.** Theoretical frequency dependence of longitudinal and transverse relaxivities and their low field approximation (lines) divided by  $C_i$  using the same parameters as in Figure 8 of reference no. 25.

As the absolute values of the terms in brackets multiplying  $C_1$  and  $C_2$  in Eq. 1 and 2 hardly change with the magnetic core diameter  $D_p$ , in the low frequency range the most important contribution to the size dependence of  $R_1$  and  $R_2$  comes from the term  $\mu_{SP}^2 N_{SP}/R$ . It is important to note that the iron concentration, commonly used to normalize the NMRD curves of different samples, is implicit in the particle density or number of particles per litre ( $N_{SP}$ ) so that, for a fixed iron concentration, the particle density differs among samples with different particle size.

Figure 7 shows that  $r_1$  and  $r_2$  absolute values at low frequency increase quite linearly with  $\mu_{SP}^2 \left( \frac{N_{SP}}{R} \right)$ . Therefore, the main reason for the increase with size of  $r_1$  and  $r_2$  along the series of samples is caused by an increment of  $\mu_{SP}$ .

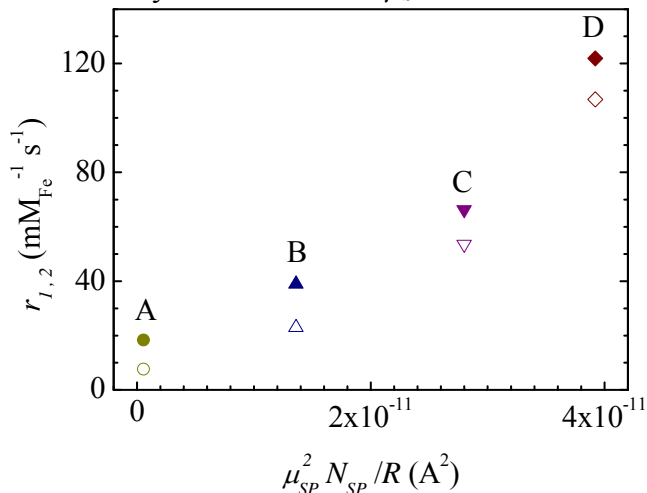




**Figure 7.** Low frequency  $r_1$  (open symbols) and  $r_2$  (full symbols) absolute values as a function of  $\mu_{SP}^2 \left( \frac{N_{SP}}{R} \right)$  for samples A to D.  $\mu_{SP}$  and  $N_{SP}$  are extracted from the fit of  $\sigma$  vs.  $H$  in Figure 4. Color online.

Samples with the highest  $r_2$  values at 8.5 MHz (C and D, Figure 5b) were selected for MRI experiments. Prior to imaging, the iron concentration of all samples was carefully fixed at 0.02 g/L.

In Figure 8 images of samples C, D and the commercial CA are presented for two different pulse sequences, a) High resolution Gradient Echo and b) High resolution Spin Echo. It is apparent for both sequences that sample D signal is darker than Endorem and therefore shows a better performance as negative contrast agent at the imager operating frequency (8.5 MHz).

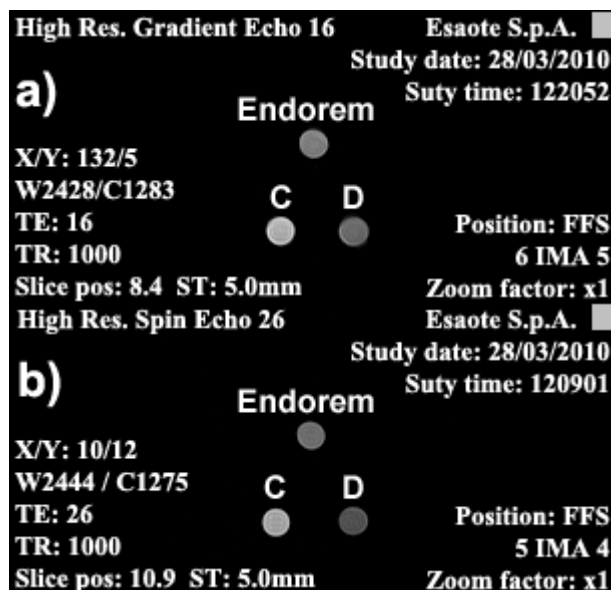


**Figure 8.** MRI images of vials containing samples C, D and Endorem with the same concentrations (0.02 mg/ml) obtained by Artoscan (by Esaote SpA) imager at 8.5 MHz: a) High resolution Gradient Echo and b) High resolution Spin Echo.

### 3. Conclusions

In summary, we report on the efficiency as contrast agents for MRI of a series of multifunctional maghemite/polymer composite ferrofluids, made of fully biocompatible ingredients, with several particle sizes. Both longitudinal and transverse relaxivities show a strong increase with the particle size in relation to the increase of magnetic moment, the best efficiency (i.e. the highest transverse relaxivity as usual for superparamagnetic CA) being reached for the maximum magnetic core diameter. This is in accordance with the predictions of the heuristic model by A. Roch and R.N. Muller.<sup>[27]</sup> Remarkably, the sample with the highest particle size,  $D = 15$  nm, has demonstrated a capacity as MRI contrast agent superior to a well-known commercial product, i.e. Endorem, both in

transverse relaxation measurements and *in vitro* MRI experiments. The presented multifunctional ferrofluids have thus proven to be very interesting model systems for both fundamental studies of nuclear relaxation induced by superparamagnetic nanoparticles and clinical MRI. Further investigations about the toxicology and the ability of our systems as magnetic fluid hyperthermia mediators,<sup>[28]</sup> which could allow to propose them as future theranostic agents, are under way.

#### 4. Experimental Section

The synthesis of the ferrofluids was performed in two steps: 1) synthesis of maghemite/PVP nanocomposites, and 2) synthesis of ferrofluids (using the nanocomposites) in a PBS medium.

Maghemite/PVP nanocomposites were prepared by *in situ* precipitation from iron–PVP coordination compounds, following the procedure described in Ref. [7]. A film of iron-polymer precursor was obtained by evaporation of a 50% water:acetone solution containing 0.2 g of PVP (Aldrich, 60 kD), and variable amounts of FeBr<sub>2</sub> (Aldrich) and FeBr<sub>3</sub> (Aldrich). The precursor film was treated with 20 mL of 1 M NaOH solution for 1 h, washed with water and dried in open air to obtain a maghemite nanocomposite. The size of the maghemite nanoparticles in the composites was tuned by using different Fe(II)/Fe(III) and Fe/N ratios. Composites for samples A-C were prepared using a Fe(II)/Fe(III) ratio of 0.5 and Fe/N ratios of 0.5, 0.625 and 1 respectively. Composite for sample D was prepared using a ratio of 1 for both Fe(II)/Fe(III) and Fe/N.

The ferrofluids were prepared according to Ref. [6]. The maghemite/PVP nanocomposites were dispersed in an acidic solution at pH  $\approx$  3. The resulting acidic ferrofluid was mixed with 0.18 mL of PEG (MW=200 D) acrylate (PEG(200)-A) (Monomer&Polymer), and 0.02 g of PEG (MW=1000 D) acrylate (PEG(1000)-A-COOH) (Monomer&Polymer), and was heated to 70 °C during 24 h. Then, Na<sub>2</sub>HPO<sub>4</sub> was added for a 0.01 M final concentration, the pH was adjusted to 7.40 by addition of a 0.2 M NaOH solution, and the ionic strength was adjusted to 0.15 by addition of NaCl and KCl. Finally, the dispersion was filtered through a 0.22  $\mu$ m membrane filter to obtain a bioferrofluid.

The total iron content in the samples was determined by atomic absorption in a plasma 40 ICP Perkin–Elmer spectrometer. The size of the maghemite nanoparticles was determined by transmission electron microscopy (TEM) images in a Philips CM30 microscope. The samples were prepared by dip coating of carbon coated copper grids in the ferrofluid solution. The hydrodynamic size distribution of the dispersed nanoparticles in the ferrofluids was determined by Dynamic Light Scattering (DLS) using the Zetasizer Nano ZS of Malvern.

The magnetic properties of these ferrofluids were studied by means of dc magnetization as a function of field at room temperature and ac magnetic susceptibility measurements as a function of temperature and frequency in a MPMS-XL SQUID magnetometer from Quantum Design.

The MRI contrast efficiency was assessed studying the behaviour of the nuclear relaxation rates per iron concentration, expressed in mM. The <sup>1</sup>H NMR technique was employed to measure the longitudinal and transverse relaxivities in a wide range of

frequencies covering most of the clinical imagers ( $\nu \approx 8.5, 21$  and  $63$  MHz corresponding to about  $0.2, 0.5$  and  $1.5$  T respectively). For  $10\text{ kHz} \leq \nu \leq 10$  MHz, the NMR data were collected with a Smartracer Stellar relaxometer using the Fast-Field-Cycling technique, while for  $\nu > 10$  MHz a Stellar Spinmaster and an Apollo-Tecmag spectrometers have been used. Standard radiofrequency excitation sequences CPMG-like and saturation-recovery were applied to determine  $T_2$  and  $T_1$  values.

MRI experiments were performed at  $8.5$  MHz using an Artoscan Imager by Esaote SpA. The employed pulse sequences were: a) High resolution Gradient Echo with TR/TE/NEX =  $1000\text{ms}/16\text{ms}/4$ , matrix =  $256*192$ , FOV =  $180*180$ , flip angle =  $90^\circ$  and b) High resolution Spin Echo sequence with TR/TE/NEX =  $1000\text{ms}/26\text{ms}/4$ , matrix =  $192*192$ , FOV =  $180*180$ . Here TE is the echo time, TR the repetition time and NEX the number of averages.

### Acknowledgements

Financial support from the Spanish Ministry of Science and Innovation research grants MAT2007-61621, and Project Consolider-Ingenio in Molecular Nanoscience CSD2007-00010 are gratefully acknowledged. Thanks to EU-NoE MAGMANet for partly funding the project, and to E. Micotti, F. Orsini, and M. Pasin for their collaboration. R. Bustamante would like to thank ICMA-CSIC for the JAE-predoc grant. N. J. O. S. acknowledges FCT for Ciencia 2008 program.

- [1] Y. Piao, A. Burns, J. Kim, U. Wiesner, T. Hyeon, *Adv. Funct. Mater.* **2008**, 18, 3745.
- [2] J. Kim, Y. Piao, T. Hyeon, *Chem. Soc. Rev.* **2009**, 38, 372.
- [3] S. Mitragotri, J. Lahann, *Nature Mater.* **2009**, 8, 15.
- [4] Q.A. Pankhurst, J. Connolly, S.K. Jones, J. Dobson, *J. Phys. D: Appl. Phys.* **2003**, 36, R167.
- [5] W. Cai, X. Chen, *Small* **2007**, 3, 1840.
- [6] A. Millan, F. Palacio, G. Ibarz, E. Natividad, Patent ES2308901.
- [7] A. Millan, F. Palacio, A. Falqui, E. Snoeck, V. Serin, A. Bhattacharjee, V. Ksenofontov, P. Gütllich, I. Gilbert, *Acta Mater.* **2007**, 55, 2201.
- [8] R. Villa-Bellosta, G. Ibarz, A. Millan, R. Pinol, A. Ferrer-Dufol, F. Palacio, V. Sorribas, *Toxicol. Lett.* **2008**, 180, S221.
- [9] N. Lewinski, V. Colvin, R. Drezek, *Small* **2008**, 4, 26.
- [10] a) P.A. Rinck, *Magnetic Resonance in Medicine*, 3rd ed. Blackwell, Oxford, UK **1993**; b) S. Laurent, L. Vander Elst, A. Roch, R.N. Muller, in *NMR-MRI,  $\mu$ SR and Mossbauer Spectroscopies in Molecular Magnets* (Eds. P. Carretta, A. Lascialfari), Springer-Verlag, Italia **2007**, p. 71; c) A. Lascialfari, M. Corti, “*NMR-MRI,  $\mu$ SR and Mossbauer Spectroscopies in Molecular Magnets*” (Eds. P. Carretta, A. Lascialfari), Springer-Verlag, Italia **2007**.
- [11] H.J. Weinmann, R.C. Brasch, W.R. Press, G.E. Wesbey, *American Journal of Roentgenology* **1984**, 142, 619.
- [12] M. Laniado, H.J. Weinmann, W. Schörner, R. Felix, U. Speck, *Physiological Chemistry & Physics & Medical NMR* **1984**, 16, 15.

- [13] D.J. Widder, W.L. Greif, K.J. Widder, R.R. Edelman, T.J. Brady, *American Journal of Roentgenology* **1987**, 148, 399.
- [14] R. Weissleder, G. Elizondo, J. Wittenberg, C.A. Rabito, H.H. Bengel, L. Josephson, *Radiology* **1990**, 175, 489.
- [15] R. Weissleder, A. Moore, U. Mahmood, R. Bhorade, H. Benveniste, E.A. Chiocca, J.P. Basilion, *Nature Med.* **2000**, 6, 151.
- [16] S. Laurent, D. Forge, M. Port, A. Roch, C. Robic, L. Vander Elst, R.N. Muller, *Chem. Rev.* **2008**, 108, 2064.
- [17] M.F. Casula, P. Floris, C. Innocenti, A. Lascialfari, M. Marinone, M. Corti, R.A. Sperling, W.J. Parak, C. Sangregorio, *Chem. Mater.* **2010**, 22, 1739.
- [18] a) A. Boni, M. Marinone, C. Innocenti, C. Sangregorio, M. Corti, A. Lascialfari, M. Mariani, F. Orsini, G. Poletti, M.F. Casula, *J. Phys. D: Appl. Phys.* **2008**, 41, 134021; b) M. Corti, A. Lascialfari, M. Marinone, A. Masotti, E. Micotti, F. Orsini, G. Ortaggi, G. Poletti, C. Innocenti, C. Sangregorio, *J. Magn. Magn. Mater.* **2008**, 320, e316.
- [19] M. Corti, A. Lascialfari, E. Micotti, A. Castellano, M. Donativi, A. Quarta, P.D. Cozzoli, L. Manna, T. Pellegrino, C. Sangregorio, *J. Magn. Magn. Mater.* **2008**, 320, e320.
- [20] H. B. Na, I. C. Song, T. Hyeon, *Adv. Materials* **2009**, 21, 1.
- [21] U. I. Tromsdorf, N.C. Bigall, M.G. Kaul, O.T. Bruns, M.S. Nikolic, B. Mollwitz, R.A. Sperling, R. Reimer, H. Hohenberg, W.J. Parak, S. Forster, U. Beisiegel, G. Adam, H. Weller, *Nano Lett.* **2007**, 7, 2422.
- [22] a) M.C. Franchini, G. Baldi, D. Bonacchi, D. Gentili, G. Giudetti, A. Lascialfari, M. Corti, P. Marmorato, J. Ponti, E. Micotti, U. Guerrini, L. Sironi, P. Gelosa, C. Ravagli, A. Ricci, *Small* **2010**, 6, 366; b) C.G. Hadjipanayis, M.J. Bonder, S. BalaKrishnan, X. Wang, H. Mao, G.C. Hadjipanayis, *Small* **2008**, 4, 1925.
- [23] L. Néel, *Ann. Geophys.* **1949**, 5, 99.
- [24] W.F. Brown Jr., *Phys. Rev.* **1963**, 130, 1677.
- [25] A. Millan, A. Urtizberea, N.J.O. Silva, F. Palacio, V.S. Amaral, E. Snoeck, V. Serin, *J. Magn. Magn. Mater.* **2007**, 312, L5.
- [26] P. Langevin, *Annales de Chimie et de Physique* **1905**, 5, 70.
- [27] A. Roch, R.N. Muller, P. Gillis, *J. Chem. Phys.* **1999**, 110, 5403.
- [28] R. Bustamante, A. Millan, F. Palacio, et al., work in progress.